An investigation of efficient room temperature luminescence from silicon which contains dislocations

A thesis submitted for the degree of Doctor of Philosophy

in the University of Oxford

by

DAVID J. STOWE

ST. ANNES'S COLLEGE, OXFORD

Michaelmas Term 2006

To my mother, my father and Laura

for their continuous love and support and without

whom this thesis would not have be possible

Abstract

An investigation of efficient room-temperature luminescence from silicon which contains dislocations

David J. Stowe — Doctor of Philosophy
St. Anne's College — Michaelmas Term 2006

This thesis presents an investigation of the phenomenon of efficient, room-temperature luminescence from dislocation-engineered (DE) silicon. Previous work had demonstrated that the introduction of near-surface dislocation loops to a silicon substrate by boron ion implantation and high temperature annealing produced efficient electroluminescence at room temperature. However, the mechanism by which high efficiency luminescence is produced was not understood.

A wide matrix of specimens containing dislocations was fabricated by a variety of methods, including ion implantation, and their luminescence efficiencies were correlated to their physical properties.

Transmission electron microscopy was used to characterise the defect structures created by ion implantation. In the majority of specimens a band of dislocation loops in close proximity to the surface was observed. The dislocation loops were shown to be consistent with a mixture of Frank and perfect dislocation loops, the relative proportions of which were dependent upon processing conditions. The thermal evolution of the dislocation loop size distribution was investigated. For the first time, a size distribution displaying a double peak was observed. The size distribution was shown to be consistent with the Gaussian distribution of two defect populations of different mean diameter. The thermal evolution of the size distribution was investigated in silicon implanted samples. A flux of self-interstitials from Frank dislocation loops to perfect dislocation loops was deduced. The evolution of the dislocation loop sizes was found to be consistent with Ostwald ripening.

Cathodoluminescence (CL) was used to investigate the luminescent properties of silicon at room temperature for the first time. A new CL system was installed for this work, initially the CL system was characterised and a routine to ensure a high degree of reproducibility was formed.

The luminescence mechanism of DE-silicon was shown to be the same as in unprocessed silicon wafers; TO phonon-assisted recombination. The mechanism of enhanced luminescence from DE-silicon was unambiguously shown to be due to the gettering of electrically active impurities from the specimen bulk. A reduction in the bulk transition metal impurity concentration of up to 35 times was inferred.

In samples which were implanted with boron the degree of gettering was found to show a logarithmic dependence on the dislocation density. Using a cross-sectional mapping technique, implanted samples were shown to contain a lower concentration of transition metal impurities throughout the entire wafer in comparison to as-received, unprocessed specimens. Furthermore, the impurity concentration was found to be lowest in close proximity to the band of dislocation loops. The dislocation loops were found to act as non-radiative recombination centres and their strength was strongly influenced by the local carrier concentration. The high doping levels of samples implanted with boron were found to minimise the non-radiative recombination action of the dislocations. Low temperature annealing was used to improve the luminescence efficiency of DE-silicon further.

Preface

This thesis is an account of the work carried out by the author in the Department of Materials, University of Oxford, under the supervision of Dr. P. R. Wilshaw.

No part of this thesis has been previously submitted for a degree at this or any other university. The work of other authors has been freely drawn upon and is duly acknowledged in the text. A list of cited references is given at the end of the thesis.

Some of the work described in the thesis has been presented in four international conferences (ICDS 2003, EMAG 2003, MOSM 2005 and EDS 2006) and published in the following papers:

1) Fraser, K.J., Stowe, D.J., Galloway, S.A., Senkader, S., Falster R.J. and Wilshaw, P.R. (2006) "The role of dislocations in producing efficient near-bandgap luminescence from silicon" *Accepted for publication in Phys. Stat. Sol. C.*

2) Stowe, D.J., Fraser, K.J., Galloway, S.A., Senkader, S., Falster, R.J. and Wilshaw, P.R. (2005) "Efficient, room-temperature, near-band gap luminescence by gettering in ion implanted silicon" *Springer Proc. in Phys.* **107** (eds. Cullis, A. G. and Hutchinson J. L.) 355.

3) Stowe, D.J., Galloway, S.A., Senkader, S., Kanad Mallik, Falster, R.J. and Wilshaw, P.R. (2004) "A room temperature cathodoluminescence study of dislocations in silicon" *Inst. Phys. Conf. Ser.* **179** 67.

4) Stowe, D.J., Galloway, S.A., Senkader, S., Kanad Mallik, Falster, R.J. and Wilshaw, P.R, (2003) "Near band gap luminescence at room temperature from dislocations in silicon" *Physica B*, **340-342** 710.

Oxford, 24/11/2006

David J. Stowe

……

Acknowledgements

I would like to thank everyone from the Semiconductor group past and present who have made my years in Oxford such a pleasure. A special mention must go to my supervisor, Dr. Peter Wilshaw, for his continuous support, enthusiasm and the many whiteboard discussions, not to mention for buying the odd beer or two – I will always remember THAT conversation in the pub. I would also like to thank Semih Senkader for the hours spent reading this thesis, Chris Marsh for help with all things TEM related, Kanad Mallik for help with the DLTS (even though it missed the final cut) and Andrew Walpole who made writing-up a (slightly) less painful experience.

I would also like to thank Dr. Robert (Bob) Falster at *M.E.M.C. Electronic Materials S.p.a. (Italy)*, who has made this project possible by providing all the Cz-silicon wafers and facilitated the implantation and annealing processes kindly performed by Dr O. Krause and Dr P. Pichler at the University of Erlangen-Nuremberg. Many thanks also to Dr. O Andersen and his R&D group at *Topsil Semiconductor Materials S.A. (Denmark)* for supplying the FZ-silicon wafers used in this thesis. Many thanks also to Dr. Simon Galloway who helped to install the cathodoluminescence system and provided training and was on call whenever needed.

I would also like to thank the many friends who have made my time in Oxford such a wonderful experience, there are too many of you to mention individually but you know who you are, and my parents who have helped me through to the end. And finally to Laura - the light at the end of the tunnel - I would never have written this without your love, support and encouragement; thank you.

Contents

List of Figures and Tables

Chapter 1

Introduction and literature survey

1.1 Background

In 2004 the estimated revenue of the microelectronics industry was $218 billion (Van Hoy, 2004). This success can largely be attributed to the many properties that make silicon the semiconductor material of choice for CMOS (complementary metal oxide semiconductor) technology, which accounts for more than 95% of the whole market of semiconductor integrated circuits (ICs) (Clemens, 1997).

Silicon is naturally abundant and can be purified to unprecedented levels: the concentration of the dominant impurity, interstitial oxygen, can be as low as ~ 10^{15} cm^{-3} (~100 ppb) (http://www.topsil.com). Silicon is easy to manufacture and handle, with good thermal and mechanical properties allowing relatively easy device processing. The natural oxide of silicon, SiO_2, is an excellent electrical insulator and can be preferentially etched with ease.

The intensive research activity into silicon processing and device fabrication has lead to a rapid improvement in IC processing power. The advancement in ICs can be demonstrated by examining the number of transistors on a single chip, which, following Moore's law, has approximately doubled every two years since 1972 due to the transistor gate length decreasing as a result of technological advances, see Figure 1.1. In practice, the latest Intel® Itanium® 2 processor contains 592,000,000 transistors and has a gate length of 50 nm, while gate lengths of sub 10 nm have been demonstrated (Ieong *et al.*, 2004). The developments have been driven by the need for shorter switching times and high-speed electronics (such as computers and wireless communications respectively).

In recent years there has been concern that the future progress of the microelectronics industry is reaching a limit as a consequence of fundamental materials and processing issues. Of particular importance is the potential limitation of

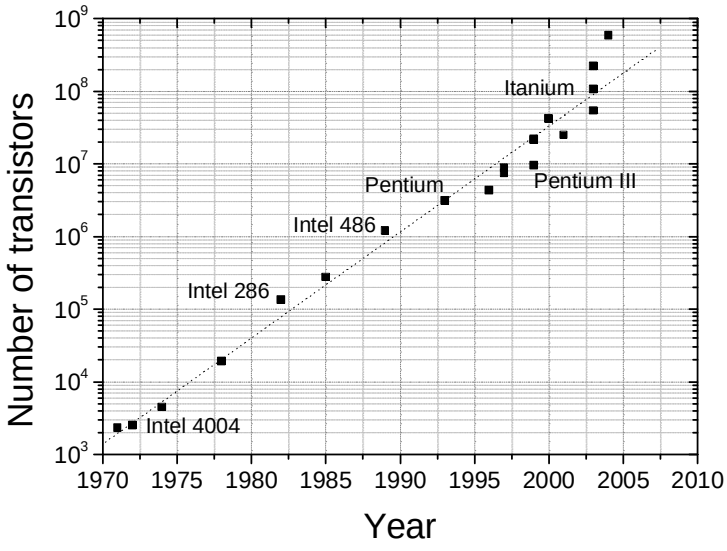

Figure 1.1

Evolution of the number of transistors on a single Intel® central processing unit since 1972. Data collected from: www.intel.com/research/silicon/mooreslaw.htm

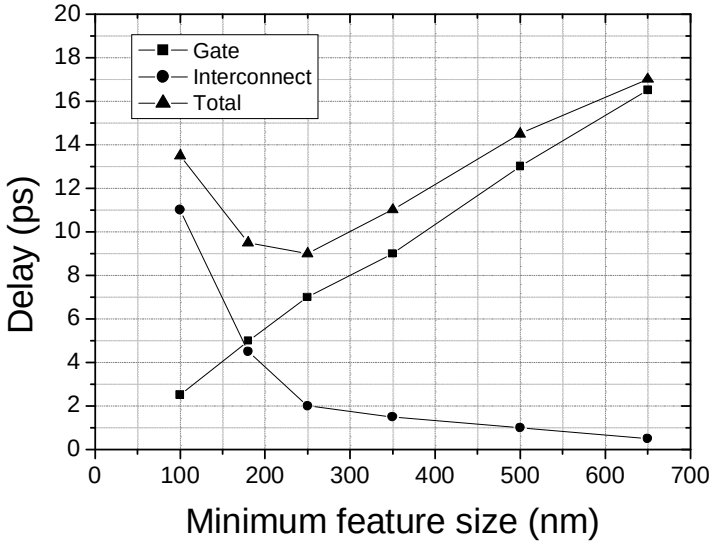

Figure 1.2

Calculated gate (Al contact, SiO_2 insulating layer) and interconnect delay as a function of the minimum device feature size (data collected from SIA roadmap 1997).

microelectronic device operating speeds by the interconnect delay (Risch, 2002). The further improvement in circuit integration requires the use of ever increasing interconnect length and complexity (5 km cm^{-2} in 2003 and an estimated 20 km cm^{-2} by 2013) (Pavesi, 2003). At present there are up to nine layers of metallic interconnects used in ICs; this is expected to increase to twelve within the next five years (www.intel.com). Figure 1.2 shows the signal delay as a function of the minimum feature size of the transistor (using aluminium interconnects and SiO_2 as the dielectric). For gate lengths of less than 200 nm the rate limiting step is the delay associated with interconnects rather than the switching time of individual components. Research aimed at reducing the influence of the interconnect delay by improving the dielectric layer and using copper wiring have reduced the limiting size to ~155 nm (Pavesi, 2003). It is estimated that the interconnect delay problem could restrict further improvements in processing speeds within the next ten years (Theis, 2000). A possible solution to this problem is through utilising optical interconnects (Miller, 2000).

Optical methods are used routinely to connect different computers using compound semiconductor lasers as signal sources and optical fibres as the transport medium. It is predicted that within 5 years different boards in the same computer will use optical connections, while the use of on-chip optical interconnects is being investigated with a view to use within the next 10 to 15 years (Pavesi, 2003).

Due to the demands of the communications industry the development of photonic based signal processing and transfer have advanced greatly in recent years. However, the photonics industry is disadvantaged in comparison to the microelectronics industry, as there is a lack of signal technology or single material leading the market; in recent years there appears to be a trend towards the acceptance

of indium phosphide as a substrate material (Communications Technology Roadmap, 2005). However, as yet, the production technology is still primitive (when compared to the silicon microelectronics industry) with high cost and good reproducibility still posing many problems. It is only recently that standard roadmaps were drawn up in an effort to identify the way forward (Communications Technology Roadmap, 2005).

The merging of microelectronic and photonic devices has, so far, largely been pursued by a hybrid technology approach, incorporating compound semiconductors with more standard silicon processing procedures. The results of this approach are often both expensive and complicated to produce. Despite this, the demonstration of a silicon-based planar lightwave circuit, using a III-V laser, has been achieved with some limited success (Kato and Tohmori, 2000). However, the most appealing solution would be devices created entirely of silicon where the extensive knowledge of fabrication and processing procedures can be utilised (Lockwood, 1998). It had been suggested that the introduction of silicon photonics would be a reality before the end of the twentieth century (Soref, 1993) and indeed many of the components for such a scheme to work have already been demonstrated with silicon based waveguides, detectors, optical modulators, routers and switching systems realised (Masini *et al.*, 2002). However, the lack of an efficient silicon-based optical emitter has proved insurmountable to date.

1.1.1 Silicon: an indirect bandgap semiconductor

The energy band structure of silicon and gallium arsenide are shown in Figure 1.3. In the case of silicon, the recombination of a hole at the X-point and an electron at the Γ-point in ***k***-space requires the participation of a phonon in order to conserve momentum making the recombination a second order process (Davies, 1989). This is

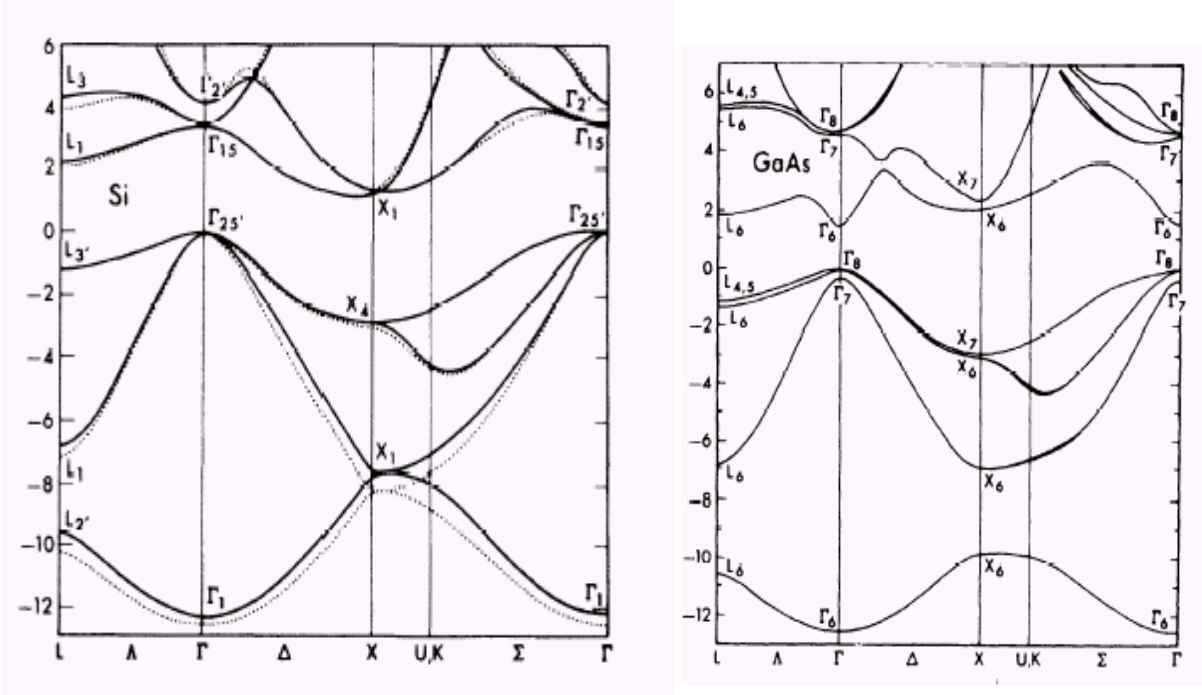

(a) **(b)**

Figure 1.3

Energy-band structures of (a) silicon and (b) gallium arsenide. Calculated using empirical non-local pseudopotential assumptions (after Chelikowsky and Cohen, 1976).

termed an indirect bandgap material. In direct bandgap materials such as gallium arsenide (Figure 1.3b) the X-point and Γ-point occur at the Brillouin zone centre allowing direct recombination between an electron and hole releasing an equivalent energy photon with the conservation of momentum. This transition, which involves only two particles, has a high probability. It has been estimated that the transition probabilities in the two cases differ by a factor of up to 10^7 (Hayes and Nilsson, 1964).

Light emission across the bandgap of silicon, at room temperature, results from the recombination of a free electron with a free hole (with the participation of a phonon) (Davies, 1989). The radiative recombination lifetimes are believed to be in the milliseconds range (Ossicini *et al.*, 2003 and Fauchet, 2004).

Despite the advances in semiconductor technology and the demonstration of many of the components required to create silicon-based photonics, the indirect bandgap of silicon has thus far proved to be an insurmountable barrier to the practical realisation of a viable light emitter, requiring novel approaches to be investigated. One such approach is based on dislocation-engineered (DE)-silicon (Ng *et al.*, 2001). Ion implantation was used to generate a band of small dislocation loops in close proximity to a *p*-*n* junction which, when forward biased, injected carriers which may recombine radiatively. Preliminary results showed relatively efficient (within a factor of ten of established techniques), bandgap-related luminescence from silicon at room-temperature. However, the mechanism for efficient luminescence from DE-silicon is not well understood and the prospect of increasing the efficiency to a useful level, based on an improved understanding, is potentially very exciting.

The work described in the remainder of this thesis is aimed at achieving a better understanding of the mechanism of luminescence from DE-silicon and an

investigation into the further enhancement of the luminescence using dislocation-engineering techniques.

The remainder of this chapter is structured as follows: firstly, electron-hole pair recombination mechanisms are introduced. This is followed by a discussion of the research activity aimed at enhancing room-temperature luminescence from silicon and silicon-based materials. The dislocation-engineering approach to achieving efficient silicon-based luminescence is then examined in detail, including a review of related work. Finally the structure and aims of this thesis are outlined.

1.2 Electron-hole recombination in silicon

At constant temperature and in thermal equilibrium the net concentration of holes and electrons in the valence and conduction band are independent of time. Consequently, the rate at which carriers are generated and the rate at which they recombine must be equal. Excess charge carriers can be generated at a particular rate by external interactions, such as high-energy photons or electrons, to a concentration above the thermal equilibrium values. The steady state generation of carriers does not however produce a continuing build up of carriers. Instead, recombination of electron-hole pairs establishes a new equilibrium carrier concentration dependent on both the generation and recombination rate.

In an infinite crystal with no defects an electron-hole pair recombines by the transition of an electron from the conduction band to the valence band, accompanied by the emission of either a photon (a radiative process), or by the transfer of energy to another free electron (the Auger process), as shown in Figure 1.4a. In reality, a second type of recombination process also occurs, where the transition between the

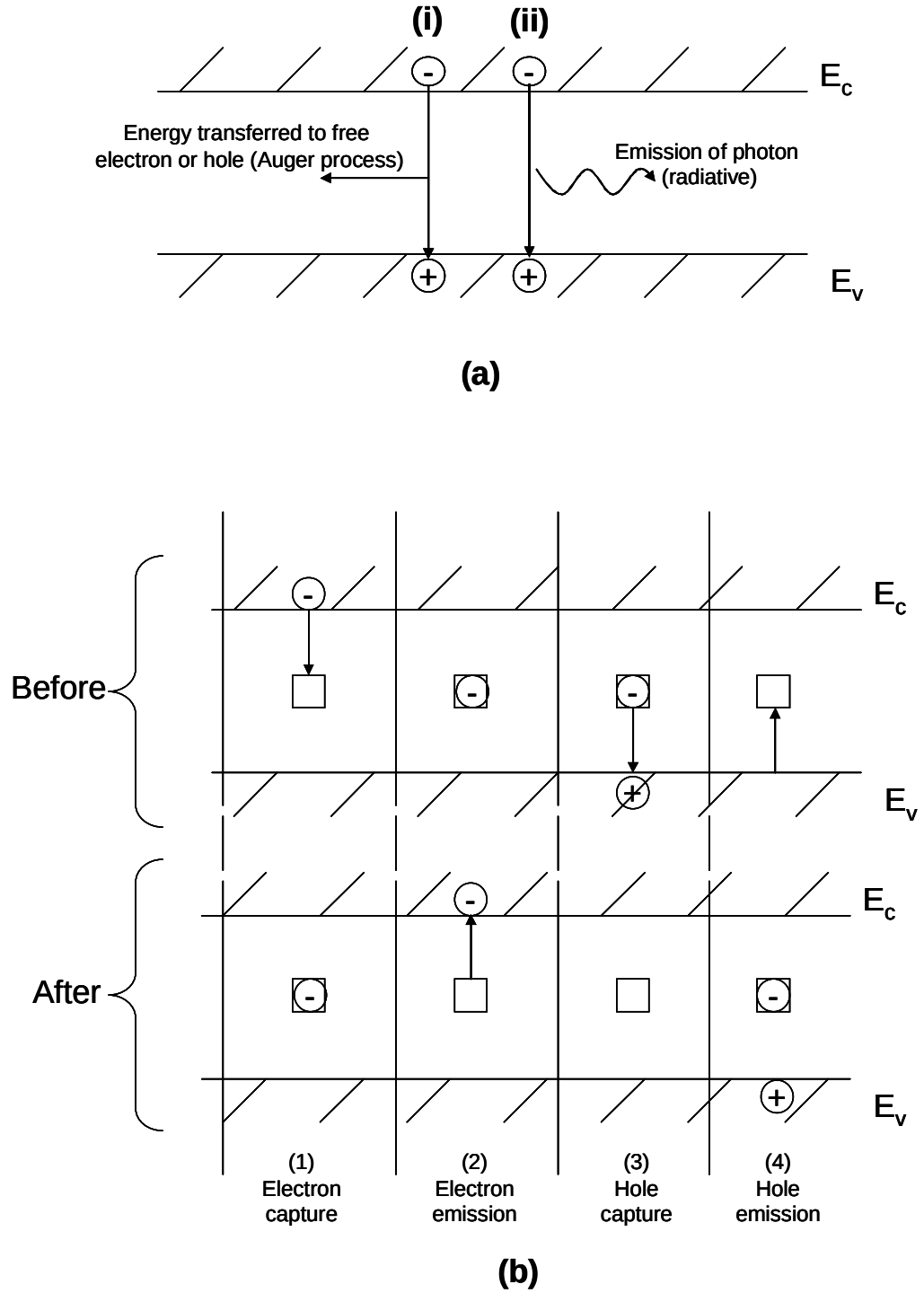

Figure 1.4

Electron-hole recombination processes in semiconductors (after Sze, 1981):

a) Band-to-band recombination i) Auger or ii) radiative

b) Single level recombination via mid bandgap defect (deep) level.

conduction band and valence band occurs via an allowed energy state in the semiconductor bandgap. This energy state may be introduced by an extrinsic recombination centre such as a point defect, extended defect or surface state, Figure 1.4b. These recombination mechanisms are described in further detail in the following sections.

The rate, R, at which a recombination event occurs via each mechanism is characterised by the lifetime, τ, where:

$$R \propto \frac{1}{\tau} \qquad \text{Eqn. 1.1}$$

The minority carrier lifetime (τ_{eff}) is dominated by the process with the shortest lifetime and is given by:

$$\frac{1}{\tau_{eff}} = \frac{1}{\tau_1} + \frac{1}{\tau_2} + \frac{1}{\tau_3} + ...\frac{1}{\tau_n} \qquad \text{Eqn. 1.2}$$

where τ_1, τ_2,….τ_n are the lifetimes of the recombination mechanisms $_1$, $_2$, …. $_n$.

1.2.1 Quantum efficiency of luminescence

The ability of a semiconductor to produce photons can be measured by one of two factors - the internal or external quantum efficiency.

The internal quantum efficiency (IQE), η_{int}, expresses the potential of a semiconductor to emit photons and is given by the fraction of electron-hole pairs that recombine radiatively:

$$\eta_{int} = \frac{\tau_{non-rad}}{\tau_{non-rad} + \tau_{rad}} \qquad \text{Eqn. 1.3}$$

where $\tau_{non\text{-}rad}$ is the lifetime for the recombination paths which do not involve the production of photons and τ_{rad} the radiative lifetime. The IQE of direct bandgap semiconductors can approach 100% (though are typically ~10%) because the radiative lifetime (a few ns) can be shorter than the non-radiative lifetime. For indirect bandgap semiconductors the IQE is typically as low as 10^{-6} to 10^{-7} (Fauchet, 2004).

The external quantum efficiency (EQE), η_{ext}, takes into account the fact that not all the photons generated internally exit the specimen surface and is defined as the ratio of photons emitted from the surface to the number of electron-hole pairs that recombine. Thus, the EQE is always lower than the IQE. In polished silicon wafers the IQE and EQE are related in the following empirical manner (Kittler *et al.*, 2005):

$$\eta_{int} = \frac{\eta_{ext}}{0.013} \qquad \text{Eqn. 1.4}$$

The following sections will consider the important recombination processes in greater detail. Firstly, non-radiative recombination will be considered followed by radiative recombination processes, including a discussion into their potential for creating silicon-based optical emitters.

1.2.2 Non-radiative recombination in silicon

1.2.2.1 Auger recombination

The energy released during an Auger recombination event is transferred to a second electron in the conduction band (shown in Figure 1.4a), which then loses its

surplus energy by thermalisation, *i.e.* by transfer to lattice phonons with no photon produced. In the case of an indirect band gap material, the recombination event requires phonon participation in order to conserve momentum.

The Auger recombination rate, R_{Auger}, can be expressed as:

$$R_{Auger} = G(n^2p + p^2n) \qquad \text{Eqn. 1.5}$$

Where G is the Auger coefficient and is found to be $1 \sim 2 \times 10^{-31}$ cm^6s^{-1} for silicon (Sze, 1981) and *n* and *p* are the electron and hole concentrations respectively.

1.2.2.2 Recombination via electrically active point defects

The addition of electrically active point defects (for example copper, iron or nickel atoms) introduces allowed energy levels (deep levels) into the forbidden energy bandgap. The introduced energy state allows the recombination of an electron-hole pair to proceed via the deep level; this process is described by Shockley-Reed-Hall (SRH) theory and tends to dominate the total recombination rate in indirect bandgap semiconductors (Sze, 1981).

According to SRH theory, single level recombination can be described by four processes where the deep states, of density N_T, are considered to be in one of two states which differ by a single unit of electronic charge, being positive, neutral or negative, these processes are termed electron capture, electron emission, hole capture and hole emission and are outlined in Figure 1.4b. The rate-limiting step is assumed to be the availability of electrons and holes for capture by the traps. By the detailed balance of the four electronic transitions the recombination rate via an electrically active point defect, R_T, is given by:

$$R_T = \frac{\sigma_n \sigma_p v_{th} (pn - n_i^{\,2}) N_T}{\sigma_n \left[n + N_c \exp\left(\frac{E_T - E_c}{kT} \right) \right] + \sigma_p \left[p + N_c \exp\left(\frac{-(E_T - E_c)}{kT} \right) \right]} \qquad \text{Eqn. 1.6}$$

where σ_n and σ_p are the electron and hole capture cross-sections respectively, v_{th} is the thermal velocity, n_i is the intrinsic carrier concentration, N_c is the density of states at the conduction band edge, E_T and E_c are the trap and conduction band energies respectively, k is the Boltzmann constant and T is the temperature. The dependence of the recombination rate at electrically active point defects on defect concentration, position of the energy level within the bandgap, carrier injection condition and temperature are shown in Figure 1.5.

The recombination rate at electrically active point defects is highly dependent upon temperature (with a ~10 order of magnitude increase between 50 and 150 K). This large increase in the non-radiative recombination rate provides a significant barrier to achieving efficient room-temperature luminescence from indirect bandgap semiconductors as at 25 K, recombination via electrically active point defects accounts for over 95% of the total recombination (Silicon handbook, 1988). However, as room-temperature is approached (from lower temperatures) the rapid increase in the recombination rate at point defects tends to dominate further and luminescence efficiencies are dramatically reduced. This is termed thermal quenching.

1.2.2.3 Surface recombination

In an infinite semiconductor at equilibrium, the net motion of holes and electrons is zero because just as many carriers move in one direction as the other. However, when the carriers are in a region of the material where they may reach the

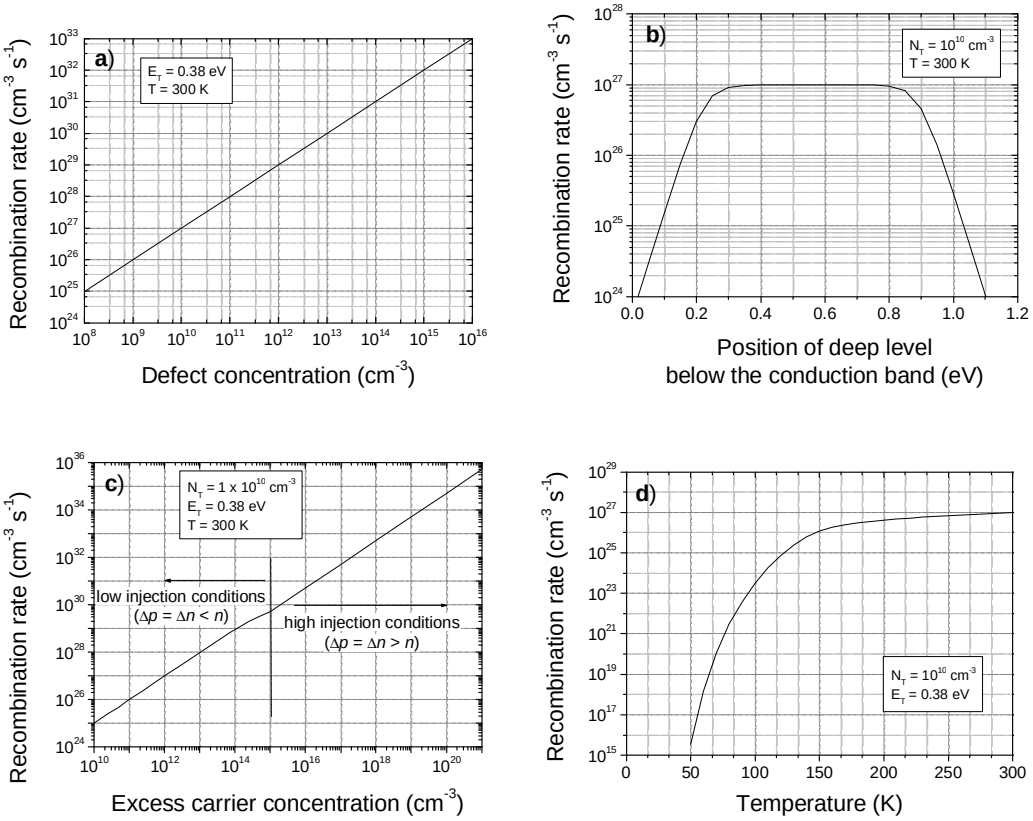

Figure 1.5

The calculated rate of non-radiative recombination at electronically active point defects using Shockley-Read-Hall theory as a function of:

a) defect concentration

b) position of deep level within the bandgap

c) excess carrier concentration

d) temperature.

Assumptions used where not stated were: $\sigma_n = \sigma_p = 1 \times 10^{15}$ cm^2, σ_n is independent of temperature, $n = 1 \times 10^{15}$ cm^{-3} and $\Delta p = 1 \times 10^{12}$ cm^{-3}.

surface of the semiconductor (or an interface), this situation no longer holds true. There are generally a large number of surface states which put deep levels into the bandgap, therefore acting as non-radiative recombination centres. As a result there is a net flow of charge carriers towards the surface. The quantity used to describe lost carriers is the velocity, v_s. More accurately the surface recombination velocity (SRV) is defined as the number of carriers recombining at the surface per unit area per unit time per unit volume of excess bulk carriers. The SRV can range from less than 10 cm s^{-1} (Schmidt *et al.*, 2001) to an appreciable fraction of the thermal velocity. The SRV is described by the Stevenson-Keyes expression, a modification of the SRH recombination theory:

$$SRV = \frac{R}{\Delta n} = N_s \frac{\sigma_n \sigma_p v_n v_p (n_0 + p_0)}{\sigma_n v_n (n_s + n_T) + \sigma_p v_p (p_s + p_T)} \qquad \text{Eqn. 1.7}$$

where n_s and p_s are the surface carrier densities, and N_s is the surface density of trapping states (~$10^{13}$$cm^{-3}$ depending on surface treatment) and σ their capture cross section (Aspnes, 1983).

If it is not possible to eliminate defects completely, the surface recombination may be reduced by minimising defect capture cross-sections, shifting energy states out of the bandgap or by pinning the Fermi energy at or near one of the band edges. SRV is also dependent on the sample doping level ($n_0 + p_0$), this follows from the fact that equilibrium between the space charge region and the bulk must exist. In samples with high bulk minority carrier lifetimes (particularly those used in photovoltaics) surface recombination can be significant and can even dominate overall recombination.

Surface passivation can be employed in order to reduce the SRV. Effective surface passivation can be achieved by producing a surface, or more often practised an interface, with a lower density of trapping states:

Silicon dioxide: The natural oxide of silicon can be an excellent passivation material. For example, Kerr and Cuevas (2002) report record effective minority carrier lifetimes of 32 and 29 ms for 90 Ωcm *n*-type and 150 Ωcm *p*-type FZ wafers. The authors produced an oxide layer at high temperature (1050 °C) and, with optimised processing, reduced the surface SRV to as low as 0.63 cm s^{-1}. A drawback to this method is the high thermal budget required to produce the passivating layers.

Silicon nitride: Chemical vapour deposited silicon nitride has been extensively studied as an alternative low temperature (typically less than 400 °C) passivating material (see for example Schmidt *et al.*, 2001 and Aberle and Hezel, 1997). Schmidt *et al.* (2001) report an effective minority carrier lifetime of ~0.95 ms for a silicon nitride passivated 1 Ωcm *p*-type wafer. The non-stochiometric nature of the passivating layer has, however, lead to difficulties in subsequent processing, particularly the wet etching required in device fabrication and stability issues upon further annealing. Schmidt *et al.* (2001) also report that the deposition of silicon nitride films upon thin (10 – 80 nm) SiO_2 films can result in an increase of the effective lifetime of nearly three orders of magnitude.

1.2.2.4 Non-radiative recombination at dislocations

The nature of dislocations as a site of non-radiative recombination has been known and investigated since the 1950s; a single dislocation in the active region of a

transistor can have a catastrophic effect on the device performance, often killing the device (Figielski, 1978).

Weber and Alexander (1979) discovered, using electron spin resonance (ESR) studies, that dangling bonds at the dislocation core are largely reconstructed resulting in a low concentration of defect states in the silicon bandgap to act as non-radiative recombination centres. The remaining dangling bonds were suggested to occur at jog or kink sites along the dislocation length. Experimental evidence suggests that it is the role played by transition metals such as Fe, Ni and Cu segregated or precipitated at the dislocation that affects the minority carrier lifetime rather than any defect core states as a result of the incomplete reconstruction (Kveder *et al.*, 2001). The recombination characteristics (with respect to temperature and minority carrier concentration) show five distinct trends which have been suggested to be related to transition metal contamination levels (Kittler *et al.*, 1995 and Shen *et al.*, 1996).

The temperature dependence of a typical electron beam induced current (EBIC) contrast (a measure of the increased recombination occurring at the dislocation compared to the bulk) reported in the literature is shown in Figure 1.6a (Kveder *et al.*, 2001). Types L1 and L2 are characterised by small contrast at room temperatures (less than 1%) and by increasing contrast with decreasing temperature, exhibiting a maximum between 50 and 90 K. The value of peak contrast varies significantly between studies. Kveder *et al.* (2001) attribute this to a variation in contamination levels at the dislocation. Thus type L1 dislocations, with peak contrast ~0.5% are considered to be 'clean' and type L2 dislocations, peak contrast up to 10%, contaminated by impurities. Increasing the contamination level leads to a further class of behaviour with dislocations exhibiting significant contrast at room temperatures with a decreasing contrast as the temperature is lowered (type H1). The

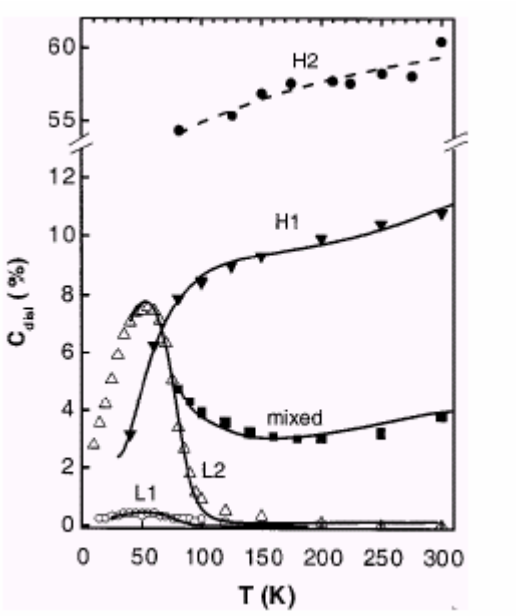

Figure 1.6a

The temperature dependence of electron beam induced current contrast (C_{disl}) of dislocations for different contamination levels (increasing contamination levels from L1 → L2 → mixed → H1 → H2) (after Kveder *et al.*, 2001).

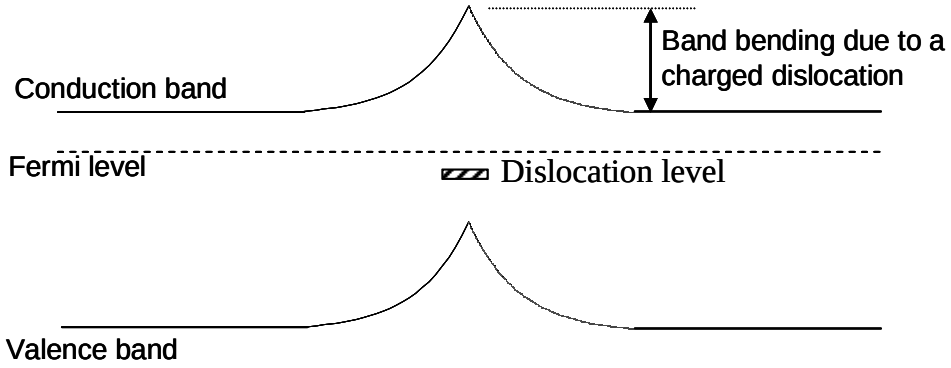

Figure 1.6b

Band diagram of a negatively charged dislocation in *n*-type material. The dislocation is below the Fermi level and is thus negatively charged. This negative charge increases the energy of electrons in the vicinity of the dislocation and is illustrated by the conduction and valence bands bending upwards.

final class has been associated with the formation of metal silicides at the dislocation (type H2) with contrast being typically 50-60% and greatest at room temperature. Nickel silicide precipitates have been observed by electron holography to act as internal Schottky junctions, attracting minority carriers and facilitating fast non-radiative recombination. There is a last class which exhibit a mixture of L2 and H1 behaviour. A contrast of ~4% is observable at room temperature (H1 behaviour) and upon cooling shows an increase in contrast below 150 °C (L2 type behaviour) (Formanek and Kittler, 2005).

All models used to describe the behaviour of carrier recombination are based on a band bending concept; in *n*-type silicon, acceptor states are introduced into the bandgap (Wilshaw, 1984) - these are normally considered to form a band of states below the Fermi level. Some of the states are occupied and thus the dislocation charges negatively. This negative charge increases the energy of electrons in the vicinity and this is represented by the valence and conduction bands bending upwards on an energy diagram, Figure 1.6b. An equilibrium charge state is reached when the Fermi level runs through the dislocation band. The recombination proceeds by the capture of minority carriers, a process aided by the coulombic band bending whereas majority carriers require excitation over the repulsive potential barrier in order to make the transition to the dislocation level. One model of recombination at dislocations by Wilshaw *et al.* (1989) has been widely applied to explain the contrast observed at dislocations as both a function of the electron beam current and temperature in EBIC studies between 120 and 370 K. The model assumes that the transition to the bound hole states is the rate limiting step and that the capture process relates to holes within the space charge region of the dislocation.

Kveder *et al.* (2001) have adapted previous models in order to take into account the strain field surrounding the dislocation which locally reduces the bandgap. Their model of recombination at a dislocation is shown in Figure 1.7. Deep levels (contamination related) and one dimensional bands (strain field related) are assumed to exchange electrons and holes. The main recombination channels are indicated. The probability of direct recombination between carriers trapped in the one dimensional bands (path A in Figure 1.7) is low. Thus, in 'clean' dislocations with a low concentration of deep level states the recombination activity is very small. There are two further possible recombination paths: (B) recombination of carriers trapped in the 1D bands via the deep level and (C) recombination of free carriers in the conduction and valence band by mediation of the deep level. Seifert and Kittler (2001) calculate that recombination channel B is dominant in material containing decorated dislocations. Results based on this assumption are shown in Figure 1.6a. Calculated data (solid lines) reproduces all the essential features of experimental results and shows the importance of the contamination level at the dislocation. Further to this Seifert and Kittler also suggest that the position of the deep level within the bandgap has little or no influence on the dislocation recombination strength as long as it is deeper than 0.3 eV below the conduction band edge; again this is consistent with experimental findings.

1.2.3 Radiative recombination in silicon

As described in Section 1.1 silicon is an indirect bandgap semiconductor with the recombination of a hole at the X-point and an electron at the Γ-point in ***k***-space requiring the participation of a phonon in order to conserve momentum. However, at low temperatures the electron and hole may be bound by coulombic attraction,

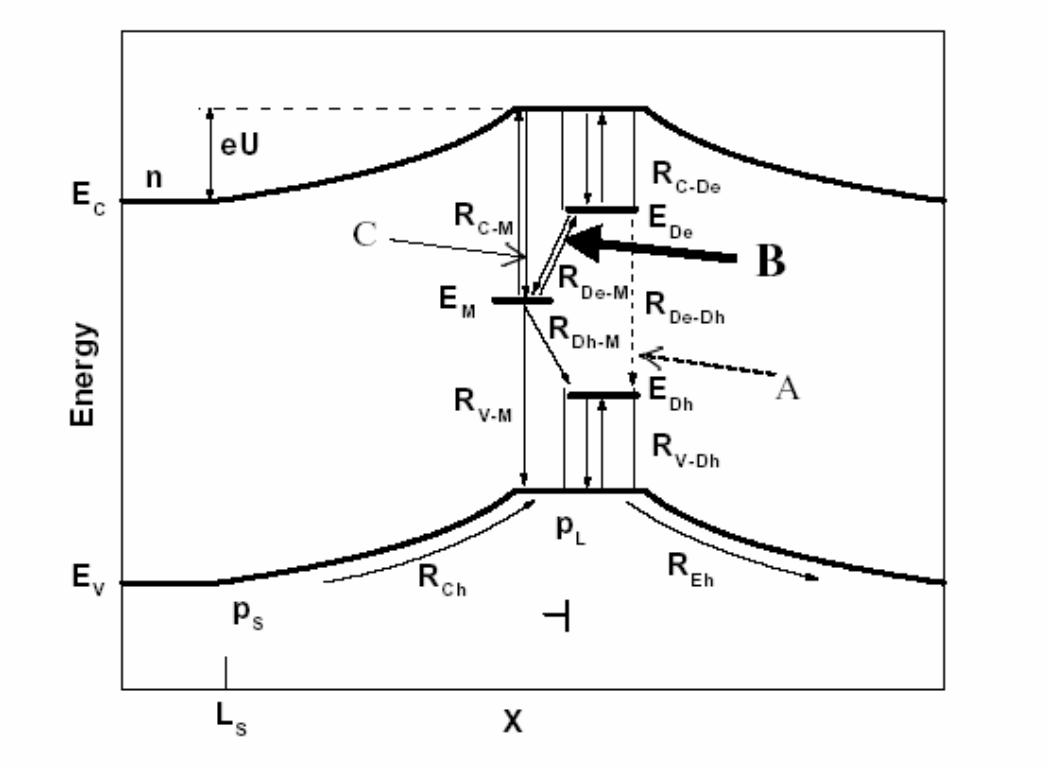

Figure 1.7

Schematic representation of electron-hole recombination at dislocations (after Kveder *et al.* (2001)). Recombination at clean dislocations occurs via direct exchange between the 1-dimensional dislocation bands E_{De}, E_{Dh} (path A). When deep levels (E_m) are present, recombination processes involving the deep levels dominate (paths B and C).

forming an exciton. At temperatures less than 30 K the free exciton consists of electron and hole states widely separated in ***k***-space and as a result their probability of recombination is low. This is evident when examining a typical luminescence spectrum; the recombination of the free exciton without participation of a phonon (peak labelled 0) is significantly weaker than the other phonon-assisted peaks, as shown in Figure 1.8.

During the lifetime of the free exciton there is a significant probability of the exciton being trapped at crystal defects where recombination can occur. The probability of radiative recombination of the trapped exciton at a defect may be significantly greater than in the case of the free exciton due its localisation. The radiative recombination process results in an emitted photon with an energy characteristic of the defect level.

The binding energy of the free exciton, 14.3 ± 0.05 meV, is however insufficient for significant concentrations to be present at room temperature, thus room temperature radiative recombination in silicon takes place via free-carrier phonon-assisted mechanisms (Davies, 1989).

1.2.3.1 Phonon-assisted recombination

Phonon dispersion curves are shown in Figure 1.9 for the major symmetry directions in silicon, measured at 300 K. The three dominant phonon modes are the transverse acoustic (TA), longitudinal optical (LO) and transverse optical (TO) modes. The energies of which have been found to be:

$$h\omega/2\pi = 18.4 \pm 0.2 \text{ meV, TA mode,}$$

$$h\omega/2\pi = 56.2 \pm 1.0 \text{ meV, LO mode,}$$

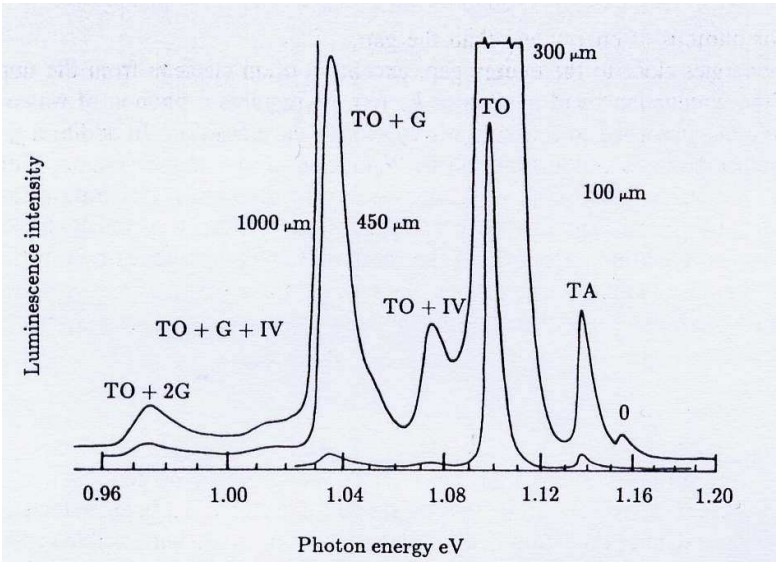

Figure 1.8

Intrinsic photoluminescence spectrum of silicon at 26 K recorded with four different slit widths (100 to 1000μm) to give varying resolution and amplification. Labels refer to the phonon combinations involved. G is $\boldsymbol{k} = 0$ optic mode. LO and TO components are not resolved. Radiative recombination without the participation of a phonon (peak labelled 0) is much weaker than radiative recombination involving at least one phonon (after Davies, 1989).

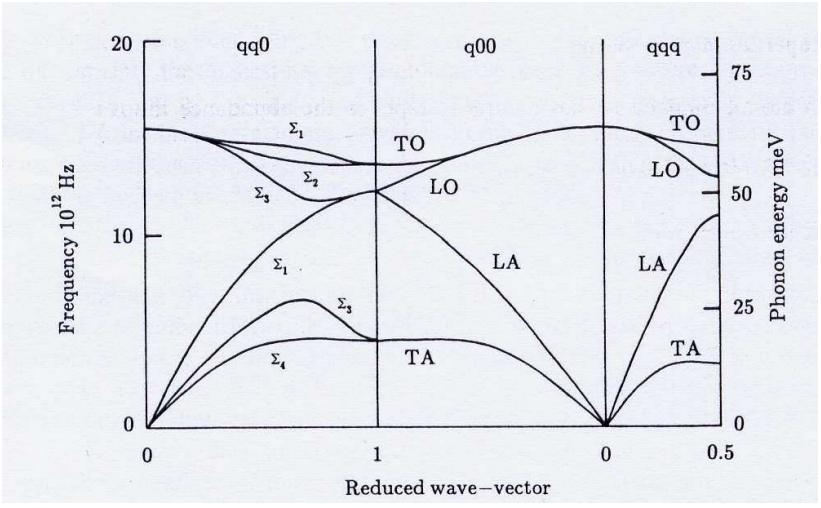

Figure 1.9

Silicon phonon dispersion curves at 300K for propagation on $\langle 001 \rangle$, $\langle 111 \rangle$ and $\langle 110 \rangle$ axes calculated using a five-neighbour Born-Von Karman model (after Zdetsis, 1979).

$h\omega/2\pi = 58.0 \pm 1.0$ meV, TO mode.

The relative ratios of the phonon-assisted luminescence peaks at temperatures above15 K are (Vouk and Lightowlers, 1977):

$$TA : LO : TO = 0.03 : 0.1 : 1$$

This is in agreement with the ratios measured by the absorption technique (Nishino *et al.*, 1973). The dominant luminescence peak observed at room temperature is that due to radiative TO phonon-assisted recombination. Room temperature luminescence has been reported in silicon for several decades (see for example Ong *et al.*, 1983 and Kramer *et al.*, 1993), the maximum IQE reported however has only been 4×10^{-5} and hence is insufficient for practical use. A typical spectrum, at room temperature is shown in Figure 1.10, see peaks labelled "Planar" and "Space cell". The peak apparent at 1130 nm is due to TO phonon-assisted recombination, the inflexion apparent at 1180 nm corresponds to the transition between the single TO phonon and the two phonon process of the TO phonon plus the Raman phonon (68 meV) (Green *et al.*, 2001).

1.2.3.2 The rate of radiative recombination in silicon

The rate of radiative recombination is given by:

$$R_r \sim B(T)(\Delta n + n)(\Delta p + p) \qquad \text{Eqn. 1.8}$$

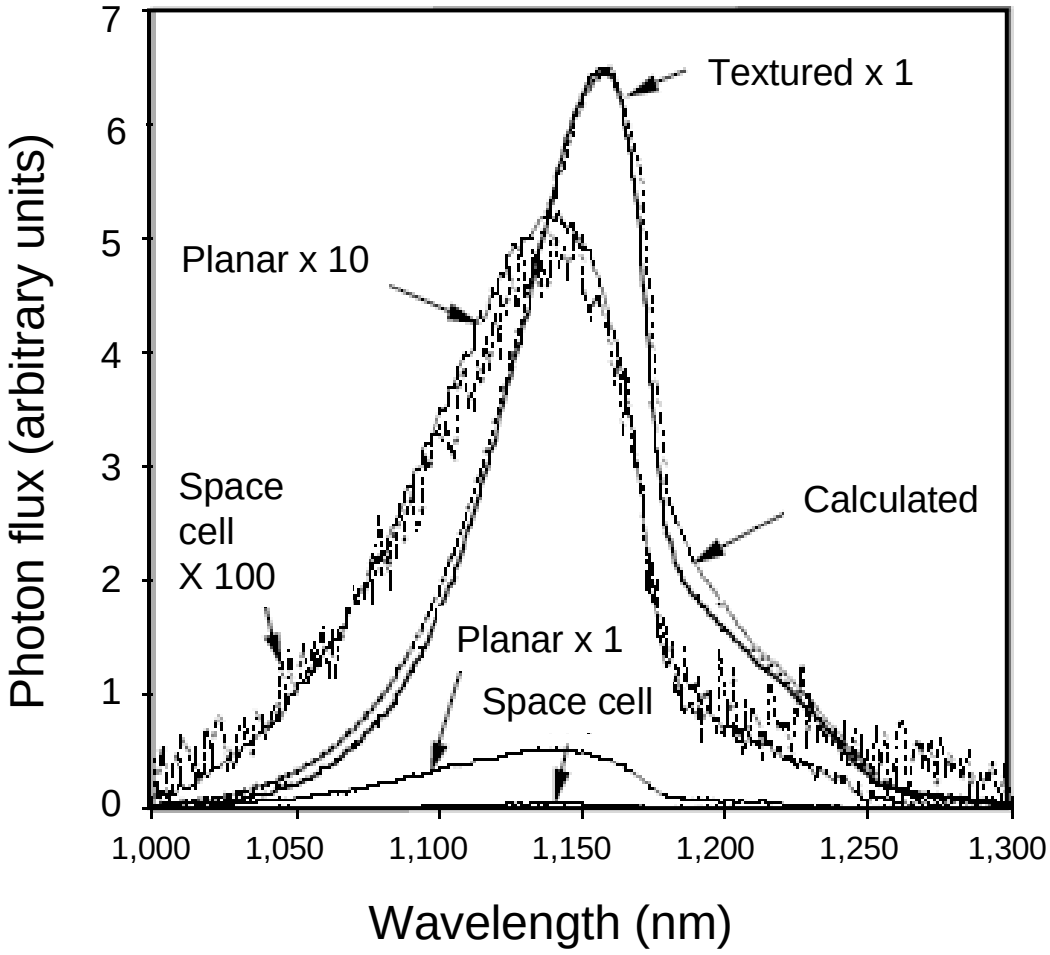

Figure 1.10

Room temperature luminescence spectra from a variety of bulk crystalline silicon light emitting diodes. Spectra labelled "Planar" and "Space cells" are 'standard' emission spectra with a peak due to TO phonon-assisted recombination apparent at ~1130 nm. The "Textured" spectrum relates to the work of Green *et al.* (2001) with a peak at ~1160 nm due to the effect of photon re-absorption.

where B(T) is the radiative recombination coefficient and Δn and Δp the excess electron and hole concentrations respectively. The radiative recombination coefficient B(T) (for band-to-band recombination) was experimentally determined in bulk crystalline silicon to be ~10^{-14} cm^3 s^{-1} at 300 K (Schlangenotto *et al.*, 1974). This is consistent with the recent reports of Trupke *et al.* (2003b) and Ruff *et al.* (1993) who report values of 4.73 x 10^{-15} and ~8 x 10^{-15} cm^3 s^{-1} respectively. Schlangenotto *et al.* (1974) and Trupke *et al.* (2003b) observe the radiative recombination coefficient to decrease as a function of increasing temperature, Figure 1.11. This is in contrast to the earlier reports of Varshni (1967) and Michaelis *et al.* (1969) who calculate a rise in B(T) from 1 x 10^{-15} cm^3 s^{-1} at 20 K to 2 x 10^{-15} cm^3 s^{-1} at 300 K, though Trupke *et al.* (2003b) suggest that errors in estimating the intrinsic carrier concentration leads to the under-estimation by a factor of 50 at low temperatures and 55% at room temperature in both these studies, so explaining the difference in temperature dependence of the recombination co-efficient.

1.2.3.3 Efficient room temperature luminescence from bulk silicon

Bulk silicon is generally perceived to be a poor light emitter due to the indirect bandgap nature; however some success in producing room temperature electroluminescence (EL) has been achieved using the established processing techniques of solar cell technology. Green *et al*. (2001) report an increase in the EQE to 1% at room temperature, comparable to representative direct bandgap emitters of little more than a decade ago (Meyer *et al.*, 2000). Further work by the same group (Trupke *et al.*, 2003a) has seen an increase in the peak efficiency to ~6%. The device is based on the normally weak TO phonon-assisted band edge luminescence and

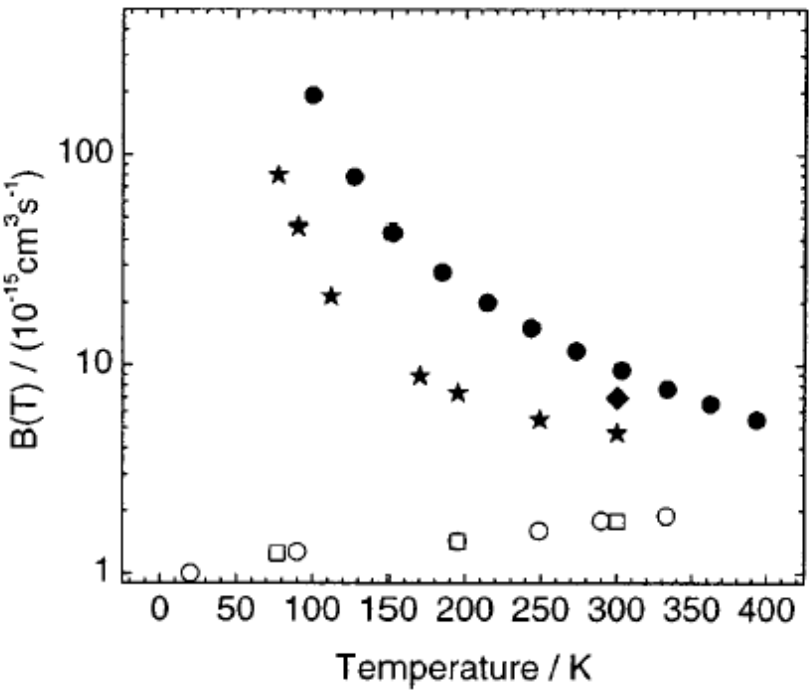

Figure 1.11

Comparison of data from the literature for the radiative recombination coefficient, B(T), as a function of temperature. Stars: Trupke *et al.* (2003), filled circles: Schlangenotto *et al.* (1973), diamond: Ruff *et al.* (1993), open circles: Varshni (1967) and open squares: Michaelis and Pilkuhn (1969) (after Trupke *et al.* (2003)).

several simple design concepts are employed in order to maximise the quantum efficiency.

The IQE is maximised by firstly using high quality Float Zone (FZ) substrates with long minority carrier lifetimes; competing SRH non-radiative recombination is minimised. Secondly, high quality silicon dioxide surface passivation is employed reducing surface recombination which can dominate in high minority carrier lifetime semiconductors.

The EQE is maximised by minimising free-carrier absorption. A moderate substrate doping level (~1.4 x 10^{16} cm^{-3}) and small metal contact areas are employed. The emissivity of the device is increased (compared to a polished wafer) by using a textured surface with antireflection coating. In silicon, this emissivity increase may be by as much as a factor of ~25 ($2n^2$, where n is the refractive index).

The luminescence spectrum, at 300 K, is shown in Figure 1.10 labelled as "Textured". The device structure and efficiency as a function of temperature are shown in Figure 1.12. The luminescence is attributed to TO phonon-assisted recombination. Unlike the reports of Ong *et al*. (1983) and Kramer *et al*. (1993), the peak position is observed at 1160 nm rather than 1130 nm. This was ascribed to the effect of photon re-absorption due to the large photon exit path length (many times the thickness of the wafer). The absorption co-efficient of silicon falls from 3.5 cm^{-1} at silicon's bandgap (1103 nm), to 10^{-3} cm^{-1} at 1250 nm (Green and Keevers, 1995); this results in a red shift in the peak position due to the non-uniform re-absorption of generated photons across the spectrum.

Despite the high efficiency levels there are several problems that are likely to hinder the successful implementation of this technology as an optical emitter for interconnect technology. The requirement of high purity FZ substrates and the wet

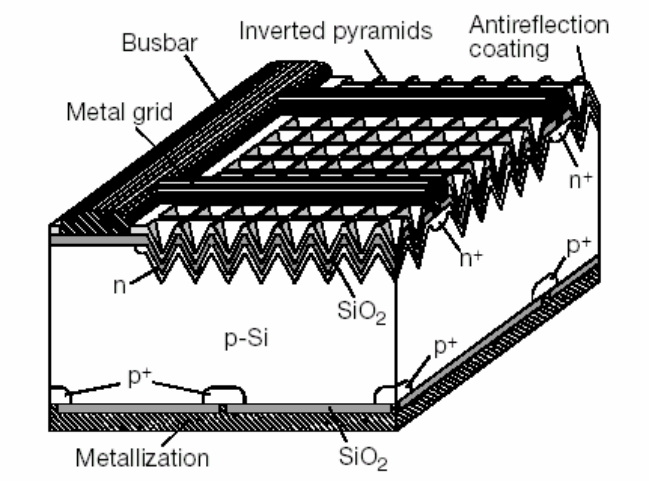

Figure 1.12a

Schematic illustration of the high-efficiency silicon light emitting diode showing the technological steps to maximise efficiency: textured surface, SiO_2 passivation, small high doping regions and antireflection coating (after Green *et al.*, 2001).

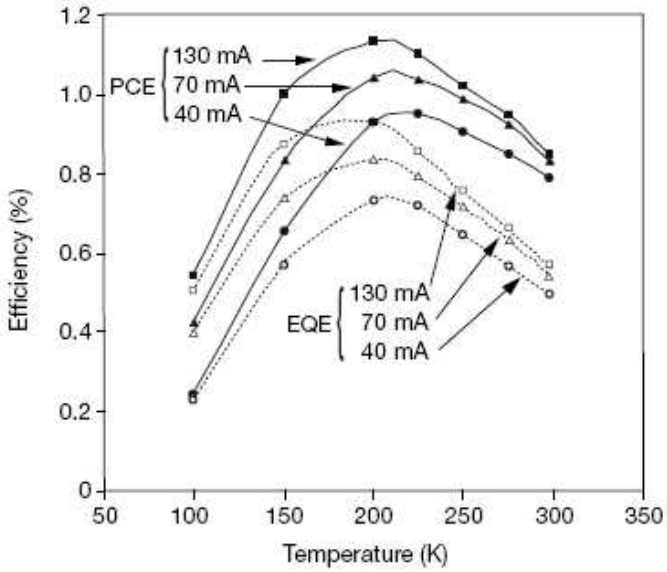

Figure 1.12b

External quantum efficiency (EQE) and power efficiency (PCE) as a function of temperature for three diode currents (after Green *et al.*, 2001).

chemistry required to produce the surface texturing are seen to be incompatible with standard CMOS technology. Furthermore, the CMOS production process necessarily degrades the substrate quality by the introduction of transition metal impurities. The long lifetimes of the excited carriers (~10 ms) measured in the work of Green *et al.* (2001) is also thought to make modulation difficult to achieve (Pavesi, 2003). A simple calculation also demonstrates that the production of a sufficiently large photon flux from a reasonable volume of silicon is likely to be prohibitive:

If it is assumed that:

- Operation at 10 Ghz is required ($\equiv$1 operation every 10^{-10} s)
- 10^4 photons/operation needed (10^{14} photons/sec emitted required)
- 10% operating efficiency (10^{15} recombinations/sec required)
- Maximum operating volume 10 x 10 x 10 μm (1×10^{-9} cm^3)

Then we require the rate of recombination to be $\frac{10^{15}}{10^{-9}} = 10^{24}$ $cm^{-3}\,s^{-1}$

Using a radiative lifetime of τ_r = 10 ms (Green *et al.*, 2001) an excess carrier concentration of ~10^{22} cm^{-3} is required. At this carrier concentration the Auger lifetime is calculated using Eqn. 1.5 to be 5 x 10^{-18} s. The significantly shorter lifetime of Auger recombination results in a low IQE (see Section 1.2.1), thus, a device operating at these carrier concentrations is highly unrealistic.

1.3 Enhancing silicon luminescence

Other methods investigated as potential routes for efficient luminescence use materials engineering with the aim of overcoming the indirect bandgap nature of silicon. These approaches aim to either enhance the (intrinsic) luminescence efficiency of silicon by quantum confinement/band gap engineering, or induce (extrinsic) radiative recombination at intentionally added impurities or defect centres. In some cases a combination of the two methods are used in an attempt to engineer efficient room temperature luminescence.

1.3.1 Quantum confinement

The radiative recombination efficiency of excitons or free carriers can be increased by their quantum confinement in small volumes which are free of defects. Yoffe (1993) suggests that strong quantum confinement effects are expected in nanostructures when the crystallite size is less than the size of the exciton Bohr radius for the given material. In silicon, this dimension is 4.3 nm. The bandgap of the nanostructure is highly dependent on the crystallite size and shape. Figure 1.13a shows the calculated change in bandgap for quantum dots and wires using *ab initio* calculations. Theory suggests that the bandgap increases as $d^{-1.3}$, where d is the quantum dot diameter (Delerue *et al.*, 1999). Figure 1.13b shows the comparison between the theoretical calculations and experimental results. The theoretical results qualitatively agree with the absorption results of Lockwood (1994). However, a lesser degree of blue shift is consistently observed in some photoluminescence (PL) studies (Lockwood, 1994 and Schuppler *et al.*, 1994). In contrast, the PL results of Ehbrecht *et al.* (1997) for crystallite sizes greater than 3.5 nm in diameter are in good agreement with the absorption and theoretical data.

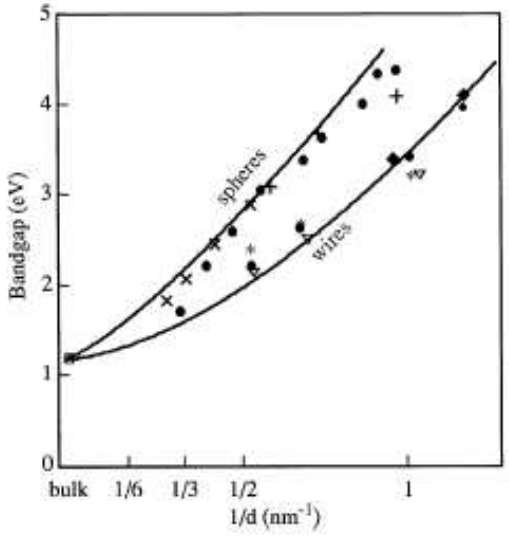

Figure 1.13a

Hydrogen passivated silicon quantum dot and quantum wire bandgaps versus size. Calculated using empirical tight binding approximation (lines) and other techniques (markers) (after Delerue *et al.*, 1999).

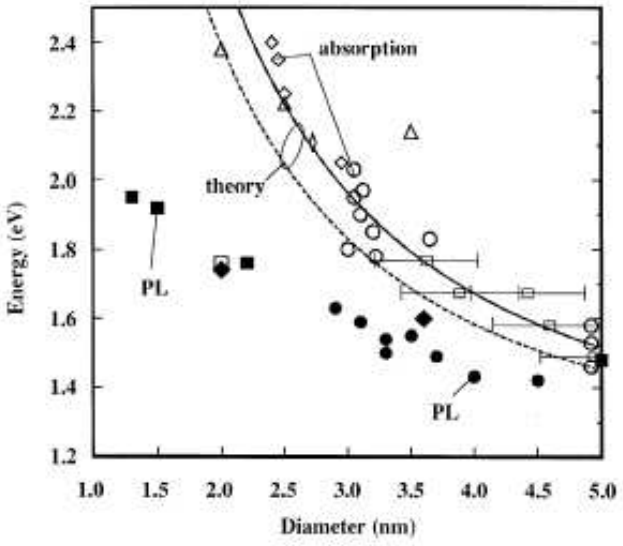

Figure 1.13b

Compilation of the optical bandgaps of silicon crystallites and porous silicon samples obtained from optical absorption (unfilled symbols) and luminescence (filled symbols). Dashed and continuous lines are the tight binding approximation curves calculated values with and without the excitonic correction (after Delerue *et al.*, 1999).

The increasing localisation of the electron and hole wavefunctions in nanostructures of decreasing size results in the increasing spread of the energy states in ***k***-space. This increased overlap of the electron and hole states increases the probability of radiative recombination (Hybertsen, 1994). The calculated phonon-assisted recombination lifetime is shown in Figure 1.14 by the continuous line and is shorter by nearly two orders of magnitude (~3 x 10^{-6} s compared to 2 x 10^{-4} s) in a crystallite of dimensions 1 x 1 x 1 nm compared to a 4 x 4 x 4 nm crystallite. Also plotted is the zero phonon recombination rate, which is also faster in smaller crystallites. For very small quantum nanostructures (diameter less than ~1.5 nm), the zero phonon transition is thought to become the dominant radiative recombination mechanism.

The surface to volume ratio in nanostructures is large and great care must be taken into ensuring that surface is passivated as a single dangling bond (non-radiative recombination centre) corresponds to a bulk defect concentration of ~10^{20} cm^{-3} for a crystallite of dimensions ~1 x 1 x 1 nm (Fauchet, 2004). This reliance on achieving the correct surface chemistry in quantum nanostructures is a significant hurdle to be overcome for the many approaches aiming to achieving room temperature luminescence using quantum confinement.

Research aimed at utilising the quantum confinement of carriers in silicon based nanostructures has focused on porous silicon, quantum wells and nanoclusters (quantum dots).

1.3.1.1 Porous silicon

Porous silicon is created by the electrochemical dissolution of silicon wafers in hydrofluoric acid (HF) based electrolytes. HF dissolves silicon very slowly, at the

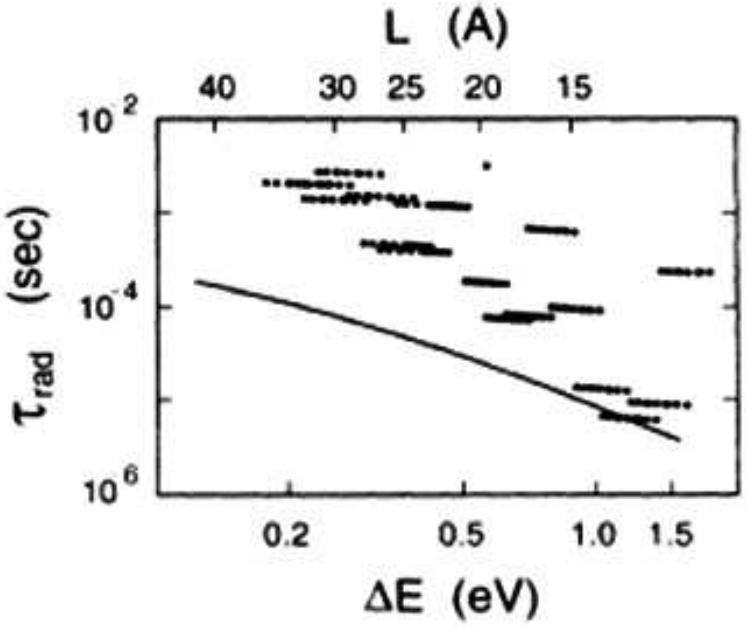

Figure 1.14

Radiative recombination lifetime as a function of the blueshift of the photon energy away from the bulk silicon bandgap: zero-phonon transition (dots) and TO phonon-assisted transition (line). Top scale indicates equivalent cube size of crystallite (after Hybertsen, 1994).

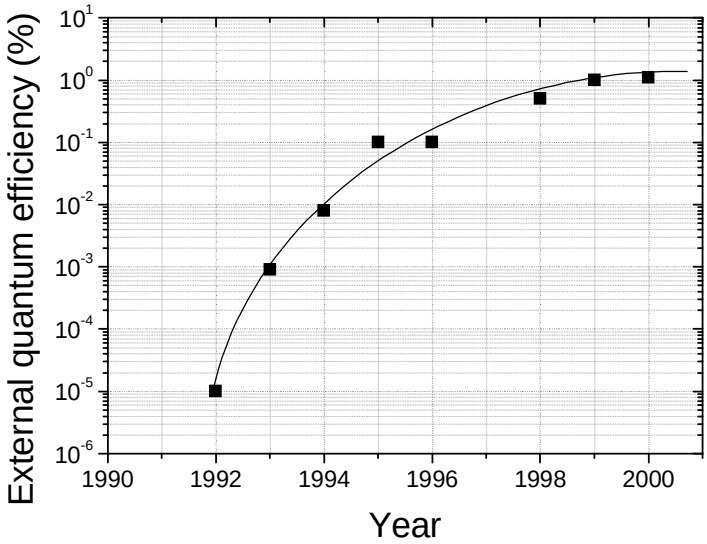

Figure 1.15

The advancement of the external quantum efficiency of porous silicon LEDs since 1992. The solid line is provided as a guide to the eye (after Pavesi, 2003).

rate of only a few nanometres per hour, however Uhlir discovered that the passing of an electric current between the acid electrolyte and the silicon sample increases the etching rate significantly (Uhlir, 1956). Under suitable conditions, an array of narrow pores that run deeply and in general perpendicular to the surface can be created. Canham conceived the idea of fabricating this porous structure and then, by further HF etching, create a sample with an irregular array of crystalline silicon pillars only several nanometres wide. Canham (1990) observed intense visible PL at room temperature, with the mechanism ascribed to quantum size effects in wires of ~3 nm diameter and the added advantage of spatial confinement of carriers reducing the non-radiative probability.

The initial publication of efficient luminescence from porous silicon lead to an intense production of papers describing similar results, including those by Bseisy *et al.* (1991), Koshida and Koyama (1991) and Gardelis *et al.* (1991). Strong PL signals have been observed in porous silicon from near infrared (Lockwood, 1994) to red (Canham, 1990) and blue (Lockwood, 1994). It has even been possible to observe "white" light (Bensahel *et al.*, 1993). This subject is comprehensively reviewed elsewhere by Cullis *et al.* (1997) and Canham, (1997).

The wide range of results obtained from porous silicon is a clear indication of the flexibility of the material. However, this also leads to difficulty in correctly analysing results. The surface chemistry of porous silicon is extremely varied and indeed, can significantly alter within a single sample. Crystalline silicon pillars, amorphous silicon and silicon spherites can be formed within a sample increasing the difficulties in analysing their optical properties. The disadvantages of porous silicon are the wet fabrication procedures, which are hard to integrate into current microelectronics, the strong deterioration of the mechanical properties with increasing

porosity (Fauchet *et al.*, 1998), and its EL degradation during operation (Lalic and Linnros, 1996). It has been suggested that the latter problem can be avoided by oxidation and has led to device operational lifetimes of the order of weeks (Tsybeskov *et al.*, 1996).

Despite these difficulties some success has been achieved in creating optical components. The increased EQE (1 to 2% (Gelloz and Koshida, 2000), see Figure 1.15) and the tuneable wavelength has lead to porous silicon light emitting diodes (LEDs) being incorporated into microelectronic circuits to provide an addressable LED display (Hirschman *et al.*, 1996).

1.3.1.2 Silicon nanoclusters

Rather than using the etching method, as in porous silicon above, nanoscale silicon crystallites can be produced by direct growth from the gas phase or more commonly, indirectly by recrystallisation within a matrix (Bisi *et al.*, 1999; Kamimura, 1994; Nayfeh *et al.*, 2001; and Kimerling *et al.*, 1997). These crystallites, for luminescence studies, are typically 3 to 5 nm in diameter. As observed with porous silicon the PL wavelength is again reported to be dependent upon the crystallite size. One of the most exciting results of silicon nanoclulster techniques is that unlike porous silicon, some authors have reported population inversion, and optical gain has been observed (Nayfeh *et al.*, 2002 and Fauchet and Ruan, 2003).

The literature is still somewhat contradictory in several areas, particularly in the interpretation of the PL results (as in the case of porous silicon) and the complexities of the nanocrystal-matrix interface are proving difficult to understand unambiguously.

Nanostructures of silicon trapped within a matrix are an attractive method for device fabrication when compared to porous silicon due to the mechanical and chemical stability. Silicon nanocluster systems generally report a slow recombination (microseconds range) but there is also evidence to suggest a fast contribution (nanoseconds range) which is suggested to be due to stimulated emission (Pavesi, 2003).

The silicon nanocrystal technique is proving to be a very promising technique in achieving the first all-silicon based laser; indeed, several important ingredients for a laser have been achieved. Optical micro-cavities based on the Fabry-Perot structures formed by nanocrystals dispersed in SiO_2 have already been demonstrated (Iacona *et al.*, 2001). Rebohle *et al.* (2001) have also reported the first all-silicon integrated optocoupler (quantum efficiency 0.5%) using an ion-implantation method into SiO_2. Silicon LEDs have been fabricated using the nanocluster systems with efficiencies in excess of 0.1% achieved (Franzò *et al.*, 2002). There has also been an unconfirmed report of near-laser action of these LEDs in the literature (Lin *et al.*, 2002). Despite the apparent success of this technique the role played by in the nanocrystals, embedding medium and interface in determining the luminescence efficiency is still unclear.

1.3.1.3 Quantum well structures

Quantum wells (QW) are produced by growing thin layers of Si separated by wide bandgap dielectrics such as SiO_2, CaF_2 and Al_2O_3 (Tsu, 1993). Lu *et al.* (1996) first reported visible luminescence from ultrathin-layer Si/SiO_2 superlattices grown by molecular beam epitaxy that exhibited the expected wavelength shift associated with quantum confinement. The wavelength of PL obtained from this superlattice structure

is highly dependent on the thickness of the Si layers, thus a tunable emission (wavelengths from 500 to beyond 800 nm) is possible. This is therefore an interesting prospect for silicon based light emitters. However, whether this luminescence is due to quantum confinement is still a matter of debate. Xuan (2002) suggests that from modelling calculations the role of quantum confinement does not provide the observed optical functionality, instead suggesting that the strong PL is due to the chemical modification of the silicon band structure by foreign atoms.

1.3.2 Atomic layer superlattices

Gnutzmann and Clausecker (1974) conjectured theoretically that it would be possible to form a quasi-direct band gap in thin layer superlattices where the layer thicknesses were of the order of the unit cell. Growth of high quality $(Si_xGe_y)_z$ (x and y are the number of atomic planes in a layer and z the number of periods) atomic layer superlattices by molecular beam epitaxy lent significant weight to this argument. The superlattice periodicity of d results in a smaller Brillouin zone of size $\pm\pi/d$ compared to the original lattice $\pm 2\pi/a$ (where a is the lattice constant), Figure 1.16. The electronic band structure is then folded back into this reduced zone scheme. Using this theory the material becomes direct band gap when there are 10 monolayers of silicon. However, this simple description does not fully explain the situation as strain effects and band offsets play an important role (Brey and Tejedor, 1987). Pearsall *et al.* (1987) showed the first experimental evidence that modification to the SiGe superlattice band structure was possible. However, Zachai *et al.* (1990) and Kasper and Schaffler (1991) showed experimentally for the first time the reduced bandgap and increase in luminescence intensity predicted using this scheme.

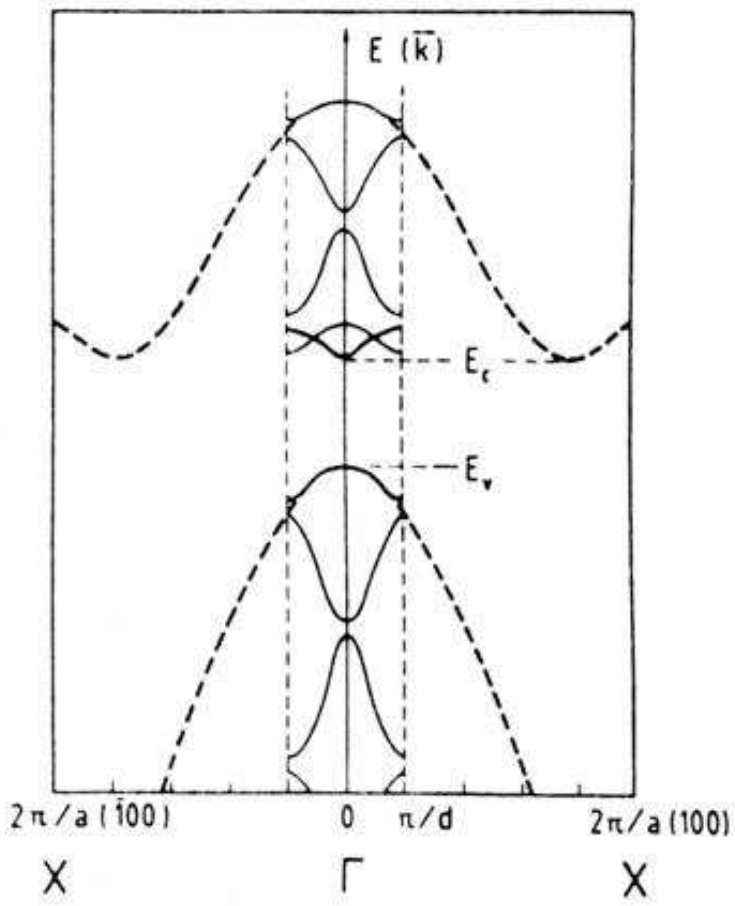

Figure 1.16

Schematic representation of the Brillouin zone-folding concept used in atomic layer superlattice structures. Here the conduction band minimum along the X direction is folded back into the Γ point when the silicon layer thickness is 10 monolayers (after Kasper and Schaffler, 1991).

From an applications point of view, this scheme at present shows few signs that it may be applicable to optoelectronic communications. The PL has so far only been observed at low temperatures with essentially full quenching of the luminescence at room temperatures. Rodrigues *et al.* (1999) however identified radiative recombination paths in ultra-thin germanium quantum wells and suggest that a fuller understanding of the recombination processes may allow some small steps towards room temperature luminescence to be taken.

1.3.3 Radiative emission via defect engineering

The luminescence mechanisms discussed thus far have been via intrinsic routes, *i.e.* using silicon itself as the optically active material. An alternative approach is to use silicon as a host material in which charge carriers are produced and transported to a second luminescence medium. The inherent difficulties of using an indirect bandgap material are therefore avoided.

1.3.3.1 Luminescence via impurity centres

Rare earth elements: The optical properties of rare earth (RE) ions in solids are fairly well understood and have been investigated in great detail (for a review see Dieke, 1968). The emission properties of the RE elements are relatively unaffected by placement in a silicon matrix and have thus been investigated as potential silicon-based light emitters. Sub-bandgap EL has been observed from erbium, ytterbium and terbium ions in a host bulk silicon matrix (Castagna *et al.*, 2003). Of particular interest is erbium luminescence, because the generated photons are of a wavelength very much compatible with optical fibre communication.

The Er^{3+} ion emits photons at 1.54 eV as a result of internal intra 4f shell transitions between the $^4I_{15/2}$ and $^4I_{13/2}$ manifolds when the ion is placed in a solid matrix (Franzò *et al.*, 1999). An important characteristic of the erbium luminescence mechanism is the fact that it can be excited via an electron-hole mediated process. This transition is relatively independent of the host material and ambient temperature (Zheng *et al.*, 1994). However, the long radiative lifetime (~2 ms) exposes the excited erbium ion to several non-radiative de-excitation processes. As a result the EQEs of erbium based LEDs at room temperature are relatively low (~0.05% Franzò *et al.*, 1999). An extra two non-radiative recombination paths are available in erbium based devices compared to bulk silicon: 1) an erbium Auger de-excitation process, where the energy released from the Er^{3+} transition is given to a free carrier in the silicon matrix (Franzò *et al.*, 1999) and 2) an energy backtransfer process has been attributed to the cause for strong thermal quenching of the luminescence signal above 130 K (Coffa *et al.*, 1994). An excited electron in the 4f shell of the erbium ion can decay non-radiatively by promoting an electron from the valence band to a trap level (erbium related) in the silicon matrix situated 0.15 eV below the bottom of the conduction band. This is essentially the reverse of the excitation process and is thus described as an energy backtransfer. It is thought that the performance of erbium based silicon LEDs cannot be improved much further due to the thermal quenching due to the non-radiative paths described above and the limit of erbium concentration levels below the solid solubility in order to avoid clustering (Fauchet, 2004). However, a potential solution to the seemingly insurmountable problems experienced with erbium ions in a silicon matrix is the use of silicon quantum dots embedded in a SiO_2 matrix as a host to erbium ions.

The increased bandgap of nanoclusters reduces the likelihood of the non-radiative backtransfer process and the use of the SiO_2 matrix ensures there are no free carriers to participate in Auger recombination. LEDs operating at room temperature have been developed with this system, where an EQE larger than 1% (Iacona *et al.*, 2002) has been demonstrated. Even higher EQEs (10%) are reported for erbium in silicon rich oxide films (Castagna *et al.*, 2002); reliability is still an issue in these films however. The efficiencies reported are comparable to III-V semiconductor LEDs. This coupled system appears to be very promising for laser applications, as the active material (Er^{3+} in SiO_2) has already been shown to exhibit lasing properties (Becker *et al.*, 1999). In addition to this the processing technology is highly compatible with modern CMOS processing.

Second phase precipitates - Iron disilicide: The ion-implantation of iron into a silicon matrix and subsequent annealing to form β-$FeSi_2$ has also been studied in an attempt to achieve luminescence from silicon based materials. Under suitable processing conditions the β-$FeSi_2$ is an optically active direct bandgap material which is compatible with standard silicon processing technology (Christensen, 1990). Typical processing conditions are iron implantation (dose ~10^{17} cm^{-2}, 180 keV) followed by annealing at 900 °C for 18 hours (Lourenço *et al.*, 2001). The direct bandgap luminescence from the β-$FeSi_2$, peak wavelength 1500 nm, suggests that this approach is ideal for fibre optic type communications. Efficiencies of ~0.1% have been quoted at 80 K (Leong *et al.*, 1997). However, thermal quenching has proved to be of particular importance and has limited research in recent years.

Lourenço *et al.* (2002) report a scheme which shows encouraging signs of being able to develop β-$FeSi_2$ as a potentially efficient room temperature luminescent material, with a reported EQE of ~0.05% at room temperature. Dislocation

engineering is used in order to minimise the effects of thermal quenching; a boron ion-implantation is performed on the pre-fabricated devices (~10^{15} cm^{-2} at 30 keV) and annealed at 900 °C for 1 minute; introducing dislocation loops. The authors report that the thermal quenching between 80 and 200 K is reduced by a factor of greater than 50. It is suggested that the dislocation loops prevent the diffusion of carriers to non-radiative recombination centres as a result of the dislocation strain field modifying the silicon bandgap causing spatial confinement.

It is unclear whether the mechanism described would be capable of producing the results suggested. Dislocations are known to be centres of strong non-radiative recombination, particularly in materials where there is a large transition metal concentration at the dislocation (see Section 1.2.2.4), as is likely to be the situation in this case considering the levels of Fe present in the wafer. Lourenço *et al*. (2002) also assume that the dislocations formed by ion implantation are of sufficient density to create a significant continuous barrier (up to 0.5 eV in height). However, transmission electron microscopy results reported by Milosavljević *et al.* (2005) suggest that the density is insufficient to produce a continuous barrier to minority carrier diffusion.

1.3.3.2 Dislocation related D-band luminescence

Dislocations were introduced as non-radiative recombination centres in Section 1.2.2.4. However, under certain conditions dislocation-related luminescence (DRL) can be observed. There are four spectral lines that are reported most commonly in the literature, these are generally referred to as *D*-band luminescence and are labelled *D*1 (0.80 - 0.82 eV), *D*2 (0.87 eV), *D*3 (~0.95 eV) and *D*4 (~ 1.0 eV) as shown in Figure 1.17. The PL intensity of DRL has been shown to be directly

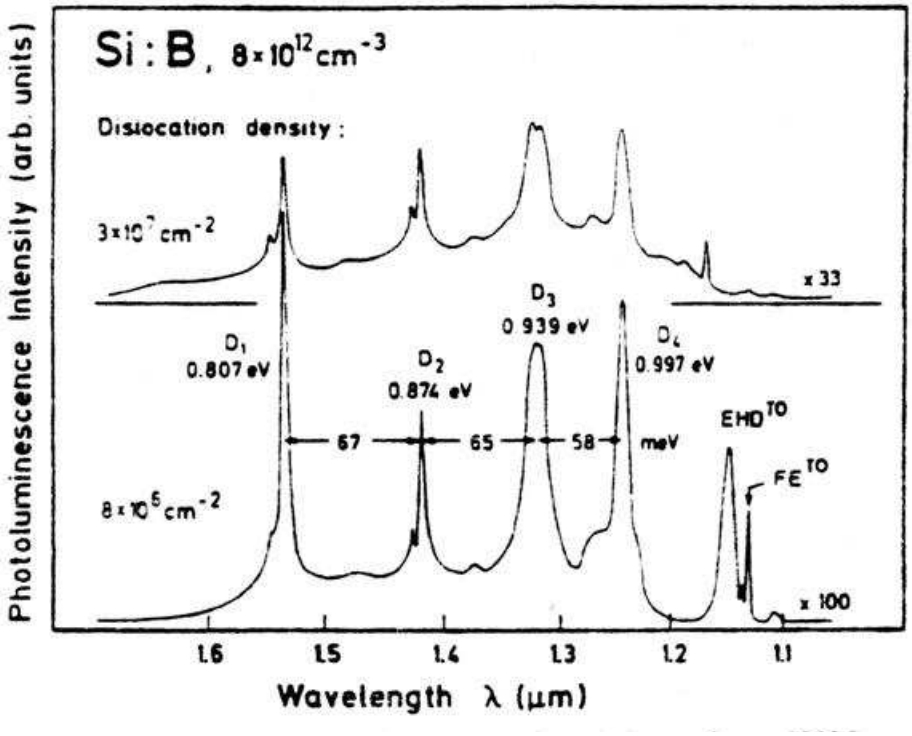

Figure 1.17

Photoluminescence spectra from samples deformed at 650 °C along [213] for dislocation densities as indicated. Temperature 4.2 K; resolution $\Delta\lambda$ = 2 nm; excitation by 647 nm Kr laser line (after Sauer *et al.*, 1985).

related to the dislocation density, thus these bands have been attributed to originate at dislocations (Sauer *et al.*, 1985 and Drozdov *et al.*, 1977). The luminescence is universal, *i.e.* seen in plastically deformed, abraded, lattice mismatched silicon surfaces and interfaces, and ion-implanted material or materials that contain grown-in dislocations and oxidation-induced stacking faults (Kimerling *et al.*, 1997).

There is strong evidence that *D*1/*D*2 and *D*3/*D*4 are produced by two different underlying mechanisms (Suezawa *et al.*, 1982 and Bradfield *et al.*, 1989). Sauer *et al.* (1986), Izotov *et al.* (1992) and Steinmann (1994) all suggest, using low-temperature high-stress experiments that the energy position of the *D*3 and *D*4 bands, observed at low temperatures, are strongly dependent on the distance between partials in dissociated perfect dislocations. The authors conclude that *D*3 and *D*4 originate from recombination processes at straight segments of 60° dislocations, and further to this Steinmann also suggests that *D*3 is most probably a phonon-assisted replica of *D*4.

Despite much research, the origin of the *D*1 and *D*2 bands remain difficult to assign unambiguously. The literature suggests Lomer-Cottrell dislocations, dislocation kinks or jogs as well as the presence of self-interstitial or vacancy clusters at dislocation cores as possible explanations for the origin of *D*1 and *D*2 (see for example Kenyon *et al.*, 2003 and Kveder *et al.*, 1995).

A large uncertainty also remains over the role of impurities in the *D*-band luminescence. There are reports in the literature that the presence of small concentrations of transition metal impurity atoms is a prerequisite for *D*-band luminescence (Kenyon *et al.* 2003). However, total quenching of *D*-band luminescence is thought to occur if contamination is sufficiently high that metal silicides are formed. Even this though can lead to ambiguity in the analysis of results

as β-$FeSi_2$ produces a luminescence peak about 0.80 eV, with a similar peak width to *D*1 (Leong *et al.*, 1997).

At high dislocation densities, the *D*1 line is dominant in terms of the PL intensity (the *D*1energy coincides with the absorption minimum in silica-based glass fibres and as such has been thought of as a potential candidate for use as a silicon-based optically active material). The *D*1 band had been previously thought to vanish at temperatures above 200 K (Sauer *et al.*, 1985). However, Kveder *et al.* (1995), Sveinbjörnsson and Weber (1996) and Kittler *et al.* (2002) report observations of the *D*1 line at room temperature with EQEs of ~10^{-6} (comparable to the phonon-assisted indirect bandgap efficiency also observed in these studies). There is clear evidence that the presence of oxygen can stabilise the emission. However, the role that oxygen and oxygen-related defects play is not well understood (Kenyon *et al.*, 2003).

Recent work by Kveder *et al.* (2004) has demonstrated efficient room temperature *D*1 luminescence; they report an EQE of greater than 0.1%. This is the first report which suggests *D*-band luminescence as a realistic option in producing silicon optical emitters. The macroscopic plastic deformation used in the work however is incompatible with standard CMOS technology. The authors suggest that the generation of the dislocations by ion-implantation, punched-out loops from oxygen precipitates or misfit dislocations at a Si/SiGe interface may lead to similar results with processing techniques more compatible with the microelectronics industry.

1.3.3.3 Deep luminescence bands

Magnea *et al.* (1984), Weman *et al.* (1985) and Wagner *et al.* (1984) all report the observation of broad, often featureless PL bands in silicon. These bands have

been largely observed in materials containing small precipitates (oxygen and antimony) or clusters of Si atoms. Weman *et al.* (1990) suggests that these broad bands are strain related quantum confinement at the interface between the precipitates (or clusters) and the Si matrix. PL peaks observed at 4.2 K have been observed at 0.85 eV and 0.94 eV for extended defects (platelets, gas bubbles) in hydrogen-plasma-treated silicon (Weman *et al.*, 1985). These peaks show little potential as efficient room temperature emitters; the potential wells suggested by Weman *et al.* are insufficient to produce quantum confinement above ~77 K due to the thermal energy of carriers.

1.4 Luminescence from dislocation-engineered silicon

There may have been significant progress in the design of silicon-based optical emitters during the last fifteen years, indeed, Liang and Tsang (2004) and Boyraz and Jalali (2004) have recently successfully demonstrated light amplification in silicon-based waveguides using stimulated Raman scattering, however, despite the many promising results, there is still no obvious candidate for achieving CMOS compatible optical emitters.

Section 1.1.1 introduced the concept of dislocation-engineering as a novel route to achieving potentially efficient room-temperature luminescence. In this section the sample manufacturing route, the electroluminescence and photoluminescence results, and the proposed mechanism of high efficiency luminescence of Ng *et al.* (2001) are reviewed.

1.4.1 Specimen production

Ng *et al.* (2001) used *n*-type phosphorous-doped (100) Cz-silicon (2 – 7 Ωcm), containing interstitial oxygen at a concentration of ~10^{18} cm^{-3} (Ng, 2000). A boron implantation (1 x 10^{15} cm^{-2}, 30 keV and off-axis tilt ~8°) was performed to create a p^+-*n* junction. The sample was then annealed at 1000 °C for 20 mins in a rapid thermal anneal furnace. The depth of the p^+-*n* junction was calculated, using the TRIM code, to be ~275 nm below the wafer surface (Milosavljević *et al.* (2003). Ng *et al.* (2001) observed by cross-sectional transmission electron microscopy (TEM) an array of dislocation loops in a planar region, parallel to, and ~100 nm closer to the surface than the p^+-*n* junction. The dislocations themselves were reported to be 80-100 nm in diameter and spaced ~20 nm apart.

In order to perform EL measurements ohmic contacts of 1 mm^2 and 3 mm^2 were deposited on the (implanted) and wafer reverse surfaces respectively after mesa etching. The larger back contact contained a window through which emitted photons could be collected. A schematic diagram of the final structure, showing the position of the p^+-*n* junction, the band of dislocations and electrical contacts is shown in Figure 1.18a.

1.4.2 Luminescence results

EL spectra are shown in Figure 1.18b for a forward biased, injection current of 50 mA. The peak wavelength at 300 K was found to be ~1150 nm and an inflexion was apparent at ~1180 nm. No other emission peaks were observed at any other wavelengths, even at low temperatures (80 K). The peak wavelength of the spectrum was observed to follow the temperature dependence of the bandgap. A PL investigation showed similar results (Ng, 2000).

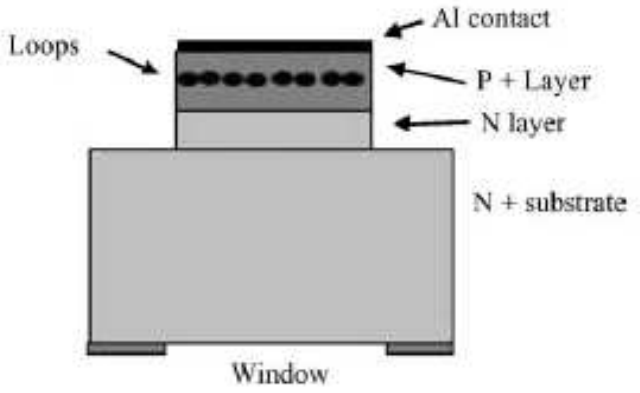

Figure 1.18a

Schematic illustration of a dislocation-engineered light-emitting diode. The top and bottom ohmic contacts are formed by Al and AuSb respectively. The infrared light is collected through the window of the bottom contact (after Gwilliam *et al.*, 2005).

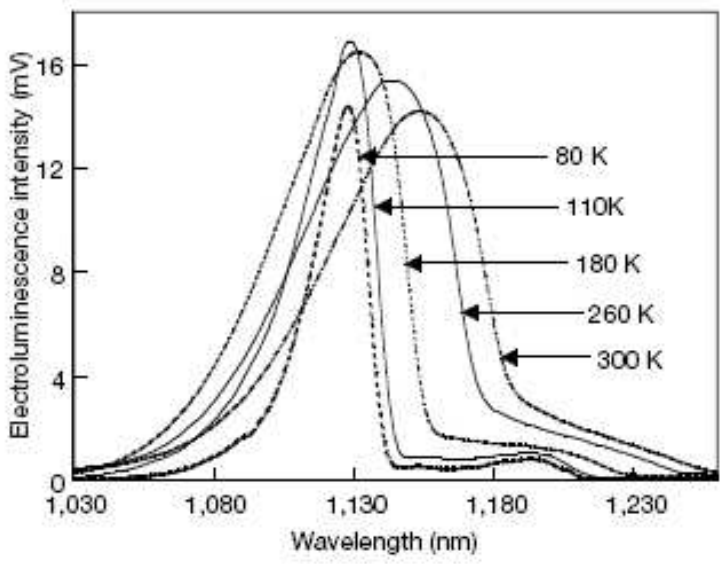

Figure 1.18b

Electroluminescence spectra of a dislocation-engineered silicon specimen. The device was operated at a forward current of 50 mA for all temperatures (after Ng *et al.*, 2001).

Using EL, with a forward biased injection current of 100 mA, the EQE of the unpackaged planar device measured from light collected through the window was found to be $(2.0 \pm 0.1) \times 10^{-4}$. When edge luminescence was taken into account the EQE was estimated to be $\sim 10^{-3}$. This efficiency is comparable to many of the more established methods for creating silicon-based photonic devices reported in Section 1.3.

Remarkably, unlike most systems used to demonstrate light emission from silicon, the EL and PL integrated luminescence was observed to increase by a factor of 3 from 80 to 300 K, Figure 1.19. The increase in efficiency was found not to be dependent on the carrier injection mechanism and was said to be intrinsic to the recombination mechanism (Ng *et al.*, 2001).

In subsequent publications by the same group (Lourenço *et al.*, 2002 and 2003 and Gwilliam *et al.*, 2005) the dependence of the luminescence efficiency on the boron implantation energy, the annealing temperature and the annealing time were reported, see Figure 1.20. The following trends were observed:

Implant energy (20 to 70 keV) (Figure 1.20a): In both PL and EL measurements the EQE was observed to increase with decreasing implant energy. However, in the EL investigation the maximum EQE was observed at an implantation energy of 30 keV.

Annealing temperature (20 mins at 400 to 1150 °C) (Figure 1.20b): The maximum intensity was observed at an annealing temperature of 975 °C for both PL and EL experiments and increased gradually to this peak value as the temperature was raised from 400 °C. The efficiency was observed to fall sharply after 975 °C, such that by 1100 °C the luminescence was negligible.

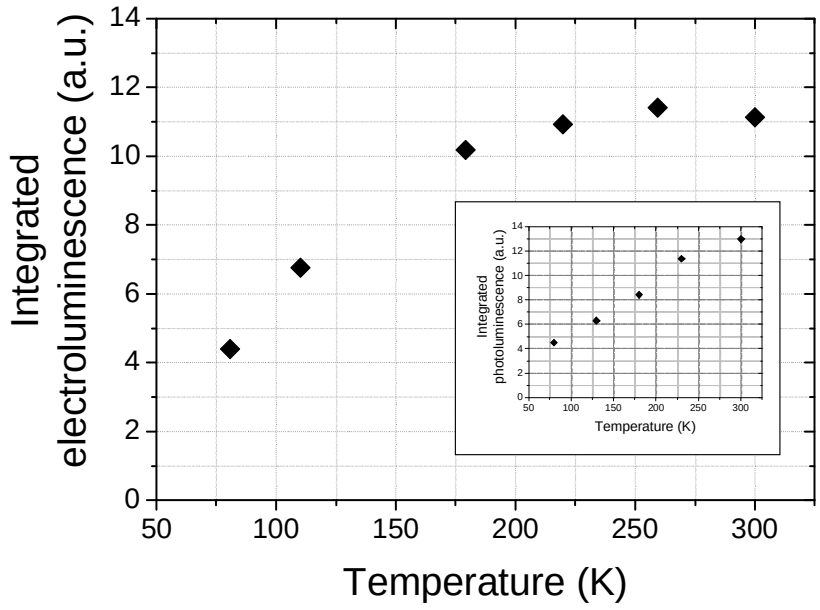

Figure 1.19

The integrated electroluminescence and inset, photoluminescence intensity, as a function of measurement temperature. The photoluminescence was excited by the 488 nm line of an argon laser at a power of 150 mW (after Ng *et al.*, 2001).

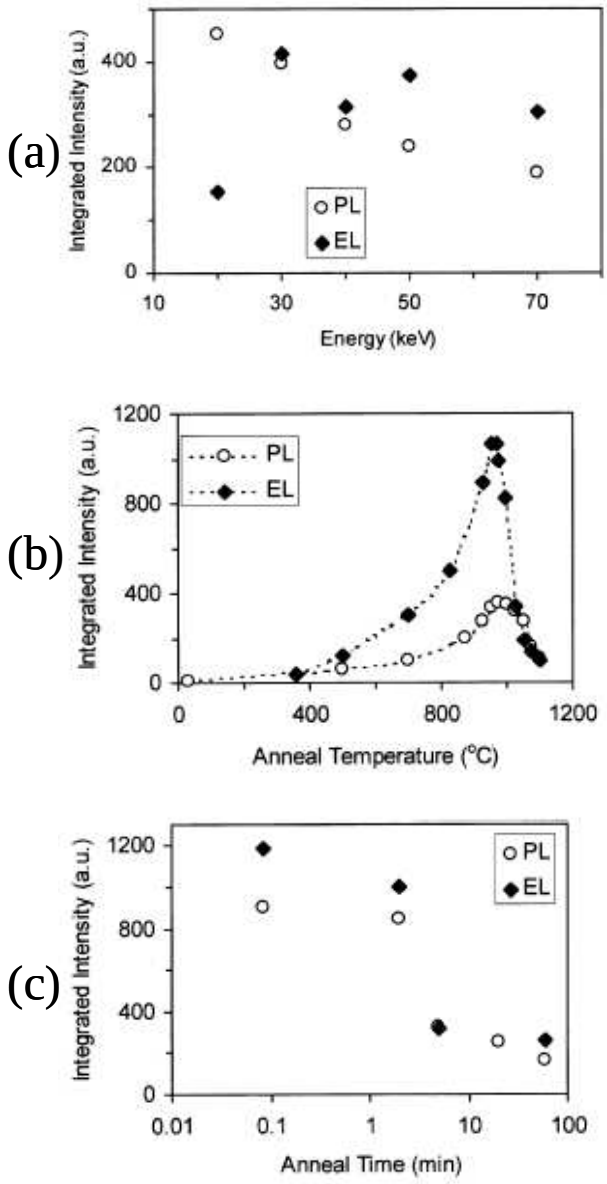

Figure 1.20

Room temperature photoluminescence (◦) (input power 150 mW) and electroluminescence (♦) (forward biased current 100 mA) integrated intensities as a function of:

(a) Implant energy; for samples implanted with boron in the energy range of 20 – 70 keV and at the same peak concentration of 1×10^{20} B cm^{-3}.

(b) Post-implant anneal temperature; for samples implanted at 1×10^{15} B cm^{-2} and annealed for 20 mins. The dashed lines are guides for the eyes.

(c) Post-implant anneal time; for samples implanted at 1×10^{15} B cm^{-2} and annealed at 950 °C.

(After Lourenço *et al.*, 2003).

Annealing time (0.08 to 60 mins at 950 °C) (Figure 1.20c): The maximum integrated intensity was observed in the specimen with the shortest anneal time and observed to fall until a plateau was reached after ~3 mins.

Ng (2000) briefly reported that samples created by arsenic implantation (1.01 x 10^{14} cm^{-2}, 150 keV) into *p*-type Cz-silicon (6 - 22 Ωcm) also exhibited room temperature dislocation-enhanced luminescence. The efficiency and temperature dependence of the luminescence were not reported.

1.4.3 Discussion

The high luminescence efficiency suggests that DE-silicon is a promising route towards efficient room temperature luminescence from silicon, especially considering the relatively limited investigation thus far. It is also an important consideration that all processing steps are highly compatible with the ultra-large-scale integration technology used in CMOS production.

The room temperature spectrum observed in the work of Ng *et al.* displayed a peak at 1150 nm and an inflexion at ~1180 nm. The inflexion is consistent with the reports of the transition between the single TO phonon and the two phonon process of the TO phonon plus the Raman phonon (Green *et al.*, 2001). However, the position of the main peak was observed at a different wavelength to the standard TO phonon peak, generally observed at 1130 nm (see for example Ong *et al*., 1983).

Ng *et al*. (2001) suggest that the high EQE is due to the confinement of carriers to a region of material between the band of dislocations and the p^+-*n* junction, Figure 1.21. The strain field of the dislocations was suggested to modify the silicon bandgap resulting in a blocking potential for minority carriers injected towards them, Figure 1.22. It was proposed that carriers confined to the region between the

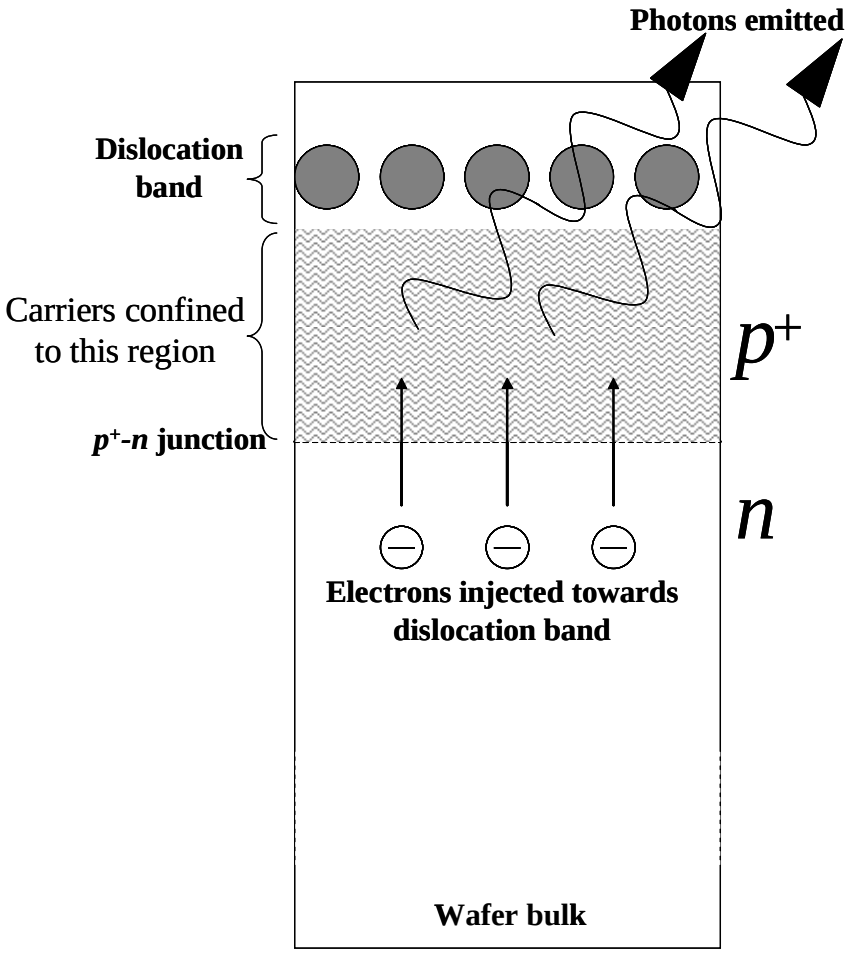

Figure 1.21

Schematic interpretation of the mechanism suggested by Ng *et al.* (2001) for high efficiency band-to-band luminescence in dislocation engineered silicon. Minority carriers are injected towards the dislocation band where they are confined by the strain field of the dislocation loops. The electron-hole pairs are therefore isolated from non-radiative recombination centres in the specimen bulk and at the surface.

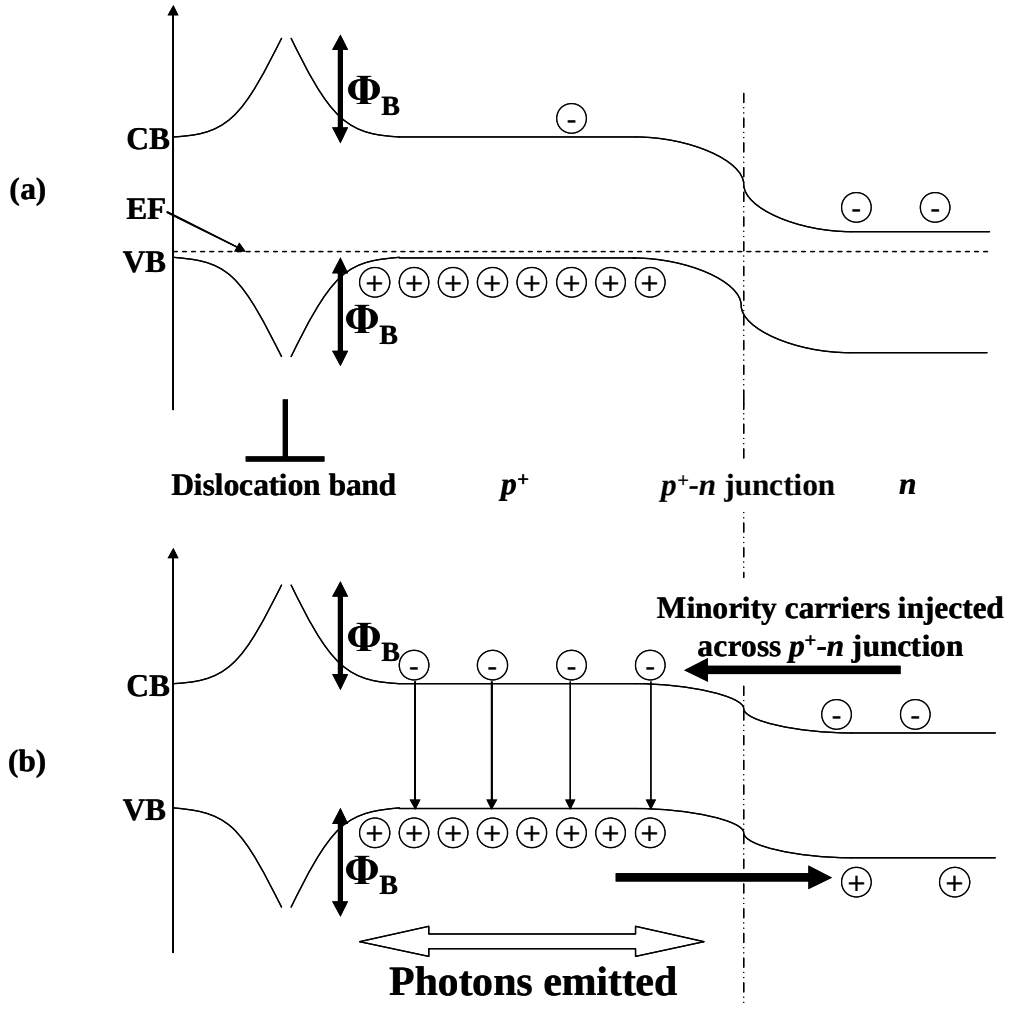

Figure 1.22

Schematic energy band diagrams of the proposed luminescence mechanism of Ng *et al.* (2001) for dislocation engineered light emitting diodes:

(a) Under no applied bias.

(b) Under forward bias. Minority carriers injected into the p^+- region encounter a blocking potential, Φ_B, preventing the diffusion of carriers to non-radiative traps in the bulk and at the surface.

dislocations and the junction were unable to diffuse to regions of the wafer with a high rate of non-radiative recombination - such as the surface and non-radiative centres in the bulk - thus allowing efficient luminescence.

The increasing efficiency with temperature is a surprising result and is in contrast to results generally observed in semiconductor luminescence studies. Further to this, the results appear to contradict the latest experimental findings of Trupke *et al.* (2003b) who found a decrease in the radiative recombination coefficient of more than an order of magnitude between 80 and 400 K for unprocessed silicon wafers (shown previously in Figure 1.10). Ng *et al.* (2001) suggest that thermal quenching is avoided due to the confinement of carriers decoupling the radiative recombination carrier population from non-radiative recombination routes.

The suggested mechanism of Ng *et al.* (2001) describes how both the dislocations and *p*-*n* junction are necessary for efficient luminescence. There is, however, little experimental evidence to support this conclusion, as all specimens investigated contained both the dislocation loops and a p^+-*n* junction. The mechanism is however qualitatively supported by the results of the annealing experiments. The fact that luminescence appears to be fully quenched at 1100 °C is consistent with reports in the literature of the complete dissolution of extended defects at this temperature (see for example Sobolev *et al.*, 2003).

Despite the mechanism seeming to explain a large number of the experimental results there do appear to be several flaws. The asymmetrical doping of the p^+-*n* junction results in the vast majority of carriers being injected into the bulk of the specimen in a direction away from the dislocation band making the proposed mechanism appear inconceivable considering the low concentrations of carriers in the suggested, active region. Secondly, the effect of the long range coulombic band

bending associated with dislocations is ignored. Dislocations are known to act as centres of non-radiative recombination (Wilshaw, 1984 and Kveder *et al.*, 2001) with minority carriers effectively trapped at the defects. Thus, the dislocations are likely to act as non-radiative centres to any injected carriers rather than acting as a barrier to carrier diffusion.

In order to place the work of Ng *et al.* (2001) and Lourenço *et al.* (2002 and 2003) into context a short review of the ion implantation process, resulting defects, the effects on the minority carrier lifetime and luminescence studies follows.

1.5 Ion implantation of semiconductors

Ion implantation is a standard industrial semiconductor process to controllably dope the near surface region of semiconductors. High-energy dopant ions are implanted at a depth from about 10 to 1000 nm below the silicon surface. Ion implantation produces damage to the silicon lattice through nuclear stopping of incident ions or recoils. In addition to the production of a high concentration of point defects and damage during elastic collisions (vacancies, interstitials and Frenkel pairs; a silicon self interstitial and an associated vacancy), there is also a net increase in the density of the material in the implanted region (Williams, 1998). Above a critical dose, amorphisation of the host lattice can occur (*e.g.* greater than 10^{14} cm^{-2} for As^{+} ions). An annealing step must be performed to activate the dopant and to recrystallise the lattice, during which process extended defects may be formed.

1.5.1 Ion implantation damage

The energy loss of the incident ions is as a result of the interaction between the high energy implant ion and the electrons and nuclei of the substrate atoms. At typical implant energies of between 25 keV and 1 MeV, light ions, such as boron ions, will lose most of their kinetic energy through inelastic collisions, whereas heavier ions decelerate via elastic collisions which result in lattice displacements of the host lattice atoms (creating Frenkel pairs; a silicon self interstitial and an accompanying vacancy). A large amount of research has been aimed at modelling the damage to the host lattice after ion-implantation and prior to annealing. An extensive review of the topic has been made by Jones and Rozgonyi (1993). For a sufficiently high concentration of implantation damage it is possible to transform the crystalline silicon into an amorphous phase (see for example Polk, 1971 and Verpek *et al.*, 1982). The threshold for amorphisation to occur is highly dependent upon the implant ion energy, dose rate and wafer temperature. For example, the critical boron dose required for amorphisation is ~2 x 10^{16} cm^{-2} when the wafer is held at 100 ºC during implantation (Jones and Rozgonyi, 1993).

Annealing of the wafer must be carried out after ion implantation, regardless of whether amorphisation has occurred, in order to activate the dopant. It is during this annealing process that recrystallisation of the damaged region occurs and extended defects may be formed. Extended defects may form even if amorphisation of the substrate has not occurred; the threshold ion flux for extended defect formation without amorphisation is ~1 x 10^{14} cm^{-2} for boron ions implanted at under 100 keV (Jones and Rozgonyi, 1993).

1.5.2 Defect formation and evolution

The defects that form during the annealing conditions used in DE-silicon are extrinsic and formed by interstitial ions condensing on a crystallographic plane. There are four sources of these interstitials that may form defects: (a) the implanted ions themselves, which when greater in concentration than the vacancy level of the host silicon become excess interstitials; (b) recoil atoms from the surface - implanted ions strike a surface atom of the host material with sufficient momentum to drive the atom further into the host sample; (c) recoils from the amorphous-crystalline interface (when an amorphous layer is produced) and (d) separated Frenkel pairs.

A classification of defects has been produced which enables a distinction to be made between different secondary defects that occur during annealing as a result of the implant conditions (Prussin and Jones, 1986). The categories distinguish defects in terms of their proximity to the amorphous-crystalline interface (if any) and the defect morphology. The most commonly observed, and consequently studied, defects are the "end of range" (EOR) defects, also known as type 2 defects, which consist of a mixture of {311} rod-like defects and interstitial dislocation loops or only interstitial dislocation loops, depending on the annealing temperature. Type 2 defects form below the amorphous/crystalline interface at or beyond the end of range. The defects observed in the samples described by Ng *et al*. (2001) are termed type 1; these defects form when the implant dose exceeds a critical value and simultaneously no amorphous layer is formed. Type 1 defects are typically located at a depth corresponding to the projected range of the implanted species (Vandervorst *et al*., 1985).

It is thought that the evolution of type 1 defects, upon annealing, takes place from a supersaturation of point defects through the formation of intermediate defect

configurations to a layer of perfect dislocation loops (Tan *et al.*, 1981). The resulting perfect dislocation loops tend to lie on {111} habit planes, are elongated in <110> directions and have a/2[110] type Burgers vectors perpendicular to the long axis of the loop. Annealing at temperatures below 850 °C has also lead to the observation of {311} rod-like defects, these are relatively unstable and dissolve upon annealing after only three minutes at 815 °C (Eaglesham *et al.*, 2004). Since the processing conditions in the present work, and also that of Ng *et al.* (2001), are above this temperature these defects will not be considered here.

Type 1 dislocation loops are much more stable than {311} rod-like defects, requiring temperatures of 1100 °C to dissolve (Sobolev *et al.*, 2003). Annealing in oxygen containing atmospheres can result in oxidation-induced interstitial injection, resulting in the growth of the dislocation loops into large stacking fault areas rather than their complete dissolution (Jones, 1999).

1.5.3 TEM studies of dislocation engineered silicon

Milosavljević *et al.* (2003 and 2005) reported TEM studies of the DE-silicon investigated by Ng *et al.* (2001). A band of dislocation loops (density ~1 x 10^9 cm^{-2}) was observed with the loops lying on the four non-parallel {111} lattice planes with an extended axis along a [110] direction, see Figure 1.23. The dislocation band was observed to be of width 200 ± 25 nm and centred 130 ± 25 nm below the surface. This is consistent with type 1 extended defect formation at the projected range. The projected range was calculated, using the TRIM code, to be 120 nm (Ziegler *et al.*, 1985). A bimodal distribution in the mean loop diameter was observed; loops identified to be faulted Frank loops (a/3<111>) were ~175 nm in diameter whereas the

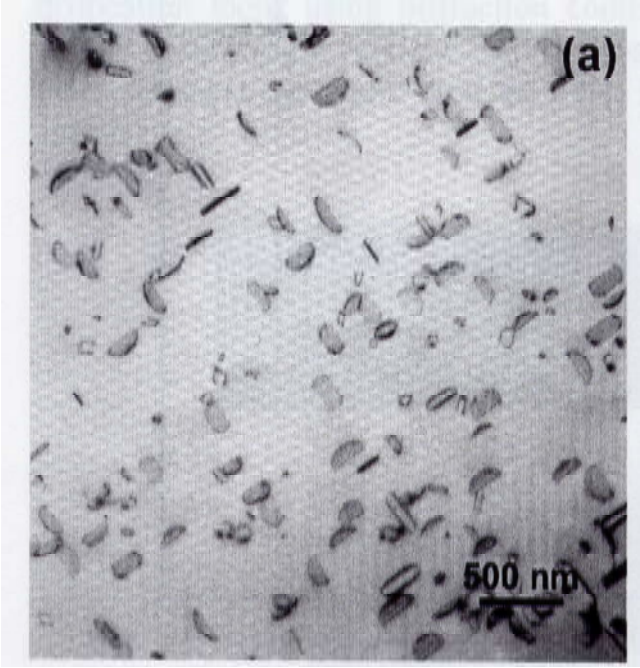

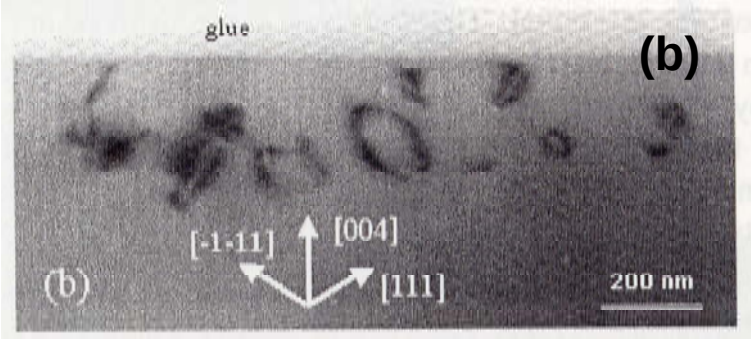

Figure 1.23

a) Plan view [001] and b) cross-sectional [110] bright field TEM images of dislocations created by boron ion-implantation in dislocation-engineered silicon. Annealed 950°C for 20 mins, implant energy a) 35 keV and b) 25 keV.

After Milosavljević *et al.*, (2003).

perfect a/2<100> loops were much larger, mean diameter ~350 nm. The majority of defects were found to be of the faulted nature (~90%).

Sobolev *et al.* (2004) reported, for a similarly processed specimen to Milosavljević *et al.* (2003), a mixture of perfect (2.5 x 10^8 cm^{-2}) and faulted Frank loops (4 x 10^8 cm^{-2}). The faulted loops had two characteristic sizes with diameters in the range 200 - 230 nm or 380 - 515 nm, the larger diameter defects were not observed by Milosavljević *et al.* (2003). The prismatic loops were observed to be only 50-190 nm in diameter. The defects were located in a similar region of the specimen.

The vast majority of the ion implantation literature concerns investigation of type 2 extended defects, where both faulted and perfect loops are observed to be only several tens of nanometres in diameter (Pan and Tu, 1997 and Pan *et al.*, 1996). It is suggested by Milosavljević *et al.* (2005) that this may have a role to play in the surprisingly efficient luminescence observed in DE-silicon.

1.5.4 Influence of extended defects on the minority carrier lifetime

The extended defects resulting from the ion implantation process are widely reported as being deleterious to the minority carrier lifetime of bulk wafers (see for example Ioannou and Davidson (1979), MacDonald *et al.* (2003) and Huang *et al.*, (2006)), suggesting that the ion implantation process should decrease the radiative efficiency.

Minority carrier diffusion lengths have been observed to fall ~21% (17.5 to14.5 μm) after the implantation of 1 x 10^{14} cm^{-2} boron ions at 400 keV (the implanted wafer and a control were annealed at 1000 °C for 30 mins) and ~53% lower

(41 μm compared to 84 μm) when the anneal was carried out at 700 °C (Ioannou and Davidson, 1979).

MacDonald *et al.* (2003) report a reduction in the minority carrier lifetime in silicon implanted wafers (36 keV, $1x10^{14}$ or $3x10^{15}$ cm^{-2}, annealed for 60 mins at 900 °C). The effective lifetime fell from 105 μs to 10 and 5 μs in the low and high dose samples respectively after annealing. Removal of surface material by chemical etching recovered the lifetime slightly to 65 and 15 μs for the low and high dose specimens respectively. These values are still lower than the control wafer, annealed in the same manner. The reduction in the effective lifetime in these samples shows both surface and deeply propagated defects, of uniform concentration to depths of at least 100 μm, remaining after anneals at 900 °C, see Figure 1.24. MacDonald *et al.* attribute the high recombination near the surface to end-of-range dislocation loops. The deeply penetrating recombination centres are suggested to be silicon interstitials, though it is unclear how a 36 keV silicon implantation can influence a material at such depths.

Dislocations introduced by alternative methods are also known to reduce the minority carrier lifetime. Kittler *et al.* (2001) report modelling results, where an increase in the dislocation density (from 10^4 to 10^6 cm^{-2}) reduces the diffusion length from ~ 65 μm to ~ 15 μm in bulk crystalline silicon with a transition metal concentration of 10^{12} cm^{-3}. Extended defects have, however, been intentionally introduced to processed wafers, in regions far from active devices, to act as gettering centres. Here the defects act as trapping centres for metallic impurities ensuring that precipitation does not occur in active device regions. The bulk minority carrier lifetime is reduced as a result. However, the devices are in a region of material where locally the minority carrier lifetime is greater (Istratov *et al.*, 2000).

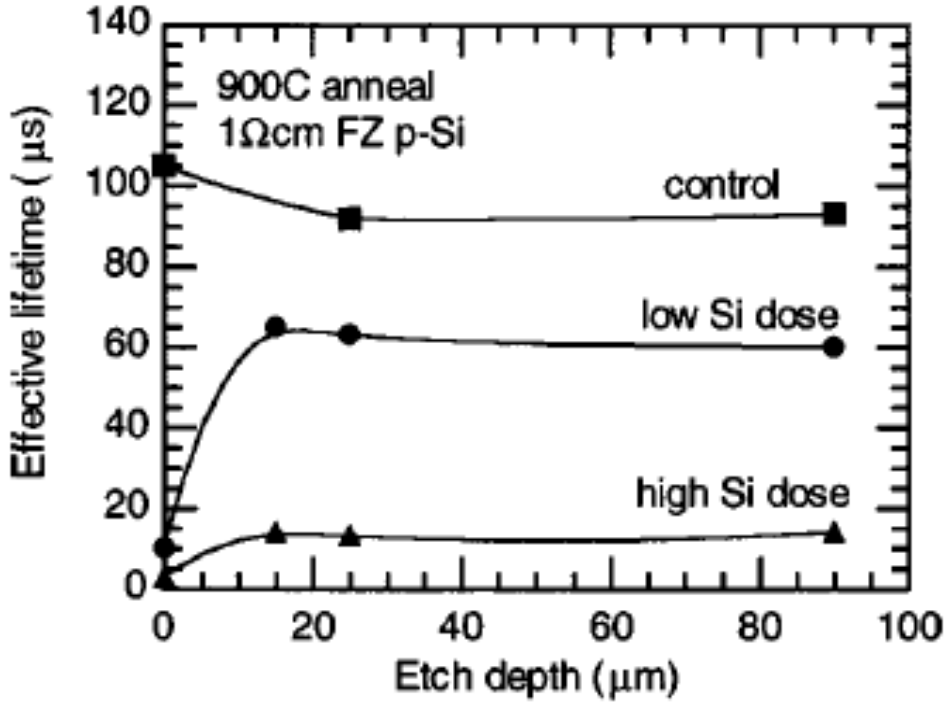

Figure 1.24

Effective minority carrier lifetime as a function of the depth of silicon etched from the front surface for self-implanted (36 keV) silicon wafers annealed at 900 °C for 60 mins in a nitrogen atmosphere. Low dose = 1 x 10^{14} cm^{-2}, high dose = 3 x 10^{15} cm^{-2} (after MacDonald *et al.* 2003).

1.6 Conclusions, aims and structure of thesis

Despite the fact that silicon is an indirect bandgap material there is a large research effort into producing an all silicon-based optical emitter for interconnect applications. However, the ability to produce a room temperature, highly efficient, silicon-based light-emitter compatible with standard CMOS technology is a goal that has thus far proved unattainable. However, the field of research is relatively new and as such there is room for novel techniques to be actively researched. Just such an approach is the use of DE-silicon (Ng *et al.*, 2001).

The ion implantation and annealing processes used in the production of DE-silicon are standard industrial techniques and, as such, a large number of studies have been made into the physical properties of the resulting defects and their effect on material performance. However, to the best of the author's knowledge, no reports prior to the work of Ng *et al.* (2000), suggested that the ion-implantation and annealing processes produced sufficiently efficient room-temperature luminescence to be considered as a potential silicon-based optical emitter. Indeed, the implantation and annealing processes were thought to have a deleterious effect on radiative processes (see for example Ioannou and Davidson (1979) and MacDonald *et al.* (2003)). Thus, it is widely assumed that the wafer minority carrier lifetime is a maximum prior to specimen processing. As a consequence, the effect of extended defects on the room-temperature optical properties of silicon has not been studied extensively.

The luminescence results of DE-silicon, in particular the relatively high efficiency, suggests that DE-silicon is worth further investigation with the view to being used as a potential light source for optical interconnects, especially due the lack of comprehensive understanding. Thus, this project was aimed at understanding the

mechanism of efficient luminescence and to improve the efficiency yet further. This was done through the correlation of the luminescence properties of a wide range of silicon samples with and without dislocations present. The defect structures of ion implanted samples were characterised by TEM.

The structure of the remainder of the thesis is as follows: Chapter 2 introduces the experimental techniques used during the investigation and Chapter 3 characterises the cathodoluminescence system. A routine through which the system collection efficiency is maximised and the reproducibility between experimental sessions is optimised are described. Chapter 4 details the specimens investigated and their methods of production. The subsequent chapters are aimed at fully characterising the samples: the dislocation structure, the morphology of ion implanted samples and the thermal evolution of the defects are investigated using TEM in Chapter 5. In Chapter 6 the cathodoluminescence from a single DE-silicon specimen and a single unprocessed, as-received wafer are investigated as a function of the microscope conditions. The mechanism of efficient luminescence from DE-silicon is investigated in Chapter 7 and a survey of the luminescence efficiencies of a wide range of silicon specimens presented. The luminescence efficiencies are discussed in terms of the non-recombination recombination mechanisms present in a specimen and attempts to improve the efficiency yet further are outlined. Finally, in Chapter 8, the results and conclusions of the present work are summarised and suggestions for further work made.

Chapter 2

Experimental methods

2.1 Introduction

In order to investigate enhanced luminescence from dislocation-engineered (DE) silicon, a large range of samples was created and systematically characterised. In this chapter the experimental techniques used in the study are reviewed. DE-silicon can be created by an ion implantation and annealing process which forms a band of dislocation loops below the wafer surface. The location of the defect band, the nature of the dislocation loops and their density and size were investigated by transmission electron microscopy (TEM). The luminescence properties of all samples were investigated using cathodoluminescence (CL) at room temperature.

2.2 Transmission electron microscopy

TEM was used for the detailed examination of defects associated with the ion implantation and annealing processes. The nature and location of the band of extended defects, the defect density and sizes were determined for each specimen and in a few chosen cases the extended defect (dislocation) Burgers vectors were determined.

Philips CM20 and JEOL JEM-200CX microscopes, operating at 200 kV, were used for the TEM investigation. Both microscopes were equipped with double tilt holders, with one tilt axis being eucentric.

All TEM investigations used in this study were carried out using diffraction contrast analysis, the theory and practice of which has been described in several textbooks (Hirsch *et al.*, 1965; Eddington, 1976 and Williams and Carter, 1996) and as such the contrast mechanisms will only be described here in outline.

2.2.1 Diffraction contrast in the transmission electron microscope

To undertake diffraction contrast imaging, a uniform thin crystal (a foil) is tilted so that a set of lattice planes with Miller indices **g** = (h k l) are at an angle θ to the electron beam, where θ is close to the Bragg angle, θ_B. The latter is given by $\lambda = 2 d \sin\theta_B$, where λ is the wavelength of the electrons illuminating the specimen, $d^2 = a^2/(h^2 + k^2 + 1^2)$ and a is the lattice parameter.

The deviation from the Bragg condition is characterised by the vector **s**, called the deviation parameter and defined as the vector parallel to the beam from the point **g** to the Ewald sphere in reciprocal space.

The image obtained in the TEM is an intensity map of electrons leaving the back surface of the specimen in a direction selected by the objective aperture. In the case where the direct beam is selected (bright-field), the image appears dark where electrons have been scattered out of the direct beam path. Conversely, by imaging using a selected diffracted beam (dark-field), the image appears bright where electrons have been scattered into the selected diffracted beam path relative to a dark background. Thus, contrast arises because of the perturbation of the local diffracting conditions. The contrast mechanism for a dislocation depends on the conditions of observation.

*Kinematical condition (**s** > 0):* Figure 2.1 shows schematically an edge dislocation in a thin foil. In the region far from the dislocation, the crystal is tilted significantly away from the Bragg condition and the incident beam is not strongly diffracted. This is the case of a perfect crystal, which, when of uniform thickness and not bent, will be of uniform intensity in the resulting image. However, near the dislocation the planes are bent into the Bragg condition by the dislocation strain field.

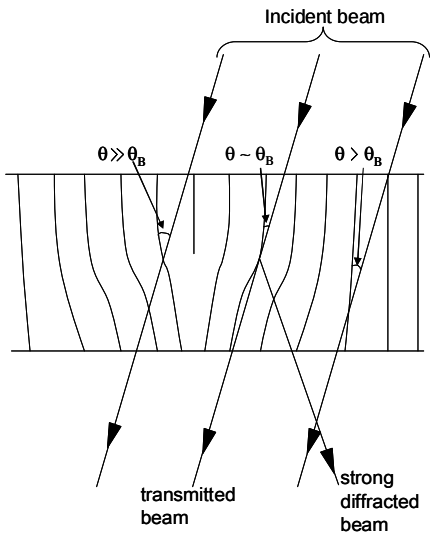

Figure 2.1

Schematic representation of an electron transparent single crystal containing a single dislocation (represented by the extra half-plane), θ is the angle between the electron beam and the lattice plane. When the planes immediately to the right-hand side of the dislocation are bent so that they closely approach the Bragg condition ($\theta = \theta_B$, the Bragg angle) the intensity of the direct beam emerging from the crystal is reduced. The dislocation appears as a black line in the bright field image. This corresponds to 'kinematical bright-field' diffraction conditions.

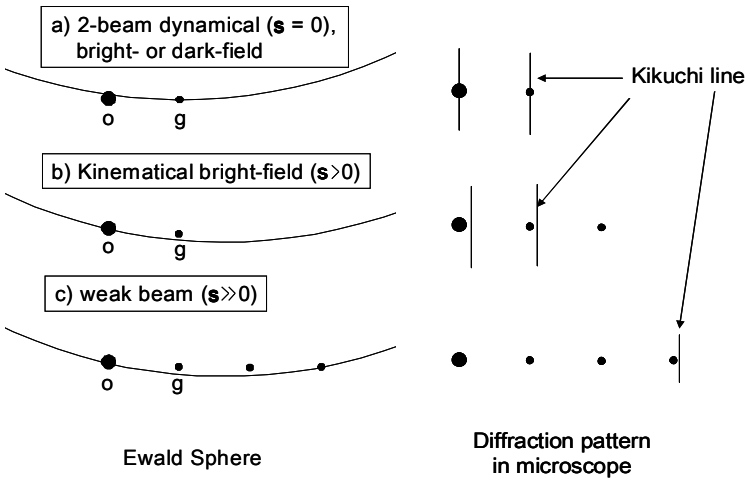

Figure 2.2

Schematic representation of the diffraction conditions used in diffraction contrast imaging, where **s** is the deviation parameter: a) two-beam dynamical, b) two-beam kinematical, c) weak beam. In each case the Ewald sphere is sketched on the left-hand side, and a schematic diffraction pattern showing the position of the relevant Kikuchi lines on the right-hand side. The curvature of the Ewald sphere has been exaggerated for clarity.

In this situation there will be stronger scattering into the diffracted beam. We would expect a bright-field image of the dislocation to be a dark line, and a dark-field image to consist of a complementary bright line.

*Dynamical conditions (**s** = 0):* In this case, the crystal is tilted in order to satisfy the Bragg condition (**s** = 0), and the dislocation strain field tilts the lattice planes away from the Bragg conditions. So, simplistically we would expect the dislocation to appear as a white line in a bright-field image and a dark line in a dark-field image. However, the image contrast theory under dynamical conditions is more complex due to the strongly dynamic nature of electron diffraction (*i.e.* it is necessary to include the scattering from the diffracted beam back into the incident beam). There are also effects due to anomalous absorption. Nevertheless, the physical mechanism of observed contrast is as described above.

*Weak-beam condition (**s** >> 0):* In this mode, the specimen is tilted such that only very highly strained planes near the dislocation core satisfy the Bragg condition. Despite the low intensity of the scattered electron beam this is relatively strong compared to the surrounding matrix. The technique is not straight forward because almost nothing is seen on the screen, making adjustments difficult. Moreover, long exposure times are needed which are only practical with a very stable instrument. The weak beam technique provides the highest resolution of conventional diffraction contrast techniques due to only very highly strained regions, close to the dislocation core, providing crystallographic planes satisfying the Bragg condition.

The diffraction conditions and diffraction patterns observed in the microscope used in the three modes of diffraction-contrast imaging outlined above are shown in Figure 2.2. For a dislocation to be visible it must distort the planes which are forming the diffracted beam, thus the Burgers vector, **b**, of a dislocation can be determined

from images if the conditions are chosen to satisfy the dislocation contrast criteria **g**.**b** = 0 (Hirsch *et al.*, 1965).

2.3 Cathodoluminescence using scanning electron microscopy

Cathodoluminescence (CL) was used to study the luminescence efficiency of the DE-silicon specimens. The following section describes the manner in which the luminescence signal is generated and detected.

The basis of a scanning electron microscope (SEM) is its ability to produce a focused probe of electrons which may be scanned across a specimen surface. The interaction of the electron beam with the specimen may be monitored using a suitable detector. The most common method of using the detected signal is to modulate the brightness of a visible display screen; at each point on the screen the brightness is proportional to the signal collected from a corresponding point on the specimen surface. The choice of a suitable detector allows a variety of specimen information to be gained. The workings of an SEM and the many modes of operation are widely covered in the literature and only those concerning CL will be discussed here. In the CL mode it is the luminescence produced by recombination of electron-hole pairs generated by the interaction of the incident beam of energetic electrons and the semiconducting specimen that is exploited.

2.3.1 Electron-solid interactions

A high energy electron beam, typically 0.5 – 40 keV in an SEM, penetrating a semiconductor slows down by a series of inelastic collision events with the valence and core electrons. These events result in only a small deviation in path and so result in the continuous slowing down of the electrons while they travel in approximately straight lines. When a core or valence electron takes part in such a scattering event it may acquire sufficient energy to make a transition to the conduction band, leaving a hole in the valence band, so generating an electron-hole pair. Less frequently, the injected electrons undergo an elastic scattering event caused by the interaction with an atomic nucleus of the host lattice, this is a Rutherford scattering event caused by the Coulombic interaction and results in a large change in direction with little energy lost to the host lattice. These two categories of scattering events result in the initially collimated incident electron beam spreading out as the electrons penetrate the specimen and slow down. Each high energy incident electron leaves a trail of lower energy electron-hole pairs along its path, with the path periodically deviating due to an elastic collision.

The total number of carrier pairs generated per second, U, is given by:

$$U = \frac{E_{beam} I_{beam} (1 - f_b)}{E_{eh} q} \qquad \text{Eqn. 2.1}$$

where E_{beam} and I_{beam} are the beam energy and beam current respectively, f_b is the fraction of energy scattered back off the specimen and E_{eh} is the energy required to generate an electron-hole pair. f_b is approximately 0.08 for silicon and is mainly accounted for by the backscattered electrons which leave the specimen. The energy to create an electron-hole pair is, in general, about three times the bandgap energy for

the semiconductor and is found to be 3.6 eV for silicon (Klein, 1968). This energy is larger than the bandgap as some energy is lost through phonon heating and the electron-hole pairs themselves possess large amounts of kinetic energy upon creation, which they subsequently lose as they approach thermal equilibrium with the lattice.

2.3.1.1 Spatial distribution of generated carriers

The spatial generation of electron-hole pairs has been widely investigated experimentally and also theoretically using Monte Carlo type calculations. The results of each are in good agreement and show that the distribution of carriers generated by an electron beam follows a universal curve for incident electrons in the range 5 - 50 keV and materials whose atomic number are in the range 10 to 15. For elements outside this range a correction factor must be used. Figure 2.3 shows this curve. The standard interpretation of the range was defined by Gruen as the extrapolation of the linear portion of the depth generation curve to the abscissa (Gruen, 1957). The Gruen range, R_G, is given by $R_G \propto E_{beam}^{1.75}$, where E_{beam} is the beam energy.

The Gruen range describes the energy dissipation as a function of depth. However, this describes the energy dissipated in a slice at a given depth and provides no information about the lateral distribution of the energy lost. The lateral distribution is also a universal function and can be scaled according to the beam energy and the specimen density in order to find the spatial distribution of carriers in a given semiconductor, as shown in Figure 2.4. The generation of carriers is essentially confined to a volume, termed the “generation volume”, of several microns (or less) in radius for the beam energies typically used in an SEM.

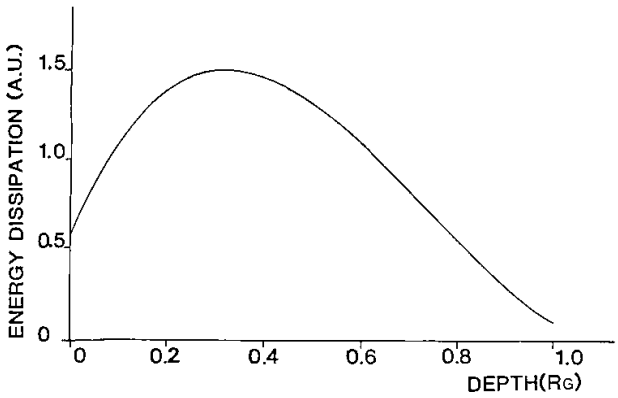

Figure 2.3

Experimentally determined generation rate of carriers below specimen surface. In order to convert depth to microns, multiply by $4.28 \times 10^{-6} E_{beam}^{1.75} \rho^{-1}$, where E_{beam} (keV) is the beam energy and ρ the material's density (kg m^{-3}) (after Everhart and Hoff, 1971).

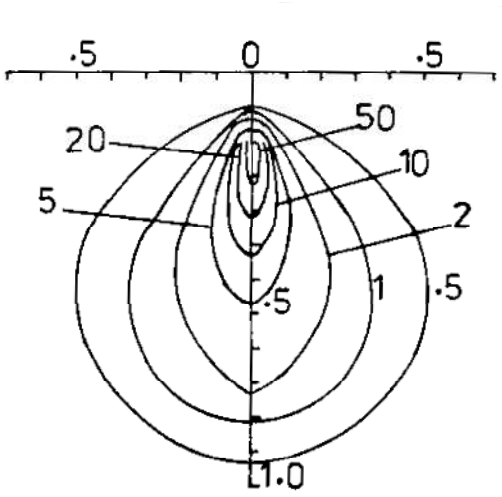

Figure 2.4

Lateral variation of the generation of carriers. Scales normalized to the Gruen range of incident electron. Generation rate shown by contours of equal ionization rate (after Cohn and Caledonia, 1970).

2.3.2 Cathodoluminescence emission

The generation of electron-hole pairs in the semiconductor specimen by the incident electron beam disturbs the local equilibrium concentration of both majority and minority carriers (i.e. $p\,n > n_i^2$, where p, n and n_i are the hole, electron and intrinsic carrier concentrations respectively). As described previously in Section 1.2.3, the excess carriers recombine, releasing a photon of characteristic energy. CL is the process where carriers generated by a high energy electron beam recombine radiatively to emit a photon. The actual number of photons produced is dependent on two factors. Firstly, the number of carriers generated by the beam and, secondly, the proportion of these which are able to combine radiatively. Clearly, high radiative recombination efficiency corresponds to a high CL intensity.

2.3.3 Comparisons of different luminescence techniques

Luminescence techniques operate by creating free electrons and holes, which subsequently recombine producing a photon of characteristic energy. They are differentiated by the manner in which electron-hole pairs are generated. In CL carriers are generated by the specimen's interaction with a high energy electron beam, in photoluminescence (PL) electron-hole pairs are generated by the absorption of photons with energy greater than the band gap, whereas, in electroluminescence (EL) minority carriers are injected into the semiconductor by an applied potential. The spectra produced by the three techniques have the same form (Hare *et al.*, 1972) and temperature dependence (Davies *et al.*, 1989). There are, however, significant differences between the techniques which will be outlined in the following section in order that the results of this investigation may be compared with the literature.

2.3.3.1 Carrier Generation

The generation of electron-hole pairs by the electron beam in an SEM is a near-surface event with nearly all carriers generated within 5 μm of the surface, as described in Section 2.3.1. The carrier generation profile in PL experiments is determined by the photon energy of the exciting laser and the absorption co-efficient of the substrate. An appropriately chosen wavelength can generate carriers within the first few microns only (for example ~2 eV for silicon substrates), or produce approximately uniform excitation of defects distributed throughout the bulk of the wafer (for example exciting with 1064 nm (1.165 eV) Nd-YAG radiation, to which silicon is almost transparent). The EL technique generates excess carriers by their injection into the material substrate by a forward biased Schottky barrier or a *p-n* junction. In this case, the source of the excess carriers is the interface between the junction depletion region and the bulk material.

2.3.3.2 Input Power

The total power deposited into the substrate in the PL technique is dependent on the exciting laser. Lasers of several watts may be used to generate large concentrations of electron-hole pairs. In practice, due to thermal considerations, a lower power is often used, with moderate powers considered to be several hundred milliwatts. The total power deposited using the CL technique is considerably lower, limited to less than a milliwatt by the beam current and accelerating voltage of the SEM. EL can produce input powers typically up to 100 mW over an area the size of the injecting diode (typically up to a few square millimetres for research purposes).

2.3.3.3 Resolution

Both the CL and PL techniques have the potential to investigate the optical properties of semiconductors with good spatial resolution. The resolution of the PL technique is limited by the wavelength of the exciting laser and the focusing optics. In practice, PL is rarely used for high resolution mapping; the specimen is uniformly illuminated over a wider area (~1 x 1 mm). Higher resolution may be achieved by the use of focusing optics (scanning PL or μ-PL) and wide-area mapping achieved by the translation of the specimen relative to the focal point of the laser. The resolution of the CL technique can be easily varied, with resolution (limited by the generation volume) better than a micron routinely achieved. The uniform injection of excess carriers from a planar interface in EL limits the spatial resolution. In general, the EL technique averages the luminescence properties over the whole junction area.

2.3.3.4 Surface recombination

Excess carriers which diffuse to the surface tend to recombine non-radiatively at the surface via surface recombination; this process reduces the number of electron-hole pairs which may recombine radiatively. In EL, excess carriers may be injected away from the specimen surface directly into the specimen bulk. The large-area, uniform injection into the specimen bulk results in low numbers of carriers diffusing to and recombining at the specimen surface. However, in CL many carriers may diffuse to the surface regions of the material resulting in a significantly higher surface recombination velocity, particularly in samples with large minority carrier lifetimes. The larger area over which carriers are generated in PL results in a lower number of carriers diffusing to the surface than in CL, but, more than in EL. As a result of the

increased surface recombination of the CL technique, lower quantum efficiencies are generally observed.

2.3.4 Operation of a Cathodoluminescence system

2.3.3.1 Modes of operation

The CL equipment can be operated in three main modes. The first is the total-light (panchromatic) micrograph mode. In this mode the electron beam is scanned to form a point-by-point image whose brightness is dependent on the intensity of CL emission over a wide range of wavelengths. The second mode is the monochromatic micrograph mode. The beam is again scanned and a point-by-point image is formed, but a dispersive element is included between the CL collector and the detector. In its simplest form, this may be an optical bandpass filter, but most work, including that reported in this thesis, uses a diffraction grating monochromator since this enables a desired spectral wavelength to be selected with ease. The signal-to-noise ratio of the image is dependent upon the intensity of CL emission at the selected wavelength.

The third mode is the CL spectrum mode. In this case no image is formed; the electron beam is placed on the feature of interest on the specimen and the emitted luminescence spectrally analysed. Instead of being set to a fixed wavelength, the monochromator runs through a range of wavelengths and the CL intensity is measured as a function of wavelength.

2.3.3.2 Light collection and detection system

Important considerations in the design of the CL collection and detection system are the solid angle of collection, the field of view of the optics, the transfer efficiency at the wavelength of interest (i.e. ratio of light arriving at the detector to the

light emitted by the specimen) and the detectivity (a measure of the noise) of the detector system at the wavelength of interest.

The design of a CL collection system in an SEM is constrained by the limited distance between the final lens and the specimen. If this distance, the free working distance, is too large, the probe diameter is significantly increased. In the present system the CL collection optics consist of an off-axis, diamond-turned aluminium paraboloidal mirror.

The final lens, the collection optics and the specimen are illustrated in Figure 2.5. The specimen is held in position at the mirror focus by the specimen stage. The electron beam passes through a 1mm diameter hole in the mirror. The electron beam axis is normal to the specimen and impacts the specimen at the mirror focal point; emitted photons are collimated along one axis of the mirror, at right angles to the incident electron beam and guided to the photon detector. The angular dependence of emission intensity is close to that of an ideal Lambertian source.

For the Department of Materials, University of Oxford, system in the monochromatic collection mode, the operation is the same as before (Figure 2.5) except that the collimated light is incident on the monochromator entrance slit, illuminating the diffraction grating. The light is diffracted into a spectrum and reflected onto the plane of the exit slit by a second mirror. The exit slit selects a narrow band of wavelengths and this light passes through an exit slit which leads to the same detector and housing as used for the total-light mode. For monochromatic images the signal is processed as before. The monochromator is illustrated schematically in Figure 2.6.

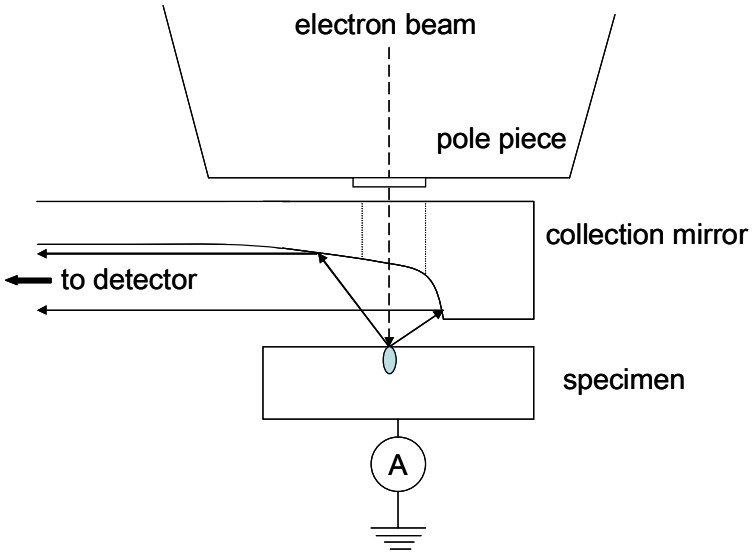

Figure 2.5

Schematic representation of the cathodoluminescence collection optics. The electron beam passes through a 1mm diameter hole in the mirror. Photons emitted from the specimen are collimated along one axis of the mirror, at right angles to the incident electron beam.

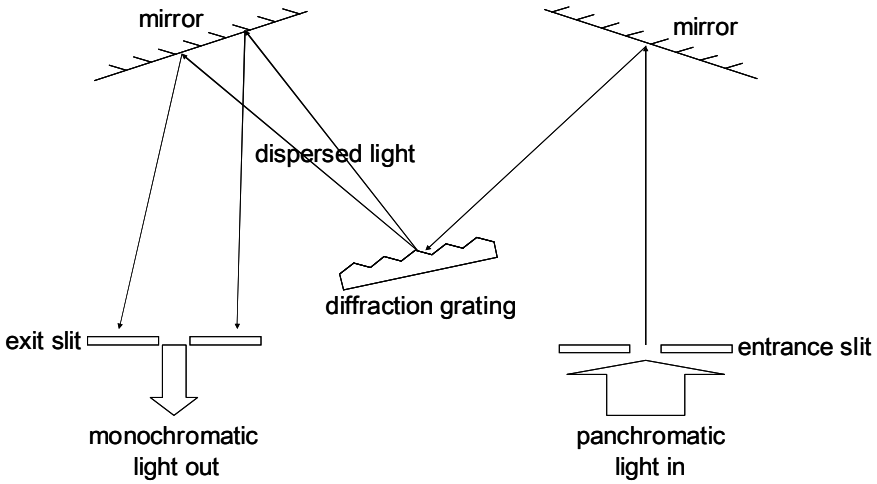

Figure 2.6

Schematic representation of the monochromator. The light path is indicated by the black arrows.

Chapter 3

Setup and characterisation of the Oxford Materials cathodoluminescence system

3.1 Introduction

The Department of Materials, University of Oxford, CL system comprised of a JEOL JSM-6500F field emission gun scanning electron microscope (SEM), a Gatan MonoCL3 system (monochromator, collection optics and photon counting electronics) and the Gatan DigitalMicrograph™ software suite. The CL system was fitted to the microscope during the course of this project and a significant amount of time was taken calibrating and optimising the system for room temperature luminescence from silicon.

3.2 Cathodoluminescence system setup

3.2.1 The scanning electron microscope

The JSM-6500F electron column consisted of a field-emission electron gun, three magnetic lenses, double deflection scan coils, stigmator coils and the final aperture. The accelerating voltage could be varied from 500 V to 30 kV. The microscope was equipped with a eucentric specimen stage, motorised in x, y, z, tilt and rotation. The minimum step sizes in the x and y directions were less than 0.5 μm and in the z direction 0.05 mm. The vacuum system consisted of a diffusion pump with two liquid nitrogen traps. A chamber pressure of better than 1×10^{-4} torr was required before use.

3.2.2 Photon collection

The collection mirror of the Gatan MonoCL3 system was a diamond-turned, off-axis paraboloidal mirror containing a central 1 mm diameter hole through which the electron beam could pass. This restricted the SEM field of view to an area of an

approximately equivalent diameter. The mirror was inserted manually (along the x-axis) to a position directly beneath the SEM pole piece and aligned in the y- and z-directions prior to initial use by Gatan with the assistance of the author, such that the electron beam passed centrally through the hole in the mirror and that the maximum number of photons were collected by the mirror and reflected to either the monochromator entrance or the detector. At the beginning of each session, the optimum mirror position was determined by maximising the collected signal as the mirror was moved along the x-direction.

3.2.3 Photon detection

As described in Chapter 1, silicon is an indirect bandgap material with low external quantum efficiency (EQE) (typically 10^{-6} – 10^{-7} (Fauchet, 2004)). The bandgap luminescence at room temperature (RT) is infra red (IR) and typically peaked at ~1130 nm (Green *et al*., 2001). Thus, in order to observe and investigate RT luminescence from dislocation engineered (DE)-silicon, a high sensitivity liquid-nitrogen cooled germanium detector (North Coast E0-817L, diode area 0.25 cm^2) operated at a constant bias of -250 V was used rather than the standard photomultiplier tube. The germanium detector has a spectral response in the range 800 – 1800 nm with a nominal responsivity of 5 x 10^9 V W^{-1}. The responsivity across the spectral range is shown in Figure 3.1 and corrected for within the Gatan DigitalMicrograph^{TM} software. The detector was pre-set to have a rise time of 300 ms in order to achieve optimum sensitivity.

The collected light was guided by the insertion (or retraction) of flat, high reflectance MgF_2 coated, aluminium mirrors to the detector (panchromatic), or in to the

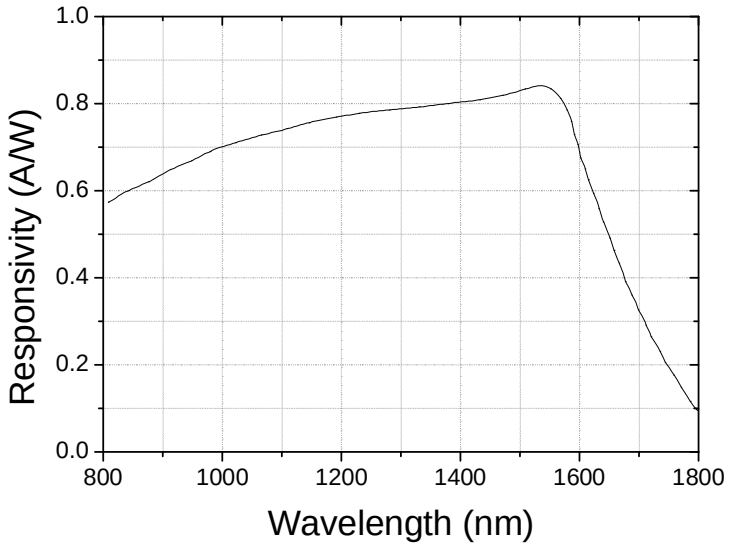

Figure 3.1

The responsivity curve for a germanium detector at 77 K (after http://www.newport.com/file_store/PDFs/tempPDFs/Germanium_Detectors_e5575.pdf)

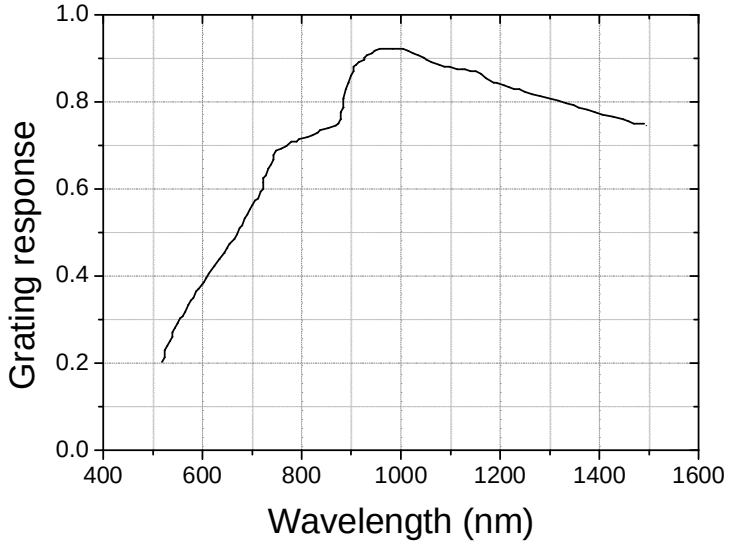

Figure 3.2

Response curve for actual diffraction grating (600 lines/mm blazed for 1200 nm), supplied by Gatan Inc.

monochromator. In order that quantitative data could be obtained, the detector output signal was filtered from the background noise by lock-in amplification by modulation. In order to do this, the light entering the detector had been 'chopped' at a frequency of ~220 Hz. The Gatan MonoCL3 system contains an optical chopper in the light path between the entrance slit and the diffraction grating as standard. A second, additional, optical chopper was installed in the light path directly between the collection mirror and the detector (this was kindly loaned from, and installed with the help of Dr S. A. Galloway of Gatan UK.). The long rise time of the detector severely limited the ability of the system to produce CL images, even for the slowest scan rates, and these were not used except for aligning the system optics. In order to maximise performance the detector was pumped to a high vacuum prior to initial use.

3.2.3.1 The MonoCL3 monochromator

The MonoCL3 system contains a chamber mounted Czerny-Turner monochromator, F# 4.2 and focal length 300 mm. The layout of a Czerny-Turner monochromator has been shown schematically in Chapter 2. Important experimental considerations are the selection of appropriate entrance and exit slit widths and the choice of diffraction grating. The system was periodically calibrated using the 404.66 and 546.07 nm mercury spectral lines of an in-line discharge lamp.

An Oriel 600 lines/mm diffraction grating blazed for 1200 nm was selected for use in the monochromator to maximise the system efficiency in the appropriate wavelength range. The spectral response of the grating is shown in Figure 3.2 and was used in order to correct the experimentally collected spectra within the Gatan DigitalMicrograph^{TM} software.

The widths of the monochromator slits play an important role in determining the maximum spectral resolution: the smaller the slit widths, the greater the system resolution. However, reducing the monochromator slit widths reduces the total light throughput of the system and, thus, the monochromator slit widths were selected to achieve the spectral resolution required while maintaining optimum throughput. The effect of increasing the slit width is dependent on the source image in the slit plane and the source spectrum. In the case of near bandgap luminescence from silicon, the source image on the entrance slit is large and uniform and approximates to a broadband source with a relatively broad spectral distribution. It was found, in accordance with theory, that doubling the monochromator slit widths gave approximately four times as much radiation into the monochromator. The slit widths of 1.5 mm, used for all spectra reported in the remainder of this thesis, were selected to give a spectral resolution of 8.3 nm which was found not to significantly affect the luminescence peak (which had a full width half maximum of 90 nm).

3.2.4 Signal processing

The Gatan MonoCL3 system was controlled using the DigitalMicrograph^{TM} software. The software read the output of the lock-in amplifier as a fraction of the full-scale deflection and thus the sensitivity range of the lock-in amplifier was recorded for intensity comparisons between spectra. The lock-in amplifier was set to zero with the electron beam off prior to recording a spectrum. A small positive offset was then added to ensure no negative values were observed - this was then subtracted from the spectrum in retrospect within the DigitalMicrograph^{TM} software.

Due to the use of the North Coast E0-817L germanium detector, spectra were taken in serial mode *i.e.* the grating was positioned for the measurement of a selected

wavelength and a reading taken for a length of time (the dwell time - which must be longer than the lock-in amplifier's time constant), before the grating was moved, by a stepper motor, to the next wavelength. The starting wavelength, range of wavelengths sampled, number of steps and dwell time are all user defined within the software environment. The photons may be counted either using the total photon count (dwell time dependent) or as the number of counts per second. The total time taken for a spectrum with a dwell time of 2 s, step size of 2 nm and range of 500 nm is approximately 8 mins (typical for spectra reported in this work).

The software includes detector and grating response curves which may be applied to the collected data. All spectrum reported in this work have been corrected for both grating and detector responses so giving an accurate spectrum.

3.2.5 Estimation of the system efficiency

The system efficiency may be estimated by determining the signal loss at each component of the light collection and detection system:

Paraboloidal mirror (data supplied by manufacturer): ~75% of photons emitted from a specimen, located at the mirror focal point, are collected.

Monochromator throughput: The monochromator throughput may be summarised using the following equation (Oriel Instruments, 2005):

$$\frac{P_o}{P_i} = FVE_m R^5 \qquad \text{Eqn. 5.1}$$

where P_o is the output power, P_i is the input power, F reflects any mismatch in the focal length of the illumination and that of the monochromator (in this case ~1), V is a vignetting factor due to the slit aperture being smaller than the source image (slit width dependent), E_m is the efficiency of the grating (~80%) and R equals the reflection efficiency of one of the monochromator mirrors (the R^5 factor implies 5 reflections before light reaches the detector, R ~ 95%). In this case, with wide slit widths, the maximum fraction of power to exit the monochromator is ~62%. Thus, the optical throughput of photons emitted from the specimen arriving at the detector, via the monochromator, is a maximum of 46%.

Detector responsivity: The efficiency of typical germanium detectors, at 1150 nm, is ~80%.

Total system responsivity: The system responsivity in panchromatic mode was estimated to be 3.6×10^9 VW^{-1} and, in monochromatic mode at a wavelength of 1150 nm and slit widths of 1.5 mm, is estimated to be a maximum of 2.3×10^9 VW^{-1}.

3.3 Ensuring reproducibility of data acquisition

In order that a high level of reproducibility could be achieved it was necessary to develop a procedure by which the area of a sample being investigated could be located at the focal point of the mirror. The mirror focal point is located approximately 1 mm below the bottom of the mirror; at this point the collection efficiency of the mirror is greatest. Two methods may be used to determine whether a sample is at the focal point of the mirror: the first is the appearance of a bright central spot in the CL image (rather than crescent shapes for the over- and under-focused

states). This is illustrated in Figure 3.3 where a monochromatic CL image (1150 nm) of a silicon sample at the focal point is shown. The low luminescence intensity emitted by a silicon sample and the long rise time of the detector make this technique difficult. The second method, used as routine, found the focal point by maximising the collected signal (as recorded directly from the CL detector output). This is shown in Figure 3.4 where the normalised collected signal is shown as a function of the specimen distance below the mirror. Due to the discrete nature of the specimen height adjustment process (minimum 0.05 mm), the focal point of the mirror could not be found precisely. This introduces an error in the measured luminescence signal of ~5-10%. The difficulty in mounting the specimen exactly flat can actually be used to decrease this systematic error. A small translation of the sample in the x-y plane results in a very small change in the collected signal due to change in relative distance of the specimen from the mirror. The actual focal height was found more accurately by maximising the collected signal using this method. This procedure was carried out for each and every quantitative measurement reported in the remainder of this thesis, unless otherwise stated.

At the start of each microscope session a standard sample was used to align the system to ensure optimal set up. The systematic error introduced between sessions was found to be less than 1.5%, allowing the direct comparison of results between different experimental sessions. Therefore, all experimental results presented in the remainder of this thesis are self-consistent.

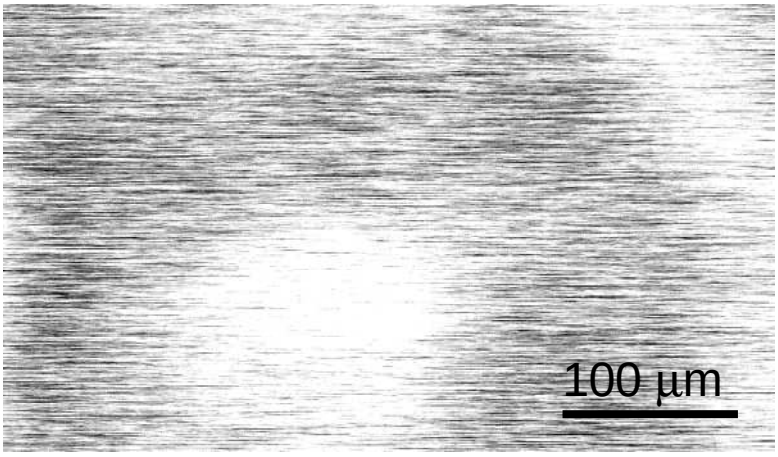

Figure 3.3

Low magnification monochromatic cathodoluminescence image of a silicon sample at the mirror focal point as illustrated by the bright central spot. λ = 1500 nm, slit widths = 1.5 mm, beam current = 200 nA and accelerating voltage = 30.0 kV.

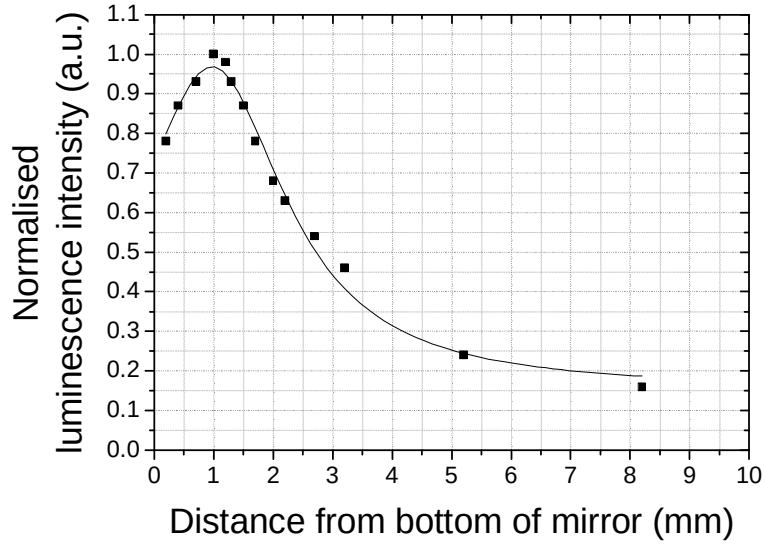

Figure 3.4

Normalised luminescence intensity as a function of the collection mirror and specimen separation distance. The peak indicates the distance at which the specimen is at the focal point of the mirror. The solid line is a Lorentzian fit of the data points.

3.4 Effect of system parameters on the cathodoluminescence efficiency

3.4.1 Variation in the collection efficiency across the field of view

The variation in the collection efficiency of the mirror across the field of view was investigated by focusing the electron beam to a small stationary spot which was moved point-to-point across the field of view, recording the luminescence intensity at a constant absorbed specimen current. The variation in the collection efficiency of the system was investigated using two samples; a gallium arsenide and a silicon specimen. The results are shown in Figure 3.5.

The variation in the luminescence intensity with position across the field of view was found to be large in the gallium arsenide sample. A small, central region ~200 x 200 μm was observed to display high collection efficiency and outside of this a low efficiency was observed. However, the silicon sample was observed to show a significantly lower variation in the collection efficiency.

The gallium arsenide sample has a short diffusion length (~3 μm) and thus, photons are emitted from the sample in close proximity to the electron beam. Therefore, the results from the gallium arsenide specimen accurately show the collection efficiency of the mirror from photons emitted from a specific point on the sample. However, in the silicon sample, due to the long minority carrier diffusion length (typically several hundred microns) photons can be generated far from the position of the electron beam, averaging the collection efficiency from a wide area and resulting in the low variation in the collection efficiency across the field of view. Furthermore, in samples with long diffusion lengths the measured luminescence intensity is significantly less than the emitted luminescence intensity as: i) photons are collected from regions in which the mirror has low collection efficiency and ii)

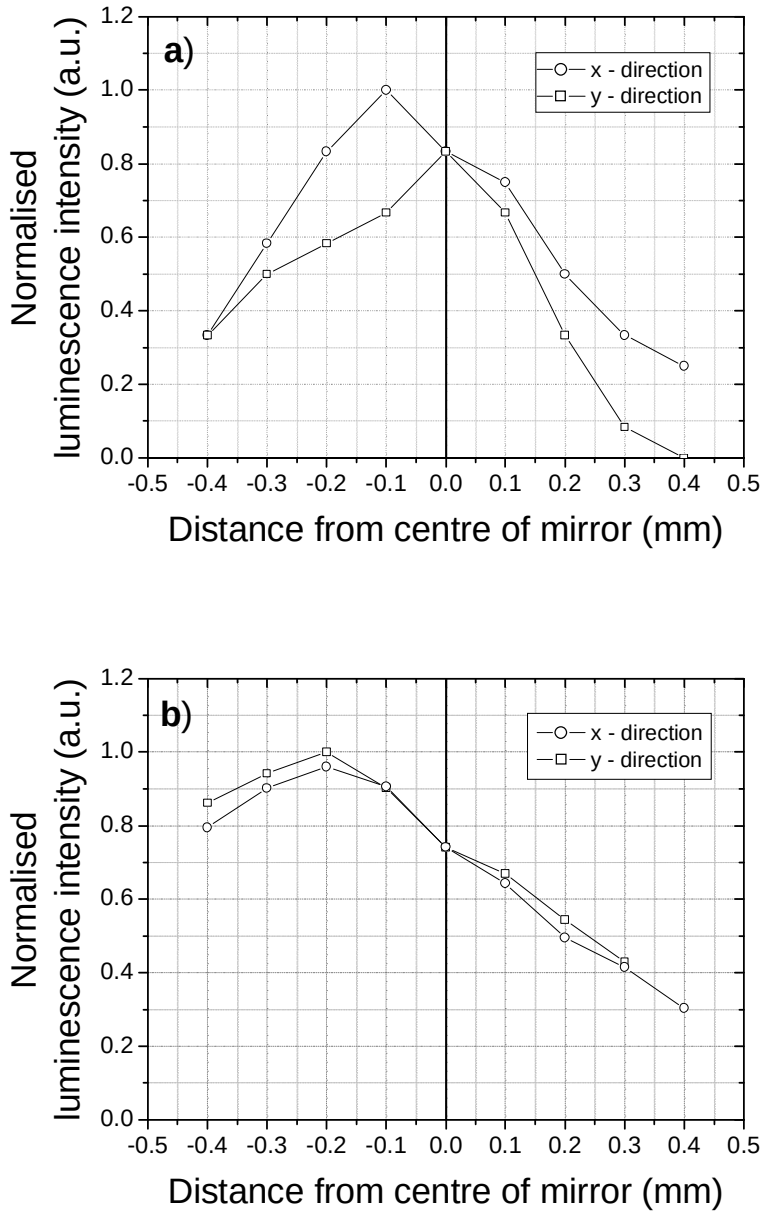

Figure 3.5

Variation in the collection efficiency of the system across the field of view for: a) a silicon doped, gallium arsenide specimen (5 nA) and b) a silicon specimen (150 nA) (Courtesy of K. J. Fraser).

some electron-hole pairs diffuse outside of the field of view and are not collected. This reduction in the fraction of detected luminescence is greater the longer the sample's minority carrier diffusion length.

3.4.2 Scan area

The luminescence intensity as a function of the scan area is shown in Figure 3.6 and was found to be approximately uniform when the scanned area is significantly greater than the generation volume. However, as the generation volume of the electron beam approached an appreciable size in comparison to the scanned area (~50%), a small reduction, ~3%, in the luminescence efficiency was observed.

3.4.3 Scan rate

The luminescence intensity was investigated as a function of the electron beam scan rate in the range 10 to 0.01 Hz. For the highest scan rate possible, ~10 frames per second and 600 lines per frame, minority carriers are calculated to diffuse a distance of 600 μm for one line time. Thus, the electron beam characterises in a point-by-point manner rather than over the larger scanned area. This was observed experimentally; the luminescence intensity was observed to be independent of the scan rate for all samples investigated.

3.5 Effect of specimen production

3.5.1 Sample fixation

Samples were mechanically and electrically attached to a microscope stub using either electrically conductive Acheson Silver Electrodag or carbon loaded sticky pads.

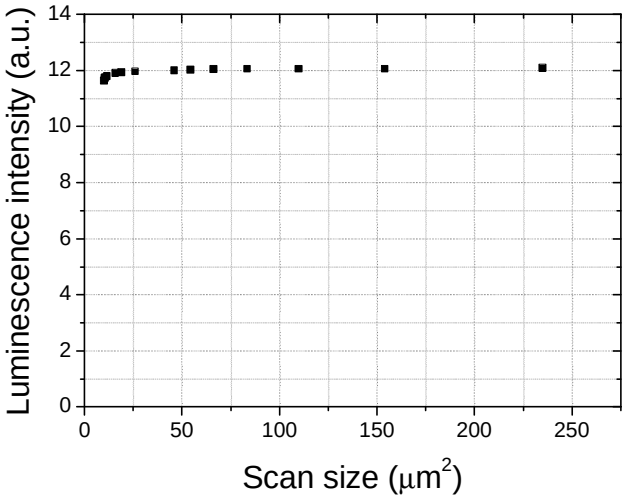

Figure 3.6

Variation in the luminescence intensity as a function of the area in which electron-hole pairs are generated by the electron beam in the dislocation-engineered sample nB2a (B, 30 keV, 10^{15} cm^{-2}, 900 °C for 15 mins). The electron beam was focused to a small point and the diameter of the generation volume was assumed to be 6.5 μm.

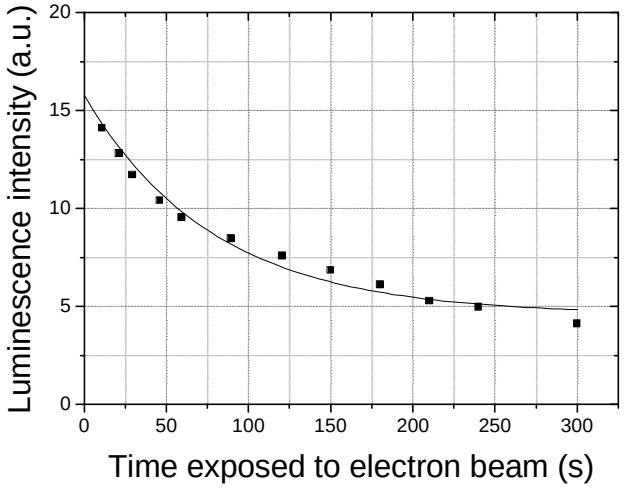

Figure 3.7

Illustration of the decay in the panchromatic luminescence intensity as a function of time of a chemically etched sample exposed to the electron beam. As-received, phosphorous doped, ~10 Ωcm wafer. Beam current 100 nA and beam energy 30 keV.

Little difference was observed between the two fixation techniques: some limited contamination of the sample surfaces was observable in the secondary electron imaging mode for both, though the carbon loaded sticky pads seemed to produce slightly greater surface contamination levels. The surface contamination, however, did not produce an observable drop in the luminescence intensity. Thus, the carbon pads were favoured for their ease of use and liquid-nitrogen traps were employed in the microscope to minimise the contamination effect.

3.5.2 Presence of a native oxide

Samples were investigated in the as-received condition, and after a ~30 sec dip in 40% hydroflouric acid to remove any native surface oxide. No difference was observed between the two sets of specimens and thus a hydrofluoric acid preparatory dip was deemed unnecessary for further samples.

3.5.3 Sample processing

In the course of the investigation of DE-silicon, it was necessary to submit specimens to further processing; some samples were chemically etched whilst others were chemomechanically polished, these processes are outlined in detail in the following chapter.

For samples that were chemomechanically polished, specimens were subsequently placed in an acetone ultrasonic bath (at room temperature) for 10 mins and then cleaned using the RCA routine outlined in Section 4.4.3. Samples were given a final rinse in methanol before examination in the microscope. The luminescence intensity was found to be identical prior to and after processing.

For samples which were chemically etched, a rapid fall in the luminescence intensity was observed when samples were exposed to the electron beam. Rigorous specimen cleaning using the RCA process was found to minimise this effect, but it was often necessary to use only moderate beam currents (less than 50 nA) as even rigorous cleaning often proved insufficient. Below a critical threshold current, no decay in the luminescence signal was observed. For samples which did not exhibit the luminescence quenching, the luminescence efficiency of an as-received and a chemically etched and cleaned specimen was observed to be identical.

The quenching of the recorded luminescence intensity is illustrated in Figure 3.7 for an as-received, 10 Ωcm, phosphorous-doped wafer. Upon initial exposure to the electron beam high luminescence intensity was recorded (times less than ~1 s). The magnitude of this signal was unknown due to the slow rise time of the detector. The luminescence intensity then fell to a low value (less than the unprocessed wafer) within a few seconds and continued to fall to a value significantly less than in an as-received sample.

There are several explanations for this phenomenon, however, at the present time, the mechanism is not understood. Firstly, the electron beam may cause the cracking of organic compounds on the sample surface which absorb emitted photons. These would be invisible in a secondary electron image due to their low atomic density. Secondly, the chemical etching process has previously been associated with the injection of hydrogen to depths of up to 10 μm at room temperature (Sacshe *et al.*, 2000). Hydrogen is known to be an excellent passivator of electrically active defects (Kittler, 2005). Exposure of the sample to the electron beam may disassociate the hydrogen from the defect resulting in an increase in the competing deep-level recombination rate. Thirdly, hydrogen liberated during chemical etching may

passivate the surface reducing surface recombination (Martin *et al*., 2004). Exposure to the electron beam may then de-activate the surface passivation, resulting in the decay of the luminescence efficiency.

Chapter 4

Production of specimens

4.1 Introduction

Dislocation-engineered (DE)-silicon was described in Chapter 1 as a potential route by which relatively efficient room temperature luminescence from silicon may be achieved. However, the mechanism of this efficient luminescence is not understood well. The work reported in the remainder of this thesis is an attempt to produce efficient luminescence, understand the mechanism of enhanced efficiency and, if possible, improve this further. In order that these aims may be achieved a range of samples containing dislocations was produced by a variety of methods: ion implantation and annealing (as used by Ng *et al.* (2001) to produce DE-silicon), abrasion, oxidation induced stacking faults (OISFs), mechanical deformation and oxide precipitation.

This chapter introduces the specimens and processing conditions used in the investigation. The substrate materials and the processing conditions used for the production of a wide matrix of specimens containing dislocations will be described. The Cz-grown and FZ samples were kindly provided by Dr R.J. Falster of MEMC Materials Ltd and Dr O. Anderson of TOPSIL Semiconductor Materials A/S respectively.

4.2 Production of specimens containing dislocations by ion implantation

4.2.1 Substrate material

One-side mirror-polished, Cz-grown (100) silicon wafers (5 - 10 Ωcm), *n*- or *p*-type (phosphorous or boron doped respectively) were used as substrates. The wafers were eight inch in diameter and ~660 μm thick.

The *back surface* of the wafer (non-mirror polished side) contained dislocations generated by soft backside damage (SBD). SBD is a technique in which high velocity silica slurry is directed at the surface; this produces damage in the form of surface pits, typically 100 - 500 nm in diameter. Observation by TEM has shown that the pits have associated dislocation tangles of density ~1 x 10^4 cm^{-2} (de Coteau, 1993). SBD is known to be effective at gettering transition metals from the wafer bulk, so increasing the wafer minority carrier lifetime. However, due to the near-surface nature of SBD defects, only sufficiently-fast diffusing elements are efficiently removed from the specimen bulk (Istratov *et al.*, 2000).

4.2.2 Implantation conditions

Ion implantation of boron, silicon or gallium was made into the polished *front surface* of each substrate material. The boron and silicon implants were kindly performed at the University of Erlangen-Nuremberg by Dr O. Krause and Dr P. Pichler. Each wafer was blanket implanted. The gallium implantations were performed in Oxford using an FEI focused ion beam (FIB) 200 microscope. The gallium source was quoted to be 99.99% pure. Only small areas (0.25 mm^2) of a wafer could be implanted with gallium due to instrument time constraints. The implantations produced six distinct sample categories, schematically illustrated in Figure 4.1:

1) 'nB' – Boron implantation into *n*-type material (dislocations present in a highly *p*-doped region with a p^+-*n* junction present), analogous to the samples investigated in the University of Surrey studies (see for example Ng *et al.*, 2001).

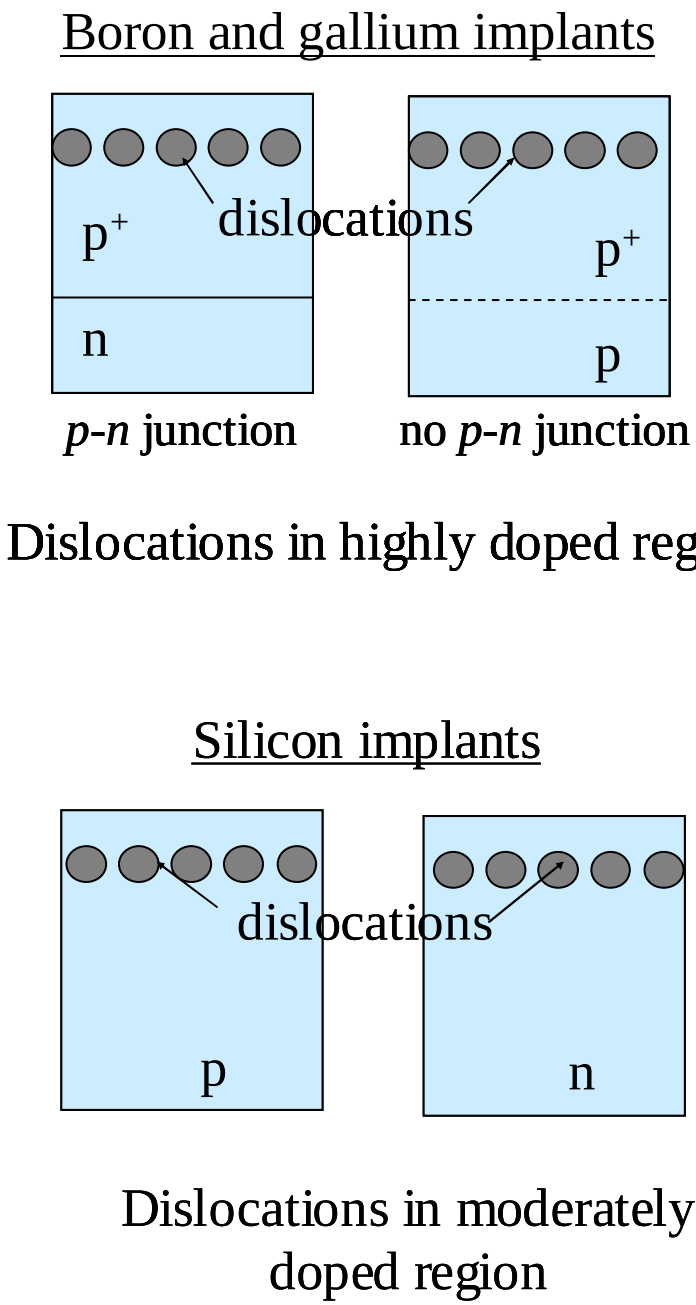

Figure 4.1

Schematic representation of the specimen structure after ion implantation and annealing. The dislocation band and specimen doping are indicated. Note: this morphology was deduced from the transmission electron microscopy investigation reported in Chapter 5.

2) ‘pB’ - Boron implantation into *p*-type substrates (dislocations present in a similarly highly *p*-doped region but with no p^+-*n* junction).

3) and 4) ‘nGa’ and ‘pGa’– Gallium implantation into *n*- or *p*-type material respectively, (dislocations present in a highly *p*-doped region with or without a p^+-*n* junction present).

5) and 6) ‘nSi’ and ‘pSi’ - Silicon self-implantation into *n*- and *p*-type substrates respectively (dislocations present in moderately doped material with no *p*-*n* junction).

The boron and gallium implantations were carried out at 30 keV and the silicon implantations at 80 keV. An off-axis tilt of 7° was used in order to avoid ion-channeling. The wafers were maintained at room temperature during the implantation process. The boron implantation conditions were below the amorphisation threshold whereas the silicon and gallium implantation conditions used have been shown to generate a buried amorphous layer (Jones and Rozgonyi, 1993).

The six categories (nB, pB, nGa, pGa, nSi and pSi) are used in the sample identification code used to label specimens in the remainder of this thesis.

A selection of implantation doses and annealing routines were used to create a wider matrix of specimens. Three boron doses 5×10^{14}, 1×10^{15} and 1×10^{16} cm^{-2} (represented by 1, 2 and 3 respectively in the sample code), a single silicon dose of 1×10^{15} cm^{-2} (2 in the sample code) and gallium doses of 1×10^{15} and 1×10^{16} cm^{-2} (2 and 3, respectively, in the sample code) were investigated.

4.2.3 Annealing routines

The annealing routines performed on the boron and silicon implanted specimens were largely performed at the University of Erlangen-Nuremberg. For boron implanted samples these were carried out at either 900 or 1000 ˚C for 15 or 60 mins. Specimens implanted with silicon were annealed at 900 °C for 10, 30 or 120 mins. All anneals were performed in an inert atmosphere. Each annealing routine is identified by a letter (a - g) in the sample code. The gallium implanted samples were annealed at 900 °C for 15 mins in evacuated silica capsules. The cooling schedule of all the annealing routines followed a standard pattern. Samples were cooled to 800 °C at a rate of 10 °C/min at which point samples were removed from the furnace and air cooled.

As an example of a full specimen code, nB2a represents the specimen(s) made from an *n*-type substrate, implanted with boron at a dose of 1 x 10^{15} cm^{-2} and given an anneal of 900 °C for 15 mins, followed by cooling to 800 °C at a rate of 10 °C/min before being air cooled to room temperature.

During the course of the investigation several samples were further annealed in Oxford in an effort to understand the luminescence mechanism and enhance the efficiency. Specimens nB3a, pB3a, nSi2e and a 0.01 Ωcm as-received sample were annealed at 1150 °C for 5 mins in an argon atmosphere (anneal h). This was performed in a sealed and evacuated silica tube in order to minimise contamination. The silica tubes were given a 10% HF etch prior to sealing as a cleaning process. This anneal was performed to remove all the dislocations from the specimen.

Other parts of the same wafers were also annealed for up to 6 months at 200 °C in an ambient atmosphere. These low temperature annealed specimens were further split into 2 categories, with half annealed in the dark, wrapped in aluminium

foil, (anneal j) and half annealed under white light (anneal k). The white light was produced by a 20 W halogen bulb operating within the furnace at a distance of ~30 mm from the polished surface.

Table 4.1 shows the sample identification codes describing the specimen processing conditions of all ion implanted specimens. A fold out page is included in Appendix A the ion implanted sample codes and the corresponding processing conditions are given for ease of reference. These codes will be referred to throughout the remainder of this thesis.

4.3 Non-thermal processing applied to some ion implanted specimens

In order to investigate fully the role of dislocations in the luminescence from ion implanted specimens it was necessary to remove the near surface regions of some specimens. This was done using two methods: chemomechanical polishing and chemical etching.

4.3.1 Removal of surface layers by chemomechanical polishing

Chemomechanical polishing with colloidal silica (Morisol W30, Morrisons) was used on some wafers to remove surface material leaving an extended defect-free, 'mirror' finish. In order to measure the amount of material removed by this polishing process, a small area of each sample was covered with a thin piece of mica adhered to the specimen surface using Crystal Bond wax. The mica was subsequently removed by dissolving the Crystal Bond wax in acetone and the sample then cleaned using the procedure outlined in Section 4.3.3. A profilometer was then used to determine the amount of material removed relative to the original (mica protected area) surface.

Anneal (°C, mins)	Boron Dose (cm^{-2})			Silicon Dose (cm^{-2})	Gallium Dose (cm^{-2})	
	5×10^{14}	1×10^{15}	1×10^{16}	1×10^{15}	1×10^{15}	1×10^{16}
900, 15	B1a	B2a	B3a	-	Ga2a	Ga3a
900, 60	B1b	B2b	B3b	-	-	-
1000, 15	B1c	B2c	B3c	-	-	-
1000, 60	B1d	B2d	B3d	-	-	-
900, 10	-	-	-	Si2e	-	-
900, 30	-	-	-	Si2f	-	-
900, 120	-	-	-	Si2g	-	-
1150, 5	-	-	B3e*	Si2h†	-	-
200 in the dark	-	-	B3j*	Si2j†	-	-
200 in the light	-	-	B3k*	Si2k†	-	-

* Indicates that this sample has been previously processed as B3a

† Indicates that this sample has been previously processed as Si1a

Table 4.1

Processing conditions of the ion-implanted and annealed specimens; all samples are identified by either n or p followed by the sample code indicated. Thus for example nB2a represents the specimen(s) made from an *n*-type substrate wafer, implanted with boron at a dose of 1×10^{15} cm^{-2} and given an anneal of 900 °C for 15 mins. followed by cooling to 800 °C at a rate of 10 °C/min before being air cooled to room temperature.

4.3.2 Removal of surface layers by chemical etching

A planar etch, 40 wt% HF : 70 w.% HNO_3 : >99 wt% CH_3COOH in the ratio 1:7:2, was used to remove surface material from selected wafers. Small areas of the wafer surface were protected from the etching solution using 'lacomit varnish' (Agar Scientific Ltd.). After etching the lacomit was removed using xylene and the sample cleaned using the procedure outlined in Section 4.3.3. The amount of material removed was determined using profilometry and the etch rate was determined to be ~1 μm/min for an etching solution made immediately prior to use for etch times less than 30 mins.

This chemical etching was found to produce large-scale planar areas with a uniform amount of material removed on unprocessed wafers with a doping density of $<10^{16}$ cm^{-3}. However, the etching process was found to work less satisfactorily for samples with a doping density $>10^{16}$ cm^{-3}.

4.3.3 Specimen cleaning after surface removal

After the removal of material, careful specimen cleaning was necessary before CL examination. Each of the following cleaning steps was carried out:

- Acetone (in an ultrasonic bath at room temperature)
- Methanol (60 °C)
- Trichloroethane (60 °C)
- Methanol (60 °C)
- Trichloroethane (60 °C)
- H_2O : H_2O_2 : HCl (6:1:1) (120 °C)
- H_2O : H_2O_2 : HNO_3 (6:1:1) (120 °C)

Specimens were left in each solvent for 10 mins and were given a final rinse in methanol before examination. All chemicals used were BDH Aristar grade. This cleaning routine will be referred to as the RCA cleaning process throughout the remainder of this thesis.

4.4 Other silicon specimens investigated

In order to understand fully the role of dislocations in the luminescence mechanism of implanted specimens, a number of other dislocation containing specimens were investigated. The fabrication processes are outlined below.

4.4.1 Starting material

All material used in this investigation was single crystal silicon, the majority of which was grown by the Cz process, though some FZ grown substrates were also investigated. A range of wafers (500 – 0.01 Ωcm) doped with a variety of elements have been studied. The Cz substrates were thought to contain ~10^{18} cm^{-3} oxygen atoms and less than 5 x10^{10} cm^{-3} transition metal impurities when received from the manufacturers. The luminescence efficiency of some of these wafers was then studied without further processing whilst others were processed to introduce dislocations using: mechanical deformation, abrasion using silicone carbide paper, oxygen-induced stacking faults and oxide precipitates. Each of these techniques will be described separately in the following sections.

4.4.2 Wafers containing oxidation-induced stacking faults

Five wafer substrates have been investigated that have been processed in order to produce large oxidation-induced stacking faults (OISF). These substrates are (100)

orientation Cz-Si. The five substrates were: boron doped (10 Ωcm, 1.2 x 10^{15} cm^{-3}), boron doped (10 mΩcm, 9 x 10^{18} cm^{-3}), antimony doped (10 to 20 mΩcm, 4 x 10^{18} cm^{-3}), arsenic doped (1 to 5 mΩcm, ~1 x 10^{19} cm^{-3}) and phosphorous doped (1 to 2 mΩcm, ~4 x 10^{18} cm^{-3}).

The substrates were exposed to high velocity silica slurry to introduce SBD, and were subsequently oxidized in a dry oxygen atmosphere at 1100 ˚C for 5 hrs. The defects formed by the SBD process are shown in Figure 4.2. The oxidation process induces extrinsic stacking faults lying on {111} planes bounded by a dislocation with Burgers vector ⅓(111).

In order to estimate the surface defect densities, the wafers were Schimmel etched (CrO_3 (0.3 M):40 wt.% HF in the ratio 5:4) for one minute. An optical micrograph of the etched surface is shown in Figure 4.3. The wafers produced line features 10 - 15 μm in length along the <110> directions. These are assumed to be the OISFs intersecting the wafer surface. The smaller, dot like, features are assumed to be the residual small dislocation tangles as further etching did not lead to the production of line features. The dislocation density was estimated to be ~ 6 x 10^{5} cm^{-2}. According to measurements made by the manufacturer prior to shipping the wafer's average minority carrier diffusion length in the 10 Ωcm material was reduced from ~1000 μm to ~500 μm after the formation of OISFs.

4.4.3 Mechanically deformed specimens

Several ~5 Ωcm specimens were mechanically deformed in order to introduce dislocations with the assistance of Dr A. Giannattasio. This was performed using a six step process:

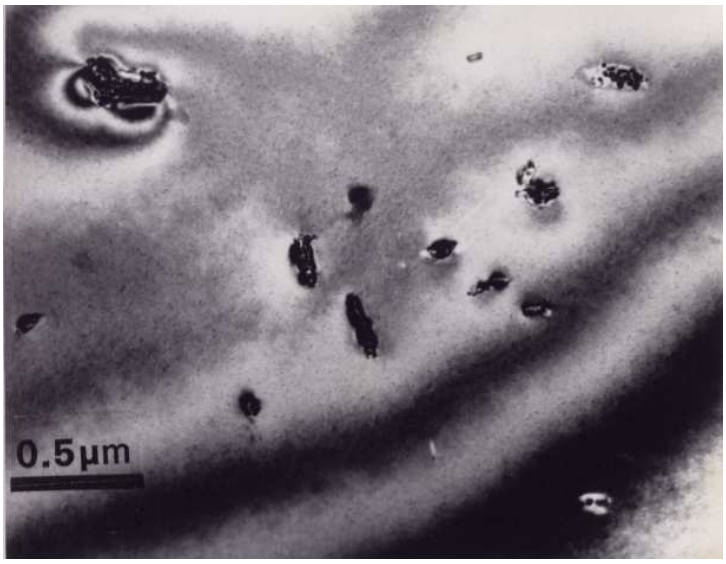

Figure 4.2

TEM (001) pole image of silicon sample after exposure to silica slurry. Surface pits and associated dislocation tangles can be readily observed (from de Coteau, 1993).

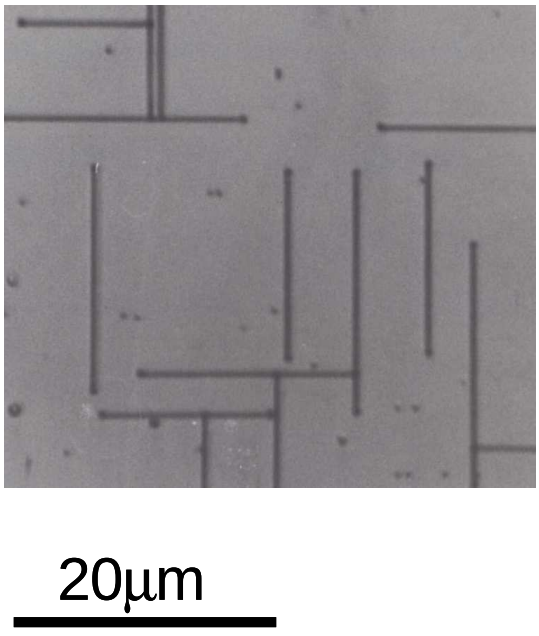

Figure 4.3

Optical micrograph of oxidised sample after one minute in a defect revealing etch solution. Dark lines and small etch pits can be clearly observed.

1) Bar cleaved with edges in [-1-12], [1-10] and [111] directions from (111) FZ-Si.
2) The edges of the bar were ground and polished to remove cleavage damage to produce a bar ~ 40 × 5 × 0.6 mm.
3) Approximately 50 Vickers mechanical indentations were performed on the polished surface, centrally along the length of the bar with a load of 10 g for 10 s. The average indent spacing was ~250 μm.
4) Samples were mechanically deformed using the four-point bending technique at 500 °C for 120 mins, stress ~100 MPa.
5) Approximately 5 μm of surface material removed by planar etching in order to remove indentation and associated dislocation tangles.
6) A further mechanical deformation using the three-point bending technique at 600 °C for 60 mins was used to produce a range of dislocation densities along the length of the specimen. A load of 5 kg was used and the distance between the outer knife edges was 12 ± 0.4 mm.

The mechanical deformation was performed using an Instron 1195 and a molybdenum jig. Quartz bars (1mm diameter) were inserted into the rig to act as knife edges in performing the three- and four-point bends. All quartz apparatus was cleaned using the RCA procedure prior to use. All high temperature bending processes were carried out in a nitrogen atmosphere. An indent is produced with a diagonal of ~5 μm and depth of ~1 μm. At room temperature relaxation of the crystal occurs by punching out prismatic dislocation half-loops from the indent. Tangles of dislocations can also form underneath the indent. The four point bending technique then generates elongated half-loops with three segments parallel to the three <110>

directions in the glide plane, a long straight segment parallel to the surface and two shorter emerging segments - the character of which was either screw or 60° (Giannattasio, 2004). The planar etch removes the indent and associated dislocation tangle, leaving a regular array of elongated half-loops grown by the four-point bend process. The three-point bend creates a range of dislocation densities from 0 cm^{-2} to ~10^{8} cm^{-2} between the outer knife-edges and the internal knife-edge of the specimen as the controlled dislocation half-loops multiply and expand according to the stress they experience, see Figure 4.4.

4.4.4 Abraded specimens

Abrasion using No. 600 silicon carbide paper was performed on both 0.01 and 5 Ωcm *p*-type Cz wafers at room temperature, followed by cleaning using organic solvents. Previous work by Stickler and Booker (1963) showed the abrasion produces cracks and fragmentation in the wafer surface with associated disordered dislocation tangles, largely of Burgers vector ½(100), up to 15 μm below the wafer surface. Stickler and Booker report typical dislocation densities of 10^{10} cm^{-2}, see Figure 4.5.

4.4.5 "Saw-damaged"/swirl defect

The investigation of a high nitrogen concentration wafer ([N] = 2.2×10^{15} cm^{-3}) FZ (100) wafer (*n*-type, 5 Ωcm, 1 x 10^{15} cm^{-3}) in other work by Dr A. Giannattasio revealed large scale bands of defects in a concentric arc pattern after Schimmel etching. These defects were not characterised further but may have been either "saw-damage" from the wafering process that had not been fully removed during subsequent polishing or A/B swirl-defects, resulting from the crystal growth process.

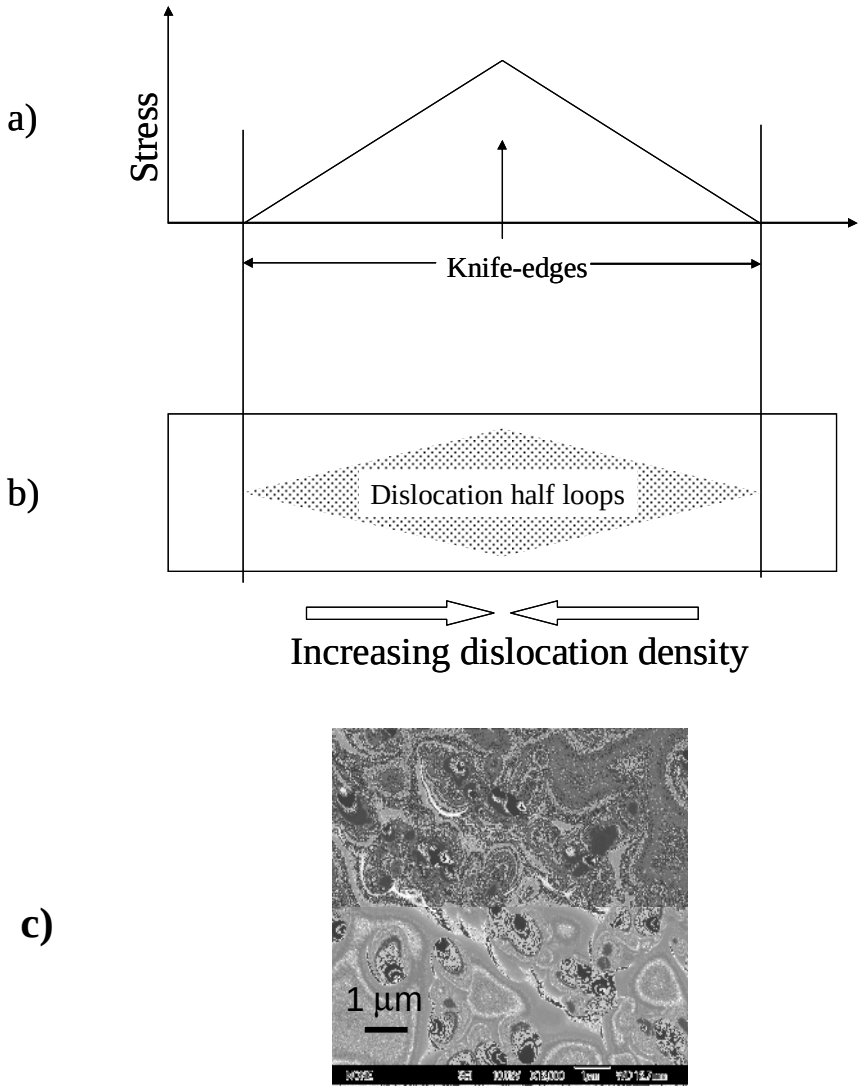

Figure 4.4

a) Schematic representation of the stress distribution between the knife edges in the three-point bending technique.

b) Schematic representation of the dislocation density along the length of the bar after three-point bending (observed in top view).

c) Scanning electron microscope image of etch pits revealing the presence of glide dislocations on the surface of (111) silicon samples. Typical of the central portion, of a mechanically deformed, sample.

Figure 4.5

TEM bright field image of the severely distorted dislocation network formed after abrasion with No. 400 silicon carbide paper. Specimen has been chemically thinned from the reverse side (from Stickler and Booker, 1963).

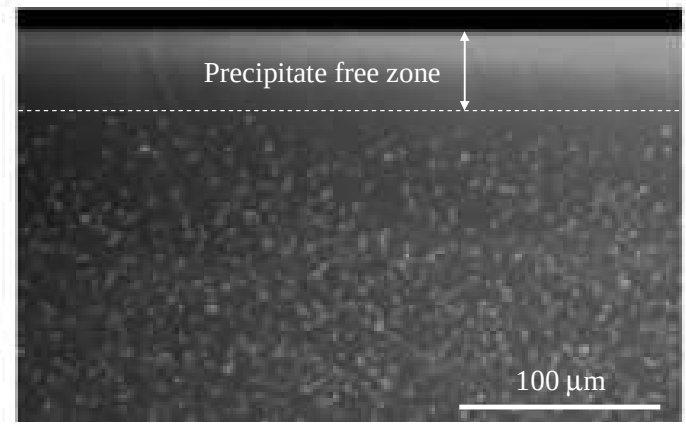

Figure 4.6

Cross-sectional scanning electron micrograph of an internally gettered wafer after a defect revealing etching. Oxygen precipitates can be observed through the bulk of the specimen, with the exception of the precipitate-free zone in the near-surface region (from http://www.memc.com/t-oxygen-gettering.asp).

If the defects are due to saw damage the resulting defect structure would probably be similar to that caused by abrasion as described above. The A/B swirl defects, on the other hand, are created by the incorporation and agglomeration of self-interstitials during the growth process (Falster and Voronkov, 2000). The A defects have been found to be extrinsic ⅓(111) dislocation loops (Foel and Kolbsen, 1975) and the B defects small, globular clusters of interstitials (Petroff and de Kock, 1976).

4.4.6 Specimens containing oxide precipitates

Internal gettering is a common technique employed to reduce the transition metal impurity concentration in the active regions of Cz wafers using the large oxygen concentration inherent to Cz-grown silicon. A large oxygen precipitate concentration throughout the bulk of the specimen is created, while the near surface regions (~80 nm) are precipitate-free, see Figure 4.6. A three stage thermal annealing process was used so that the bulk of a 100 Ωcm (1 x 10^{14} cm^{-3}) *p*-type wafer contained a high density (typically 10^{8} – 10^{11} cm^{-3}) of oxygen precipitates (less than 600 nm in diameter): an initial high temperature (1000 °C, 15 mins) homogenisation anneal was used to dissolve the as-grown precipitates. The oxygen concentration in the near surface regions is lowered considerably by out-diffusion during this anneal. A nucleation anneal was then carried out at 650 °C for 32 hrs and a growth anneal (800 °C for 4 hours followed by 1000 °C for 8 hrs) was then performed.

The oxygen precipitate concentration, measured by Schimmel etching on a cleaved surface, was estimated to be ~10^{10} cm^{-3} (Reznic, 2002). TEM investigation revealed spherical precipitates ~100 nm diameter with associated punched out dislocation loops produced during the growth process (Reznic, 2002).

4.5 Specimen preparation for experimental techniques

4.5.1 Specimen preparation for the TEM study

TEM was used to evaluate the extended defects created by the ion implantation and annealing processes. In this investigation all defects studied by TEM were in the near-surface regions on the polished side of the silicon wafers and were observed using electron transparent specimens in both (001) plan view and (110) cross-section orientations. Specimens were prepared using the ion milling technique.

Plan view specimens: In order to prepare an (001) orientation plan view specimen a ~3 mm × 3 mm sample with edges parallel to the <110> directions was cleaved from the wafer. This sample was then mounted on a Pyrex disc using melted Crystal Bond wax with the polished surface against the Pyrex disc. Two scrap silicon 'backing' pieces were placed either side of the specimen in order to aid uniform thinning of the sample. The sample and backing pieces were then mechanically ground to a thickness of ~35 μm using 600 and 1200 grit silicon carbide papers sequentially. The damage created by the silicon carbide grinding process was then removed by mechanical polishing using 6 and 1μm Kemet oil-based diamond pastes. The specimen was then dissolved from the Pyrex disc using acetone, carefully cleaned using a sable-haired paint brush and acetone before being mounted on a copper ring support (TEM grid, 3.05 mm diameter, with 2.00 mm central hole), suitable for the TEM specimen holder, using cyanoacrylate glue. The sample was then mounted in a Gatan dual ion mill with the polished surface protected by a piece of scrap silicon. The sample was rotated and thinned from the backside using an Ar^+ beam until a small hole was obtained and the damage remaining from the diamond polishing was removed (approximately 7-8 hours were required). The milling conditions used were:

ion beam energy 5 keV, gun current 0.4 mA and a beam to specimen angle of 16°. In order to remove any surface milling damage, a final ion milling was performed for 10 minutes with: ion beam energy 2 keV, gun current 0.25 mA and an incidence angle of 12°.

Cross–sectional specimens: For the preparation of the (110) cross-sectional specimens, two bars ~ 2 mm × 3 mm were cleaved from the wafer with edges parallel to the <110> directions and glued with the polished surfaces facing each other using Araldite Rapid® adhesive. In order to achieve as thin a glue line as possible this process was carried out with adhesive, which was heated and stirred at 150 °C for ~15 sec immediately prior to use with pressure applied during fixation. This sample was then mounted such that the glue line was perpendicular to the Pyrex disc surface between two scrap silicon 'backing' pieces using Crystal Bond wax. The specimen was then ground to a thickness of ~500 μm using 1200 grit silicon carbide paper and then turned over. The sample was again ground using 1200 grit silicon carbide paper and polished using 6 and 1μm diamond polishing paste at a thickness of ~300 μm. The sample was then turned over again, ground to a thickness of ~35 μm and polished using 6 and 1 μm diamond polishing paste. The specimen was then dissolved from the Pyrex disc, cleaned and mounted to a copper TEM grid as described for the plan view case. The specimen was then rotated and ion milled from both sides using an Ar^+ ion miller until a small perforation near the glue line was obtained, taking approximately 4 hours. The milling conditions used were identical to those described for plan view specimens. This procedure produced an electron transparent specimen without introducing any damage into the crystalline 'bulk' of the specimen. The

sputtering process can, however, leave a thin amorphous layer on the specimen surface which could occasionally be observed in the TEM.

4.5.2 Specimen preparation for cathodoluminescence study

Plan view specimens: Little preparation was needed to examine specimens using CL. Small pieces (typically 5 mm x 5 mm) were cleaved from the silicon wafers with their edges parallel to the <110> directions.

Cross-sectional specimens: A cross-sectional specimen (~660 μm x 10 mm x 10 mm) was cleaved from a wafer with edges parallel to the <110> directions. The sample was then mounted in the slot of an aluminium disc (~5 cm diameter, 1cm thick with a single slot cut into a face of ~1 x 0.5 cm) using Crystal Bond wax with a cleaved <011> surface contacting the large surface flat of the slotted disc between two silicon 'backing' pieces, Figure 4.7. The cleaved edge was then mechanically ground flat using 1200 grit silicon carbide paper. The specimen was then dissolved from the disc using acetone and then re-attached to the slotted disc with the ground <011> surface now acting as a stable base, hence easing the fabrication process. The second <011> surface of the sample and 'backing' pieces were then mechanically ground flat using 1200 grit silicon carbide paper, polished, using Kemet oil-based diamond pastes (6 then 1 μm grade). A final chemomechanical polish (colloidal silica Morisol W30, Morrisons) was then used to produce a mirror finish and the sample dissolved from the slotted disc using acetone.

In order that the specimens could be examined with the cross-section surface normal to the incident beam in the CL system, the samples were sandwiched between

two ~5 mm stainless steel nuts which were adhered to the surface of the microscope stub using carbon-loaded sticky pads.

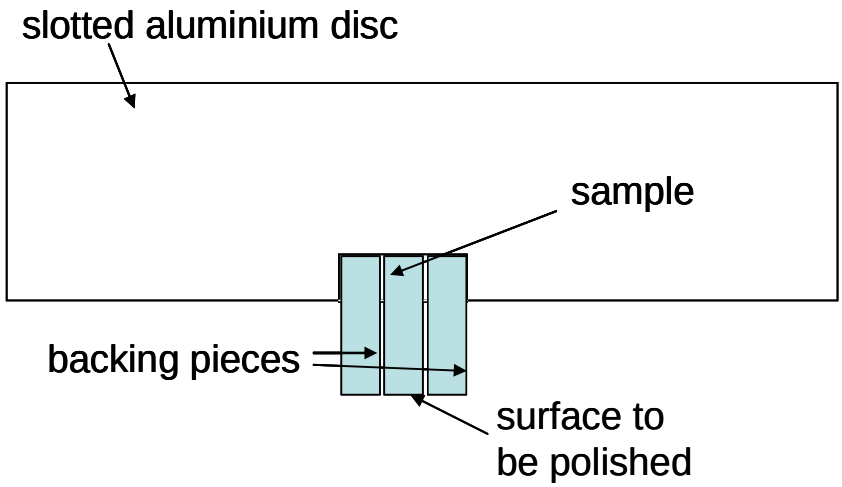

Figure 4.7

Schematic representation of the specimen production method for cross-sectional CL. Specimens are mounted in the slot of an aluminium disc using Crystal Bond wax and supported by two backing pieces.

Chapter 5

Ion implantation defects, investigated by transmission electron microscopy

5.1 Introduction

In order to investigate the efficient luminescence of DE-silicon, a matrix of specimens containing a range of defect structures was created. These were formed by the implantation of either boron or silicon (at several different doses and at different energies) and subsequent annealing (for different temperatures and lengths of time). It is the purpose of this chapter to describe the defect morphologies formed, and furthermore, to investigate their evolution.

This chapter begins by presenting typical transmission electron microscopy (TEM) images which allow the nature of the implantation and annealing related defects present in a specimen to be ascertained. The main body of the results summarises the defect morphology. The thermal evolution of the defects is described and discussed in relation to the work published in the literature. In contrast to some reports in the literature, it will be shown that the thermal evolution of ion implantation related defects may be described using classic Ostwald ripening. A small number of samples displayed anomalous results; these are investigated in Section 5.4.

5.2 Experimental methodology

So that the defects resulting from the boron or silicon implantation and annealing processes could be characterised, all specimens with *n*-type substrates and selected specimens with *p*-type substrates were analysed in the TEM. Cross-sectional specimens were used in order to observe the location of the near-surface defects and for the examination of such specimens the samples were inserted into the microscope such that the glue line lay along the eucentric tilt axis. The length of sample imaged in each case was ~1 - 5 μm.

In order that all defects could be observed, cross-sectional TEM specimens were initially examined by imaging along the [110] zone axis, using the central spot (000). Images in both {220} and {004} two-beam conditions were then used in order to observe specific defects in greater contrast. The specimen thickness was determined by a small rotation of the sample around the (100) axis. This produces thickness fringes under **g** = {220} imaging conditions and allowed the specimen thickness to be determined using tabulated extinction length data (Hirsch *et al.*, 1965). A number of specimens were also investigated in plan view along the [001] zone axis, the sample area in each case was ~20 μm^2. The central (000) spot was used to observe all defects and both {220} and {004} two-beam conditions were used to observe specific defects in greater contrast.

For some specimens the defect density was sufficiently high that individual defects could not be imaged using standard diffraction contrast techniques and hence weak beam dark field imaging was required. The diffraction conditions used were **g** = 5**g** for both {220} and {004} imaging conditions.

5.3 Experimental results

5.3.1 Identification of the defect types present

A typical plan-view TEM micrograph of a boron implanted sample (specimen nB2a) is shown in Figure 5.1. All defects are observed in Figure 5.1a, imaged using the central (000) spot along the [001] zone axis. The implantation related defects were observed to be small dislocation loops; no rod-like defects were ever observed in

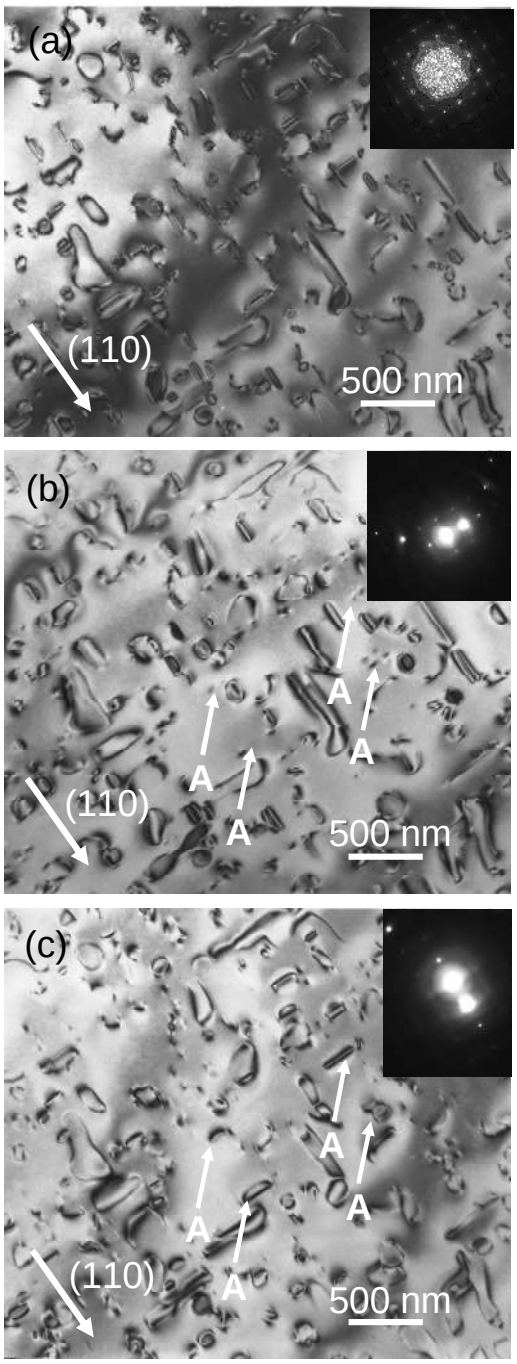

Figure 5.1

Bright field plan-view TEM micrographs of specimen nB2a (B, 30keV, 10^{15} cm^{-2}, 900°C, 15mins) illustrating the analysis used to determine ⅓(111) Burgers vector dislocation loops using different {220} two-beam conditions. Some of the disappearing (and re-appearing) loops are indicated by 'A'. (a) **g** = (000), (b) **g** = (220) and (c) **g** = (-220).

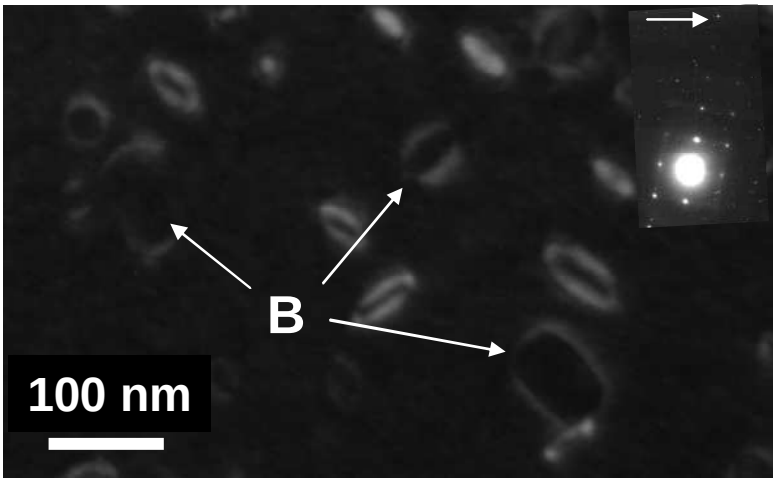

Figure 5.1 continued

d) Weak beam dark field plan-view image (**g**, 5**g**, with **g** = 400) of sample nSi2g (Si, 80 keV, 1 x 10^{15} cm^{-2}, 900 °C, 120 mins) illustrating how 'elliptical' and 'elongated' defects, assumed to be faulted and perfect dislocation loops respectively, could be differentiated. The marker 'B' indicates those identified to be perfect dislocation loops.

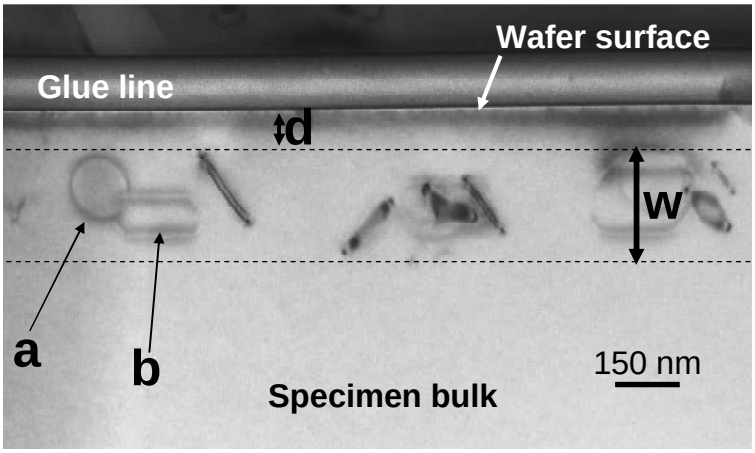

Figure 5.2

Cross sectional bright field TEM image of sample pB2b illustrating the parameters used in the description of the implantation related dislocation band: w - width of the dislocation band, d - depth of the band below the wafer surface, a – an example of an elliptical faulted dislocation loop and b – an example of an elongated perfect dislocation loop.

any samples studied in this research. All defects were observed to lie on {111} habit planes. Some of the dislocations were observed in the TEM images to be elliptical whilst some were found to be elongated, with straight segments parallel to <110> directions, these are marked as 'a' and 'b' in Figure 5.2. The Burgers vector of the dislocation loops may identified using the **g**.**b** = 0 criterion. Figure 5.1 illustrates the analysis of sample nB2a, showing how under suitable orientation of the sample, those dislocations which satisfy this condition disappear, or only show a weak residual contrast. For two-beam conditions, using {220} reflections as in Figures 5.1b and 5.1c, some of the loops disappear (indicated by the markers 'A'). These are faulted Frank dislocation loops (FDLs) with Burgers vectors ⅓<111>. From a similar analysis, using {004} reflections, the Burgers vectors of the larger loops were determined to be perfect ½<100> loops (PDLs). In the silicon implanted samples, the defects were observed to be small dislocation loops and, as in the case of the boron implanted samples, no rod-like defects were ever observed. Weak beam dark field imaging was used for the characterisation of defects in the silicon implanted samples. Figure 5.1d shows how 'elliptical' and 'elongated' dislocations were able to be distinguished. The dislocation loops were found to be a mixture of FDLs and PDLs. The marker 'B' indicates those dislocation loops identified to be 'elongated' PDLs.

A small number of samples were found to contain second phase precipitates rather than the dislocation loops, these specimens are discussed in Section 5.4.

5.3.1.1 Discussion

Previous work presented in the literature shows that the ion implantation and annealing process creates a band of defects below the wafer surface; the nature of the defects is governed by the processing conditions used. The most commonly reported

defects have been found to be small {311} rod-like defects, extrinsic faulted Frank dislocation loops (FDLs) [**b** = ⅓(111)] and extrinsic perfect dislocation loops (PDLs) [**b** = ½(110)] (Jones and Rozgonyi, 1993). However, other workers investigating material using similar ion implantation and anneal conditions to those used in this study observe a mixture of only FDLs and PDLs (see for example de Mauduit *et al.*, 1994). The results of this investigation are entirely consistent with the findings of the bulk of the literature (see for example de Mauduit *et al.*, 1994 and Milosavlejvić *et al.*, 2005).

FDLs have been found, by trace analysis, to lie on {111} habit planes and have a Burgers vector of ⅓<111> perpendicular to the loop plane (De Mauduit *et al.* 1994). There are four variants of this circular shaped defect which, when projected on to the plan-view TEM image plane, appear elliptical. The PDLs were also found to lie on {111} planes and have a Burgers vector of ½<110> (De Mauduit *et al*. 1994) and it has been observed that they are elongated along that particular <110> direction on their habit plane which is perpendicular to the Burgers vector (Seibt *et al.*, 1994), 12 variants of this defect exist.

5.3.2 Quantification of defect densities and distribution

The ion implanted specimens were investigated in the TEM in order to characterise for each set of implant and anneal conditions the following:

a) defect band width, w (see Figure 5.2)

b) defect band depth, d (see Figure 5.2)

c) dislocation densities

d) mean dislocation loop diameter

And, in a few selected specimens: e) the proportion of faulted and perfect loops.

In order to investigate the dislocation distribution, their number was counted and their diameter measured along their longest axis directly from TEM images. In common with other workers in the field, the dislocation loops were assumed to be circular (for example Pan *et al.*, 1996).

In general, the defect density in a band of dislocation loops may be described using four different criteria: i) The number of dislocation loops per unit volume of crystal (cm^{-3}), ii) the number of dislocation loops per unit area of crystal (cm^{-2}), iii) the dislocation line length per unit volume of crystal (cm^{-2}) and iv) the total dislocation line length per unit area of crystal (cm^{-1}). In the present work, the dislocation density is defined as the dislocation line length per unit volume of crystal and measured between the top and bottom of the dislocation band and the loop density as the number of dislocation loops per unit volume of the crystal measured between the top and bottom of the dislocation band.

5.3.2.1 Boron implanted samples

Representative, two-beam, bright field cross-sectional TEM micrographs of boron implanted specimens containing a band of sub-surface dislocation loops are shown in Figure 5.3. These include specimens implanted with a dose of 5×10^{14}, 1×10^{15} or 1×10^{16} cm^{-2} and annealed at 900 or 1000 °C for 15 or 60 mins. In some cases these images are sufficient for the parameters described in Section 5.3.2 to be quantified. However in others (for example Figure 5.3c) the defect densities are too low for statistically meaningful data to be obtained from a single micrograph.

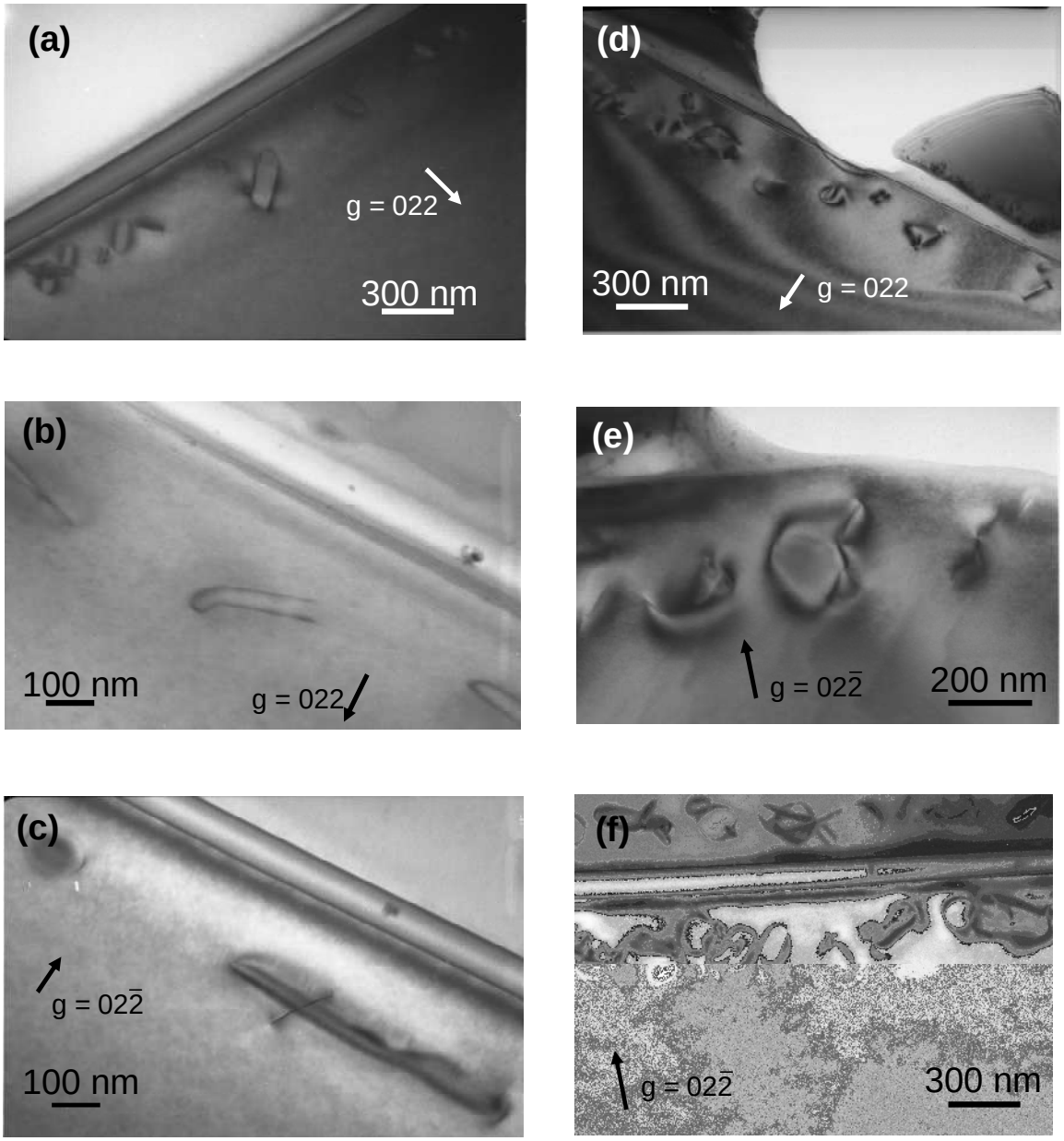

Figure 5.3

Representative cross-sectional TEM bright field micrographs of boron implanted (30 keV) samples, imaged using **g** = {220}

a) Sample nB1a ($5x10^{14}cm^{-2}$, 900°C, 15 mins)

b) Sample nB1b ($5x10^{14}cm^{-2}$, 900°C, 60 mins)

c) Sample pB1b ($5x10^{14}cm^{-2}$, 900°C, 60 mins)

d) Sample nB2a ($10^{15}cm^{-2}$, 900°C, 15 mins)

e) Sample pB2a ($10^{15}cm^{-2}$, 900°C, 15 mins)

f) Sample nB2b ($10^{15}cm^{-2}$, 900°C, 60 mins)

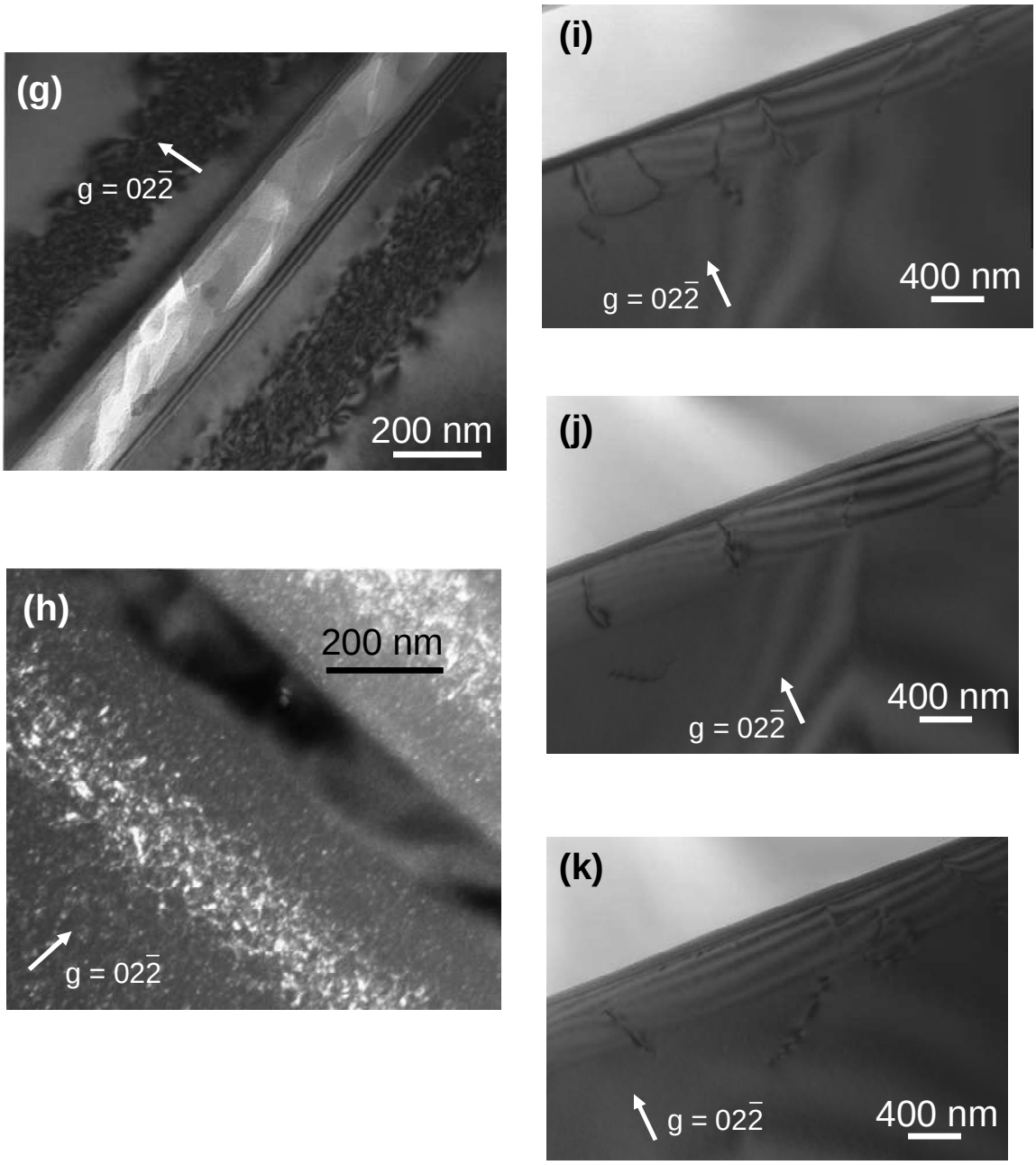

Figure 5.3 continued

Representative cross-sectional TEM bright field micrographs of boron implanted (30 keV) samples, imaged using **g** = {220} unless otherwise stated

g) Sample nB3a (10^{16}cm^{-2}, 900°C, 15 mins)
h) Sample nB3b (10^{16}cm^{-2}, 900°C, 60 mins)
weak beam dark field (**g** = 5**g**) conditions

i) Sample pB3c (10^{16}cm^{-2}, 1000°C, 15 mins)
j) Sample nB3d (10^{16}cm^{-2}, 1000°C, 60 mins)
k) Sample pB3d (10^{16}cm^{-2}, 1000°C, 60 mins).

For these specimens a montage of micrographs was analysed. The quantitative data obtained from this set of samples is presented in Tables 5.1 and 5.2.

The error in the magnification of the microscope was estimated to be ~10% (Marsh, 2001) and ~3% for the estimation in specimen thickness. Typically several hundred defects were analysed in each specimen introducing an additional error of a few percent, resulting in an estimated error in the dislocation density and dislocation loop density of typically 15% and the error in the mean loop diameter of typically ~12%. However, for specimens nB1c and nB1d the defect density was so low that only 6 and 3 dislocation loops respectively were imaged.

In summary, the following trends can be identified:

Increase in dose: An increase in the implant dose resulted in a large increase in the dislocation density but the mean dislocation loop diameter tended to decrease. This can clearly be observed in samples nB1a, nB2a and nB3a (Figures 5.3a, 5.3d and 5.3g), where the dislocation loop densities were 3.1×10^{12}, 4.7×10^{13} and greater than 10^{16} cm^{-3} and mean loop diameters 165, 145 and less than 10 nm for implant doses of 5×10^{14}, 1×10^{15} and 1×10^{16} cm^{-2} respectively.

Increase in annealing temperature: An increase in the annealing temperature from 900 to 1000 °C resulted in a large decrease in the dislocation density and a large increase in the mean loop diameter. A population of small regular loops tended to become a lower density of larger diameter, irregular shaped loops, see for example samples nB3b and nB3d (Figures 5.3h and 5.3j). Sample nB3b, processed at 900 °C, had a dislocation loop density of 9.1×10^{15} cm^{-3} and mean loop diameter of 15 nm, whereas sample nB3d processed at 1000 °C, had a dislocation loop density of 1.5 x

Sample	Mean dislocation density (cm^{-2})	Dislocation loop density (cm^{-3})	Mean diameter (nm)	Defect band	
				width (nm)	depth (nm)
nB1a	3.1×10^{8}	3.1×10^{12}	160	260	80
nB1b	2.0×10^{8}	9.2×10^{11}	360	200	60
nB1c	$8.0 \times 10^{7\dagger}$	$5.0 \times 10^{11\dagger}$	$260^{\dagger}$	$240^{\dagger}$	$50^{\dagger}$
nB1d	$4.2 \times 10^{7\dagger}$	$2.4 \times 10^{11\dagger}$	$280^{\dagger}$	$250^{\dagger}$	$45^{\dagger}$
nB2a	4.1×10^{9}	4.7×10^{13}	140	210	50
nB2b	5.5×10^{8}	4.9×10^{12}	190	250	60
nB2c	2.8×10^{8}	2.5×10^{12}	180	220	100
nB2d	-	-	-	-	-
nB3a	$> 1 \times 10^{11}$	$>1 \times 10^{16}$	< 10	230	100
nB3b	8.3×10^{10}	9.1×10^{15}	15	240	100
nB3c	-	-	-	-	-
nB3d	3.9×10^{8}	1.5×10^{12}	420	880	10
pB1b	2.3×10^{8}	1.1×10^{12}	350	210	55
pB2a	5.6×10^{9}	7.1×10^{12}	130	230	50
pB2d	-	-	-	-	-
pB3c	6.8×10^{8}	2.5×10^{12}	450	600	10
pB3d	3.6×10^{8}	1.1×10^{12}	540	960	10

Table 5.1

Summary of the mean dislocation density, dislocation loop density, position of the dislocation band and mean loop diameters of boron implanted samples directly calculated from the TEM images. The error in the data is estimated to be typically 13%. † indicates that less than five dislocations were imaged in each case and the errors are significant. Samples nB2d, nB3c and pB2d were found to contain second phase precipitates rather than a band of dislocations.

Sample	Perfect loop percentage	Faulted loop mean diameter (nm)	Perfect loop mean diameter (nm)
nB1b	~ 45	110	380
nB2a	~ 18	120	340
nB2b	~ 25	180	380
nB3d	~ 90	150	520
pB2a	~ 20	120	320

Table 5.2

Summary of the nature of the dislocation loops in selected boron implanted samples and mean loop sizes for both perfect and faulted Frank loop dislocations.

10^{12} cm^{-3} and mean loop diameter of 420 nm. The increase in mean loop diameter was observed to correspond to an increased proportion of PDLs compared to FDLs.

Increase in annealing time: An increase in annealing time from 15 to 60 mins resulted in an increase in the mean loop diameter and a decrease in the total dislocation loop density. This may be clearly observed in samples nB1a and nB1b (Figures 5.3a and 5.3b respectively) and samples nB2a and nB2b (Figures 5.3d and 5.3f respectively). The dislocation loop density of sample nB1b (annealed for 60 mins, 9.2 x 10^{11} cm^{-3}) was lower than in sample nB1a (annealed for 15 mins, 3.1 x 10^{12} cm^{-3}) but the mean loop diameter of sample nB1b (360 nm) was larger than sample nB1a (160 nm).

Variation between n- and p-type substrates: The substrate doping was found to have no effect within experimental error on the overall dislocation structure formed after implantation and annealing. For example, samples pB1b and nB1b (Figures 5.3c and 5.3b respectively), pB2a and nB2a (Figures 5.3e and 5.3d respectively) and samples pB3d and nB3d (Figures 5.3k and 5.3j respectively) exhibited similar dislocation loop densities and location of the defect band.

Position of the dislocation band: The width of the defect band, w, was found to be approximately 230 nm and the depth , d, ~50 nm in most specimens (see for example Figure 5.3f) however for samples implanted at the highest dose (10^{16} cm^{-2}) and annealed at 1000 °C the defect band extended much further into the specimen, see for example Figure 5.3i (sample pB3c) where the defect band width was ~600 nm and located only ~10 nm from the wafer surface.

Proportion of faulted Frank dislocation loops compared to perfect dislocation loops: The FDLs tended to dominate in the majority of specimens displaying small

dislocation loops; for example 82% in sample nB2a (mean loop diameter 140 nm). However, as the mean dislocation diameter increased a reduction in the density of FDLs was observed, for example only ~10% in sample nB3d (mean diameter 420 nm).

The implantation and anneal conditions used in this work have created a large matrix of samples exhibiting a wide range of dislocation morphologies; a low density, 2.3×10^8 cm^{-2}, of relatively large (350 nm) diameter loops (sample pB1b), to small ~15 nm loops with a density greater than 10^{11} cm^{-2} (sample nB3a). Specimens with similar dislocation densities with significantly different dislocation loop characteristics have also been created; dislocation densities of $\sim 5 \times 10^8$ cm^{-2}, with predominantly small FDLs, 190 nm diameter, or larger predominantly PDLs, 420 nm in diameter (sample nB2b and nB3d respectively).

The dislocation densities can be analysed further in terms of the depth within the defect band and this can be correlated with the doping concentration produced by the implantation. This is illustrated for specimens nB1a, nB2a and nB3a in Figure 5.4. The dislocation density in these samples was calculated in strips of 10 nm width along the length of the dislocation band parallel to the specimen surface. The relative position of the band of dislocations, the variation in defect density across the band, the *p-n* junction and the boron concentration profile, calculated using the TRIM-95 code (Ziegler *et al*., 1985)[1] are shown. The dislocations were observed to be located at or below the projected range of the implanted ions. The dislocations were situated in highly doped regions of the wafer (boron concentrations greater than 10^{18} cm^{-3}) and extended often beyond the depth of the *p-n* junction. In all specimens, the general

[1] The TRIM-95 code is a Monte Carlo simulation of the energy loss of an implanted ion. Each ion is modelled individually with the ion's energy, angle of incidence and the host material's physical properties input by the user. The stopping point of each ion is determined, and many trajectories used to determine the concentration profile.

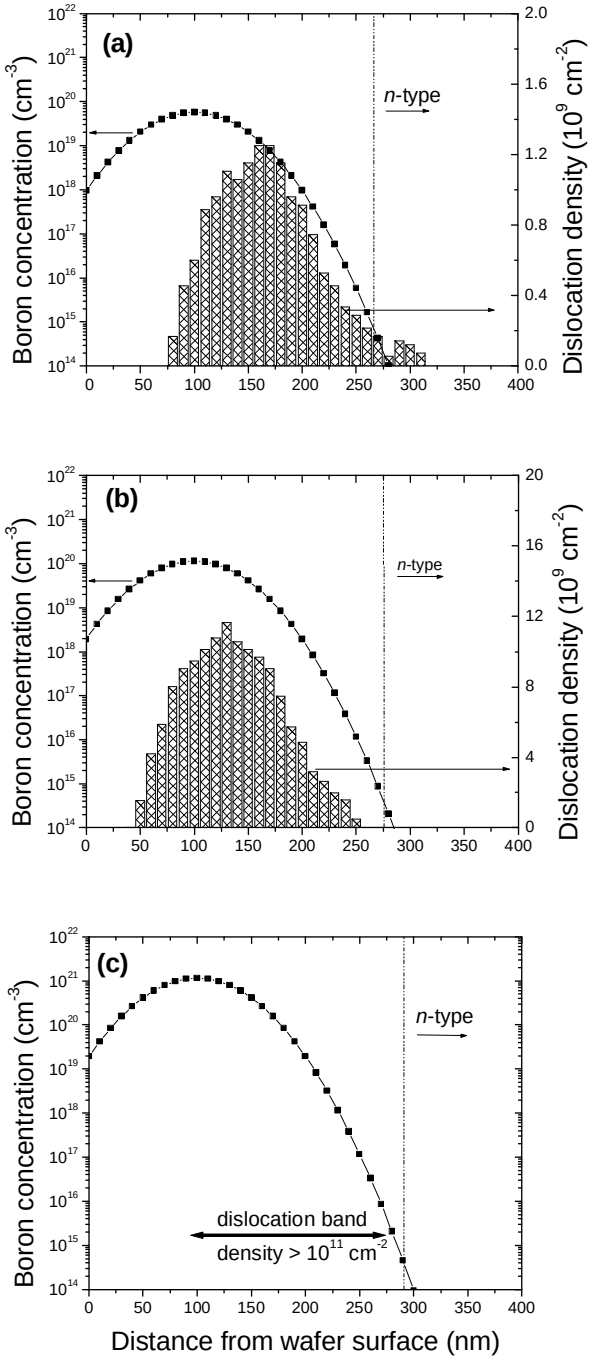

Figure 5.4

Representation of selected boron implanted (30 keV) samples a) nB1a (5 x 10^{14}cm^{-2}, 900°C, 15mins), b) nB2a (10^{15}cm^{-2}, 900°C, 15mins) and c) nB3a (10^{16}cm^{-2}, 900°C, 15mins) indicating the location of the band of dislocations, dislocation density variation within the band of dislocations, the boron concentration (background doping level ~6 x 10^{14} cm^{-3}) and the *p-n* junction.

sample structure was of a band of dislocations predominantly located in highly doped material, between the specimen surface and a p^+-n junction or p^+-p junction.

A histogram of the dislocation density as a function of the loop diameter is shown in Figure 5.5 for samples nB2a and nB2b. An overall reduction in dislocation density by almost an order of magnitude was observed, coupled with an increased mean diameter with annealing time, from 140 to 190 nm after annealing for 15 and 60 mins respectively. The distribution of the loop sizes in samples nB2a and nB2b, after normalisation showed a similar distribution curve, independent of annealing time (see Figure 5.6). The frequency of occurrence is normalised to a maximum value of one and the loop diameter normalised by the modal loop diameter. The curve shows an asymmetrical distribution with a peak at smaller loop diameters and a large tail up to five times the peak value.

5.3.2.2 Discussion of boron implanted samples

In this work the following observations were made: i) a mixture of FDLs and PDLs located at/or below the projected range, ii) the dislocation population was heavily dependent on the implantation and annealing conditions used and iii) the dislocation loops underwent a coarsening process with increased annealing times, where a high density of small loops evolved to become a lower density of larger loops. These results are consistent with 'type-1' ion-implantation defects reported in the literature, where a band of dislocation loops are found in samples where no amorphisation of the crystal lattice during implantation occurs (Jones and Rozgonyi, 1993 and Milosavlejvić *et al.*, 2005).

Sample nB2a was processed using similar conditions to the DE-silicon specimen of Ng *et al.* (2001). They observed a band of interstitial dislocation loops of

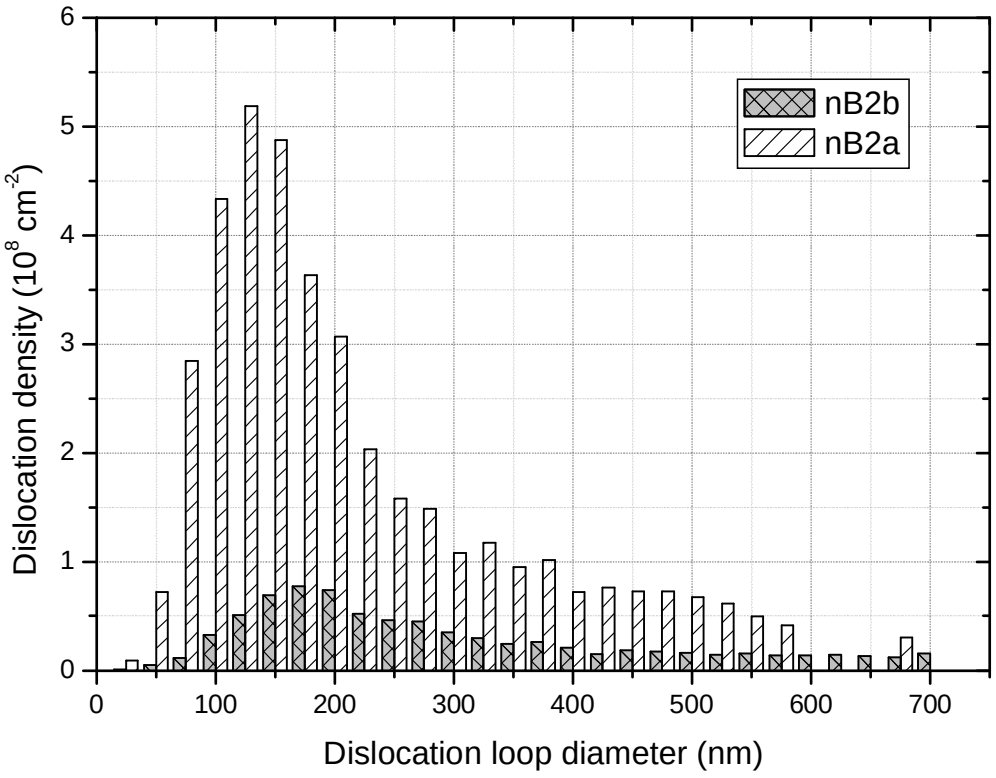

Figure 5.5

The dislocation density versus dislocation loop diameter for samples nB2a (B, 30 keV, 10^{15} cm^{-2}, 900°C, 15 mins) and nB2b (B, 30 keV, 10^{15} cm^{-2}, 900 °C, 60 mins).

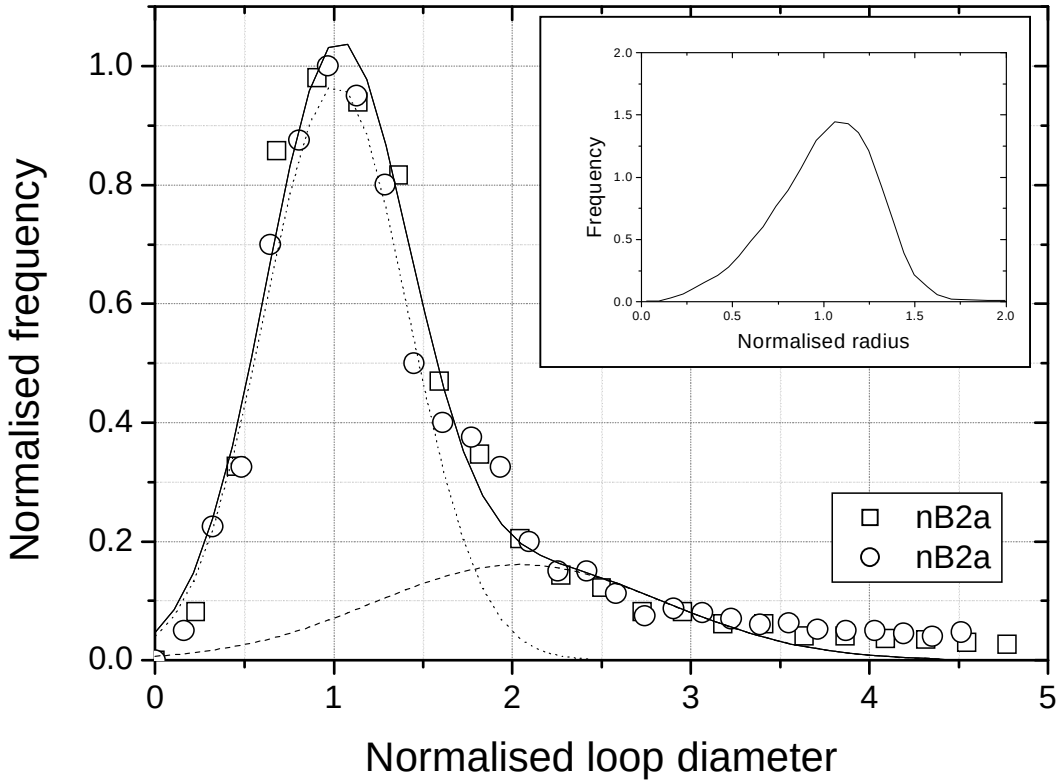

Figure 5.6

Plot of the normalised dislocation loop diameter versus the normalised frequency of occurrence for the specimens shown in Figure 5.5. The loop diameter is normalised by the modal diameter and frequency by the most commonly recorded. A universal distribution in samples nB2a (B, 30 keV, 10^{15} cm^{-2}, 900°C, 15 mins) and nB2b (B, 30 keV, 10^{15} cm^{-2}, 900 °C, 60 mins) was observed. The solid line corresponds to the summation of the two Gaussian fits (the dotted and dashed lines). The inset shows the two dimensional distribution frequency versus normalised size curve for Ostwald ripening (after Yao *et al.*, 1992).

width 200 ± 25 nm and centred 130 ± 25 nm below the surface. The dislocation density was estimated to be 1 x 10^9 cm^{-2}. A bimodal distribution in the mean loop diameter was observed; loops identified to be faulted Frank loops (a/3<111>) were ~175 nm in diameter whereas the perfect a/2<100> loops were much larger, mean diameter ~350 nm. The majority of defects were found to be of the faulted nature (~90%). The dislocation density, the location and the width of the dislocation band and the nature of the dislocation loops are entirely consistent with the observations of this study.

The size distribution and evolution of such dislocation loops has been studied by a number of authors, with suggestions that the distribution is described by a single Gaussian function (Laanab *et al.*, 1994), an asymmetrical triangular distribution (Chandhry, 1995) and a distribution displaying a similar form to that observed in this study (Figure 5.5) (Pan *et al.*, 1996) – that is, the smaller diameter dislocation loops dominate the distribution profile with a long tail of larger diameter loops. Pan *et al.* (1996) report the observation of a universal curve, independent of annealing time, which describes the dislocation loop population after the normalisation of the loop diameter (by the modal value) and the frequency of occurrence (to a maximum value of one). The authors consider the distribution as a single population of defects and show that coarsening is a conservative process, *i.e.*, the total number of atoms bounded by the dislocation loops as a function of annealing time is constant. The results of this work are in agreement with the results of Pan *et al.* (1996). In general, the conservative evolution of defects is described by the classic Ostwald ripening model. This predicts a defect size distribution as shown in the inset of Figure 5.6 for a population of two dimensional defects. The maximum size is only ~1.5 times larger than the modal size and a large tail towards smaller sizes is observed (Yao *et al.*,

1992). The size distribution of defects observed in this study, and those reported by Pan *et al*. (1996), are clearly inconsistent with this Ostwald ripening model. Pan *et al*. (1996) postulate that the discrepancy may be due to the effect of the strain field associated with dislocations. The distortion energy per unit area, E, is shown to depend on the radius, R, of the dislocation loop by the following relationship (Pan *et al.*, 1996):

$$\frac{dE}{dR} = -\frac{2}{R^2}\left(C \ln\left[\frac{2R}{r_c} \right] + L \right) \qquad \text{Eqn. 5.1}$$

where C is a constant depending on the modulus of rigidity, Poisson's ratio, the Burgers vector and the type of dislocation loop, r_c is the dislocation core radius and L is the energy per unit length.

From Eqn. 5.1 it can be seen that the growth of a dislocation loop is energetically favourable, in terms of the dislocation energy, for all practical loops sizes and that this favourability decreases as the average loop size increases. Pan *et al.* (1996) note that the varying loop line energy enhances growth by a logarithmic dependence of the stress field on the loop radius, this suggests that the growth of large coherent loops would tend to be more energetically favourable than the equivalent growth of large incoherent precipitates as in classic Ostwald ripening where the surface energy is assumed to be constant. Thus, Pan *et al.*, (1996) propose that it is this effect which leads to the difference in the observed size distribution of dislocation loops compared to classic Ostwald ripening. However, analysis of the size distribution profile of sample nB2a, assuming two defect populations, shows that a fitting using two Gaussian peaks recreates the observed profile accurately, Figure 5.6.

Moreover, the two fitted peaks agree well with the experimentally observed mean loop diameters of FDLs and PDLs and the total area under each of the two fitted Gaussian curves reflects the fractions of FDLs and PDLs that was observed experimentally (see Tables 5.1 and 5.2). This suggests that the two fitted Gaussian curves represent the size distributions of FDLs and PDLs. This effect is clearer in the silicon implanted specimens and described in more detail in Section 5.3.2.4.

5.3.2.3 Silicon implanted samples

Representative, two-beam, bright field cross-sectional TEM micrographs of silicon implanted specimens containing a band of sub-surface dislocation loops are shown in Figure 5.7. These include specimens implanted with a dose of 1 x 10^{15} cm^{-2} at 80 keV, annealed at 900 °C for 10, 30 or 120 mins.

In each case a band, 110 nm wide and 190 nm deep, of small dislocation loops, 10 to 140 nm in diameter, was observed. The dislocation band was situated at a distance beyond the 'end of range' (1600 Å) as calculated by the TRIM-95 programme. The dislocations were a mixture of FDLs and PDLs (as reported in Section 5.3.1). In the sample annealed for 10 minutes an additional band of dislocations, 100 nm wide and 25 nm deep, was also observed (labelled 'Upper dislocation band' in Figure 5.7a). These dislocations were also found to be a mixture of FDLs and PDLs. This additional band will be referred to as the 'upper dislocation band' and the defect band observed at all three annealing times referred to as the 'main dislocation band'. The quantitative data obtained from this set of samples is presented in Table 5.3. In summary, the following trends were observed:

Upper dislocation band: The upper-band of dislocation loops exhibited a lower dislocation density than the band of dislocation loops situated beyond the 'end of

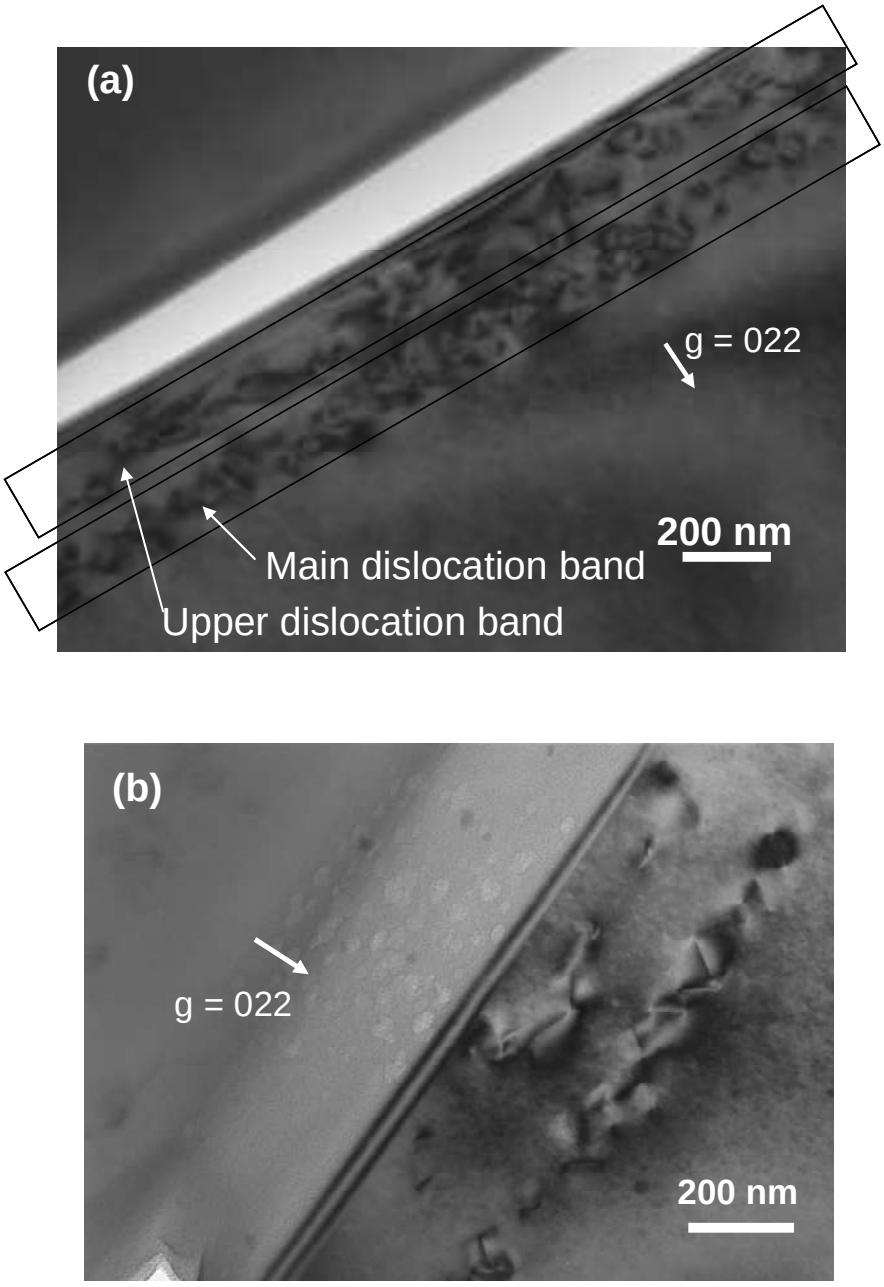

Figure 5.7

Representative cross-sectional transmission electron bright field micrographs of silicon implanted (10^{15} cm^{-2}, 80 keV) samples

a) Sample nSi2e (900 °C, 10 mins) - the 'upper' and 'main' dislocation bands can be clearly seen

b) Higher magnification of (a) showing individual defects

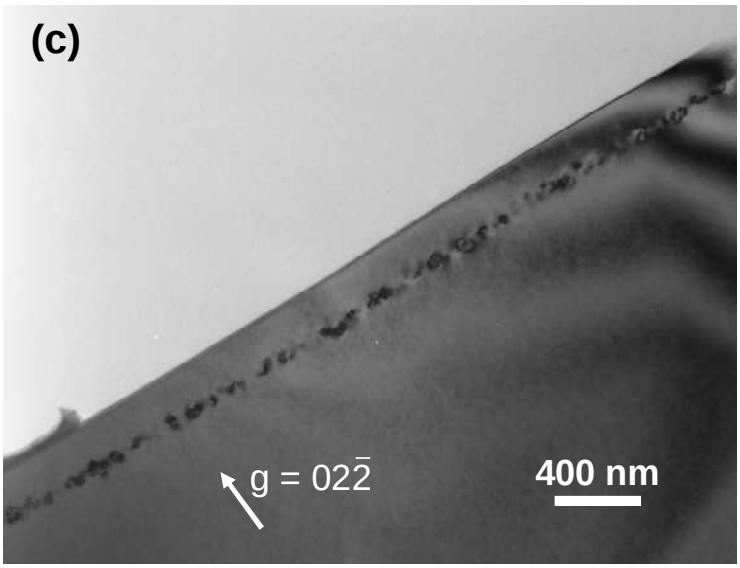

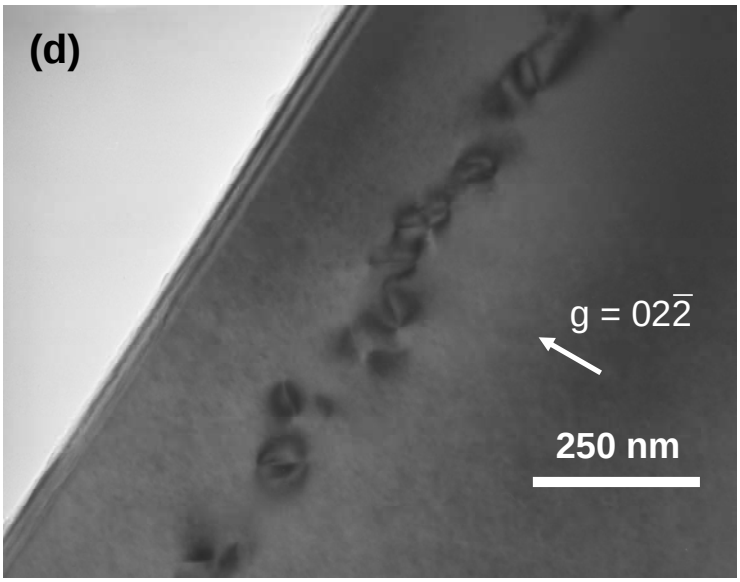

Figure 5.7 continued

Representative cross-sectional transmission electron bright field micrographs of silicon implanted (10^{15} cm^{-2}, 80 keV) samples

c) Sample nSi2f (900 °C, 30 mins) – only the main defect band present. The dislocation band closer to the surface has been annealed out of the sample

d) Sample nSi2f (900 °C, 30 mins) – increased magnification to reveal individual dislocation loops

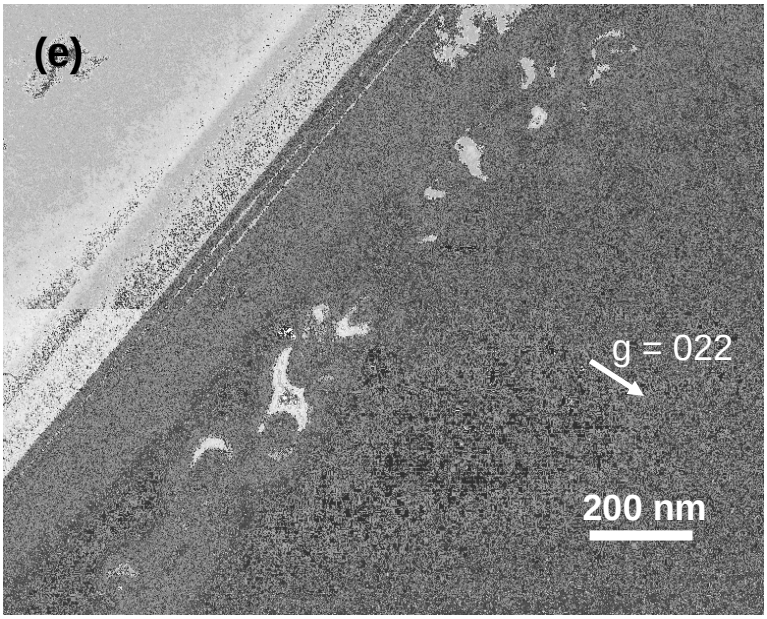

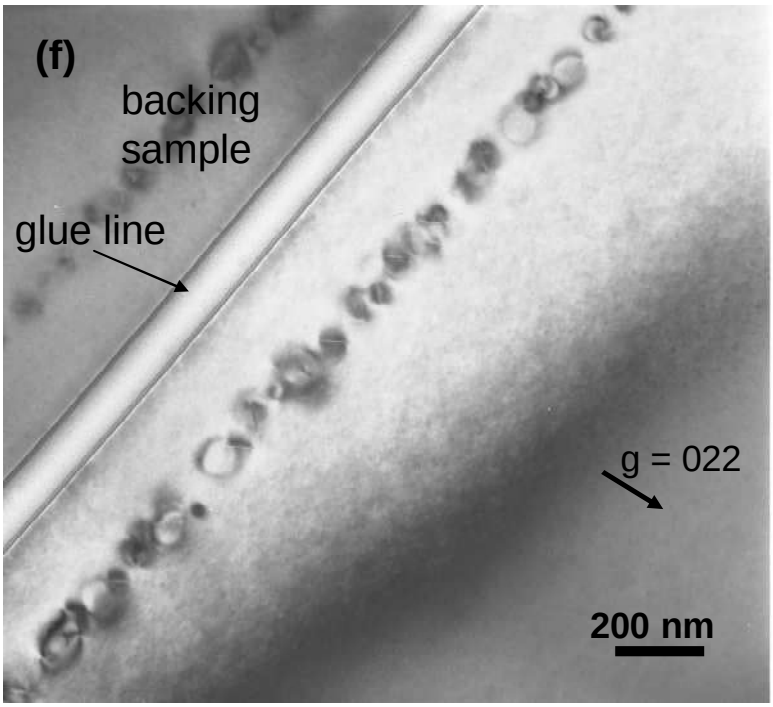

Figure 5.7 continued

Representative cross-sectional transmission electron bright field micrographs of silicon implanted (10^{15} cm^{-2}, 80 keV) samples

e) Sample nSi2g (900 °C, 120 mins)

f) Sample pSi2g (900 °C, 120 mins).

Defect parameters	Specimen		
	nSi2e	nSi2f	nSi2g
Upper band			
Defect band width (nm)	100	-	-
Defect band depth (nm)	25	-	-
dislocation density (10^9 cm^{-2})	4.3	0	0
Mean defect diameter (nm)	54	0	0
Main Band			
Defect band width (nm)	110	110	110
Defect band depth (nm)	190	190	190
FDL density (10^9 cm^{-2})	6.8	3.0	1.3
PDL density (10^9 cm^{-2})	3.1	3.0	1.9
Total dislocation density (10^9 cm^{-2})	9.9	6.0	3.2
FDL loop density (10^{12} cm^{-3})	51	23	12
PDL loop density (10^{12} cm^{-3})	8.0	10	3.8
Total loop density (10^{12} cm^{-3})	59	32	16
Mean FDL loop diameter (nm)	32	40	52
Mean PDL loop diameter (nm)	51	56	90
N_b FDL (10^{13} cm^{-2})	3.4	2.4	2.2
N_b PDL (10^{13} cm^{-2})	1.3	1.9	2.0
Total N_b (10^{13} cm^{-2})	4.7	4.3	4.2

Table 5.3

Summary of the dislocation densities, loop densities, mean diameter, character and location of the defect band in selected silicon implanted samples. Implanted at 80 keV to a dose of 1 x 10^{15} cm^{-2} and annealed at 900 °C for 10 (nSi2e), 30 (nSi2f) or 120 mins (nSi2g).

range' (4.3×10^9 cm^{-2} compared to 9.9×10^9 cm^{-2}). The dislocation loops in the upper dislocation band were generally larger in diameter with a maximum observed loop diameter (190 nm) significantly larger than observed in the main defect band (60 nm). The upper dislocation band was annealed out at some time greater than 10 but less than 30 mins.

Main dislocation band: An increase in annealing time from 10 to 30 to 120 mins resulted in an increase in the mean dislocation loop diameter (of both FDLs and PDLs) and a decrease in the dislocation density. This may be clearly observed from samples nSi2e, nSi2f and nSi2g (Figures 5.7b, 5.7d and 5.7e respectively) and is demonstrated in Figure 5.8 where the dislocation density, dislocation loop density and mean-loop diameter, for both PDLs and FDLs is shown graphically as a function of annealing time.

A large decrease in the FDL loop density was observed between annealing times of 10 and 120 mins; 5.1×10^{13} to 1.2×10^{13} cm^{-2} respectively. In contrast, the PDL loop density was reduced by a smaller amount; from 8.0×10^{12} cm^{-2} to 3.8×10^{12} cm^{-2} for the same annealing times. The mean loop diameter for both types of dislocation increased with annealing time; the mean FDL diameter increased from 32 nm at 10 mins to 52 nm after 120 mins and the mean PDL diameter from 51 to 93 nm for the same annealing times. An approximately linear increase of the mean loop area of both FDLs and PDLs is observed as a function of annealing time at 900 °C.

Figure 5.9 shows the dislocation loop density versus dislocation loop size in the main-band for the three annealing times. A double peak is clearly observed in each case. Each peak is well fitted by a Gaussian curve, with the sum of the two Gaussians accurately recreating the histogram. The double peak nature is confirmed

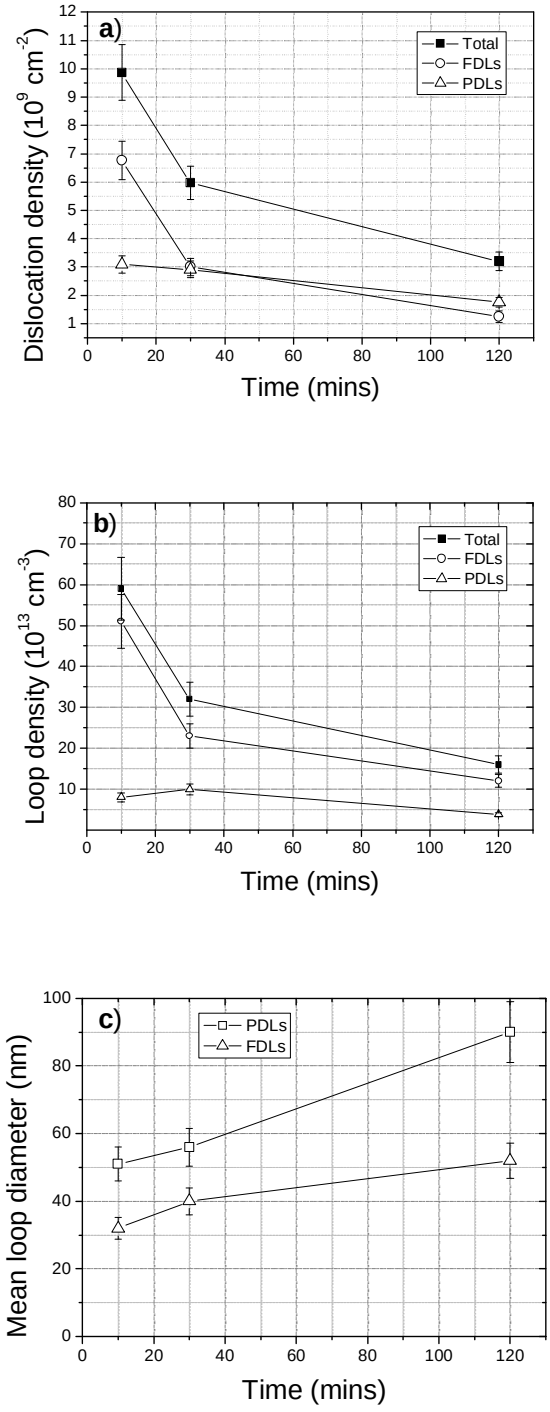

Figure 5.8

Time evolution of perfect and faulted dislocation loops in silicon implanted samples (80 keV, 10^{15} cm^{-2}, 900 °C) a) dislocation density, b) loop density and c) mean loop diameter.

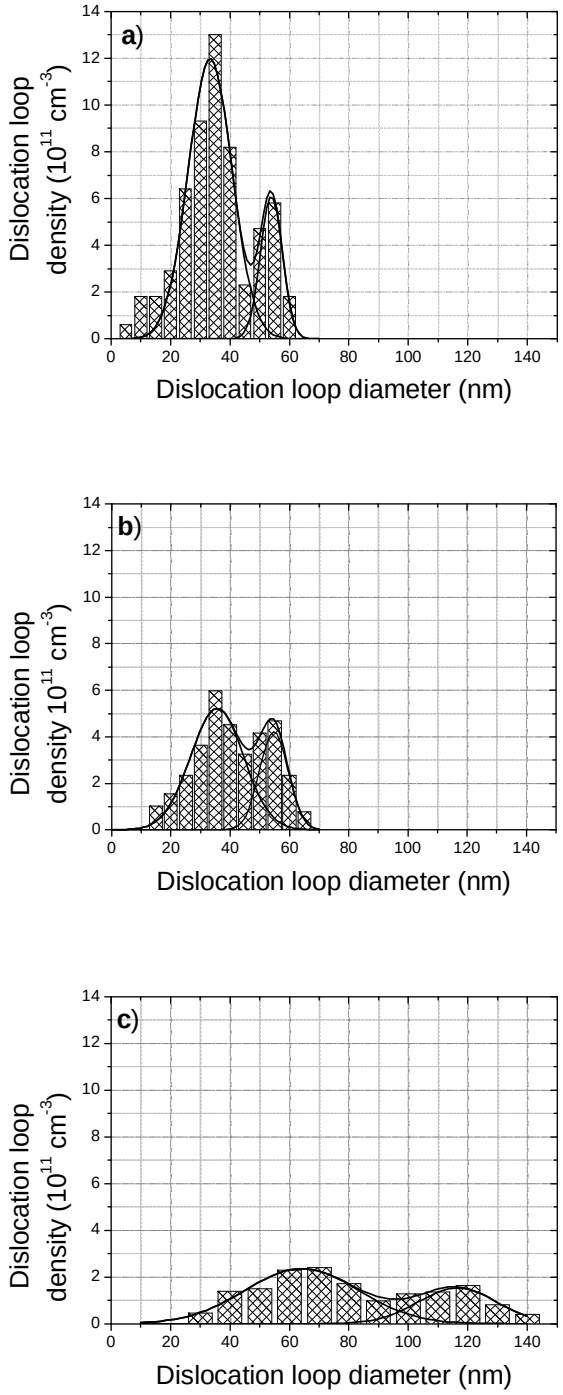

Figure 5.9

Loop density versus size distribution of silicon implanted (80 keV, 10^{15} cm^{-2}, 900 °C) samples a) nSi2e (10 mins), b) nSi2f (30 mins) and c) nSi2g (120 mins). Data is fitted using two Gaussian distributions, indicated by the solid lines.

by statistical analysis using the Kolmogorov-Smirnov (KS) test (Chakravarti *et al.*, 1967), a measure of the deviation from the ideal Gaussian distribution, with the KS value for the double peak being less than half the value for a single-peak Gaussian distribution. As is the case in the boron implanted samples, the maximum of the two peaks correspond to the observed mean diameters of the FDLs and PDLs (smaller and larger peak in each profile respectively), supporting the conclusion that the two Gaussian curves correspond to the size distributions of FDLs and PDLs.

The number of silicon atoms per unit area enclosed by the dislocation loops, N_b, may be calculated using the following expression (assuming that the dislocation loops are circular and lie on {111} planes):

$$N_b = \rho_{\{111\}} \langle A \rangle D w \qquad \text{Eqn. 5.2}$$

where $\rho_{\{111\}}$ is the density of atoms on {111} planes (1.57×10^{15} atoms cm^{-2}), <A> the mean loop area, D the dislocation loop density per unit volume and w the width of the dislocation band. The evolution of the number of atoms contained in the dislocation loops is shown in Figure 5.10. The number of atoms stored in the PDLs increased with time while it decreased in the FDLs however, the total number of atoms bounded by both types of loops was found to remain constant upon annealing (~4.2×10^{13} atoms cm^{-2}) within experimental error.

5.3.2.4 Discussion of silicon implanted samples

Defect band location and dislocation characteristics: The dislocation loops observed in the silicon implanted specimens are significantly smaller than those generated by the boron implantation process after an approximately equivalent annealing process. The lower band of dislocations was also located at, or beyond, the

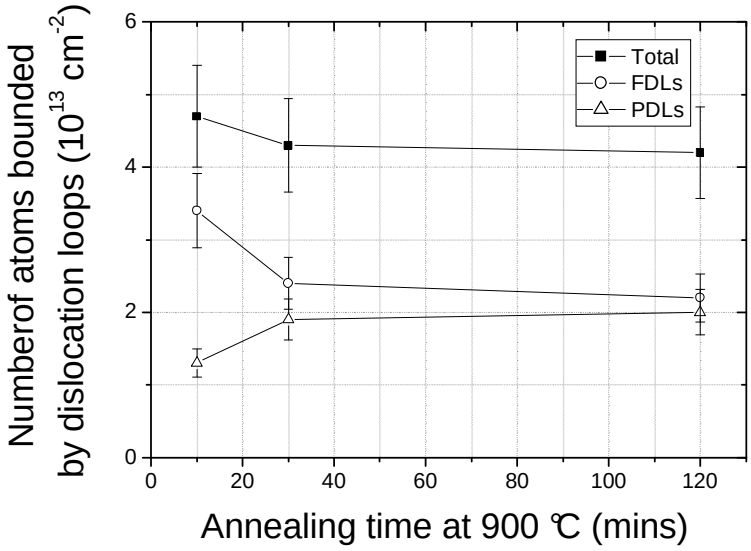

Figure 5.10

Number of atoms bounded by perfect and faulted dislocation loops in the silicon implanted samples (80 keV, 10^{15} cm^{-2}, 900 ℃, 10 mins) as a function of annealing time.

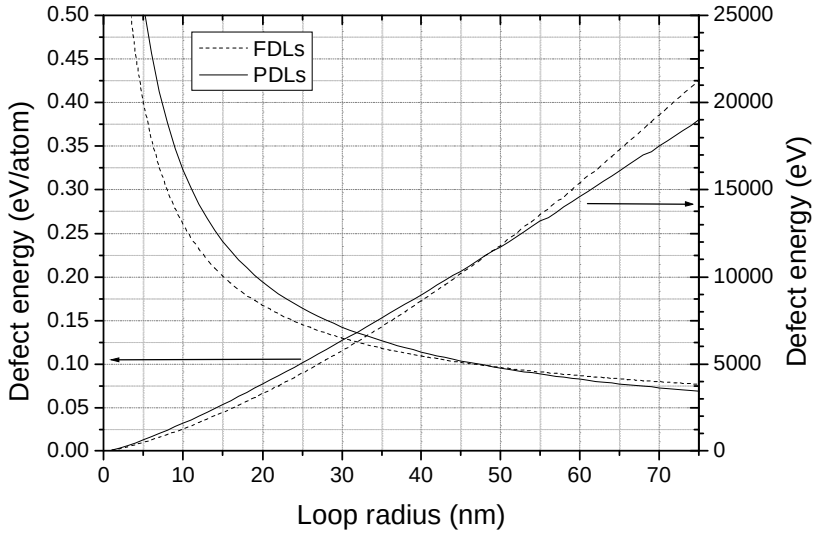

Figure 5.11

Calculated formation energies of faulted and perfect dislocation loops as a function of the loop radius.

'end of range' rather than at the projected range. This is typical of 'type 2' or 'end of range' defects which form below the lower amorphous-crystalline interface (Jones and Rozgonyi, 1993). The upper dislocation band is thought to occur at the upper amorphous-crystalline interface and is dissolved at an annealing time between 10 and 30 mins. The surface has been shown to act as a strong sink for interstitials and dislocation loops less than 100 nm from the surface have been shown to be highly unstable (Noda, 2002).

Samples created by the silicon implantation and thermal annealing have been shown to contain an approximately equivalent dislocation density to the boron implanted sample nB2a (the sample which is most closely matched to the DE-silicon sample of Ng *et al*. (2001)). The dislocation loops are located at a similar distance from the surface but are present in material doped to only ~5 x 10^{14} (*n*- and *p*-type) and the samples do not contain a *p*-*n* junction.

Thermal evolution of implantation related defects: The coarsening process during extended thermal annealing can be clearly observed, with the mean loop diameter increasing as the total defect density decreases. However, the size distribution profiles of the dislocation loops do not display the typical curve for classic Ostwald ripening. Ostwald ripening describes the defect size distribution during conservative growth *i.e.* where the total number of atoms bounded by the defects remains constant. The constant value of N_b as a function of annealing time found in this work indicates that under the conditions used and for a defect layer sufficiently far from the surface (greater than 100 nm), the defect population evolution can be considered to be a conservative process, consistent with Bonafos *et al.* (1998) and Cristiano *et al.* (2000).

Previously, authors have considered the evolution of the defect population with annealing time. Pan *et al.* (1996) postulate, as described in Section 5.3.2.2, that the growth of ion implantation related defects is described by a coarsening process which favours the growth of large coherent loops, in excess of that expected under the classic Ostwald ripening model. However, the nature (PDL or FDL) of the defects was not considered.

The results of this investigation show that PDLs grow preferentially in comparison to FDLs, as has been observed in the literature (see for example Cristiano *et al.*, 2000). Cristiano *et al.* (2000) ascribed this to be due to the difference in the defect formation energies. In contrast to these works from the literature, the thermal evolution of implantation related defects in this work may be understood in terms of the coarsening of two defect populations as the following analysis demonstrates:

The ion implantation process creates damage, producing a large excess concentration of interstitials. As in any system, any deviation of the total free energy from the minimum results in the production of a driving force for its reduction. The excess interstitial concentration, and the total system free energy, is reduced by the formation of lower energy, extended defects. Under the processing conditions used in this study, these extended defects are FDLs and PDLs. The lower energy defect configurations are characterised by the energy reduction of the system when an extra interstitial atom moves from the bulk onto the defect. As a result of the defect capturing an interstitial atom, the defect energy increases but the net system energy decreases due to the reduction in energy of the interstitial. This change in energy can be considered the binding energy, E_b, of the interstitial to the defect:

$$E_b = \Delta E = \frac{dE}{dN}\Delta N \quad \text{where} \quad \Delta N = 1 \qquad \text{Eqn. 5.3}$$

where E is the total system energy and N the number of interstitials bounded by the defect. Dislocation loops grow by the condensation of interstitials on the bounding dislocation, which then climbs outwards, increasing the area of the dislocation loop.

For a PDL of radius *r* the defect energy, E_{PDL}, is given by the elastic strain energy of the dislocation line, E_{el} (Hull and Bacon, 1984):

$$E_{PDL} = E_{el} = \frac{\mu r}{4}\left[\frac{a^2}{6} + \frac{5a^2}{6(1-\nu)}\right]\ln\left(\frac{2r}{r_0}\right) \qquad \text{Eqn. 5.4}$$

where μ is the shear modulus (7.55×10^{10} Nm^{-2}), *a* is the lattice parameter (0.543 nm), ν is the Poisson's ratio (0.3), and r_0 (assumed to equal **b)** is the dislocation core radius, where **b** is the modulus of the Burgers vector (0.338 nm).

A similar approach can be followed to evaluate the energy of an FDL, E_{FDL}, which has an associated stacking fault energy, E_{SF}:

$$E_{FDL} = E_{SF} + E_{el} = \pi r^2 \gamma + \frac{\mu r}{4}\left[\frac{2a^2}{3(1-\nu)}\right]\ln\left(\frac{2r}{r_0}\right) \qquad \text{Eqn. 5.5}$$

where γ is the stacking fault energy per unit area (70 mJm^{-2} (Cristiano *et al.*, 2000)). The other values are as stated above for the PDL case except **b**, the modulus of the Burgers vector, is now 0.313 nm.

The calculated energies of PDLs and FDLs are shown in Figure 5.11. It can be seen that the FDLs are significantly lower in energy for dislocation loop radii of less than ~20 nm, and that, though PDLs become lower energy defects for radii greater than ~45 nm, the difference in energy between the two forms of dislocation

loop is small for loop radii greater than ~20 nm. This suggests that FDLs would be preferentially nucleated in comparison to PDLs, but the mean diameter of the PDLs which are nucleated is greater than the mean diameter of nucleated FDLs. This is consistent with the experimental findings where the large majority of dislocation loops observed in the sample annealed for the shortest time (10 mins) are FDLs (~84%), but the mean PDL diameter is greater than the mean FDL diameter – 51 nm compared to 32 nm respectively.

A schematic illustration of the free energy of the system as a function of the position of an interstitial atom is shown in Figure 5.12. The system is shown to contain two defects; defect one has large formation energy and, correspondingly, a low interstitial binding energy, and defect two has low formation energy, and thus, a high interstitial binding energy. Ostwald ripening proceeds by the high energy defects tending to dissolve with a net flux of interstitials towards low energy defects. In the case of implantation related defects, the defect energy is determined by their size and character (FDL or PDL). The defects observed in this study are generally greater than 30 nm in diameter and thus the difference in energy between a FDL and PDL of similar size is small. Thus, the driving force for coarsening is simply determined by the size of the dislocation loop. As PDLs are larger upon nucleation these tend to grow in preference to the smaller FDLs.

It was observed experimentally that: i) the mean diameter of both FDLs and PDLs increased, ii) there was a significant reduction in the FDL dislocation loop density, iii) there was only a small reduction in PDL dislocation loop density and iv) there was a net flux of interstitials from FDLs to PDLs. These observations are entirely consistent with the Ostwald ripening model assuming that PDLs nucleate with a larger mean diameter than FDLs.

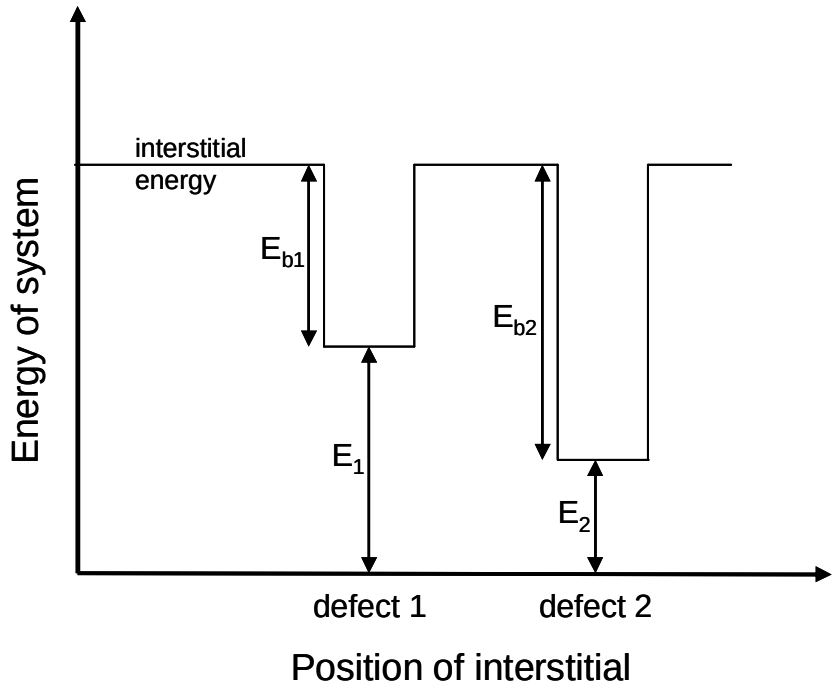

Figure 5.12

Schematic representation of the free energy of a system which contains two different defect states. E_{b1} and E_{b2} are the binding energies of an interstitial to defect 1 and defect 2 respectively and E_1 and E_2 are the energies of defect 1 and defect 2 respectively.

5.4 Analysis of samples containing second phase defects

The majority of the boron or silicon ion implanted specimens investigated were found to contain a band of dislocations below the specimen surface. However, a small number of samples, namely nB2d, pB2d and nB3c, were found to contain second phase precipitates rather than a band of dislocation loops. Two different types of defects were observed in these specimens. The defect morphologies are outlined and the likely nature of the defects postulated in the following section.

5.4.1 Evaluation of second phase precipitates

One set of defects which were observed were largely isolated, approximately spherical precipitates with a diameter in the range of 5 to 25 nm and were located at (or near) the wafer surface. These precipitates are labelled as precipitate type A in Figures 5.13 and 5.14. The precipitate density was calculated to be ~5 x 10^8 cm^{-2}. Under strong **g** = [-2-20] plan view illumination, individual precipitates exhibited moiré fringe contrast perpendicular to the {220} direction. The width of a single black or white fringe was calculated directly from the TEM images to be ~40 Å. A single colony of these precipitates was also observed in sample nB1d. The colony was observed to be approximately 300 nm in diameter and contained ~25 independent precipitates. The colony density was estimated to be less than 1 x 10^5 cm^{-2}.

The second form of defects were a group of several second phase precipitates, the group of defects is labelled B in Figure 5.13 and are made of up to 4 distinct precipitates labelled R, S, M and F in Figure 5.14. These B defects, with a density of ~1 x 10^7 cm^{-2}, were observed to consist of: i) a rod-shaped precipitate which penetrated the wafer along inclined <101> directions to depths approaching 200 nm,

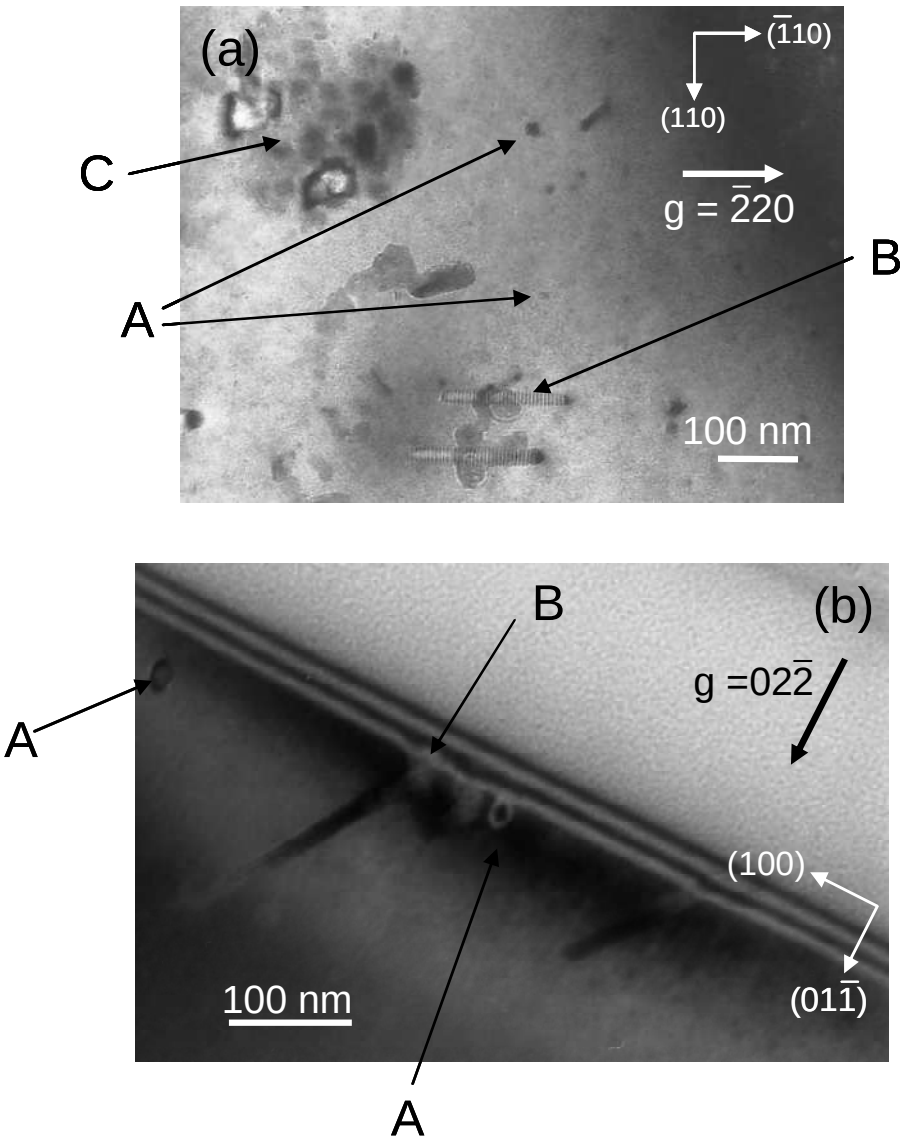

Figure 5.13

Representative bright field transmission electron micrographs of second phase defects observed in samples nB2d (B, 30keV, 10^{15} cm^{-2}, 1000°C, 60mins), pB2d (B, 30keV, 10^{15} cm^{-2}, 1000°C, 60mins) and nB3c (B, 30keV, 10^{16} cm^{-2}, 1000°C, 15mins).

a) Plan-view image of second phase defects

b) Cross-sectional image of precipitates A and B at or near the wafer surface C = colony of small spherical precipitates, A = individual spherical precipitates (copper silicide) and B = group of secondary phase particles.

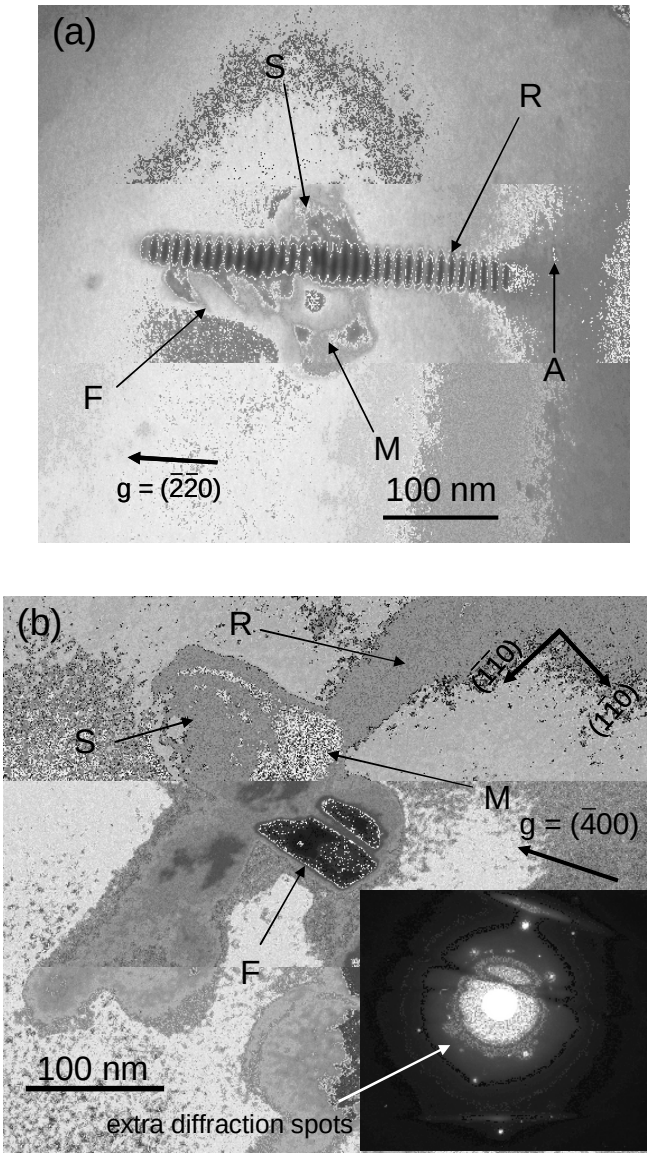

Figure 5.14

Representative plan-view transmission electron bright field micrographs of second phase defects observed in samples nB2d (B, 30keV, 10^{15} cm^{-2}, 1000°C, 60mins), pB2d (B, 30keV, 10^{15} cm^{-2}, 1000°C, 60mins), and nB3c (B, 30keV, 10^{16} cm^{-2}, 1000°C, 15mins), displaying secondary phase particles: individual spherical particles (A) and grouped second phase particles (B in Figure 5.13) consisting of a rod-shaped precipitate (R), an approximately spherical precipitate and irregular mass of material showing a mottled contrast (S and M respectively) and a faceted crystalline precipitate (F).

a) A typical defect imaged using $\mathbf{g} = (\bar{2}\bar{2}0)$

b) A similar defect imaged using $\mathbf{g} = (\bar{4}00)$.

being bound at one end by the wafer surface. This precipitate is labelled R in Figure 5.14. The rods had a lateral dimension of ~30 nm for more than 70% of their length. The precipitate was found to be tapered towards the end not bound by the wafer surface; the thickness reduced to ~15 nm in a distance of 50 nm. These rod-shaped precipitates displayed moiré fringe contrast in **g** = [-2-20] plan view illumination. The fringe width was calculated directly from the images to be 27 ± 3 Å. ii) An approximately spherical (~45 nm diameter) precipitate showing a mottled contrast under both **g** = {220} and **g** = {400} was observed with every rod-shaped precipitate. The approximately spherical precipitate was surrounded by an irregular mass of material exhibiting similar contrast, labelled S and M respectively in Figure 5.14. iii) In less than 10% of cases a third form of precipitate within the irregular mass of material was also observed. These were faceted with sides seemingly independent of the host silicon lattice, labelled F in Figure 5.14. When an electron beam (~50 nm diameter) was focused on these defects, a ring of extra diffraction spots was observed in the selected area diffraction pattern. No preferential orientation with respect to the silicon host lattice was observed. The spacing of the lattice planes which gave rise to the ring of diffraction spots was calculated to be 2.1 ± 0.2 Å.

5.4.2 Discussion

Individual spherical precipitates (and colonies): The small, isolated, spherical precipitates are thought to be individual copper silicide precipitates. The morphology and contrast fringe width are consistent with the observations of de Coteau (1993), Tice and Yan (1976) and Das (1973) who all observe precipitates of identical morphology with a moiré fringe thickness of ~40 Å.

It was not the objective of the present investigation to determine the nature of the precipitates and their formation mechanism. However, it is well established that, upon cooling, the supersaturation of the copper concentration provides a driving force for heterogeneous nucleation either at the wafer surface or at defects within the specimen bulk (Nes, 1978).

The majority of copper silicide precipitates observed in this study are in the form of isolated spherical precipitates. In samples which were intentionally contaminated these were observed to act as nucleation centres for colony growth (de Coteau, 1993). However, in this work, only a single colony was ever observed. The observation of individual precipitates suggests that there is a low concentration of copper which limits the formation of large scale colonies.

Rod defects and associated precipitates: The morphology and moiré fringe width of the rod-shaped precipitates are consistent with observations of β-iron silicide in the literature (see for example Seibt and Schröter (1989) and Cullis and Katz (1974)). The precipitates observed by Cullis and Katz (1974) were significantly larger than those observed in this work, typically 2 μm in length, and without other associated defects, though their orientation and shape were as observed in this study. Seibt and Schröter (1989) report that in some cases, iron silicide precipitates exhibited additional small precipitates. These small crystalline particles resembled precipitates of copper silicide, which were suggested to have formed the nuclei for heterogeneous iron silicide nucleation. The extra diffraction spots, associated with the faceted precipitate are consistent with the strongly diffracted $(11\bar{2}0)$ lattice planes of the hexagonal close packed η-Cu_3Si phase (Myers and Follsteadt, 1995).

The concentration of contaminants in these samples is significantly lower than in studies intentionally investigating transition metal precipitation and gettering,

shown by the vastly lower density of precipitates and their significantly smaller dimensions, and is likely to be due to contamination during sample processing. This is consistent with the fact that copper, iron (and nickel) are the most common transition metal impurity atoms unintentionally found in silicon (Falster, 2001). The source of contamination during wafer processing is unclear, though the fact that all other samples do not show second phase precipitates is likely to suggest that the ion implanter and annealing furnaces are unlikely sources of contamination, rather that the rogue samples may have been in handled incorrectly prior to processing.

5.6 Summary and conclusions

The defects created by the ion implantation and annealing process have been characterised using TEM. The vast majority of samples were found to contain a band of small dislocation loops located below the wafer surface (typically ~100 nm deep and 200 nm wide). The dislocation loops were found to be consistent with either faulted Frank or perfect dislocation loops, with Burgers vector ⅓(111) and ½(110) respectively. Samples with a wide range of dislocation densities were created, 4.2 x 10^{7} – 10^{11} cm^{-2}, with or without the formation of a *p-n* junction.

The boron implantation process was found to create defect loops consistent with 'type 1' defects, located at or below the projected ion range. Whereas, in the silicon implanted samples a band of 'type 2' or end of range defects was observed. In sample nSi2e a second band, closer to the surface was also observed. This was thought to be located at the upper amorphous-crystalline interface.

The evolution of the size distribution and nature of the dislocation loops was evaluated as a function of the annealing time. Boron implanted samples were found

to possess a universal normalised distribution, which had been previously observed by Pan *et al.* (1996). However, the silicon implanted samples were observed to display a double peak size distribution. In both cases, the size distribution could be modelled using two Gaussian curves which were assumed to be either FDLs or PDLs. The experimental observations can be accounted for using Ostwald ripening theory without needing to consider the relative formation energies of the two defects or the effect of the strain field as suggested in the literature (see Cristiano *et al.*, (2000) and Pan *et al.*, (1996)).

A small number of ion implanted samples contained a number of second phase precipitates rather than ion implantation related dislocation loops. These were consistent with individual copper silicide precipitates. Approximately 2% of these are thought to nucleate β-iron silicide precipitates heterogeneously. It is thought that rogue rather than systematic contamination is the cause of these results.

Chapter 6

Cathodoluminescence from unprocessed and dislocation-engineered silicon and its dependence on SEM conditions

6.1 Introduction

In this chapter the cathodoluminescence technique is used for the first time to investigate the room-temperature luminescent properties of several unprocessed, as-received wafers and a single dislocation-engineered (DE)-silicon wafer. For each specimen the luminescence spectrum, the measured quantum efficiency (MQE) and the variation of the luminescence intensity within a sample and wafer are investigated and compared to the literature. The dependence of the luminescence intensity from these specimens on the microscope conditions is also studied.

6.2 Cathodoluminescence from unprocessed wafers

Silicon samples: A number of unprocessed, as-received, phosphorous doped (~10 Ωcm, ~5 x 10^{14} cm^{-3}), 660 μm thick, (001) Cz- and FZ-grown silicon wafers were investigated. These unprocessed wafers were similar to the wafers used for the manufacture of the DE-samples with *n*-type doped substrates.

No luminescence could be detected from the vast majority of the unprocessed wafers investigated (MQE detection limit ~2 x 10^{-8}). However, a small number of Cz- grown wafers were found to emit weak luminescence. The luminescence spectra of all unprocessed specimens were noisy, even when using long dwell times, large beam currents and wide monochromator slit widths. However, the luminescence spectrum displayed a peak at ~1140 nm with full width half maximum FWHM ~80 nm, see Figure 6.1a.

The luminescence intensity was investigated as a function of position, representative results, from a single sample, over a distance of ~0.3 mm, are shown in

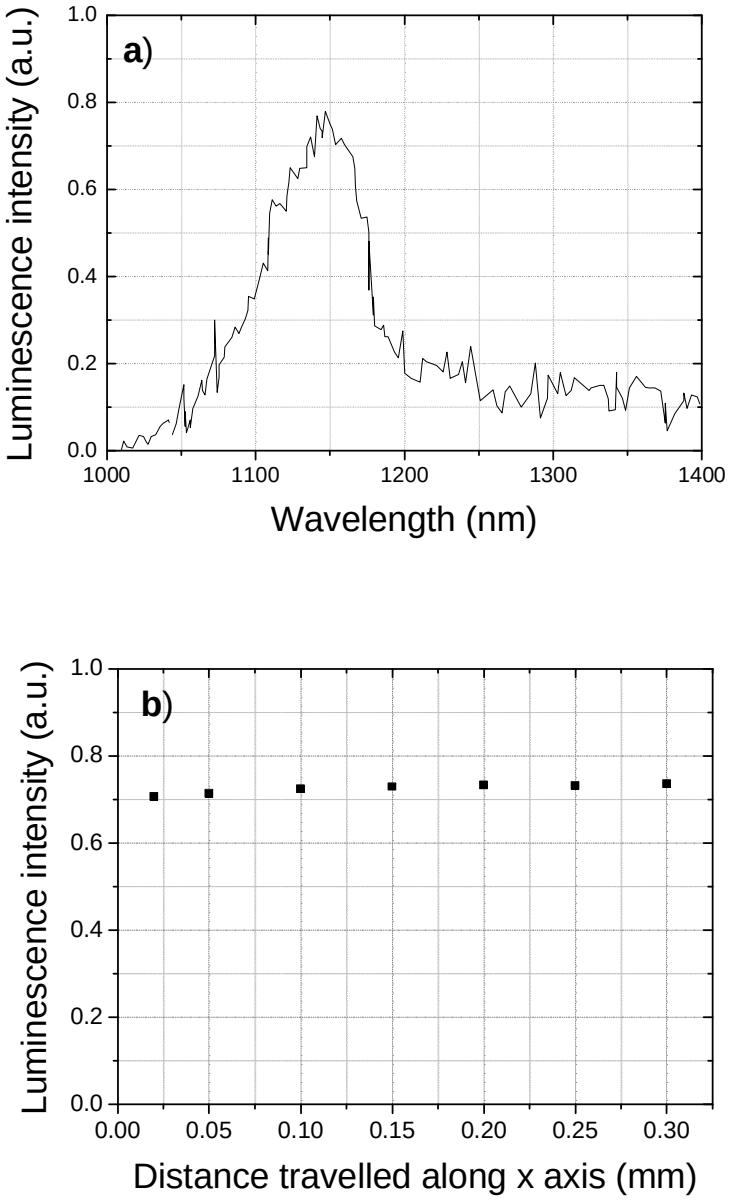

Figure 6.1

a) Room temperature cathodoluminescence spectrum and b) the variation of the luminescence intensity of a phosphorous doped, ~10 Ωcm, unprocessed specimen. I_{beam} = 250 nA, E_{beam} = 30.0 keV, dwell time = 8 s and monochromator slit widths = 1.5 mm.

Figure 6.1b. The variation in the luminescence intensity within a single sample was investigated by focusing a stationary electron beam to a small spot and then the microscope stage translates were used to move the sample relative to the fixed collection optics. This produced a luminescence intensity line-scan across the sample. The distance of the specimen below the mirror was initially set as described in Chapter 3 and not adjusted during the scan. At the end of each scan, the change in the collection efficiency (due to the change in focal height) was found; this was found to result in a change in the measured luminescence intensity of less than 5%. The data displayed in Figure 6.1b has been corrected to account for this variation, assuming a linear change in the collection efficiency with position. The variation in the luminescence intensity within a single sample was found to be negligible.

The MQE may be calculated using the number of electron-hole pairs generated (Eqn. 2.1), the measured signal and the system responsivity (see Section 3.2.5). The maximum MQE of the unprocessed wafers was estimated to be approximately 6.4 x 10^{-8} at an electron beam current of 200 nA and an electron beam energy of 30 keV.

Gallium Arsenide: A single, silicon doped, gallium arsenide wafer was also investigated. A sharp luminescence peak centred at 872 nm with FWHM 18 nm was observed, shown in Figure 6.2. The MQE at an electron beam current of 5 nA and an electron beam energy of 30 keV was estimated to be ~0.02.

6.2.1 Discussion

The cathodoluminescence technique was used, for the first time, to investigate the TO phonon-assisted, free carrier luminescence from bulk silicon at room temperature. The luminescence was observed to be nominally peaked at 1140 nm and

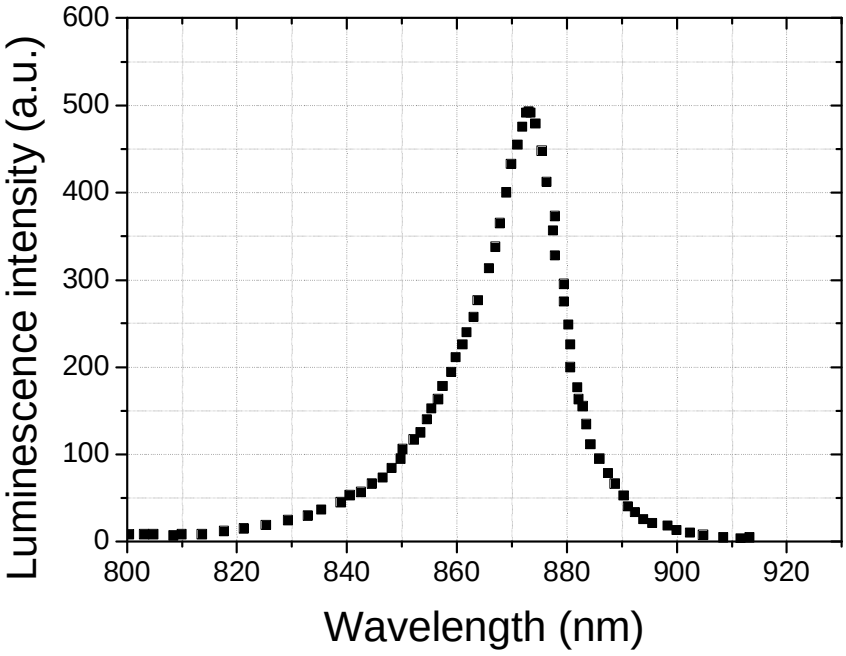

Figure 6.2

Room temperature cathodoluminescence spectrum from a silicon doped, gallium arsenide wafer. I_{beam} = 5 nA, E_{beam} = 30 keV, dwell time = 2 s and monochromator slit widths = 0.5 mm.

the MQE of 10 Ωcm, phosphorous doped, silicon wafers in the unprocessed, as-received condition was observed to be 6.4×10^{-8} or less. The luminescence peak was red-shifted by ~10 nm from that typically observed for silicon TO phonon-assisted recombination (see for example Kramer *et al.*, 1993) and that predicted theoretically (Trupke, 2006). However, the minority carrier diffusion lengths of high quality silicon wafers are typically many hundreds of microns and potentially, several millimetres (Falster and Borionetti, 1998). Thus, photons can be generated from large depths within a sample and it is necessary to consider the effect of photon re-absorption on the spectral distribution.

If photons are generated at a point x below the wafer surface (CL_x), the measured luminescence intensity ($CL_{x=x_0}$) can be calculated by assuming an exponential decay of the emitted photons due to the effect of photon re-absorption:

$$CL_{x=x_0} = CL_x \exp(-\alpha x) \qquad \text{Eqn. 6.1}$$

where α is the absorption coefficient and is a function of the photon wavelength; the band-to-band absorption coefficient drops from 3.5 cm^{-1} at silicon's bandgap (1103 nm) to 10^{-3} cm^{-1} at 1250 nm (Green and Keevers, 1995).

Figure 6.3a shows the spectrum that would be detected if all photons were generated at distances of between 0 and 500 μm from the wafer surface. The data was calculated using the theoretical spectrum from Trupke (2006) and it was assumed that the parasitic contribution to absorption was negligible and that photons which were internally reflected do not contribute to the measured signal.

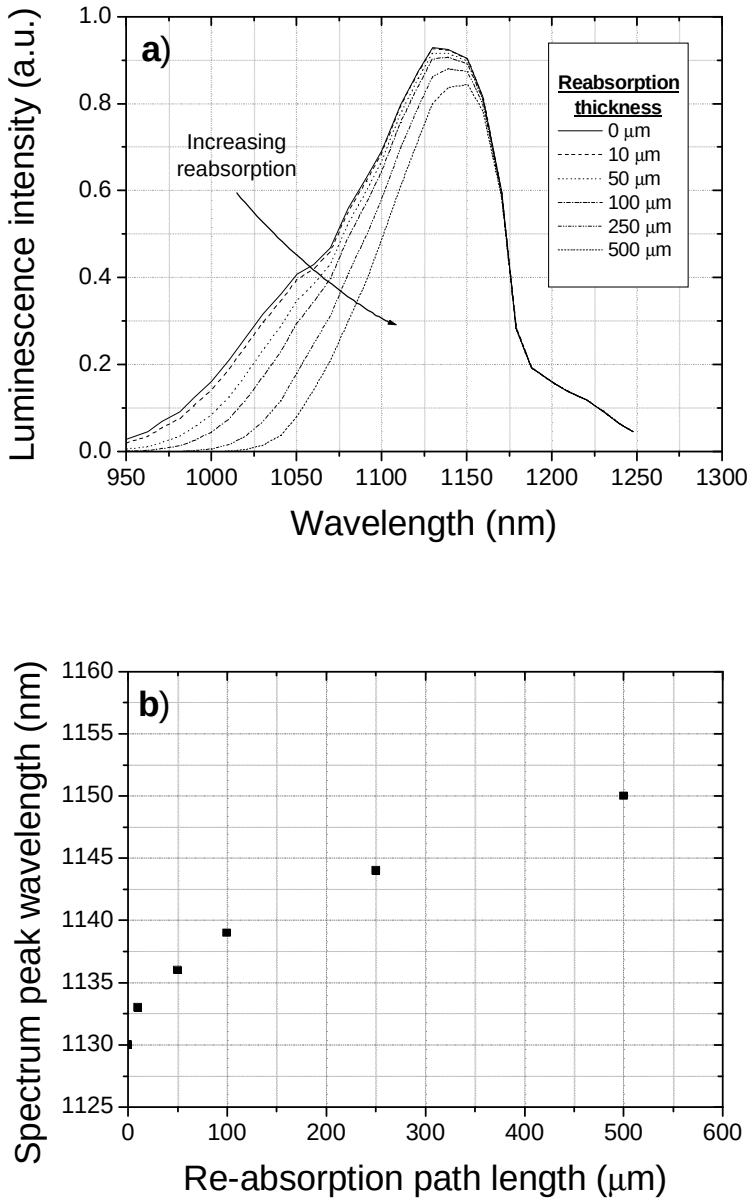

Figure 6.3

a) Calculated luminescence spectra from unprocessed silicon wafers including the effect of photon re-absorption. Calculated spectrum with no absorption after Trupke (2006).

b) Calculated wavelength of the spectrum peak as a function of the photon re-absorption path length.

The re-absorption process strongly affects wavelengths shorter than 1150 nm, whereas the spectrum at longer wavelengths remains relatively unchanged. For re-absorption distances greater than zero the spectrum peak was found to be red-shifted from the TO phonon-assisted value of 1130 nm and the FWHM to be reduced. The degree of red-shift in the peak wavelength as a function of the re-absorption distance is shown in Figure 6.3b. The experimentally measured peak position of ~1140 nm was found to be consistent with a mean photon escape length of ~200 μm.

The estimated MQE of the unprocessed silicon wafer is significantly lower than EQE values quoted in the literature, typically $5 \times 10^{-5} – 10^{-6}$ for EL studies (Green *et al.*, 2001). However, the MQE of the gallium arsenide specimen (0.02) was observed to be consistent with the literature, where EQEs of between 0.01 and 0.1 are routinely reported (see for example Coffa, 2003). The difference between the MQE of the silicon samples investigated in this study and the EQEs from the literature may be explained by: i) the collection efficiency of the CL system and ii) the increased effect of surface recombination in CL in comparison to PL and EL:

i) The characterisation of the CL system in Chapter 3 showed that high, uniform collection was realised only in the central portion of the field of view (~100 x 100 μm in size) and that for samples with long diffusion lengths the collection efficiency of the system may be significantly reduced. Thus, a significant proportion of photons emitted from the front surface of the unprocessed silicon specimen are not efficiently collected by the CL system and thus, the MQE is necessarily lower than the EQE.

ii) In the CL technique, the long minority carrier diffusion length of silicon results in a higher number of electron-hole pairs recombining non-radiatively at the specimen surface in comparison to gallium arsenide, where the minority carrier

diffusion length is short. Thus, the effect of surface recombination is not important in determining the difference between the MQE and the EQE in gallium arsenide, whereas in the silicon samples the MQE may be significantly lower. In the EL technique, minority carriers are injected directly away from the specimen surface resulting in little surface recombination.

Thus the MQE of a gallium arsenide sample investigated by CL is similar to the MQE observed when using EL; however, the MQE of a silicon sample investigated by CL may be significantly lower than when measured by EL.

6.3 Cathodoluminescence from dislocation-engineered silicon

In this section the cathodoluminescence from the DE-silicon sample nB2a is described. The DE-silicon sample closely matched the specimen investigated by Ng *et al.* (2001): the substrates were ~10 Ωcm, phosphorous doped, Cz-silicon wafers and the implantation conditions used for the two specimens were identical (boron, dose 1 x 10^{15} cm^{-2}). However, sample nB2a was annealed for 15 mins at 900 °C, rather than 20 mins at 950 °C, and contained soft backside damage (SBD). Nevertheless, the morphologies of the dislocations formed as a result of the two processing conditions were found to be similar: small, predominantly faulted dislocation loops (~140 nm in diameter), situated in a band ~200 nm wide and 50 nm below the wafer surface with a dislocation density of ~5 x 10^{9} cm^{-2} (see Chapter 5).

Figure 6.4 shows the luminescence spectrum from sample nB2a at room temperature. An asymmetrical peak was observed with a maximum at ~1150 nm (1.07 eV) and FWHM 90 nm and an inflexion apparent at ~1185 nm. No other luminescence peaks were observed at any other wavelength within the sensitivity of

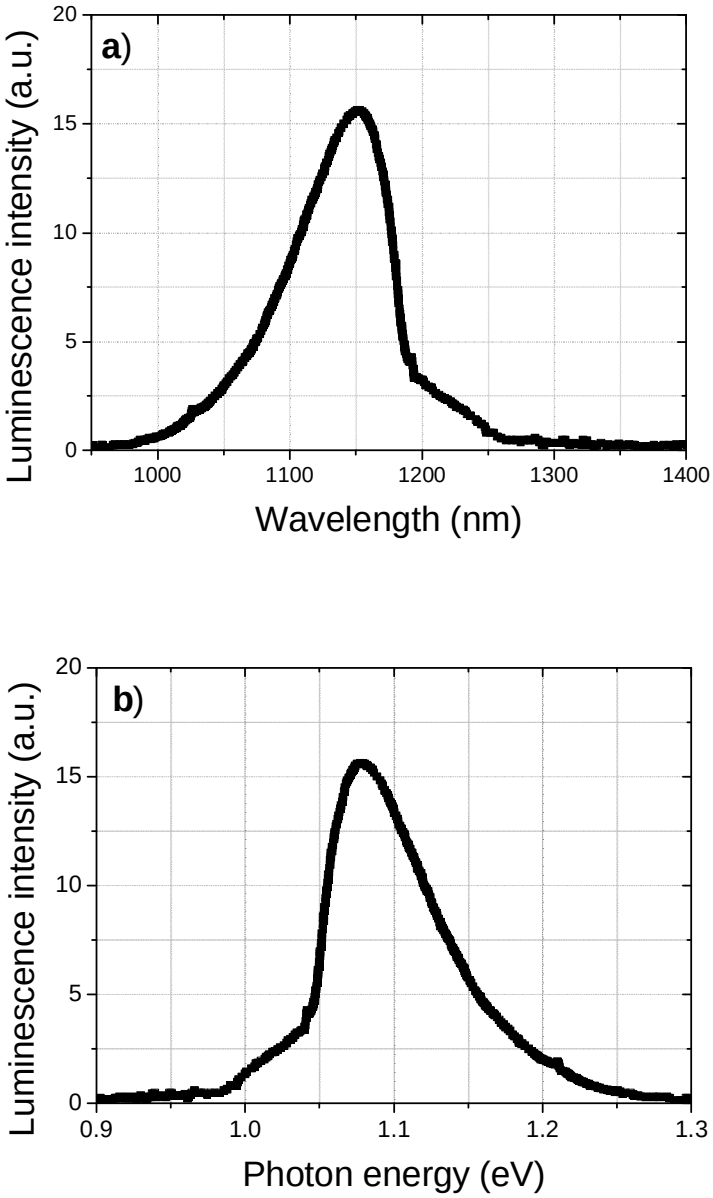

Figure 6.4

Room temperature luminescence spectra from the dislocation-engineered specimen nB2a. Processing conditions: B, 30 keV, 1 x 10^{15} cm^{-2}, 900 °C for 15 mins. I_{beam} = 200nA, E_{beam} = 30 keV, dwell time = 2 s and monochromator slit widths = 1.5 mm.

the detector (800 to 1800 nm). For a beam current of 10 nA and accelerating voltage of 30 kV, the MQE was estimated to be $(1.20 \pm 0.02) \times 10^{-6}$.

The luminescence intensity was investigated as a function of position for a single sample and from a number of different specimens from the same wafer. The luminescence within a single sample was investigated using the technique described in Section 6.2 for unprocessed samples. Figures 6.5a shows the variation in intensity over a distance of ~1 mm (within a single cleaved piece) and Figure 6.5b shows the variation over three wafer radii. The mean value of the luminescence data displayed in Figure 6.5b is 15.6 (a.u.) and has a standard deviation of 0.21 (a.u.).

6.3.1 Discussion

Relatively strong luminescence (MQE 1.2×10^{-6}) with a peak in the spectrum at ~1150 nm was observed from the DE-silicon sample nB2a. The spectrum peak is red-shifted from the TO phonon-assisted peak observed for unprocessed specimens (Figure 6.1a), though the two spectra are similar in form at wavelengths longer than 1150 nm.

Figure 6.6 shows the comparison of the normalised spectrum of sample nB2a, and the spectrum from a DE-silicon sample investigated by Ng *et al.* (2001) using EL at a forward biased current of 50 mA. The luminescence spectra are similar in form; an asymmetrical peak, with a maximum of ~1150 nm and an inflexion apparent at 1185 nm. The two spectra are identical for wavelengths longer than 1150 nm, however, the spectrum of Ng *et al.* (2001) displays a FWHM of ~80 nm, compared to ~90 nm for the spectrum observed in this work.

In the work of Ng *et al.* (2001) the emitted photons are collected from a window in the back ohmic contact of the sample and thus emitted photons travel

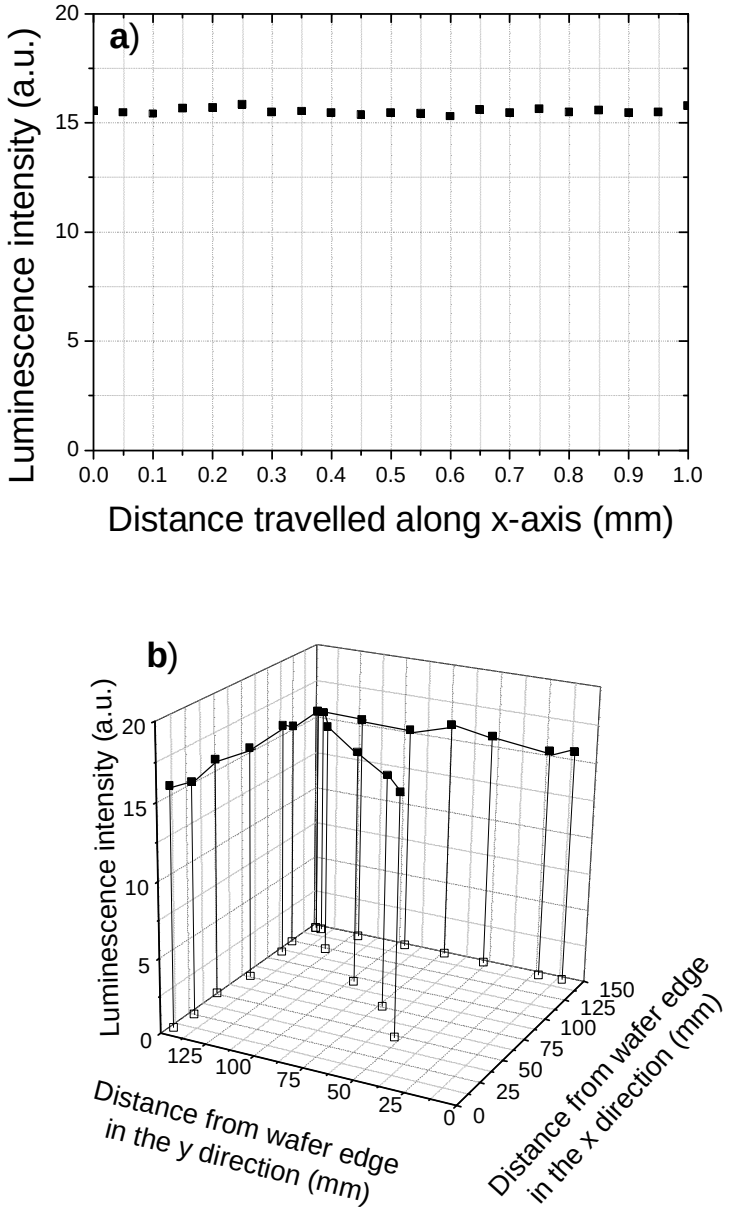

Figure 6.5

Variation in the luminescence intensity as a function of position in sample nB2a - B, 30 keV, 10^{15} cm^{-2}, 900 °C for 15 mins:

a) across an ~ 8 x 8 mm sample (data adjusted for the variation in the collection efficiency across the line scan)

b) across three wafer radii.

I_{beam} = 200 nA, E_{beam} = 30.0 keV, λ = 1150 nm and monochromator slit widths = 1.5 mm.

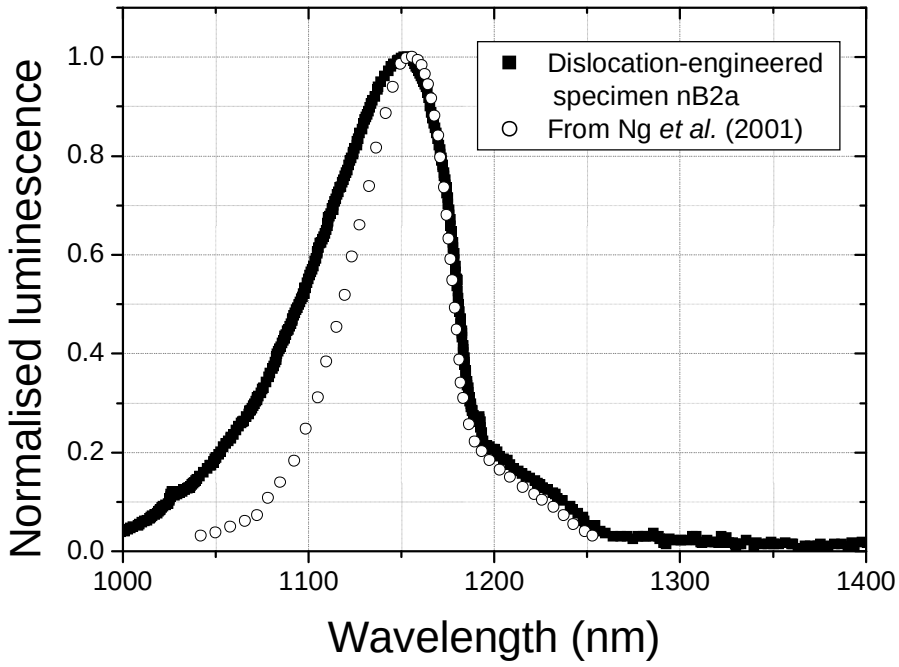

Figure 6.6

Comparison of the normalised room temperature luminescence spectra of dislocation-engineered specimen nB2a (this work) - boron implant (30 keV, 10^{15} cm^{-2}) annealed at 900 °C for 15 mins - and that of a dislocation-engineered specimen published by Ng *et al.* (2001) – boron implant (30 keV, 10^{15} cm^{-2}) annealed at 950 °C for 20 mins. The two spectra have been normalised to a maximum value of 1.

Sample nB2a (this work) was investigated using cathodoluminescence (I_{beam} = 200 nA, E_{beam} = 30 keV and monochromator slit widths = 1.5 mm) whereas the Ng *et al*. (2001) specimen was investigated using electroluminescence at a forward biased current of 50mA.

through the thickness of the wafer before being collected. The experimentally observed peak wavelength of 1150 nm in the work of Ng *et al.* (2001) is therefore consistent with TO phonon-assisted recombination and re-absorption through more than 500 μm of silicon (Figure 6.3b). However, in the present work photons are collected from the surface at which electron-hole pairs are generated by the electron beam. If the mechanism of luminescence in DE-silicon is via TO phonon-assisted radiative recombination, then a photon re-absorption length of ~500 μm is required in order to explain the experimentally observed spectrum. This is incompatible with the mechanism of high efficiency luminescence proposed by Ng *et al*. (2001) (described previously in Section 1.4).

The estimated MQE of the DE-sample nB2a is significantly lower than the EQE published in the study of Ng *et al.* (2001) (1.2×10^{-6} compared to 2.0×10^{-4}). However, other EL results from DE-silicon in the literature report a maximum EQE of 5×10^{-5} using boron implantation (1×10^{15} cm^{-2} at 30 keV) into 400 Ωcm phosphorous doped substrates (Sobolev *et al.*, 2003) and 2.6×10^{-5} for the case of phosphorous implantation into a *p*-type substrate (Arguirov *et al*., 2004). The EQE of sample nB2a is not known accurately, but with the experimental considerations described in Section 6.2.1, the EQE is likely to be consistent with other values from the literature.

6.4 Dependence of cathodoluminescence on microscope conditions

The following section describes how the panchromatic luminescence intensity (*i.e.* the total light incident upon the detector) from a 10 Ωcm, phosphorous doped, unprocessed wafer and the DE-specimen nB2a depends on the microscope conditions.

The luminescence intensity was investigated as a function of the electron beam diameter, the absorbed specimen current, and the electron beam accelerating voltage.

6.4.1 Cathodoluminescence as a function of the electron beam diameter

In order to understand the effect of the carrier concentration in the generation volume, the luminescence intensity was investigated as a function of the electron beam diameter at accelerating voltages in the range 5 to 30 kV. The beam diameter was roughly estimated using simple geometry given that: i) the objective aperture was 60 μm in diameter and ii) the focal length of the electron beam was stated by the microscope operating system. The electron beam was initially stationary and focused to a point and then defocused using the microscope optics. From time-to-time, the quality of the microscope vacuum was poor and contamination was observed on the specimen surface. The diameter of the electron beam was confirmed by secondary electron images of beam-induced surface contamination obtained when using a stationary beam and high beam currents.

The excess carrier concentration in the generation volume was estimated using the following formula (Donolato, 1978):

$$\Delta p(0) = \frac{G_0 A}{3D_h} \qquad \text{Eqn. 6.2}$$

where G_0 is the electron-hole pair generation rate, A is the area of illumination and D_h the hole diffusion coefficient. The generation volume was assumed to be spherical with a uniform excess carrier concentration. G_0 is given by:

$$G_0 = \frac{I_{beam} E_{beam}}{E_{e-h} V} \qquad \text{Eqn. 6.3}$$

where I_{beam} and E_{beam} are the beam current and beam energy respectively, $E_{e\text{-}h}$ is the energy required to create an electron-hole pair and V is the generation volume. The carrier concentration in the generation volume was calculated to be in the range of ~10^{12} to 5 x 10^{18} cm^{-3}.

No change in the luminescence efficiency was observed as a function of the beam diameter for either the unprocessed sample or the DE-specimen nB2a.

6.4.2 Cathodoluminescence as a function of beam current

The luminescence intensity was investigated as a function of the absorbed specimen current for accelerating voltages in the range of 7.5 - 30 kV. The results are shown in Figures 6.7 and 6.8 for the unprocessed sample and the DE-specimen nB2a respectively. The two sets of data were produced using identical experimental conditions and the luminescence intensities in Figures 6.7 and 6.8 are therefore directly comparable. The luminescence intensity of both the unprocessed sample and the DE-specimen were observed to depend super-linearly, with respect to the absorbed specimen current, and no saturation in the signal was observed. No data could be collected for the unprocessed sample at 7.5 kV due to the detection limits of the system.

An estimation of the luminescence efficiency (η,in arbitrary units) may be approximated by determining the measured luminescence intensity (signal) per electron-hole pair generated:

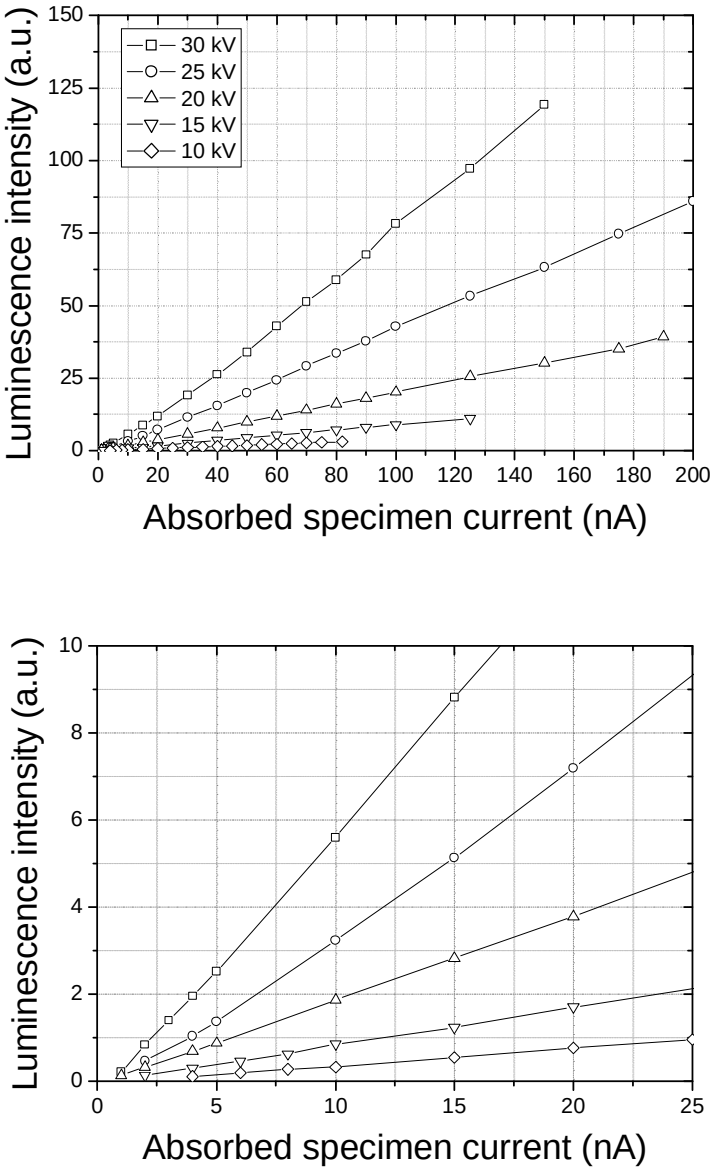

Figure 6.7

Luminescence intensity of a phosphorous doped, ~10 Ωcm, unprocessed wafer as a function of the absorbed specimen current for microscope accelerating voltages in the range 10 to 30 kV. The lower graph is a rescaled version of the upper graph.

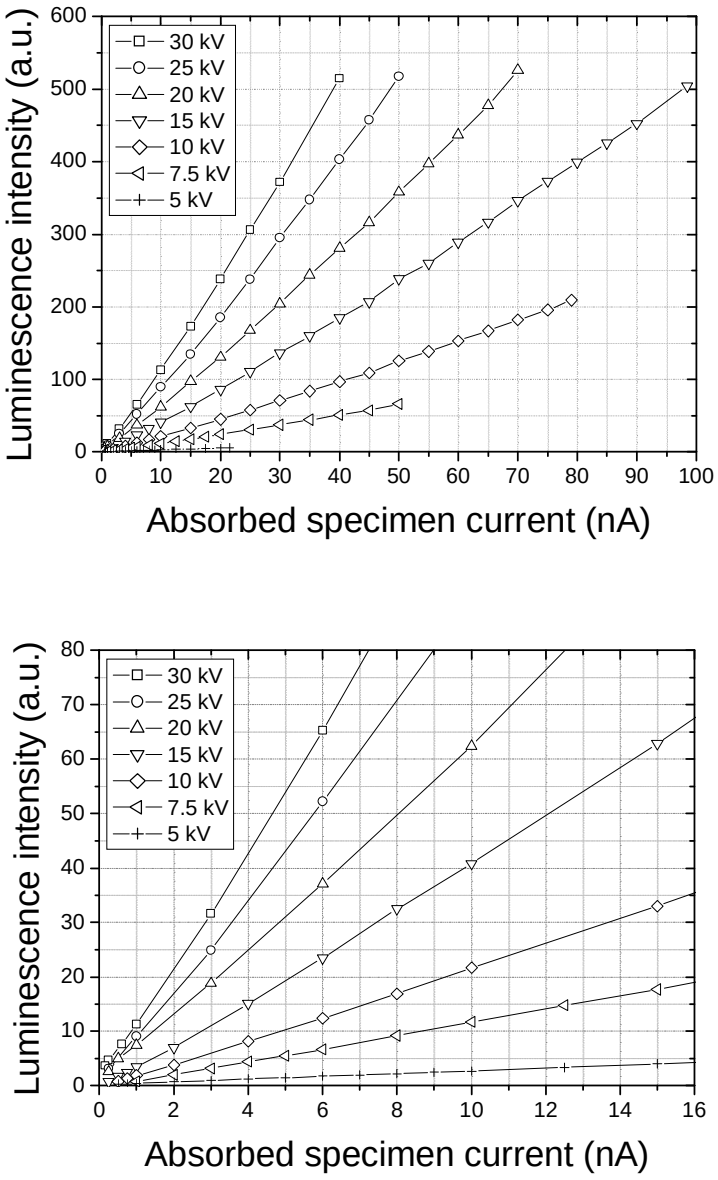

Figure 6.8

Luminescence intensity of sample nB2a (B, 30 keV, 10^{15} cm^{-2}, 900 °C for 15 mins) as a function of the absorbed specimen current microscope accelerating voltages in the range 5 to 30 kV. The lower graph is a rescaled version of the upper graph.

$$\eta = \frac{signal}{I_{beam} \times E_{beam}} \qquad \text{Eqn.6.5}$$

where I_{beam} and E_{beam} are the electron beam current and the beam energy respectively. All efficiency results presented in the remainder of this section are directly comparable. The luminescence efficiency as a function of beam current is shown in Figure 6.9 for the unprocessed sample and the DE-sample. The following trends can be identified:

- The efficiency of both the unprocessed sample and DE-specimen increases with increasing beam current for all accelerating voltages investigated. The maximum efficiency was observed at the highest absorbed specimen current and highest beam energy.

- As the specimen absorbed current was increased the luminescence efficiency was found to saturate, though the greater the efficiency, the higher the absorbed specimen current before the onset of saturation.

- For an increase in absorbed specimen current from 2.5 to 30 nA (at 30 kV) the efficiency increased by 49% for the unprocessed sample and 20% for the DE-specimen. However, the percentage increase in efficiency between 2.5 and 30 nA was found to be dependent on accelerating voltage for the unprocessed specimen; ~34% increase at 10 kV, whereas the percentage increase in efficiency was independent of accelerating voltage in the DE-specimen.

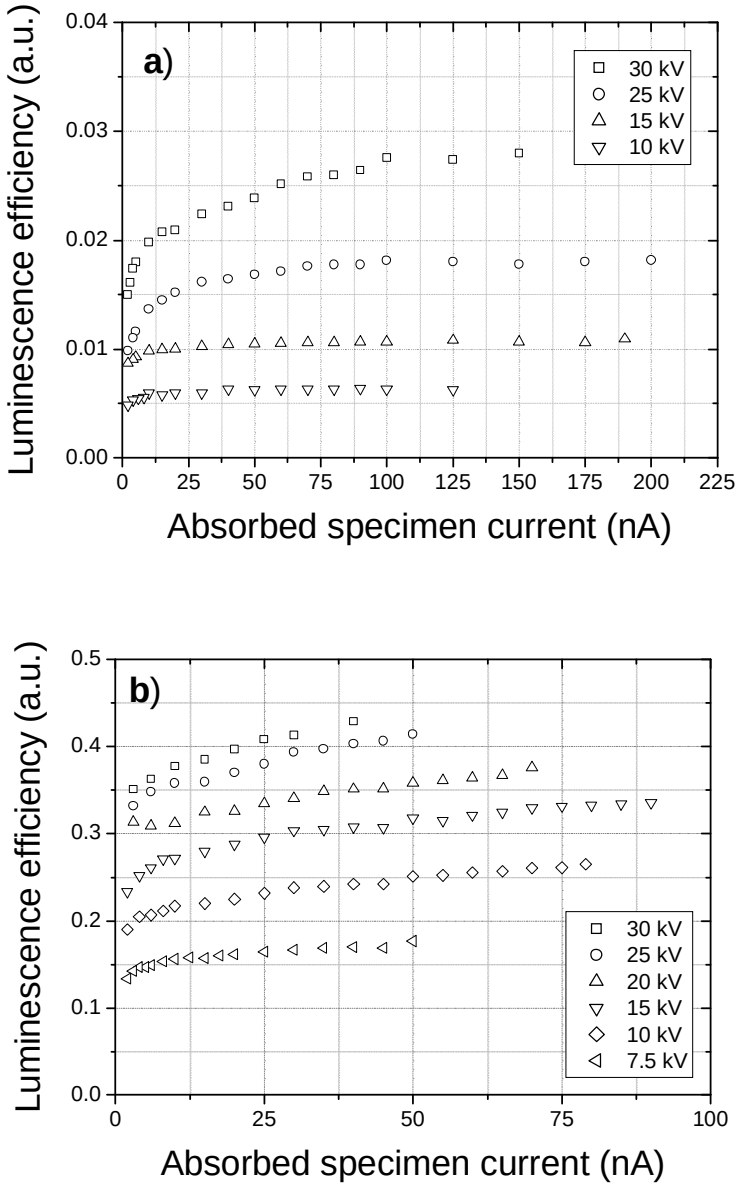

Figure 6.9

Luminescence efficiency as a function of the absorbed specimen for:

a) phosphorous doped, 10 Ωcm, unprocessed wafer
b) dislocation-engineered specimen nB2a (B, 30 keV, 10^{15} cm^{-2}, 900 °C, 15 mins).

[

The efficiency is calculated as the collected signal (a.u.) per generated carrier and the y-axes of a) and b) are directly comparable.

6.4.3 Cathodoluminescence as a function of incident beam energy

The luminescence efficiencies (luminescence intensity per generated carrier) of the unprocessed sample and the DE-specimen as a function of the accelerating voltage are shown in Figure 6.10a, for a beam current of 10 nA. In order to ensure that the low excitation regime was maintained during the experiment, a defocused electron beam (diameter ~ 20 μm) was used.

In both the DE-specimen, and the unprocessed wafer, an increase in the electron beam energy resulted in an increase in the luminescence efficiency. The unprocessed sample showed an increasing rate of change in the luminescence efficiency with increasing electron beam energy, whereas, the DE-specimen exhibited a significant increase in efficiency between 5 and 15 keV and a further more moderate increase in efficiency between 15 and 30 keV. The luminescence efficiencies of the DE- specimen and the unprocessed wafer as a function of the Gruen range are also shown in Figure 6.10b and 6.10c respectively. In the case of the DE-specimen, a relationship similar to that described for the dependence on the accelerating voltage was observed. However, the unprocessed wafer was found to display an approximately linear relationship between the efficiency and the Gruen range.

6.5.4 Discussion

It was observed that the luminescence efficiency was independent of the electron beam diameter, and hence the carrier concentration in the generation volume. This has two significant implications: firstly, the rate of Auger recombination within the generation volume is minimal and secondly, there is no change in the excitation regime in which photons are generated. The rate at which electron-hole pairs diffuse from their point of generation is sufficiently large that the rate of Auger

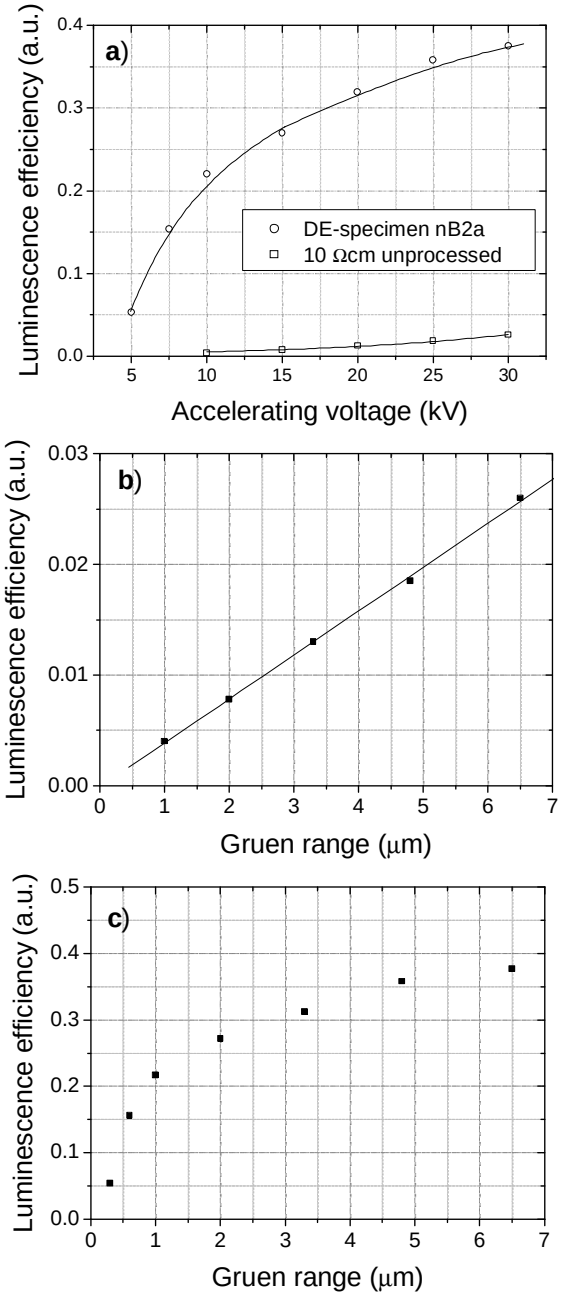

Figure 6.10

a) Luminescence efficiency as a function of the electron beam voltage for dislocation-engineered sample nB2a and an unprocessed sample

b) Luminescence efficiency as a function of the Gruen range for an unprocessed sample.

c) Luminescence efficiency as a function of the Gruen range for DE-specimen nB2a

Specimen nB2a: B, 10^{15} cm^{-2}, 900 °C, 15 mins; unprocessed specimen: phosphorous doped, 10 Ωcm, as-received wafer. Beam current = 10 nA.

recombination is not significant throughout the bulk of the specimen and photons are not generated in the high excitation regime (*i.e.* the carrier concentration is lower than the background doping level).

The luminescence intensity was found to be super-linear with the absorbed specimen current for both the DE-specimen and the unprocessed wafer, indicative of an increasing QE with increasing input power. The MQE of the DE-specimen increased from 9.7×10^{-7} to 1.2×10^{-6} as the absorbed specimen current was increased from 3 to 40 nA, at a beam energy of 30 keV. The increase in efficiency was observed to saturate for both the unprocessed sample and for the DE-specimen, though a larger absorbed specimen current was required before the onset of saturation in the DE-specimen. This is typical of luminescence results (see for example Green *et al*., 2001) in the low excitation regime. For an accelerating voltage of 30 kV, the collected signal from the DE-specimen was found to saturate the detector at beam currents in excess of 40 nA. However, a beam current of 200 nA and beam energy of 30 keV was typically used for monochromatic investigations. The MQE under these conditions is estimated to be $\sim 2 \times 10^{-6}$.

The reduction in the luminescence efficiency with the reduction of the incident beam energy was observed for both the unprocessed and DE-samples. The linear trend of the reduction as a function of the Gruen range in the unprocessed sample is most likely to be due to the increased surface recombination rate as carriers are generated in closer proximity to the specimen surface. However, the DE-specimen exhibits a large reduction in efficiency, particularly at energies less than 10 keV. This reduction is in excess of that observed for the unprocessed sample, suggesting an additional increase in the rate of non-radiative recombination beyond that expected simply due to surface recombination.

This suggests that the proposed model of Ng *et al.* (2001) for the high luminescence efficiency of DE-silicon of efficient luminescence from the region of material between the dislocation band and the *p-n* junction is unlikely to be correct. If the proposed model were to be correct an increase in the luminescence efficiency would be expected when a high concentration of carriers is injected directly into this region of the sample rather than deeper into the specimen bulk; this is not observed experimentally.

6.5 Summary and conclusions

Cathodoluminescence was used to investigate unprocessed, as-received, phosphorous doped (10 Ωcm) wafers and a single DE-silicon wafer; specimen nB2a. Weak TO phonon-assisted luminescence (MQEs less than 6.4×10^{-8}) with a peak in the spectra at ~1140 nm was observed from some of the unprocessed wafers. In comparison to the literature and theory the peak wavelength was red-shifted by ~10 nm; this was attributed to the effect of photon re-absorption through a distance of ~200 μm. In the other wafers, no detectable luminescence was observed.

Relatively strong luminescence (MQE ~2.0×10^{-6}) with a peak in the spectrum at ~1150 nm was observed from the DE-sample. The luminescence peak was found to recreate the luminescence peak of Ng *et al.* (2001), though a difference in the FWHMs was observed. When the effects of collection geometry and photon re-absorption were considered, the luminescence peak observed by Ng *et al.* (2001) was shown to be consistent with TO phonon-assisted recombination. Analysis of the DE-sample investigated in this work shows that luminescence via TO phonon-assisted

recombination and the proposed mechanism of Ng *et al*. (2001) for efficient luminescence from DE-silicon are incompatible.

The MQEs of unprocessed and DE-silicon samples investigated in this work by CL were found to be significantly lower than the EQEs of similar samples in the literature which were investigated by EL. However, the MQE of a gallium arsenide sample investigated in this work by CL was found to be consistent with EL EQEs from the literature. The lower MQEs of silicon samples were attributed to the long diffusion lengths of the samples reducing the collection efficiency of the system and increasing the rate of non-radiative surface recombination.

The luminescence efficiency of an unprocessed and DE-specimen nB2a were investigated as a function of the microscope conditions and was found to be independent of the carrier concentration in the generation volume in the rage of ~10^{12} to 5 x 10^{18} cm^{-3}. It was deduced that the effect of Auger recombination in the generation volume was negligible and that recombination occurs in the low excitation regime. The luminescence efficiencies were found to increase with increasing electron beam energy and increasing specimen absorbed current, though the efficiency was found to saturate with increased specimen absorbed currents. The luminescence efficiency of the unprocessed specimen was found to display a linear dependence on the distance at which electron-hole pairs were generated. However, in the DE-specimen nB2a the luminescence efficiency was observed to be significantly lower when carriers were generated close to the dislocation band compared to deeper in the specimen. This suggests that the mechanism for enhanced luminescence from DE-silicon is not associated with the generation of photons from between the dislocation band and the *p*-*n* junction.

Chapter 7

Understanding and improving the luminescence efficiency of dislocation-engineered silicon

7.1 Introduction

In this chapter the experiments to determine the mechanism of efficient near band-edge luminescence from DE-silicon are reported and discussed. A survey of the luminescence efficiencies of a range of silicon wafers which contain extended defects is presented and cross-sectional luminescence profiles of DE-silicon samples are used to understand electron-hole pair recombination paths in DE-silicon. This improved understanding of DE-silicon allows the design of experiments to improve the efficiency yet further. Low-temperature annealing in the dark, and under white light illumination, are used and, for the first time, shown to improve the luminescence efficiency of DE-silicon.

7.2 Experiments to determine the mechanism of efficient luminescence from dislocation-engineered silicon

In the following section an investigation of the mechanism for efficient luminescence from DE-silicon is described. This was performed by determining the influence of: i) the *p-n junction* - by comparison of DE-samples containing identical dislocation structures, with or without a *p-n* junction, ii) the *band of dislocations* – removed by high-temperature thermal annealing and iii) the *band of dislocations* and *the highly doped region* – removed by room-temperature chemical etching.

7.2.1 Investigation of a dislocation-engineered sample with no *p-n* junction

Sample pB2a, formed using identical processing conditions as the DE-sample investigated in Chapter 6, but with a *p*-type substrate, was found also to produce enhanced luminescence compared to similarly doped, unprocessed specimens. The spectrum was identical in form to that observed for sample nB2a (Chapter 6), see

Figure 7.1, and the MQE was estimated to be ~1.8 x 10^{-6} compared to a value of 2.0 x 10^{-6} for the specimen processed in an identical manner but containing a *p-n* junction.

7.2.2 Investigation of dislocation-engineered samples where the dislocation loops were removed by high-temperature annealing

Specimen nB2a, pB2a and an unprocessed (0.5 Ωcm) sample were all annealed at 1150 °C for five minutes, using the procedure outlined in Section 4.2.3. At this temperature, all dislocations are annealed from the specimen (Jones and Rozgonyi, 1993), this was confirmed by the use of a defect revealing etch on samples prior to, and after, annealing.

After annealing no detectable luminescence could be observed from the samples which previously contained a band of dislocation loops. However, no change in the luminescence efficiency of the unprocessed sample was observed, see Figure 7.1. In this case, the estimated MQE was ~3.2 x 10^{-7} both prior to, and after, annealing at 1150 °C.

7.2.3 Investigation of dislocation-engineered samples where the dislocation loops and the *p-n* junction were removed by chemical etching

The band of dislocations, the highly doped region and the *p-n* junction (if present) of samples nB2a and pB2a were removed by chemical etching at room temperature. A maximum of 50 μm of material was removed. The chemical etching process has been described previously in Section 4.3.2.

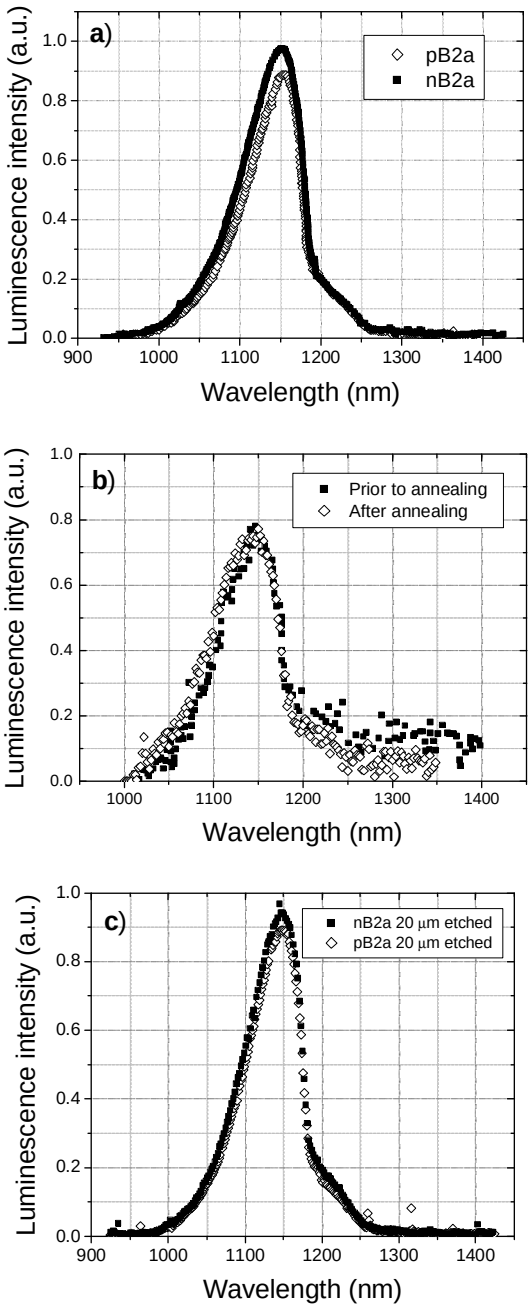

Figure 7.1

Room temperature luminescence spectrum, I_{beam} = 200 nA, E_{beam} = 30 keV, dwell time 2 secs and monochromator slit widths of 1.5 mm from:

a) dislocation-engineered specimen pB2a (*p*-type substrate, processing: B, 30 keV, 1 x 10^{15} cm^{-2}, 900 °C for 15 mins)

b) unprocessed 0.5 Ωcm sample prior to, and after annealing at 1150 °C for 5 mins

c) specimen nB2a (*n*-type substrate, processing: B, 30 keV, 1 x 10^{15} cm^{-2}, 900 °C for 15 mins) and pB2a ~20 μm removed by chemical etching.

In both samples strong luminescence was observed after chemical etching. The luminescence efficiency as a function of the thickness of material removed is shown in Figure 7.2. Spectra were taken and found to be identical in peak position and form as to when no material had been removed (see Figure 7.1). A small increase in luminescence efficiency was observed once the dislocations and high boron concentration (pB2a) or the dislocations, high boron concentration and *p-n* junction (nB2a) were removed, before small decreases in efficiency were observed as further material was removed. Data was unattainable for samples with 0.25 to 10 μm removed due to surface pitting as a result of the etching process. The luminescence efficiency of an unprocessed sample (5 Ωcm) was found to be unaffected by the etching process.

7.2.4 Discussion

The luminescence spectrum was observed to be identical in form prior to and after the dislocation loops and the highly boron doped region of DE-specimens nB2a and pB2a were removed by chemical etching. This confirms that the luminescence mechanism of DE-silicon is TO phonon-assisted free carrier recombination, observed in bulk silicon (Davies, 1989).

The *p-n* junction was observed to have little effect on luminescence efficiency as DE-samples with and without *p-n* junctions exhibit comparably strong luminescence efficiencies, with spectra of identical form. The enhanced luminescence efficiency was observed to persist to depths of at least 60 μm after the removal of the dislocation band and highly boron doped region and, if present, the *p-n* junction. The experimental results show that enhanced luminescence efficiency of DE-silicon is not directly due to: the region of material between the dislocation band

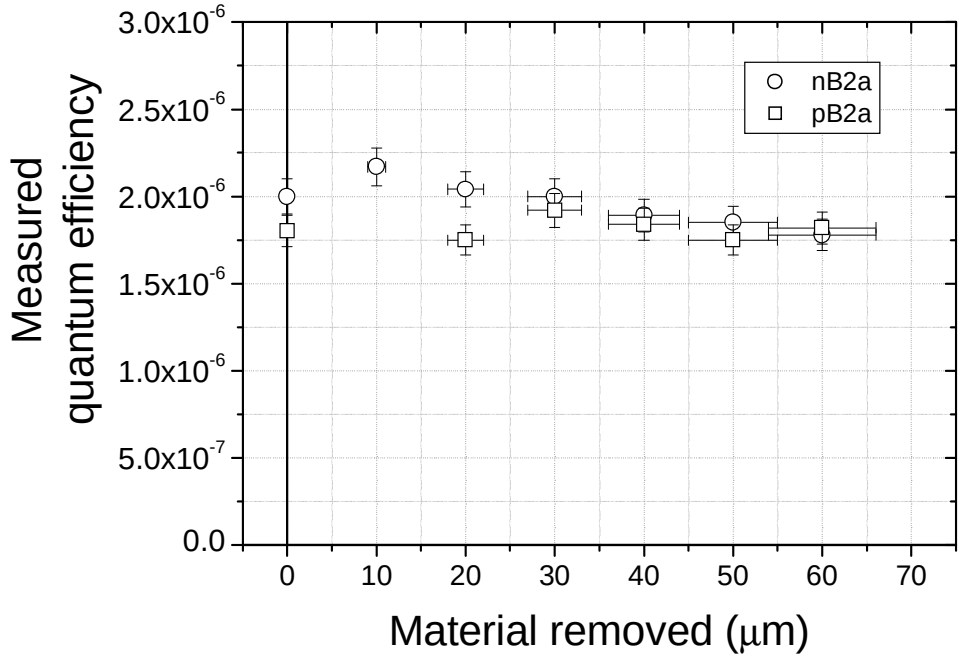

Figure 7.2

Measured quantum efficiencies of samples nB2a and pB2a (*n*- and *p*-type substrates respectively, B implanted, 10^{15} cm^{-2}, 900 °C for 15 mins) as a function of the thickness of material removed by room temperature chemical etching. Accelerating voltage = 30 kV, beam current = 50 nA.

and the *p-n* junction (as suggested by Ng *et al.* (2001)), the dislocation band itself or, the proximity of the *p-n* junction. However, it is clear that the dislocation band plays a critical role in the enhanced luminescence mechanism, as shown by the quenching of the luminescence efficiency when the dislocations were removed from the sample by annealing at 1150 °C.

The results may be explained in terms of the gettering of transition metals to the dislocation loops during the production of DE-silicon. Transition metals present in the bulk produce deep electronic levels which act as strong non-radiative recombination centres (with behaviour described by the Shockley-Read-Hall (SRH) equation described in Section 1.2). By the gettering of these impurities to the near-surface region, and hence the removal of these defects from the bulk, the non-radiative lifetime is increased and consequently the efficiency of TO phonon-assisted band-to-band radiative recombination increases.

When the near-surface region of the material is removed at room temperature by chemical etching, the dislocations, the highly doped region and the decorating impurities are removed without redistributing the impurities. Thus, the concentration of deep levels in the bulk remains low, even in the absence of dislocations and the luminescence enhancement is retained. However, when the dislocations are removed by high-temperature annealing, the gettering action is lost as the solid solubility of the impurity species rises allowing impurities to 'boil-off' the dislocations and re-enter the specimen bulk in solid solution. Thus on cooling, a substantial metal impurity concentration is again present in the bulk and the enhanced radiative recombination, originally produced by the action of the dislocations, is removed.

The change in the transition metal concentration in the specimen bulk may be estimated using the following analysis assuming that SRH recombination is the dominant bulk recombination mechanism and that low excitation conditions are used:

$$CL \propto R_{rad} = \frac{\Delta p}{\tau_{rad}} \qquad \text{Eqn.7.1}$$

$$\Delta p = \frac{G}{\tau_{total}} \qquad \text{Eqn. 7.2}$$

$$\frac{1}{\tau_{total}} = \frac{1}{\tau_{non-rad}} + \frac{1}{\tau_{rad}} \approx \frac{1}{\tau_{non-rad}} \qquad \text{Eqn. 7.3}$$

$$CL \propto \frac{G}{\tau_{rad}\tau_{non-rad}} \propto \frac{1}{N_T} \qquad \text{Eqn. 7.4}$$

where CL is the collected luminescence signal, R_{rad} is the rate of radiative recombination, Δp is the excess minority carrier concentration, τ_{rad} is the radiative recombination lifetime (fixed by the luminescence mechanism), G is the carrier generation rate per second (fixed by the microscope conditions), τ_{total} is the total recombination lifetime, $\tau_{non\text{-}rad}$ is the non-radiative recombination lifetime and N_T is the concentration of impurity centres.

The luminescence efficiency of a DE-sample after the dislocation loops were removed by room temperature chemical etching was found to be ~20 times greater than for a similarly doped, unprocessed wafer. Remarkably, following Eqn. 7.4, this suggests that the processing carried out in this investigation actually creates silicon

wafers with a lower transition metal concentration than of the highest device quality material as-received from the manufacturers. The removal of the dislocation band, and the gettered impurities, by chemical etching implies that an extended defect-free, silicon wafer with an electrically active defect level ~20 times lower than industry standard is created.

This interpretation is consistent with the reports of Sobolev *et al.*, (2003) and Arguirov *et al.*, (2005) who both propose that the enhanced luminescence efficiency of DE-silicon is as a result of the gettering of impurities from the wafer bulk. An identical system using boron implantation into 400 Ωcm phosphorous doped substrates has been studied by the Sobolev *et al.* (2003 and 2004). In contrast to the observations of the work reported in this thesis, the peak luminescence efficiency was observed after thermal annealing at 1100 °C, at which temperature dislocations are dissolved and none could be observed by TEM or preferential chemical etching. However, in common with the conclusions drawn by the author of this thesis, the results are tentatively explained as related to the gettering of the non-radiative recombination centres and/or the introduction of new recombination centres rather than the spatial confinement of carriers. However, the influence of gettering (in the work of Sobolev's group) does not fully explain their results. The observation of peak efficiency when no dislocations are present in the sample contradicts the suggested mechanism.

The case of phosphorous implantation into a *p*-type substrate has been investigated by the group of Kittler (Arguirov *et al.*, 2004 and Arguirov *et al.*, 2005) who also suggest that the gettering of electrically active defects is the mechanism of enhanced luminescence from DE-silicon. This was further demonstrated by the investigation of a sample thinned from the back (un-implanted) side by ion milling

resulting in a sample of varying substrate thickness (Arguirov *et al*., 2005). It was shown that the luminescence was largely generated in the specimen bulk rather than in the region of material between the *p*-*n* junction and the dislocations. The results of Kittler's group are entirely consistent with those reported in this thesis.

However, there are reports in the literature of similar systems that produce different although not inconsistent results. Indeed Hoang *et al.* (2006) report that the presence of dislocations is detrimental to the luminescence efficiency of DE-silicon. This can be explained by assuming that in these specimens the increase in the non-radiative recombination, associated with the implanted dislocation loops, is greater than the reduction in non-radiative recombination in the bulk by gettering.

Sun *et al.* (2003 and 2004) report the observation of a spectrum of similar form to Ng *et al*. (2001), and that observed in this work, at room temperatures. However, two extra luminescence bands with maxima around 1.05 and 0.95 eV are observed at temperatures less than 80 and 260 K respectively. The additional peaks observed were suggested to be related to the formation of *p*-type doping spikes and, at room temperature, these doping spikes act as reservoirs of excitons which are released as free electron-hole pairs where they can then contribute to efficient band-edge recombination. The doping spikes may explain the low-temperature additional luminescence peaks; however, it is unclear that the proposed mechanism would produce efficient room-temperature luminescence, which may be explained by the action of gettering as demonstrated in the present work and as proposed by Sobolev *et al*. (2003) and Arguirov *et al*. (2004). Furthermore, the presence of doping spikes is not important in the work reported in this thesis, as efficient luminescence is observed (and increased) after the removal of the near-surface layer (dislocation loops and

highly doped region) by room temperature chemical etching, thus removing any doping spikes present.

7.3 The relationship between luminescence efficiency and the dislocation and doping parameters

The following section details the luminescence efficiencies of all the samples investigated. Firstly, samples which contained intentionally introduced dislocations and unprocessed, as-received wafers are reported. The processing conditions were described in detail in Chapter 4. The variation in the luminescence of boron DE-specimens with various implant doses, *p*-type substrates and silicon DE-specimens as a function of the microscope conditions is investigated. In order to understand the luminescence efficiency variation within the thickness of the wafers, selected samples are also investigated using the cross-sectional CL technique described in Chapter 4.

7.3.1 Luminescence efficiencies of various samples containing dislocations

7.3.1.1 Boron implanted specimens

All specimens implanted with boron and annealed at 900 or 1000 °C were found to exhibit relatively strong luminescence, with spectra of the form observed for sample nB2a, investigated in Chapter 6. The MQEs were estimated to range between 1.1×10^{-6} and 3.8×10^{-6} and are shown in Figure 7.3. A variation in the luminescence efficiency of less than 10% was observed across each wafer. The maximum efficiency observed was a factor of ~2 greater than the sample investigated in

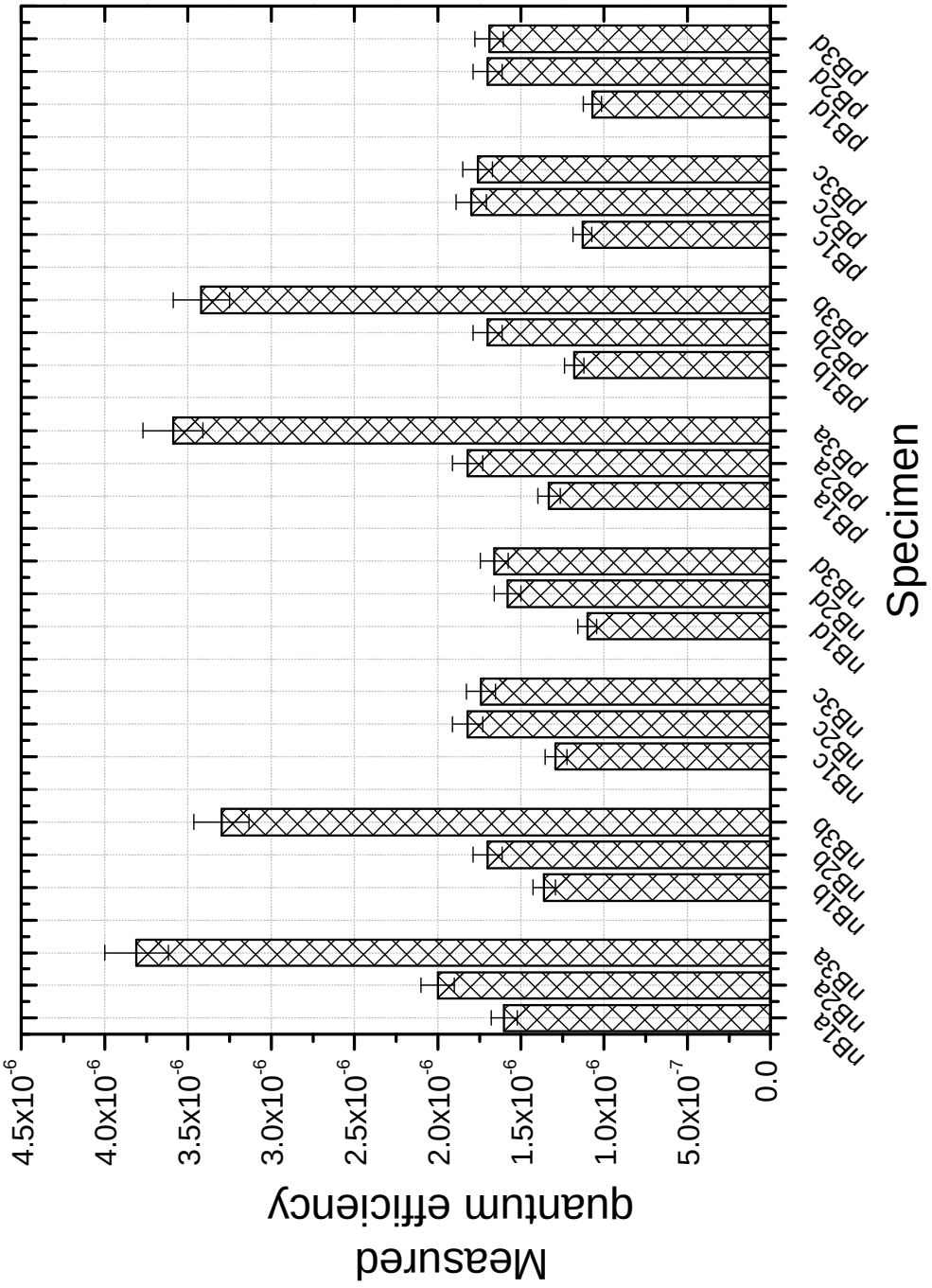

Figure 7.3

Measured quantum efficiency survey of all the boron implanted and annealed specimens. Accelerating voltage = 30 kV and beam current = 200 nA. Full specimen processing conditions may be found in Chapter 4.

Chapter 6, which had been processed in a similar manner to that investigated by Ng *et al.* (2001).

In summary, the following trends were observed:

- Samples with an *n*-type substrate were largely found to be more efficient than those with a *p*-type substrate for similar processing conditions, though the difference was often less than 10%
- Samples with increased annealing times and temperatures were found to display reduced MQEs. For example: sample nB3a (annealed at 900 °C) was found to be >50% more efficient than sample nB3c (annealed at 1000 °C)
- An increased implantation dose was observed to result in increased MQE for the same annealing conditions: 1.6×10^{-6} to 2.0×10^{-6} to 3.8×10^{-6} for an increase in dose from 5×10^{14} to 1×10^{15} to 1×10^{16} cm^{-2} - samples nB1a, nB2a and nB3a respectively.

The influence of the dislocation density on the MQE of all boron implanted samples is displayed in Figure 7.4. An approximately linear increase in efficiency was observed when the dislocation density is plotted on a logarithmic scale.

The back side of the boron implanted DE-samples was also investigated. MQEs in the range of 3.0×10^{-7} to 3.3×10^{-7} were observed for all samples investigated and no strong correlation with the implantation and annealing conditions was observed.

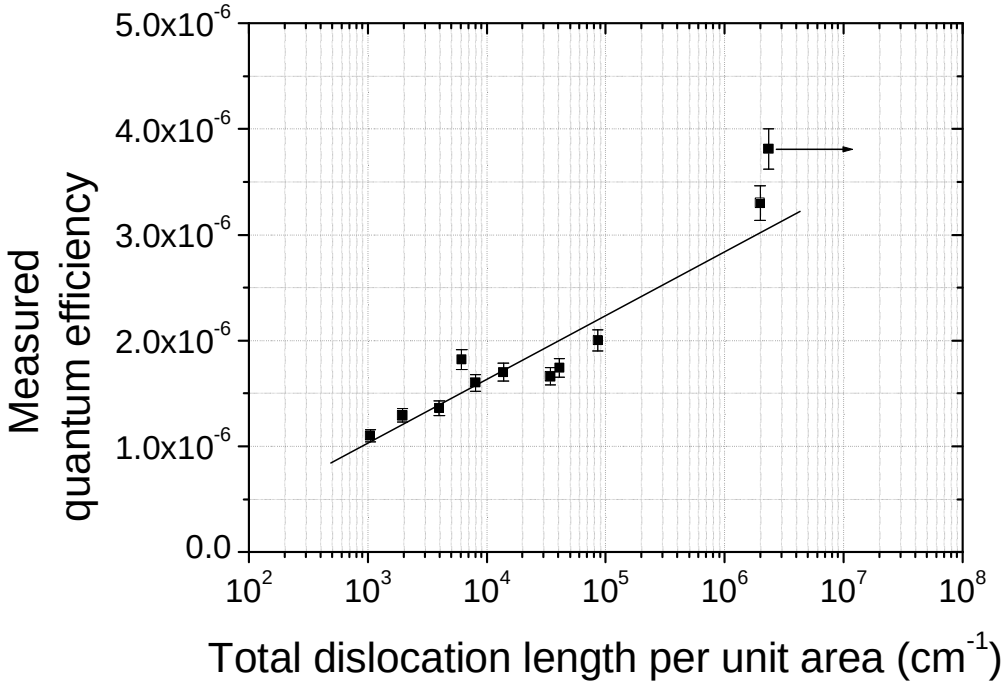

Figure 7.4

Plot of the measured quantum efficiency of boron implanted, *n*-type substrate specimens as a function of the dislocation density per unit area (as measured directly from the TEM investigation). Efficiency determined at 30 kV and 200 nA. Note: the total dislocation density of specimen nB3a was too high to be measured accurately but was estimated to be greater than 2.4 x 10^6 (cm^{-1}). This is represented on the graph by a point showing the lower limit of the dislocation density and an arrow indicating the direction of shift in the point's position. The linear best-fit line was made without considering sample nB3a.

7.3.1.2 Silicon implanted specimens

All specimens implanted with silicon ions were found to exhibit relatively weak luminescence. The MQEs were estimated to be in the range 5.8 x 10^{-8} to 9.5 x 10^{-8}, the results are shown in Figure 7.5. The silicon implanted samples with an *n*-type substrate were found to be more efficient than those with a *p*-type substrate, though the difference was observed to be less than 10%.

In contrast to the boron implanted samples, the MQE for silicon implanted samples (with both *n*- and *p*-type substrates) was observed to increase with a decrease in the dislocation density (*i.e.* an increased annealing time), Figure 7.6.

The back side of the silicon implanted DE-samples was also investigated. An MQE of ~1.9 x 10^{-7} was observed for all samples investigated and no strong correlation with the annealing conditions was observed.

7.3.1.3 Gallium implanted specimens

The two specimens implanted with gallium ions over an area of ~250 μm^2 using the FEI FIB 200 were found to emit weak luminescence with an MQE of only ~3 x 10^{-8}, shown in Figure 7.7. This was less efficient than the surrounding regions of the sample which had not been implanted.

7.3.1.4 Silicon wafers with dislocations not generated by ion implantation

The luminescence efficiencies of samples containing dislocations created by techniques other than ion implantation are presented in Figure 7.7. All specimens containing near surface-dislocations (OISF and abraded samples) were observed to emit relatively weak luminescence (MQEs ~1 x 10^{-7} to 3 x 10^{-7}) whereas, no

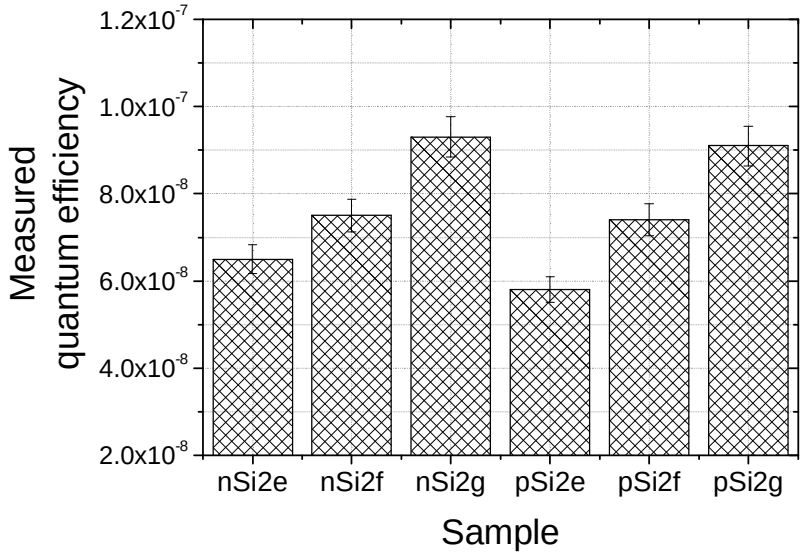

Figure 7.5

Survey of the measured quantum efficiencies of all silicon implanted specimens. Accelerating voltage = 30 kV and beam current = 200 nA. Full specimen processing conditions may be found in Chapter 4.

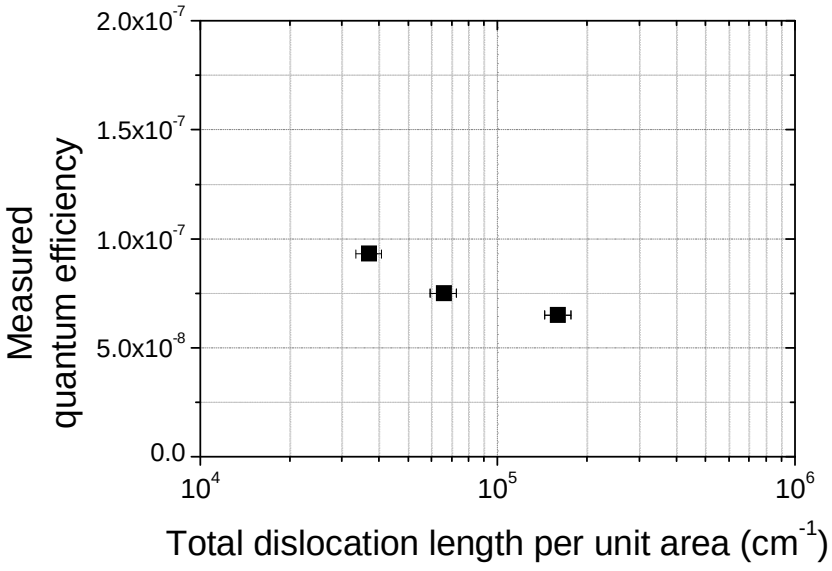

Figure 7.6

The measured quantum efficiency of silicon implanted specimens with *n*-type substrates as a function of the dislocation density (as measured directly from the TEM investigation). Accelerating voltage = 30 kV and beam current = 200 nA.

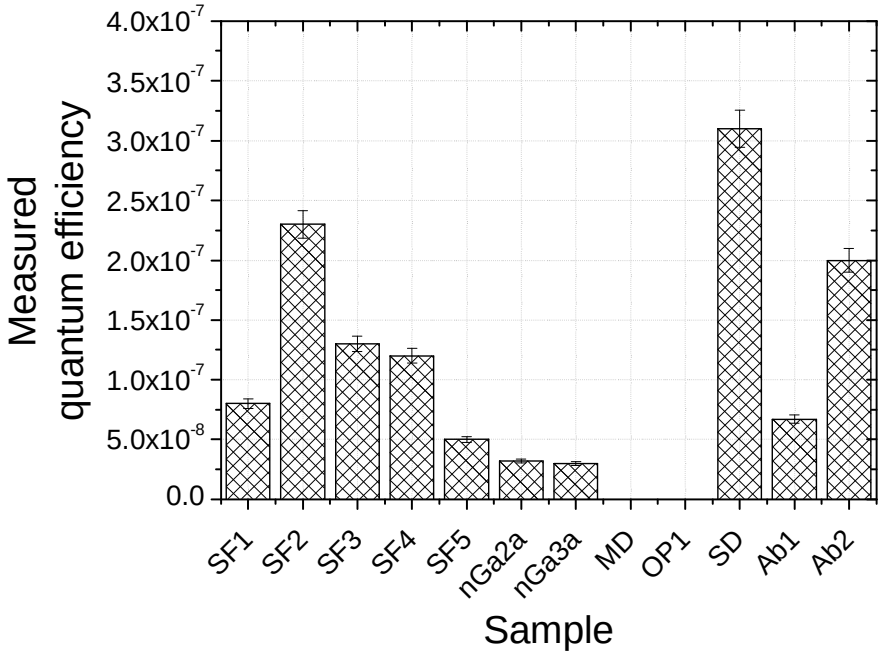

Figure 7.7

Survey of the measured quantum efficiencies of silicon samples containing dislocations not created by boron or silicon implantation. The sample codes are outlined below:

SF1 – B, 10 Ωcm (1.2 x 10^{15} cm^{-3}), OISF

SF2 – Sb, 10-20 mΩcm (4 x 10^{18} cm^{-3}), OISF

SF3 – B, 10 mΩcm (9 x 10^{18} cm^{-3}), OISF

SF4 – As, 1-5 mΩcm (1 x 10^{19} cm^{-3}), OISF

SF5 – P, 1-2 mΩcm (4 x 10^{18} cm^{-3}), OISF

nGa2a – Ga 10^{15} cm^{-2}, 900 ºC 15 mins

nGa3a – Ga 10^{16} cm^{-2}, 900 ºC 15 mins

MD – Mech. deformed, 5 Ωcm (3 x 10^{15} cm^{-3})

OP1 – Oxygen precipitate, 100 Ωcm (1 x 10^{14} cm^{-3})

SD – Saw damaged or swirl defect FZ (5 Ωcm 1 x 10^{15} cm^{-3})

Ab1 – Abraded, B, 5 Ωcm (3 x 10^{15} cm^{-3})

Ab2 – Abraded, B, 10 mΩcm (9 x 10^{18} cm^{-3}).

Full processing conditions may be found in Chapter 4.

detectable luminescence could be observed for the mechanically deformed and oxide precipitate samples.

In the samples containing near-surface dislocations, no correlation between dislocation density and the luminescence efficiency was observed. For example, the OISF specimens (SF1, SF2, SF3, SF4 and SF5 in Figure 7.7) all contained identical dislocation densities yet the luminescence efficiency varied by a factor of ~3.

7.3.1.5 Unprocessed silicon wafers

The luminescence efficiency of unprocessed, as-received wafers as a function of the doping concentration is shown in Figure 7.8. A peak in efficiency is observed at a carrier concentration of ~1 x 10^{16} and between 2 x 10^{16} and 3 x 10^{17} cm^{-3} for unprocessed *n*- and *p*-type wafers respectively. Unfortunately, no *p*-type wafers with a doping level between 2 x 10^{16} and 3 x 10^{17} cm^{-3} could be sourced for the investigation. The efficiency of unprocessed wafers was, in all cases, lower than that observed for all the boron implanted DE-silicon samples (bulk carrier concentration ~6 x 10^{14} cm^{-3}, measured using the four point probe technique).

7.3.1.6 Unprocessed wafer with surface passivation

A single antimony doped wafer (10-20 mΩcm, 4 x 10^{18} cm^{-3}) was investigated with a thermally grown oxide ~100 nm thick. The luminescence efficiency was observed to be 40% lower when the thermal oxide was removed by a hydrofluoric acid dip, for accelerating voltages in the range of 5 to 30 kV. No luminescence signal could be detected at accelerating voltages below 5 kV. The value for this specimen plotted on Figure 7.8 relates to the efficiency measured after removal of the oxide layer.

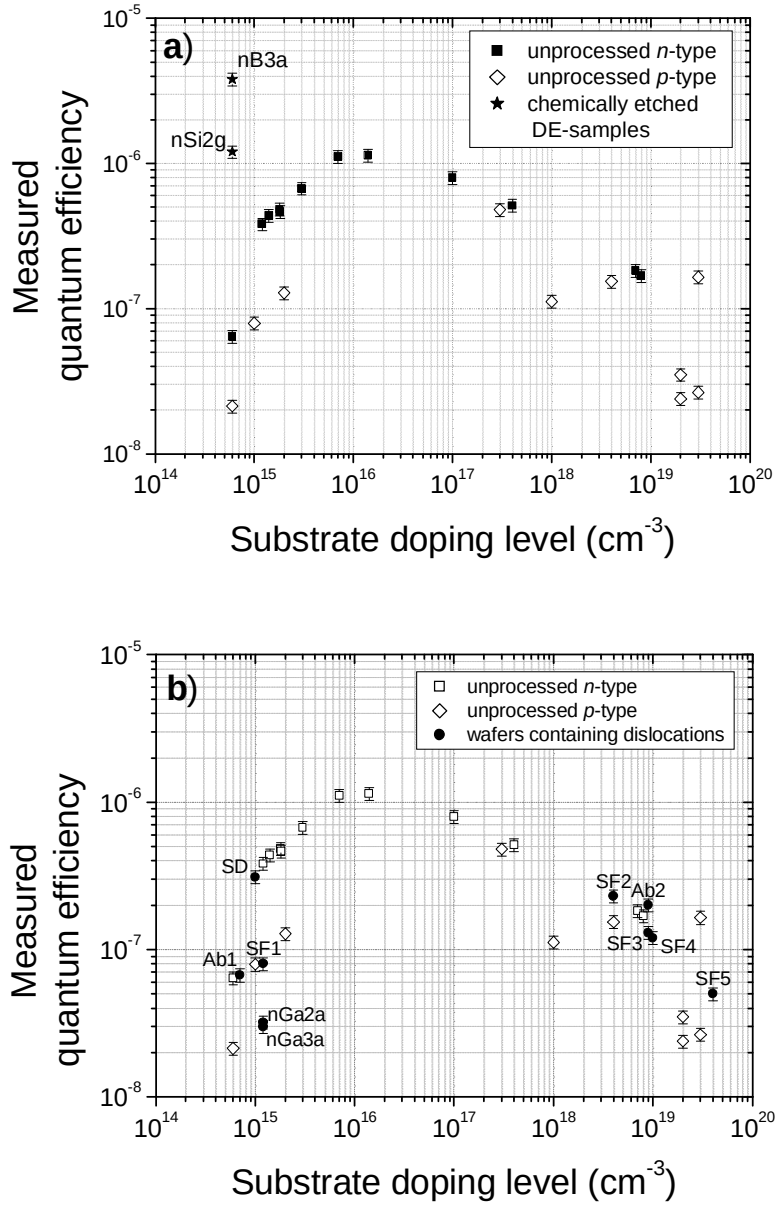

Figure 7.8

Plot of the measured quantum efficiency of unprocessed, as received, wafers as a function of the doping level including: a) dislocation-engineered samples nB3a (B, 10^{16} cm^{-2}, 900 ºC, 15 mins) and nSi2g (Si, 10^{15} cm^{-2}, 900 °C, 120 mins) after removal of the band of dislocations by chemical etching and b) silicon wafers which contain dislocations, data labels refer to the sample code described in full in Figure 7.7. Accelerating voltage 30 kV and beam current 200 nA.

7.3.1.7 Dependence of luminescence on microscope conditions

The dependence of the luminescence efficiency on various microscope conditions was investigated in Chapter 6 for an unprocessed silicon sample and a single DE-specimen, sample nB2a. DE-specimens with *p*-type substrates were observed to display similar luminescence dependencies on the beam current, electron beam diameter and accelerating voltage to sample nB2a. The following section describes the variation in efficiency of the luminescence on the microscope conditions for DE-specimens with a varying boron dose and silicon, rather than boron, implantations.

Implant dose: The variation in the normalised luminescence efficiency with the incident electron beam energy for samples nB1a, nB2a and nB3a is displayed in Figure 7.9. The samples have identical annealing conditions and differ only in the boron dose received. The highest dose sample (nB3a) showed the largest reduction in efficiency and the lowest dose (nB1a) the lowest reduction in efficiency as the accelerating voltage is reduced from 30 kV.

Implant species: For the silicon implanted samples the luminescence efficiency was observed to be dependent on the excess carrier concentration produced in the generation volume when investigated using a stationary electron beam. The carrier concentration was altered by defocusing the electron beam as described in Section 6.3.1. This dependence is shown in Figure 7.10 where an increased carrier concentration from ~10^{15} to ~5 x 10^{17} cm^{-3} was found to result in almost an order of magnitude increase in the MQE.

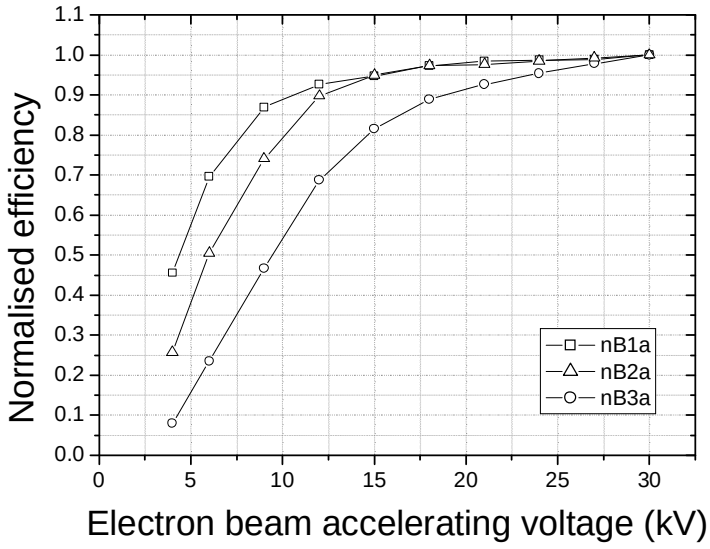

Figure 7.9

Normalised luminescence efficiency as a function of the electron beam accelerating voltage for boron implanted samples nB3a (10^{16} cm^{-2}), nB2a (10^{15} cm^{-2}) and nB1a (5 x 10^{14} cm^{-2}) annealed at 900 °C for 15 mins. Beam current = 100 nA.

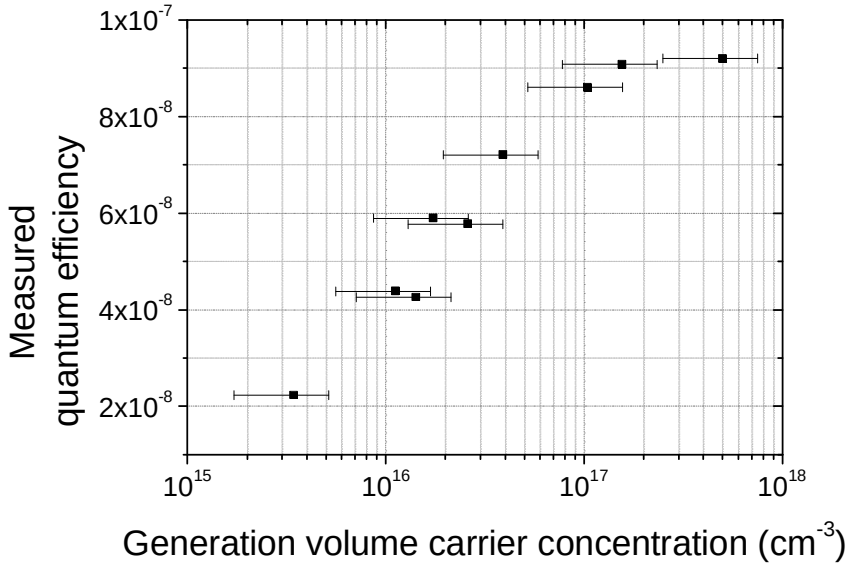

Figure 7.10

Measured quantum efficiency as a function of the carrier concentration in the generation volume for sample nSi2g (Si, 10^{15} cm^{-2}, 900 °C, 120 mins).

7.3.2 Removal of dislocations from a silicon implanted specimen

The effect of the dislocation loops on the luminescence efficiency of a silicon implanted specimen, sample nSi2g, was investigated by removing them from the sample by chemical etching at room temperature, using the method described in Section 4.4.

Removal of the dislocation band by chemical etching resulted in a large increase in the measured MQE: 8.1×10^{-7} with ~250 nm removed, compared to 9.5×10^{-8} for the original sample which still contained the dislocation loops, Figure 7.11. As further material was removed the MQE decreased before an approximately constant MQE of 5×10^{-7} is reached for specimens with greater than ~10 μm of material removed.

7.3.3 Cross-sectional investigations

Selected samples were analysed using the cross-sectional technique described previously in Section 4.5.2. The luminescence efficiencies as a function of the distance from the implanted surface were obtained from a 0.05 Ωcm, phosphorous doped, unprocessed sample, specimens nB1a, nB2a, nB3a and nSi2g. The results from these specimens are shown in Figures 7.12, 7.13, 7.14 and 7.15, the CL efficiencies are presented in arbitrary units which are directly comparable.

7.3.3.1 Unprocessed specimen

Figure 7.12 shows the cross-section CL profile of the unprocessed specimen. A symmetrical curve was observed with the central 200 μm displaying approximately uniform luminescence efficiency. As the implanted and back side of the wafer were

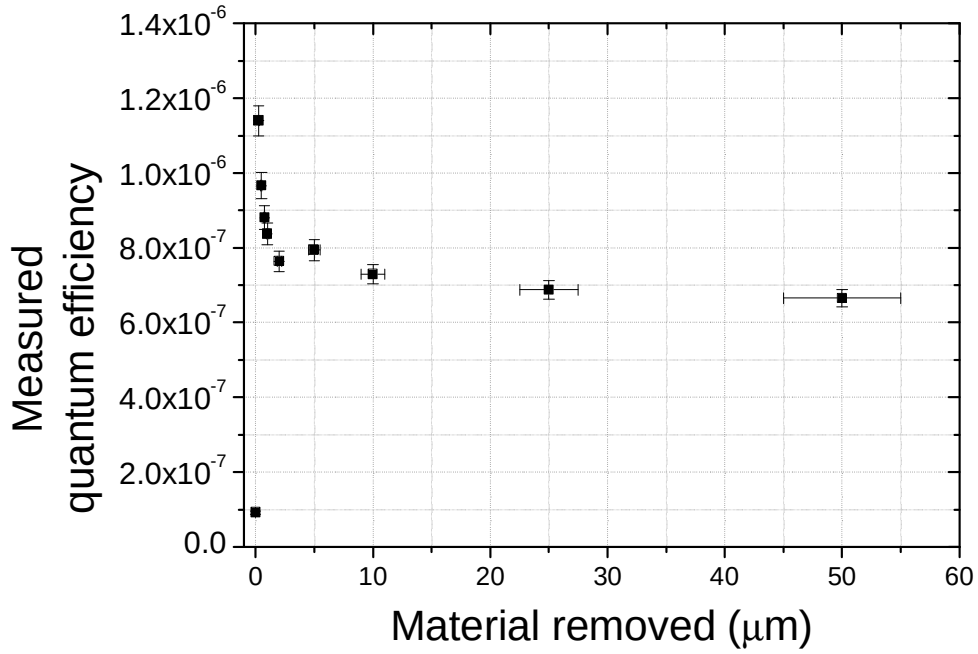

Figure 7.11

Measured quantum efficiency as a function of the thickness of material removed by room temperature chemical etching for sample nSi2g (Si, 10^{15} cm^{-2}, 900 °C, 120 mins). Accelerating voltage = 30 KV and beam current = 50 nA.

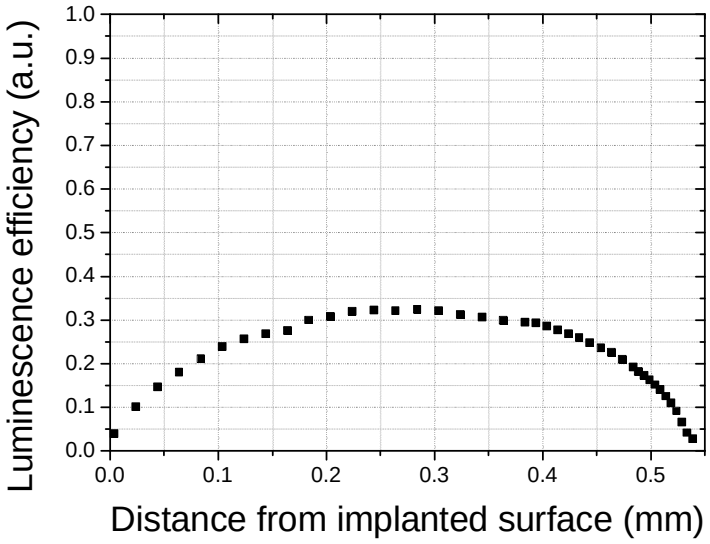

Figure 7.12

Luminescence efficiency cross-section profile of an unprocessed, 0.05 Ωcm, B doped wafer. Accelerating voltage 30 kV and beam current 50 nA.

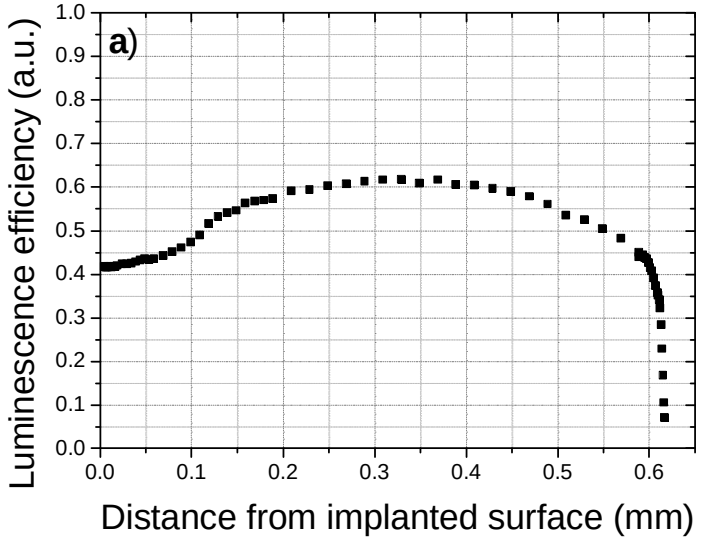

Figure 7.13

a) Luminescence efficiency cross-section profile of sample nB1a (Boron implanted 5 x 10^{14} cm^{-2}, annealed at 900 °C for 15 mins). Accelerating voltage = 30 kV and beam current = 200 nA.

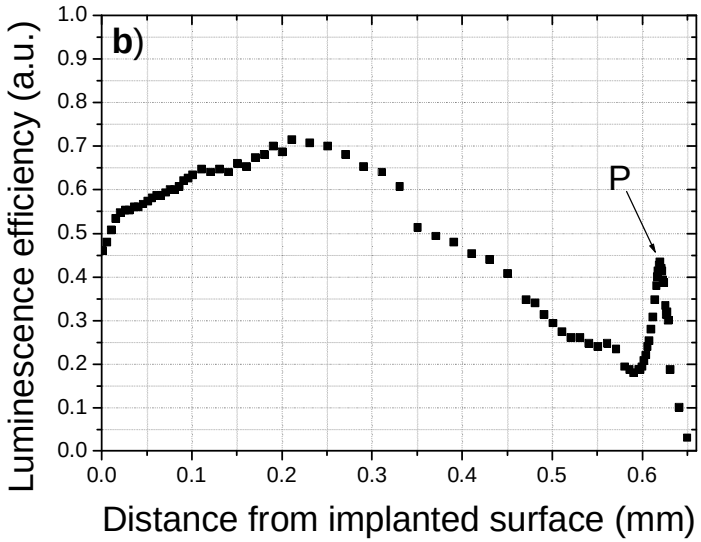

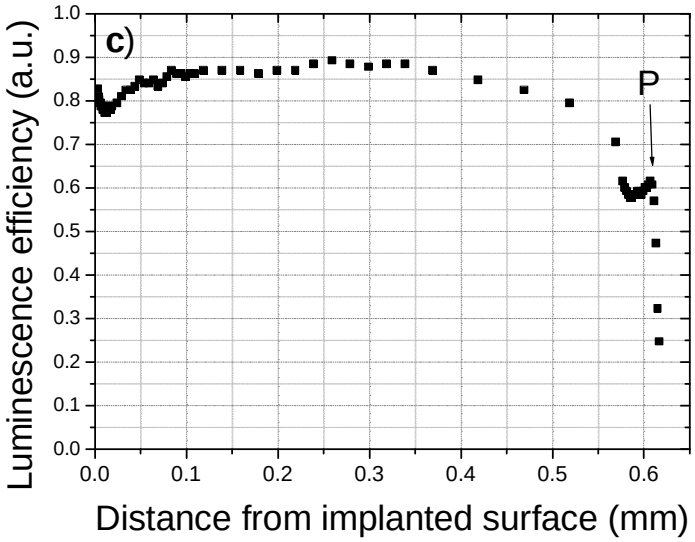

Figure 7.13 continued

Luminescence efficiency cross-section profiles of: b) sample nB2a (Boron implanted 1 x 10^{15} cm^{-2}, annealed at 900 °C for 15 mins) and c) sample nB3a (Boron implanted, 1 x 10^{16} cm^{-2}, annealed at 900 °C for 15 mins). Accelerating voltage = 30 kV and beam current = 50 nA.

approached the efficiency was observed to drop to a minimum, which was only ~5% of the efficiency observed at the wafer centre.

7.3.3.2 Dislocation-engineered specimens

Boron implanted specimens: For the three DE-specimens implanted with boron, the luminescence efficiency was observed to be higher throughout the entire wafer in comparison to the unprocessed sample (Figure 7.12) and showed a different trend; a large difference in efficiency between the material near the implantation induced dislocation loops and that near the SBD was observed, see Figure 7.13. The back surface showed reduced luminescence efficiency levels, typically only 0.5% of the maximum and the central portion of each wafer showed the maximum luminescence efficiency. A plateau in the luminescence efficiency was observed, with only a relatively small drop in efficiency close to the front surface of the wafer. The luminescence efficiency near the surface was 68, 76 and 90% of the maximum in sample nB1a, nB2a and nB3a respectively. In sample nB2a and nB3a a small peak in efficiency ~ 30 μm from the back surface was observed, labelled P in Figure 7.13.

In contrast to specimens nB1a and nB3a, the CL profile of sample nB2a (Figure 7.13b) displayed an approximately linear increase in the luminescence efficiency from the back side of the wafer to the maximum, located approximately at the wafer centre. The linear increase of the efficiency from near the back surface to the central portion of the wafer is thought to be due to poor specimen production: in this specimen, the chemomechanical polishing step is thought to be insufficient to completely remove the dislocations generated during the grinding and polishing steps.

Silicon implanted specimen: The CL cross-section trace of sample nSi2g, Figure 7.14, displayed low efficiencies at both the backside of the wafer and near the implanted side. An asymmetrical curve is observed: the front, implanted surface exhibits a lower efficiency than the wafer reverse containing SBD with an approximately continuous rise in efficiency recorded from the implanted front surface to the wafer reverse. Small peaks in the efficiency are observed ~20 μm from each edge of the specimen.

7.3.3.3 Chemically etched dislocation-engineered specimens

Specimens nB2a, nB3a and nSi2g were investigated after the samples were chemically etched to remove the implantation related dislocation loops and the SBD. ~20 μm was removed from samples nB2a and pB2a and ~2 μm was removed from sample nSi2g. Samples suitable for cross-sectional investigation were then fabricated.

Boron implanted samples: The two samples investigated displayed curves of similar form, see Figure 7.15. Increased efficiency was observed throughout the specimen bulk, a high approximately constant CL efficiency, ~210 μm wide, was observed in the central portion of the wafer. Near the implanted surface, a second plateau of lower efficiency was observed, ~150 and 200 μm wide for samples nB2a and nB3a respectively. At the wafer reverse the CL efficiency fell to ~0.5% of the maximum and no plateau was observed.

Silicon implanted samples: An approximately symmetrical curve with an increased efficiency compared to the original sample was observed, see Figure 7.15c. Small peaks in efficiency just below the implanted and reverse surface were again observed with the peak at the implanted surface being larger than at the reverse.

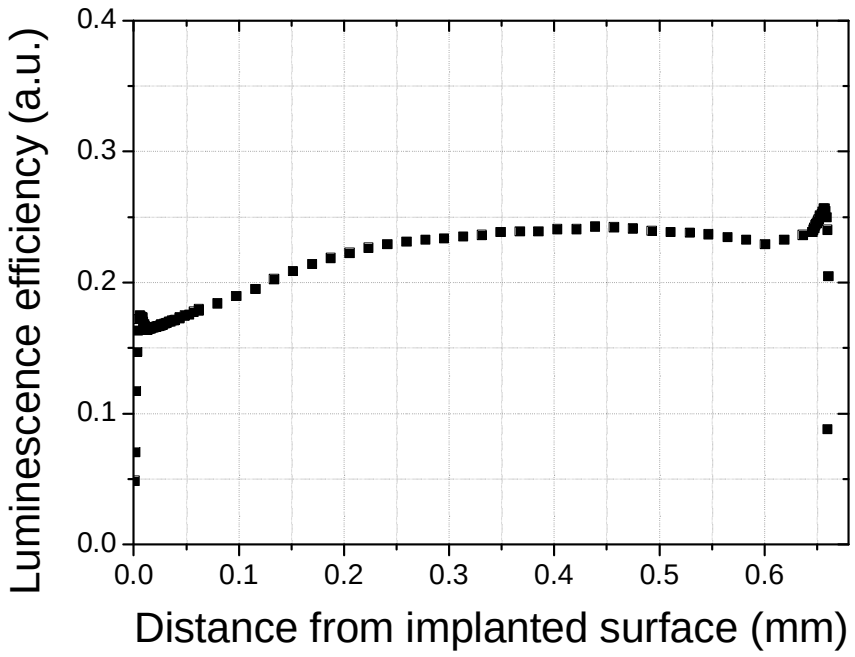

Figure 7.14

Luminescence efficiency cross-section profile of sample nSi2g (silicon implanted, 1 x 10^{15} cm^{-2}, annealed at 900 °C 120 mins). Accelerating voltage = 30 kV and beam current = 50 nA.

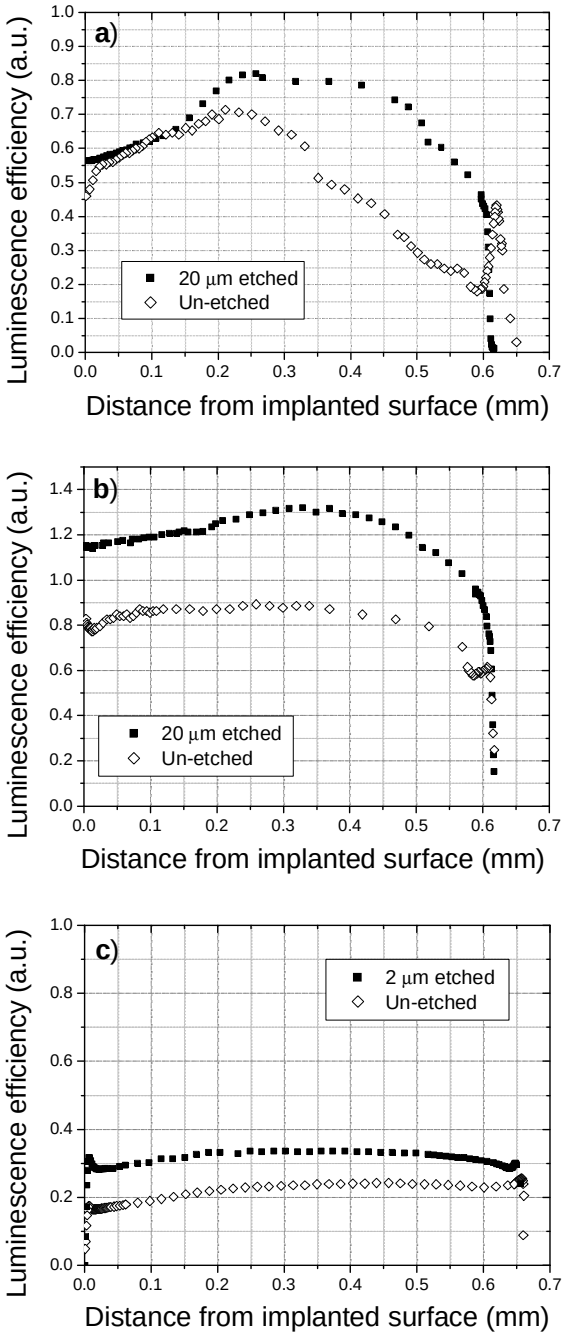

Figure 7.15

Luminescence efficiency cross-section profiles of: a) sample nB2a (boron, 1x 10^{15} cm^{-2}, 900 °C for 15 mins), b) sample nB3a (boron, 1x 10^{16} cm^{-2}, 900 °C for 15 mins) and c) sample nSi2g (silicon, 1 x 10^{15} cm^{-2}, °C 120 mins). ~20 μm removed from front and back side of boron implanted samples and ~2 μm removed from silicon implanted sample. Accelerating voltage = 30 kV and beam current = 50 nA. The un-etched data from Figures 7.13 and 7.14 are included for comparison.

7.3.4 Discussion

It was shown in Section 7.2 that the efficient luminescence mechanism of DE-silicon was due to the gettering of electrically active defects from the specimen bulk, thus increasing the efficiency of TO phonon-assisted band-to-band recombination. However, the MQE was estimated to be ~2 x 10^{-6} and thus, the total recombination rate of electron-hole pairs in DE-silicon is dominated by the competing non-radiative mechanisms (previously outlined in Chapter 1). In order that the efficient luminescence of DE-silicon may be understood fully it is therefore necessary to understand the non-radiative recombination paths throughout a sample.

7.3.4.1 Recombination in unprocessed silicon wafers

The calculated bulk minority carrier lifetime as a function of the majority carrier concentration is shown in Figure 7.16a for an unprocessed sample containing iron at a concentration of ~10^{11} cm^{-3}. The two main competing non-radiative recombination mechanisms in the specimen bulk are SRH recombination at electrically active point defects and Auger recombination. At carrier concentrations greater than ~5 x 10^{16} cm^{-3} the minority carrier lifetime is limited by Auger recombination and below this level SRH recombination tends to dominate. A peak in the minority carrier lifetime is observed at a carrier concentration of ~2 x 10^{16} cm^{-3}. The theoretical curve plotted in Figure 7.16a is recreated well by the observed luminescence efficiencies of as-received, unprocessed wafers (results shown in Figure 7.8). The peak luminescence efficiency of unprocessed wafers was observed at a doping level of ~1 x 10^{16} cm^{-3} and between 2 x 10^{15} and 3 x 10^{17} cm^{-3} for *n*- and *p*-type substrates respectively.

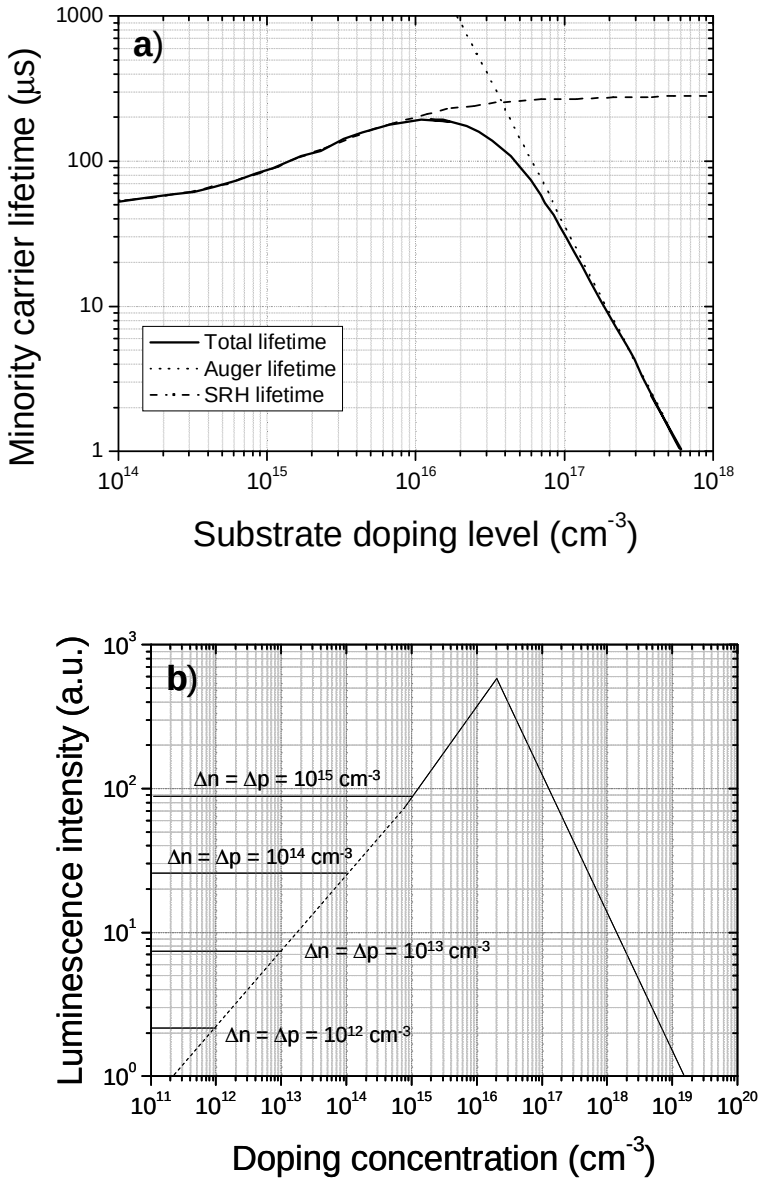

Figure 7.16

a) Minority carrier lifetime as a function of substrate doping level, illustrating the contribution of Auger and Shockley-Read-Hall lifetimes (after Palais *et al.*, 2000).

b) Schematic representation of the luminescence efficiency as a function of the substrate doping level for a range of generated minority carrier (Δp) concentrations.

The luminescence efficiency of unprocessed samples with *n*-type substrates was observed to be consistently greater than similarly doped samples with *p*-type substrates. This difference may be accounted for by the difference in the rate of SRH recombination in the two substrates.

Variation in the minority carrier lifetime throughout an unprocessed sample: The observed cross-sectional profile of the unprocessed, 0.05 Ωcm (1 x 10^{17} cm^{-3}) sample (Figure 7.12), appears to be consistent with a uniform bulk minority carrier lifetime throughout the entire thickness of the wafer: the luminescence efficiency was lower near the sample edges due to surface recombination and far from the specimen edges an approximately uniform, high efficiency was observed. The symmetrical nature of the curve implies that the surface recombination velocity at each surface is approximately equal and the transition metal concentration profile throughout the specimen is constant.

An estimate of the minority carrier diffusion length: At a majority carrier concentration of 1 x 10^{17} cm^{-3} the effective minority carrier lifetime (τ) is largely determined by the rate of Auger recombination. The Auger lifetime at this carrier concentration was determined, using Figure 7.16a, to be ~35 μs. Using this value of the effective minority carrier lifetime, the effective minority carrier diffusion length (L) of a sample may be estimated using this value of the effective minority carrier lifetime, the minority carrier diffusion coefficient (D), the luminescence efficiencies plotted in Figure 7.8a, the variation in the rate of radiative recombination as a function of carrier concentration (Eqn. 1.8) and the relationship $L = (D\tau)^{½}$. The maximum minority carrier diffusion length of an unprocessed sample (*n*-type, ~1 x 10^{16} cm^{-3})

was estimated to be ~1580 μm. This is slightly lower than measured by the manufacturers who, in similar material, observed typical minority carrier diffusion lengths of several millimetres (Falster, 2006). However, the manufacturer's measurements were performed using the electrolytical metal analysis tool (ELYMAT) technique. In the ELYMAT technique the wafer is immersed in a hydrofluoric bath which minimises surface recombination effects and the high injection regime is used to investigate the minority carrier lifetime. Falster and Borionetti (1998) report an order of magnitude increase in the minority carrier lifetime between medium and high injection conditions in samples where interstitial iron is the impurity which limits the minority carrier lifetime. The lower injection conditions and high surface recombination velocities of the CL method thus underestimates the minority carrier diffusion length in comparison to the ELYMAT technique, explaining the inconsistencies between the values for effective minority carrier diffusion lengths deduced in this work and those measured by the manufacturer.

Surface recombination: A single sample with an oxide passivated surface was investigated. The doping level of the sample was ~1 x 10^{17} cm^{-3} and thus the dominant recombination mechanism in the sample bulk was Auger recombination. The minority carrier diffusion length in this sample was estimated to be ~300 μm. An improvement in the luminescence efficiency of 40% was observed due to the reduction in surface recombination (minority carrier diffusion length = ~355 μm).

Excitation conditions: From the dependence of the luminescence efficiency on the doping level of the substrate (Figure 7.8a), it can be deduced that the carrier injection levels used in this work are in the low excitation regime as the measured

luminescence efficiency would be independent of the substrate carrier concentration if the generated carrier concentration was greater than the substrate doping level. This is illustrated schematically in Figure 7.16b. It was observed experimentally that the rate of radiative recombination was not dependent on the excitation levels and thus, the injected carrier concentration is inferred to be less than ~1 x 10^{14} cm^{-3}.

7.3.4.2 Understanding gettering in silicon which contains dislocations

Transition metal impurities are generally present in silicon wafers in concentrations which far exceed their low equilibrium solubility concentrations at room temperature. The three most common electrically active defects in silicon are copper, nickel and iron (Falster, 2001) and these elements have extremely low solubilities at room temperatures and are present in supersaturated concentrations - iron is typically present at a concentration of ~5 x 10^{10} cm^{-3} due to the wafer manufacturing process (Falster, 2006). The solubilities of these three elements are described by the following equations (Silicon Handbook, 1988) and plotted as a function of temperature in Figure 7.17a:

$$C_{copper} = 5.5\times10^{23}\exp\left(-\frac{1.49q}{kT}\right) \quad cm^{-3} \qquad \text{Eqn. 7.5}$$

$$C_{iron} = 1.8\times10^{26}\exp\left(-\frac{2.94q}{kT}\right) \quad cm^{-3} \qquad \text{Eqn. 7.6}$$

$$C_{nickel} = 1.5\times10^{24}\exp\left(-\frac{1.68q}{kT}\right) \quad cm^{-3} \qquad \text{Eqn. 7.7}$$

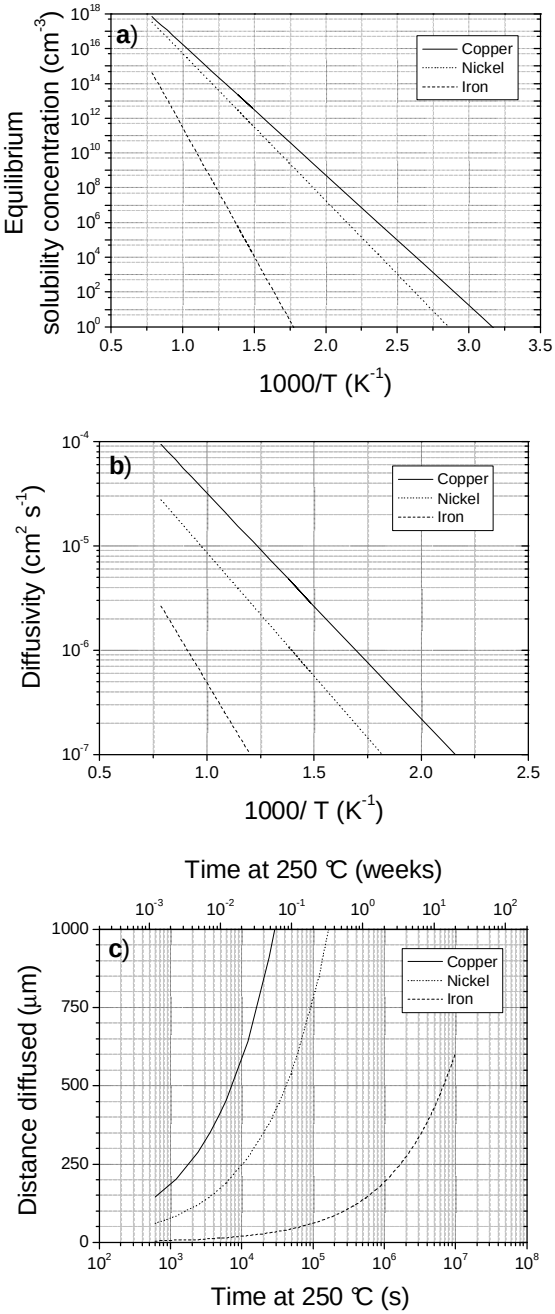

Figure 7.17

a) Equilibrium solubilities of the three major electrically active defects in silicon as a function of temperature

b) Diffusivity of the three major electrically active defects in silicon as a function of temperature

c) Distance that the three major electrically active defects in silicon diffuse as a function of the annealing time at 250 °C.

where q is the electronic charge, k is the Boltzmann constant and T is the temperature. The equilibrium solubilities of the three elements are less than 10^2 cm^{-3} at room temperatures and thus, there is a thermodynamic driving force for the reduction in their bulk concentration to lower energy (gettering) sites such as silicide precipitates and dislocations (Benton *et al.*, 1995). However, at low temperatures the gettering process may be kinetically limited due to the low diffusivities of impurity species in silicon. The diffusion coefficients of the three elements are described by the following equations (Silicon Handbook, 1988) and plotted as a function of temperature in Figure 7.17b:

$$D_{copper} = 4.7\times10^{-3}\exp\left(-\frac{0.43q}{kT}\right) \quad cm^2\,s^{-1} \qquad \text{Eqn. 7.8}$$

$$D_{iron} = 1.3\times10^{-3}\exp\left(-\frac{0.68q}{kT}\right) \quad cm^2\,s^{-1} \qquad \text{Eqn. 7.9}$$

$$D_{nickel} = 2.0\times10^{-3}\exp\left(-\frac{0.47q}{kT}\right) \quad cm^2\,s^{-1} \qquad \text{Eqn. 7.10}$$

where q is the electronic charge, k is the Boltzmann constant and T is the temperature. For example, iron, thought of as a fast diffusing species is calculated to diffuse a distance of ~3 nm in 24 hours at room temperature. Thus, the thermal history of a sample and the prevalence of gettering sites are important considerations in understanding the gettering process. In the remainder of this section the experimental results are discussed in terms of the gettering ability of the samples and the processing conditions used.

Samples containing dislocations but with no thermal processing: The abraded (Ab1 and Ab2) and saw damaged/swirl defect (SD) specimens were known to contain a high density of extended defects but were not subjected to thermal processing. In comparison to unprocessed, as-received wafers, no enhancement of the luminescence efficiencies was observed (see Figure 7.8b). This is consistent with the mobility of the dominant impurity element being too low for effective gettering at room-temperature.

Samples thermally processed but with low dislocation density: The specimens which contained OISFs have a low dislocation length per unit area, ~5 x 10^3 cm^{-1}. These samples were thermally processed at temperatures at 1100 °C, at which temperature the impurity elements are both highly mobile and, upon cooling, are present in supersaturated concentrations. However, the luminescence efficiencies of the OISF specimens do not show an improvement in the luminescence efficiency when compared to similarly doped, unprocessed wafers (Figure 7.8b).

In the highly doped OISF specimens (SF2, SF3, SF4 and SF5, majority carrier concentrations in the rage of 4 x 10^{18} to 1 x 10^{19} cm^{-3}) the effective bulk minority carrier lifetime is limited by Auger recombination. Thus, a decrease in the rate of SRH recombination due to a reduction in the bulk transition metal concentration by gettering would not be observable using CL. However, in the case of the OISF specimen SF1 (majority carrier concentration ~1 x 10^{15} cm^{-3}), a significant decrease in the rate of SRH recombination was not observed. It is thought that the low dislocation density acted as a weak gettering centre, resulting in little reduction in the bulk transition metal concentration.

Samples thermally processed with high dislocation densities: DE-specimens implanted with boron or silicon into *n*- or *p*-type substrates displayed enhanced luminescence efficiencies in comparison to similarly doped, unprocessed wafers.

All boron implanted samples investigated displayed strong luminescence in comparison to all other specimens investigated in this work. The maximum MQE observed for a boron implanted sample (3.8×10^{-6}) was ~35 times more efficient than a similarly doped, unprocessed wafer (see Figure 7.8a).

The MQEs observed for silicon implanted samples were more than an order of magnitude less efficient than the boron implanted samples. However, the silicon implanted sample MQEs were also greater than similarly doped, unprocessed wafers.

The chemical etching of DE-silicon at room temperature (Sections 7.2.3 and 7.3.2) removed the dislocation loops and, in boron implanted samples, the highly doped, near-surface region to leave an extended-defect free sample. The recombination processes in these chemically etched samples are thus directly comparable to unprocessed, as-received wafers. The DE-silicon samples investigated in this work were fabricated using substrates with a majority carrier concentration of $\sim 6 \times 10^{14}$ cm^{-3} and therefore, in comparison to the rate of SRH recombination, the rate of Auger recombination at this carrier concentration was negligible. The MQEs of DE-samples nB2a and nSi2g after chemical etching were significantly greater than unprocessed, similarly doped specimens, shown in Figure 7.8a. This increased MQE, relative to unprocessed wafers, suggests that the mechanism of enhanced luminescence efficiency of DE-silicon is not limited to the implantation of boron and subsequent annealing.

In boron implanted DE-specimens, it was observed that the degree of gettering (*i.e.* luminescence efficiency) was logarithmically dependent upon the dislocation

density present in a sample (Figure 7.4). The annealing temperature and duration were shown in Chapter 5 to determine the dislocation density, however the annealing time and duration were not observed to directly influence the luminescence efficiencies. For example, samples nB1b and nB3d are of similar dislocation density (~ 2 x 10^8 cm^{-2}) but differ in anneal conditions (900 and 1000 °C for 60 mins respectively) and the luminescence efficiency of the two samples was approximately equal. Furthermore, the Burgers vector of the dislocation loops had little or no effect either; samples nB2b and nB3d, with ~75% and 10% of dislocation loops **b** = ⅓(111) respectively, exhibited similar luminescence intensities. This suggests that the important factor in determining the luminescence efficiency of a DE-sample was the dislocation density (cm^{-1}) within a sample, and that the gettering occurs during the cooling process which was similar for all DE-samples below 800 °C.

This interpretation then explains the experimental observations of Arguirov *et al.* (2003) who observed no enhanced luminescence efficiency when samples were processed using rapid thermal annealing (RTA), but when samples are processed using conventional furnaces the enhanced luminescence efficiency was observed. The fast cooling rate of RTA processing significantly reduces the length of time in which impurity elements are both supersaturated and sufficiently mobile such that gettering may take place.

Recent modelling results have shown that the total number of impurity atoms removed from the specimen bulk to be dependent upon the strength of the gettering centre (Fraser, 2006). The total number of impurity atoms removed from the bulk displayed a regime in which there was a logarithmic dependence on the strength of the gettering centre. As the strength of the gettering centre increased further, the total amount of material removed was found to saturate. This saturation was not observed

experimentally suggesting that a further increase in the total dislocation length per unit area may further increase the luminescence efficiency of DE-samples.

After the dislocation band was removed by room temperature chemical etching the luminescence efficiency of the silicon implanted DE-sample nSi2g was found to be a factor of ~2 lower than the boron implanted samples nB2a and pB2a even though the three samples contained an approximately equivalent dislocation density. One explanation for this discrepancy in the effectiveness of the gettering may be explained by the role of boron. Benton *et al.* (1996) have shown that regions of high boron concentration can act as effective gettering sites by the electronic interaction between interstitial iron and the dopant boron ions. Interstitial iron is known to have either a neutral or a positive charge state which is dependent upon the position of the Fermi-level in the bandgap. When the Fermi level is below the deep level (E_v + 0.39 eV), iron is in the positive charge state and is attracted to the negatively charged boron ions. Thus in the boron implanted DE-silicon there is an enhanced gettering strength of the implanted layer in comparison to the silicon implanted specimens. However, the dislocation loops are still thought to be necessary for appreciable gettering as no enhanced luminescence was observed from samples nB2a or pB2a when the dislocation loops were removed by annealing at 1150 °C, leaving the high boron concentration near-surface region.

Variation in the transition metal profile: The maximum luminescence efficiency in a silicon implanted DE-specimen was observed when ~250 nm of material had been removed by chemical etching (the smallest amount removed), Figure 7.11. Upon the removal of further material, the luminescence efficiency decreased. Thus, it can be inferred (using Eqn. 7.4) that the lowest concentration of

electrically active defects was in the region of the sample in closest proximity to the dislocation loops. This is supported by analysis of the cross-sectional profiles of the chemically etched specimens (Figure 7.15). In comparison to the unprocessed specimen, all the DE-specimens investigated in cross-section displayed an increased efficiency throughout the cross-section profile; this suggests an increased minority carrier lifetime throughout the entire wafer thickness. Furthermore, the profiles differ in form to the unprocessed specimen - implying a spatial variation in the transition metal concentration. In each boron implanted DE-sample, the implanted surface does not display the large decrease in efficiency observed at the back side of the wafer, or at both edges of the specimen as observed in the unprocessed sample (Figures 7.15 and 7.12 respectively). This implies a region of material with an increasingly long SRH lifetime with increasing proximity to the dislocation band.

One explanation that may account for the transition metal profile is by the consideration of the gettering of a single impurity element, of initially high concentration during the cooling process from 800 °C. The impurity concentration is below the solid solubility at 800 °C and is distributed uniformly throughout the wafer. The solid solubility falls rapidly as the sample is cooled resulting in the impurity becoming supersaturated, and a thermodynamic driving force for gettering is generated. At this temperature the gettering process is not kinetically limited and the gettering results in the uniform reduction in the impurity concentration throughout the entire wafer. As the temperature reduces further, the gettering process becomes kinetically limited resulting in the impurity carrier concentration far from the gettering centre being ‘frozen-in’. However, closer to the gettering centre the transition metal concentration continues to reduce. As cooling proceeds the distance from which transition metals are gettered becomes less and less. This results in a transition metal

concentration which, in comparison to an unprocessed sample, is lowered throughout the entire wafer and is reduced from this level in close proximity to the gettering centre.

In boron implanted samples, the degree of gettering was shown to be logarithmically dependent on the strength of the gettering centre (Figure 7.4). The increased gettering during the kinetically limited period may also be inferred from the cross-sectional profiles of the samples nB2a and nB3a after chemical etching. The dislocation density of sample nB3a was greater than sample nB2a and correspondingly a larger plateau immediately below the implanted surface was observed, ~200 compared to 150 μm respectively.

Samples nB2d, pB2d and nB3c which were found, during the TEM investigation of Chapter 5, to contain second phase precipitates were also observed to produce relatively efficient luminescence (MQEs ~1.7×10^{-6}). This suggests that the contamination of the wafers was a localised anomaly and the TEM sample investigated in Chapter 5 was not representative of the whole wafer as the observation of efficient luminescence suggests the large scale presence of dislocation loops acting as gettering centres.

7.3.4.3 The direct effect of dislocations on non-radiative recombination

Dislocations throughout the specimen bulk: The mechanically deformed and oxygen precipitate samples contained a high density of dislocations throughout the entire specimen bulk and no detectable luminescence was observed – the high rate of non-radiative recombination at the dislocations throughout the samples is thought to effectively quench the luminescence efficiency.

Dislocation loops with high contamination levels: If the gallium implantation was directly comparable to the boron and silicon implantations then an enhancement in the luminescence efficiency of a DE-sample implanted with gallium would have been expected. However, the gallium was implanted in an area of 250 μm^2 using the FEI FIB 200 and annealed in non-cleanroom conditions. This processing is now thought to be both insufficiently clean, and too limited in scale, to produce significant gettering - this is thought to result in a greater increase in the rate of non-radiative recombination at the dislocation loops than the reduction in the rate of non-radiative recombination at point defects in the bulk.

Non-radiative recombination at dislocations in dislocation-engineered silicon: In all DE-samples the dislocations were observed to act as non-radiative recombination centres, however, the recombination strength of the dislocations was found to vary between samples. In silicon-implanted DE-specimens the dislocation loops were found to act as strong non-radiative recombination centres: removal of the dislocation band by chemical etching resulted in a large increase in the MQE from 9.8 x 10^{-8} to 1.1 x 10^{-6} (Figure 7.11) and, in specimens which still contained the band of dislocations, an increase in the dislocation density was observed to produce a decrease in the luminescence efficiency (Figure 7.6). However, in boron implanted DE-specimens the dislocation loops were found to act as relatively weak non-radiative recombination centres: when the luminescence efficiency of samples nB1a, nB2a and nB3a were investigated as a function of the accelerating voltage (Figure 7.9) an increased dislocation density was found to result in an increased non-radiative recombination rate when the carriers were generated in close proximity to the

dislocations. Furthermore, only a small increase in the luminescence efficiency was observed when the near-surface region was removed by chemical etching (Figure 7.2).

The difference in the recombination strength of the dislocation loops in the boron and silicon implanted DE-specimens may be understood in terms of the Wilshaw model of recombination at a dislocation (Wilshaw, 1984). The theory predicts that the recombination strength of a dislocation is dependent of the doping level of the material in which the dislocation is situated. The minority carrier recombination strength of a dislocation, γ, is dependent upon the minority carrier capture cross-section, *i.e.* the radius of the space charge region (SCR) associated with a contaminated dislocation core, r, according to (Wilshaw, 1984):

$$\gamma = \frac{\pi r^2}{D_h \tau'} \qquad \text{Eqn. 7.11}$$

where D_h is the minority carrier diffusion coefficient and τ' is the minority carrier lifetime within the region of the defect. The radius of the SCR is proportional to the Debye length. The dislocation loops in the silicon implanted DE-samples are situated in material with a majority carrier concentration ~5 x 10^{14} cm^{-3} compared to the boron implanted DE-samples where the dislocation loops are situated in ~10^{21} cm^{-3} material, the Debye length is 170 nm and 0.4 nm respectively (Sze, 1981). Thus, the recombination strength of dislocation loops in silicon implanted samples is significantly greater than in boron implanted samples. This is consistent with the large increase in luminescence of the silicon implanted specimens after the removal of dislocations, the reduction in luminescence efficiency with increased dislocation length in silicon implanted samples and only a small change in luminescence

efficiency after that the removal of the dislocation loops in the boron implanted samples.

Furthermore, the dependence of the luminescence efficiency of silicon implanted DE-specimens on the carrier concentration in the generation volume may be explained (Figure 7.10). The dislocation loops were observed by TEM to be located ~200 nm below the surface (see Chapter 5), thus, at the beam energies used the dislocations lie within the generation volume. Therefore, the capture cross section of the dislocations, and the rate of non-radiative recombination, is determined by the electron beam conditions rather than the substrate doping concentration. To the best of the author's knowledge, this is the first time that the doping dependence of the recombination strength of a dislocation, predicted by the Wilshaw model in 1984 has been observed experimentally.

The difference in the recombination strength of the dislocations is also shown in the cross-sectional profiles. The boron implanted samples containing dislocations (Figure 7.13) do not show a significant difference in behaviour to when the dislocations were removed by chemical etching (Figure 7.15). A small increase in the luminescence efficiency was observed throughout the wafer but the luminescence efficiency near the implanted surface remained at a high level. For the silicon implanted sample, nSi2g, the strong non-radiative recombination of the implantation related dislocations is shown by the reduced efficiency throughout the sample and, in particular close to the dislocation loops (Figure 7.14). The reduction in the efficiency close to the implanted loops is greater than at the back surface which contains SBD. This is consistent with an increased dislocation density acting as a stronger non-radiative centre as the dislocation density of the dislocation band (4×10^4 cm^{-1}) is greater than that of the SBD (~10^3 cm^{-1}).

7.4 Experiments to increase the luminescence efficiency of dislocation-engineered silicon

In an attempt to further increase the luminescence efficiency of DE-silicon, samples nB3a, pB3a and an unprocessed ~5 Ωcm boron doped wafer were annealed at 250 °C for prolonged periods of time (up to twenty weeks) in a standard metallurgical furnace. The temperature was selected such that the electrically active impurities were relatively mobile (see Figure 7.17) and to ensure that the likelihood of the in-diffusion of surface contaminants was low. Samples were annealed in the dark or under illumination by a halogen bulb (this process is described in full in Section 4.2.3). Troxell *et al*. (1979) report that the rate of diffusion of electrically active impurities in silicon may be increased by a carrier-recombination enhanced diffusion mechanism.

The generation rate, G, of electron-hole pairs when samples are illuminated by the halogen bulb is given by (Sze, 1981):

$$G = \frac{\Delta n}{\tau} = \frac{\eta\left(\frac{P_{opt}}{E_{photon}}\right)}{AD} \qquad \text{Eqn. 7.12}$$

where η is the quantum efficiency (*i.e.* the number of carriers generated per photon, 0.9 – 1 in silicon), P_{opt} is the incident optical power (0.4 W), E_{photon} is the photon energy, A is the area of the sample (~1 cm^2) and D is the sample thickness (0.66 cm).

Assuming the halogen bulb emitted uniform spectral intensity across the visible spectrum, the minority carrier concentration throughout the sample was calculated using Eqn. 7.12 to be ~5 x 10^{12} cm^{-3}. However, the rate of photon absorption decays exponentially within a sample and thus, the majority of photons

generated by the halogen bulb are absorbed within ~10 μm of entering the sample. This results in high carrier concentrations (~10^{16} cm^{-3}) close to the specimen surface. Thermal annealing at 250 °C is known to generate a carrier concentration of ~1 x 10^{15} cm^{-3} (Sze, 1981).

7.5.1 Experimental results

The luminescence efficiency as a function of annealing time is displayed for samples nB3j (dark), nB3k (light), pB3k (dark), pB3j (light) and the unprocessed sample (light and dark) in Figure 7.18. After one week, the luminescence efficiency of all samples was found to be lower than prior to annealing. The samples exposed to the white light showed a greater decrease than those specimens annealed in the dark. The largest decrease was observed for the illuminated unprocessed wafer (61%) and the smallest decrease was observed for the *n*-type DE-specimen annealed in the dark (21%).

As the annealing process was continued, the luminescence efficiency tended to increase. For the unprocessed wafer, an increase in efficiency of ~25% was observed after 16 weeks for both the samples annealed in the dark, and under white light, though the efficiencies were significantly lower than prior to annealing: MQEs of 3.5 and 3.9 x 10^{-8} for the light and dark specimens after 16 weeks respectively, compared to 6.4 x 10^{-8} initially. The efficiency of the DE-samples tended to increase with further annealing to levels which exceeded the values observed prior to annealing at 250 °C.

Despite the initial greater decrease in efficiency, there is some evidence to suggest that samples exposed to the white light displayed an increased efficiency relative to the samples processed in the dark, ultimately achieving the maximum

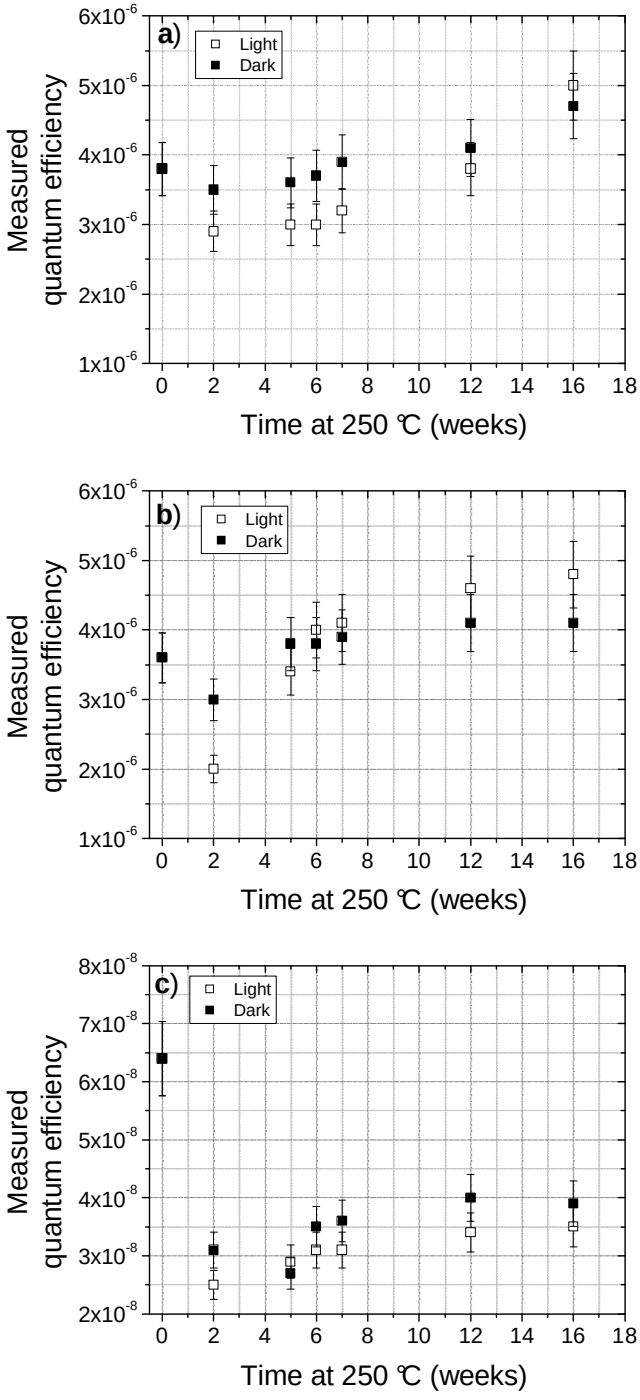

Figure 7.18

Estimated quantum efficiency as a function of annealing time at 250 °C for samples a) nB3j and nB3k and b) pB3j and pB3k (previously samples nB3a and pB3a respectively: B, 30 keV, 10^{16} cm^{-2}, 1000 °C, 15 mins) and c) unprocessed ~5 Ωcm boron doped wafer. 'j' and 'k' indicate that the specimens were annealed in the dark and light respectively.

MQE observed in this work, 5.1 x 10^{-6} for sample nB3k - annealed under illumination for 16 weeks.

7.5.2 Discussion

The luminescence was initially observed to decrease after a short (less than one week) annealing time. One explanation may be due the carrier recombination-enhanced electrical activity of defects. For example, the efficiency of boron doped solar cells is observed to decrease when minority carriers are generated thermally, by incident photons and/or through the injection of carriers from a forward biased *p-n* junction (Reiss *et al*., 1996). The mechanism for the degradation has been widely attributed to the dissociation of iron-boron pairs caused by excess carriers; this is a recombination-enhanced defect reaction (Fischer and Pschunder, 1973). The iron-boron defect pair has been shown to dissociate under illumination forming interstitial iron (Graff and Pieper, 1981). Interstitial iron is, under low-injection conditions, a more effective recombination centre than the iron-boron pair, and hence leads to a strong degradation in the minority carrier lifetime (Reiss *et al*., 1996). The increased electrical activity when electron-hole pairs recombine is not restricted to iron: Wilshaw *et al.* (1994) studied the effect of a low energy electron beam (15 to 30 keV) on the electrical activity of copper, iron and nickel in both *n*- and *p*-type silicon wafers and similar samples which contained dislocations. The authors observed that the action of the electron beam, in generating electron-hole pairs, increased the electrical activity of impurities located in the bulk or at dislocations. The initial decrease in the luminescence efficiency observed in this work is consistent with recombination-enhanced activity of electrically active defects and their relative concentrations within the samples. The unprocessed (boron doped) sample is thought

to contain a higher bulk impurity concentration than the DE-silicon samples and consequently shows the greatest reduction in efficiency.

Prolonged annealing at 250 °C resulted in the increase in efficiency from the low level recorded at the shortest annealing time investigated (1 week). The improvement was such that the highest MQE of any silicon wafer investigated in this work was observed from sample nB3k, 5.1×10^{-6}. This improvement is thought to be due to the further gettering of electrically active impurities. In the case of the DE-samples this is gettering to the dislocation band and the specimen surfaces and in the unprocessed sample to the specimen surfaces only. The rate at which the increase in efficiency occurs is consistent with the diffusion of iron through the wafer bulk to the dislocation band, see Figure 7.17c. There is some evidence to suggest that samples which were illuminated showed a faster increase in the luminescence efficiency than those samples processed in the dark. One explanation may be due to light-enhanced diffusion of point defects in silicon.

7.6 Summary and conclusions

The enhanced luminescence efficiency mechanism of DE-silicon was conclusively shown to be due to the gettering of transition metal impurities from the specimen bulk. Remarkably, this result suggests that the processing procedure used to manufacture DE-silicon creates wafers with bulk minority carrier lifetimes which are greater than as-received wafers. This interpretation is consistent with the findings of Sobolev *et al.*, (2003) and Arguiorov *et al.*, (2005).

For the first time, the SRH lifetime variation within DE-silicon was investigated. The lifetime was found to be increased through the entire thickness of the specimen. Furthermore, when the dislocation band had been removed by

chemical etching, the regions of the wafer closest to the dislocation band were found to be of even longer lifetimes than the remainder of the specimen bulk. The width of this region was found to depend on the dislocation density.

The band of dislocations was found to play a dual role in determining the luminescence efficiency. The presence of the dislocations was necessary for the gettering of impurities, but, once contaminated, the dislocations acted as non-radiative recombination centres. In boron implanted samples, the increased dislocation density resulted in an increased degree of gettering, the luminescence efficiency displaying a logarithmic dependence on the dislocation density. However, an increased dislocation density also resulted in an increased non-radiative recombination contribution from the dislocations themselves. The non-radiative contribution was found to be minimised by using a high doping level, whereby the capture cross-section of the defects is reduced.

In order to improve the efficiency of the DE-silicon by the reduction of the bulk impurity concentrations further, samples were annealed using a standard metallurgical furnace at 250 °C for extended periods of time. After the initial reduction in luminescence efficiency, which was attributed to the recombination-enhanced electrical activity of defects, the luminescence efficiency was observed to increase as a function of annealing time. After ~16 weeks, DE-samples annealed at 250 °C were observed to be more efficient than prior to annealing. The improvement was attributed to the further gettering of electrically active impurities.

Chapter 8

Summary, conclusions and suggestions further work

8.1 Introduction

The aim of this study was to investigate DE-silicon as a potential material for room temperature silicon-based photonics. Previous work had indicated that samples containing dislocation loops and a p^+-n junction, generated by ion implantation and thermal annealing, produced relatively efficient luminescence (Ng *et al*., 2001). However, the mechanism of the efficient luminescence was not understood well.

A matrix of specimens was created using either boron or silicon ions and a range of implant doses, anneal times and anneal temperatures. The nature of the defects created by the ion implantation and annealing process were characterised by transmission electron microscopy and their thermal evolution was investigated. Cathodoluminescence was used to investigate the luminescent properties of DE-silicon. The mechanism of efficient luminescence was determined and attempts at further improving the luminescence efficiency were made.

8.2 Summary and conclusions

8.2.1 TEM characterisation of the ion implantation defects

The dislocation loops generated by ion implantation and annealing were found to be consistent with a mixture of faulted Frank and perfect dislocation loops. The ratio of the two forms of dislocation loops was dependent on the processing conditions used. This is consistent with the bulk of the literature (see for example Milosavlejvić *et al.*, (2005) and de Mauduit *et al.*, (1994)).

In general it was found that a band of small dislocation loops was formed approximately 150 nm below the wafer surface. The density and size of the dislocation loops were found to be highly dependent on the processing conditions used: a high density (10^{16} cm^{-3}) of small dislocation loops (~15 nm diameter) were

observed at high doses (10^{16} cm^{-2}) and short, low temperature anneals (15 mins at 900 °C) compared to a low density (1 x 10^{12} cm^{-3}) of large loops (545 nm diameter) at low doses and long, high temperature anneals (15 mins at 1000 °C). Furthermore, a similar dislocation density was observed in samples containing very different individual loop characteristics, *i.e.*, a dislocation density of ~ 5 x 10^{8} cm^{-2} with either largely ~195 nm diameter faulted dislocation loops or ~425 nm diameter perfect dislocation loops.

The size distribution of dislocation loops was investigated and for the first time it was shown that the distribution profile could be understood using two defect populations with different mean loop diameters. It was observed experimentally that faulted dislocation loops nucleated in a higher concentration than perfect dislocation loops. Further annealing resulted in a coarsening process where a smaller number of larger diameter loops were observed. The faulted dislocation loop density was found to decrease significantly more than the perfect loop density and a net flux of interstitials from faulted to perfect dislocation loops was observed. The results were explained by classic Ostwald ripening theory, on the premise that nucleated perfect dislocation loops were larger in diameter than faulted dislocation loops. The experimental observations can be accounted for without needing to consider the relative formation energies of the two defects or the effect of the strain field as suggested in the literature (see Cristiano *et al.*, (2000) and Pan *et al.*, (1996)).

8.2.2 Determination of the mechanism of efficient luminescence from dislocation-engineered silicon

DE-silicon samples produced a cathodoluminescence peak at ~1150 nm, with FWHM ~90 nm and with an inflexion apparent at ~1180 nm. The luminescence peak

was observed to be of identical form when the dislocation loops had been removed by room-temperature chemical etching and thus the observed luminescence was ascribed to be via TO-phonon assisted recombination. The change in peak position from 1130 nm observed in the majority of the literature was attributed to photon re-absorption.

The measured quantum efficiency (MQE) of the sample analogous to that investigated by Ng *et al.* (2001) was estimated to be ~5 x 10^{-6}. This was a factor of ~20 lower than the EQE published by Ng *et al.* (2001) but is consistent with subsequent reports in the literature (Sobolev *et al.*, 2003 and Arguirov *et al.*, 2005). The low absolute value of the MQE is thought to be due to the experimental technique. The luminescence was determined to up to ~35 times more efficient than as-received, unprocessed wafers from one some of the world's leading, single crystal, Czochralski and Float Zone silicon manufacturers.

The enhanced luminescence efficiency mechanism was determined to be due to the gettering of transition metal impurities from the bulk. When the dislocation band (and gettered impurities) was removed by chemical etching, the high luminescence efficiency was found to persist throughout the thickness of the wafer. However, when the dislocations were removed by high temperature thermal annealing the high luminescence efficiency was lost as impurity atoms returned to the wafer bulk. This confirms the hypothesis of Sobolev *et al.* (2003) and Arguirov *et al.* (2005). Remarkably, this result suggests that the processing procedure used to manufacture DE-silicon creates wafers with bulk minority carrier lifetimes which are greater than as-received wafers. It has traditionally been a widely held belief that any processing after the wafering process has a deleterious effect (Falster, 2003).

8.2.3 The investigation of dislocation-engineered silicon

The results of the cross-sectional cathodoluminescence investigation were understood in terms of the gettering of impurity centres to the band of dislocations from the wafer bulk. Gettering was found to occur during the cooling of the samples and the impurity concentration was lowered throughout the entire wafer. On further cooling, as the gettering process became kinetically limited, an increased amount of gettering occurred from areas of the wafer close to the dislocation band. The region of material in closest proximity to the band of dislocations was inferred to have a lower transition metal concentration than the specimen bulk. In boron implanted samples, the luminescence efficiency was found to exhibit a logarithmic dependence on the dislocation density (dislocation length per unit area of the crystal).

The dislocations were found to play a dual role in determining the luminescence efficiency; the presence of the dislocations was necessary for the gettering of impurities from the specimen bulk, but they also acted as non-radiative recombination centres. In the case of boron implanted samples, an increased dislocation density was observed to result in increased luminescence efficiency but in the silicon implanted samples the opposite trend was observed. The increased dislocation density resulted in an increased degree of gettering and thus longer minority carrier lifetimes in the bulk. However, an increased dislocation density also results in an increased non-radiative recombination contribution from the dislocations themselves.

The experimental investigation revealed that the non-radiative recombination contribution of the dislocation loops was minimised by maintaining the dislocations in regions which were heavily doped. When the dislocation loops were removed, by chemical etching, from samples with dislocation loops situated in moderately doped

regions (silicon implanted sample nSi2e), a large increase in the overall efficiency of the sample was observed. However, in samples containing an approximately equivalent dislocation density, but, with the dislocation loops situated in highly doped regions, the removal of the dislocation loops had little effect on the luminescence efficiency of the sample. A similar finding was also discerned from samples investigated using cross-sectional analysis. Dislocations situated in moderately doped regions of the wafer (either from silicon implantation or soft backside damage) were observed to act as strong non-radiative recombination centres, whereas dislocation loops resulting from the boron implantation were observed to be only weak non-radiative recombination centres. This was found to qualitatively agree with the Wilshaw model of recombination at dislocations (Wilshaw, 1984) where the capture cross-section of a dislocation is dependent on the Debye length of the host matrix.

8.2.4 Increasing the luminescence efficiency of dislocation-engineered silicon

The investigation of DE-silicon found that the mechanism of enhanced luminescence efficiency was gettering. Furthermore, cross-sectional analysis suggested that the impurity species which dominated the bulk minority carrier recombination rate (assumed to be Shockley-Read-Hall recombination) throughout the wafer after gettering was non-uniform. A region of specimen, up to 200 μm below the dislocation band, was observed to exhibit higher minority carrier lifetimes than the remainder of the specimen bulk. Thus, the cooling process of DE-silicon was not optimised for the gettering of impurities. In order to reduce the bulk impurity concentrations further samples were annealed using a standard metallurgical furnace at 250 °C for extended periods of time. After the initial reduction in luminescence

efficiency the luminescence efficiency was observed to increase as a function of annealing time. After ~16 weeks, DE-samples annealed at low temperature (250 °C) were observed to be more efficient than prior to the annealing process. The improvement was attributed to the further gettering of impurities.

8.3 Design of an improved dislocation-engineered silicon light emitting diode

The results presented in this thesis, together with reports from the literature allow for the design of an improved DE-silicon-based light emitting diode. The design would use the features of the silicon solar cell technology which have achieved the highest quantum efficiency of any bulk, crystalline silicon device thus far: textured surface, antireflection coating and excellent surface passivation (Green *et al*., 2001). However, the work reported in this thesis shows that the dislocation-engineering process is capable of producing silicon wafers with bulk minority carrier lifetimes in excess of those in Floating Zone silicon.

The substrate should be thicker than the minority carrier diffusion length and *n*-type with a carrier concentration of ~1.2 x 10^{16} cm^{-3}. Chemical etching is used to create a textured top-surface for maximising photon output. The ion implantation and annealing process is then used to generate a high dislocation density in the back surface of the LED. A *p*-type dopant, *e.g.* boron, is used to generate the dislocation loops and a *p*-*n* junction. Low-temperature surface passivation (silicon dioxide and silicon nitride layers) is applied to the top surface and sides, and a reflective coating applied to the reverse surface and sides. A low temperature gettering anneal is then applied to reduce the bulk impurity concentration. Finally, small ohmic contacts are

fabricated in the wafer front and reverse for electroluminescence. Thus, minority carriers are injected into the specimen bulk, where the low non-radiative recombination rate and low surface recombination allows TO phonon-assisted radiative recombination to be greatly enhanced with high internal and external quantum efficiencies. A schematic illustration of the final light emitting diode is shown in Figure 8.1.

The precise processing conditions require further investigation in order that they may be fully optimised. However, the above principles should allow for the design and operation of the most efficient bulk silicon light emitting diode to date.

8.4 Prospects of dislocation-engineered silicon for use as a light emitting diode

At the beginning of this project, the mechanism for efficient luminescence from DE-silicon was not understood. This work (simultaneous with others) has shown the mechanism to be due to the enhanced band-to-band luminescence due to the reduction in transition metal impurities from the specimen bulk by gettering. Thus, the arguments used in Chapter 1, which demonstrated that bulk silicon is highly unlikely to be useful as a light emitting material, are equally pertinent when examining the potential of DE-silicon.

8.5 Proposals for further work

The results presented in this thesis suggest that the application of DE-silicon

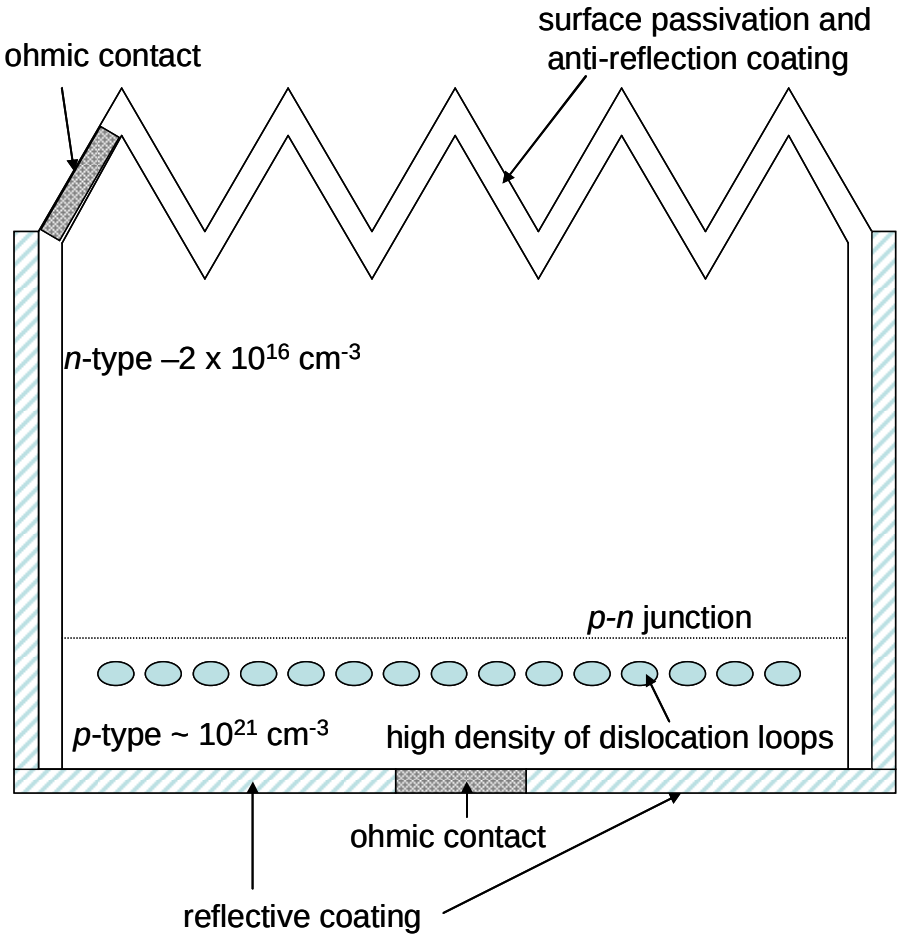

Figure 8.1

A schematic representation of an improved dislocation-engineered light emitting diode. Sample created by boron implantation into the reverse side of a textured, thick, *n*-type (1 - 2 x 10^{16} cm^{-3}) silicon wafer. Sample annealed to generate a dislocation density greater than 10^{11} cm^{-2}. Surface passivation layer and reflective coating applied at low temperature, followed by an optimised low temperature annealing regime.

as an optical source is unlikely. However, in view of the reduction in the electrically active defect concentration of the substrate by using dislocation-engineering, the knowledge and understanding gained during this investigation may still be highly useful. At present, the control of transition metal concentrations during the crystal growth process is adequately well controlled such that dislocation-engineering would not provide significant returns (Falster, 2005). However, the further development of the microelectronics industry may require the further reduction of transition metal concentrations in the future, dislocation-engineering may then become a viable option for the improvement of wafers for microelectronic applications. Thus, the low temperature gettering of impurities from the bulk should be investigated further with the aim of reducing the total processing time and further increasing the luminescence efficiency.

It was not possible to directly compare the luminescence efficiencies measured in this work by CL to those in the literature which used PL or EL due to the difference effects of surface recombination and the collection optics of the CL system. Thus, experiments on the DE-specimens using EL or using a calibrated specimen in the CL specimen would be highly desirable.

The introduction of dislocations to silicon using a number of alternative methods was also investigated; however, no thermal gettering treatment was applied to these samples. Thus, the gettering potential of silicon containing dislocations introduced by other methods is worth investigating as an inexpensive alternative to ion implantation. Cathodoluminescence has been used as a guide for the variation of minority carrier lifetime within the sample. However, the analysis of samples with long minority carrier lifetimes, and thus with long minority carrier diffusion lengths, is complicated and requires a rigorous analysis. Mathematical modelling of the

carriers would enable a full, quantitative analysis of the sample cross-sections allowing a greater evaluation of the competing recombination paths. The cross-sectional analysis of samples could then be used to understand accurately the variation in the transition metal concentration within a wafer and help to understand fully the role of gettering in DE-silicon.

References

A

Aberle, A. G. and Hezel, R. (1997) *Prog. Photovolt.* **5** 29.

Arguirov, T., Kittler, M., Seifert, W., Bolze, D., Ehwald, K.-E., Formanek, P. and Reif. J. (2004) Solid State Phenomena **95-96** p289-294.

Arguirov, T. Kittler, M. A., Seifert, W. and Yu, X. (2005) *Materials Sci. and Eng. B* **124-125** 431-434.

Aspnes, D. E. (1983) *Surface Science* **132** 406-421.

B

Becker, P. C., Olsson, N. A. and Simpson, J. R. (1999) *Erbium-Doped Fibre Amplifiers* (London: Academic).

Benton, J. L. (1990) *J. Cryst. Grow.* **106** (1) 116-126.

Benton, J. l., Stolk, P. A., Eaglesham, D. J., Jacobsen, D. C., Cheng, J.-Y., Ha, N. T., Haynes, T. E. and Myers, S. M. (1996*) J. Appl. Phys.* **80** (6) 3275-3284.

Besahel, D. C., Canham, L. T. and Osscicini, S. (1993) *Optical Properties of Low Dimensional Structures*. Kluwer Dordecht.

Binetti, S., Pizzini, S., Leoni, E., Somaschini, R., Castaldini, A. and Cavallini, A. (2002) *J. Appl. Phys.* **92** (5) 2437.

Bisi, O., Campisano, S. U., Pavesi, L. and Priolo, F. ed (1999) *Silicon based microphotonics: from basics to applications* (Amsterdam: IOS Press).

Bonafos, C., Omri, M., de Mauduit, B., Ben Assayag, G., Claverie, A., Alquier, D., Martinez, A. and Mathiot, D. (1997*) J. Appl. Phys.* **82** 2855.

Bonafos, C., Mathiot, D. and Claverie, A. (1998) *J. Appl. Phys.* **83** (6) 3008-3017.

Booker, G. R. and Tunstall, W. J. (1966) *Phil. Mag.* **13** 71.

Boyraz, O. and Jalali, B. (2004) *Opt. Expr.* **12**, 5269-5273.

Bradfield, P. L., Brown, T. G. and Hall, D. G. (1989) *Appl. Phys. Lett.* **55** 100-102.

Brey, L., and Tejedor, C. (1987) *Phys. Rev. Lett.* **59** 1022-1025.

Bseisy, A., Vial, J, C., Gaspard, F., Herino, R., Ligeon, M., Muller, F., Romestain, R., Wasiela, A., Halimaoui, A. and Bomchil, G. (1991) *Surf. Sci.* **254** 195-200.

C

Canham, L. T. (1990) *Appl. Phys. Lett.* **57** 1046-1048.

Canham, L. T. (1997) *EMIS datareviews series* **18** *Properties of porous silicon.*

Castagna, M. E., Coffa, S., Caristia, L., Messina, A. and Bongiorno, C. (2002) *Proc. ESSDDERC2002* p 439.

Castagna, M. E., Coffa, S., Monaco, M., Caristia, L., Messina, A., Mangano, R. and Bongiorno, C. (2003) *Physica E: Low dimensional systems and nanostructures* **16** (3-4) 547-553.

Castaldini, A., Cavalcoli, D., Cavallini, A., Binetti, S. and Pizzini, S. (2005) *Appl. Phys. Letts.* **86** 162109.

Chakravarti, I., Laha. R. and Roy, J. (1967) *Handbook of Methods of Applied Statistics, Volume I,* John Wiley and Sons, 392-394.

Chang, C. Y. and Sze, S. M. (1996) *ULSI technology* McGraw-Hill (ISE Editions).

Chelikowsky, J. R. and Cohen, M. L. (1976) *Phys. Rev. B.* **14** 55.

Christensen, N. E. (1990) *Phys. Rev. B* **42** 7148-7153.

Claverie, A., Colombeau, B., Ben Assayag, G., Bonafos, C., Cristiano, F., Omri, M. and de Mauduit, B. (2000) *Mat. Sci. Semicond. Process.* **3** (4) 269.

Clemens, J. T. (1997) *Bell Lab. Tech. J.* **Autumn** 76.

Cockayne, D. J. H., Ray, I. L. F. and Whelan, M. J. (1973) *J. Microsc.* **98** 170.

Coffa, S., Franzò, G., Priolo, F., Polman, A. and Serna, R. (1994) *Phys. Rev. B* **49** 16313.

Coffa, S. (2003) www.spectrum.ieee.orh/print/1886. visited August 2006.

Cohn, A. and Caledonia, G. (1970) *J. App. Phys.* **41** 3767.

Communications Technology Roadmap, (2005) (http://mphroadmap.mit.edu/). visited January 2006.

de Coteau, M. D. (1993) *DPhil thesis* Dept. Materials, Univ. of Oxford.

Cowern, N. E. B., Mannino, G.,. Stolk, P. A, Roozeboom, F., Huizing, H. G. A., van Berkum, J. G. M., Cristiano, F., Claverie, A. and Jaraiz, M. (1999) *Phys. Rev. Lett.* **82** 4460.

Cullis, A. G., Canham, L. T., Calcott, P. D. J. (1997) *J. App. Phys.* **82** (3) 909-965.

Cullis, A. G. and Katz, L. E. (1974) *Phil. Mag.* **30** 1419.

D

Das, G. (1973) *J. Appl. Phys.* **44** 4459.
Davidson, S. M. and Dimitriadis, C. A. (1980). *J. Microscopy* **118**, 275.
Davies, G. (1989) *Phys. Rep.* **176** 83-188.
Davies, G., Brian, H., Lightowlers, E. C., Barraclough, K. and Thomaz, M. F. (1989) *Semicond. Sci. Technol.* **4** (3) 200-206.
Delerue, C., Allan, G. and Lannoo, M (1999) *J. Lumin.* **80** 65-73.
Dieke, G. H. (1968). *Spectra and Energy Levels of Rare Earth Ions in Crystals.* Wiley, New York.
Donolato, C (1978) *Optik* **52** (19).
Drozdov, N. A., Patrin, A. A. and Tkachev, V. D. (1977) *Phys. Stat. Sol. B* **83** K137.

E

Eaglesham, D. J., Stolk, P. A., Gossmann, H. –J. and Poate, J. M. (1994) *Appl. Phys. Lett.* **65** 2305-2307.
Edington, J. W. (1976) *Practical Electron Microscopy in Materials Science,* Van Nostrand Reinhold Company, New York.
Ehbrecht, M., Kohn, B., Hulsken, F., Laguna, M. A. and Paillard, V. (1997) *Phys. Rev. B* **56** 6958.
Everhart, T. E. and Hoff, P. H. (1971) *J. Appl. Phys.* **42** 5837.

F

Falster, R. J. and Barionetti, G. (1998) *Recombination Lifetime Measurements in Silicon, ASTM STP 1340 (Eds. Gupta, D. C., Bacher, F. R. and Hughes, W. M.) American Society for Testing and Materials* 226-249.
Falster, R. J. (2001) *Semiconductor Fabtech 13th Ed.*
Falster, R. J. (2001) *Private communication.*
Falster, R. J. (2005) *Private communication.*
Falster, R. J. (2006) *Private communication.*
Falster, R. J. and Voronkov, V. V. (2000) MRS bulletin **June** 28-32.
Fauchet, P. M., von Behren, J., Hirschmann, K. D., Tsysbekov, L., and Duttagupta, S. P. (1998) *Phys. Status. Solidi A,* **165** (1) 3-13.
Fauchet, P. M. and Ruan, J. (2003) *Towards the First Silicon Laser (NATO Series)* eds. Pavesi, L., Gaponenko, S. and Dal Negro, L. (New York: Kluwer) 197.
Fauchet, P. M. (2004) *Silicon Photonics, Topics Appl. Phys.* (Eds Pavesi, L. and Lockwood, D. J.) **94** 177-198.
Fischer, H. and Pschunder, W. (1973) *Proc. 10th IEEE PVSC* 404.
Flynn, C. P. (1972) *Point Defects and Diffusion* (Clarendon, New York).
Foell, H. and Kolbesen, B. O. (1975) *Appl. Phys.* **8** 319.
Franzò, G., Priolo, F. and Coffa, S. (1999) *J. Lumin.* **80** 19.
Franzò, G., Irreira, A., Moreira, E. C., Miritello, M., Iacona, F., Sanfilippo, D., Di Stefano, G. F., Fallica, F. and Priolo, F. (2002) *Appl. Phys. A* **74** 1.
Fraser, K. J. (2006) *Private communication.*

G

Gardelis, S., Rimmer, J. S., Dawson, P., Hamilton, B., Kubiak, R. A., Whall, T. E., and Parker, E. H. C. (1991) *Appl. Phys. Lett.* **59** 2118-2120.
Gelloz, B. and Koshida, N. (2000) *J. Appl. Phys.* **88** 4319.
Giannattasio, A. (2004) *DPhil thesis* Dept. of Materials, Univ. of Oxford.
Giles, M. D. (1991) *J. Electrochem. Soc.* **138** 1160.
Graff, K. and Pieper, H. (1981) *J. Electrochem. Soc.* **128** 669.
Green, M. A. and Keevers, M. J. (1995) *Prog. Photovoltaics* **3** 189-192.
Green, M. A., Zhao, J., Wang, A., Reece, P. J. and Gal, M. (2001) *Nature* **412** 805-808.
Grovenor, C. R. M. (1989) *Microelectronic materials (Graduate Student Series in Materials Science & Engineering)* Inst. of Phys. Pub.
Grillot, P. N., Ringel, S. A., Fitzgerald, E. A., Watson, G. P. and Xie, Y. H. (1995) *J. Appl. Phys.* **77** (7) 3248-3256.
Gruen, A. E. (1957) *Z. Naturf:* **12A** 89.

Gnutzmann, U. and Clausecker, K. (1974) *Appl. Phys.* **3** 9-14.
Gwilliam, R., Lourenço, M. A., Milosavljević, M., Homewood, K. P., and Shao, G. (2005) *Mat. Sci. and Eng.B.* **124-125** 86-92.

H

Hare, A. P. G., Davies, G. and Collins, A. T. (1972) *J. Phys. C* **5** 1265.
Hayes, J. R. and Nilsson, N. G. (1964) in *Radiative Recombination in Semiconductors, Proc. Symp. Paris*, Dunod, Paris, 21.
Hirsch, P. B., Howie, A., Nicholson, R. B., Pashley, D. W. and Whelan, M. J. (1965) *Electron Microscopy of Thin Crystals*, Plenum Press New York.
Hirschman, K. D., Tsybeskov, L., Duttagupta, S. P., and Fauchet, P. M. (1996) *Nature* **384** 338-341.
Hoang, T., LeMinh, P., Holleman, J. and Schmitz, J. (2006) *IEEE Electron Dev. Lett.* **27** (2) 105-107.
Hull D. and Bacon, D. J. (1984) *Introduction to Dislocations* (Pergamon, New York).
Hybertsen, M. S., (1994) *Phys. Rev. Lett.* **72** (10) 1514-1517.

I

Iacona, F., Franzò, G., Moreira, E. C. and Priolo, F. (2001) *J. Appl. Phys.* **89** 8354.
Iacona, F., Pacifici, D., Irrera, A., Miritello, M., Franzò, G,, Priolo, F., Sanfilippo, D., Di Stefano, G. and Fallica, P. G. (2002) *Appl. Phys. Lett.* **81** 3242.
Ieong, M., Doris, B., Kedzierski, J., Rim, K. and Yang, M. (2004) *Science* **306** 2057.
Ioannou, D. E. and Davidson, S. M. (1979) *J. Phys. D: Appl. Phys.* **12** 1339-1344.
Istratov, A. A., Hieslmair, H. and Weber, E. R. (2000) *Appl. Phys. A* **70** 489-534.
Izotov, A. N., Kolyubakin, A. I., Shevchenko, S. A., and Steinman, E. A. (1992) *Phys. Status Solidi A* **130**, 193.

J

Jones, K. S. and Rozgonyi, G. A. (1993) *Rapid Thermal Processing Science and Technology* (ed R. B. Fair).
Jones, K. S. (1999) *Structure of ion implantation induced defects* in *EMIS Data Review Series*, Inspec publication.

K

Kamimura, H. (1994) *Supplement B to J. Phys. Soc. Jpn*. **63**. Physical Society of Japan, Tokyo.
Kasper, E., and Schaffler, F. (1991) *Strained-Layer Superlattices: Materials Science and Technology* (ed. T. P. Pearsall), Academic Press, Boston, p223-309.
Kato, K. And Tomohori, Y. (2000) *IEEE J. Sel. Top. Quantum Electron. Lett.* **6** (1) 4.
Kenyon, A. J., Steinman, E. A., Pitt, C. W., Hole, D. E. And Vdovin, V. I. (2003) *J. Phys.: Condens. Matter* **15** S2843-S2850.
Kerr, M. J. And Cuevas, A. (2002) *Semicon. Sci. Technol.* **17** (1) 35-38.
Kimerling, L. C., Kolenbrander, K. D., Michel, J., and Palm, J. (1997) *Solid State Phys*. **50** 333-381.
Kittler, M., Ulhaq-Bouillet, C. and Higgs, V. (1995) *Mater. Sci. Forum.* **196-201** 1123.
Kittler, M., Seifert, W. and Kveder, V. (2001) www.ihp-ffo.de/aboutihp/kittlnsin.pdf visited March 2006.
Kittler, M., Seifert, W., Arguirov, T., Tarasov, I. and Ostapenko, S. (2002) *Solar energy materials and solar cells* **72** (1-4) 465-472.
Kittler, M., Seifert, W. and Knobloch, K. (2003) *Microelectronic Engineering* **66** 281-288.
Kittler, M., Arguirov, T., Fischer, A. and Seifert, W. (2005) *Opt. Mater.* **27** 967-972.
Klein, C. A. (1968) *J. App. Phys*. **39** 2029.
Koshida, N. and Koyama, H. (1991) *Jpn. J. Appl. Phys*. **30** L1221-L1223.
Kramer, J. Seitz, P., Steigmeier, E. F., Auderset, H., Delley, B. and Baltes, H. (1993) *Sensors and Actuators A* **37-38** 527-533.
Kveder, V. V., Steinamn, E. A., Shevchenko, S. A. and Grimmeiss, H. G. (1995) *Phys. Rev. B* **51** (6) 10520-10526.
Kveder, V., Kittler, M. and Schröter, W. (2001) *Phys. Rev. B* **63** 115208.
Kveder, V., Badylevich, M., Steinman, E., Izotov, A., Seibt, M. and Schroter, W. (2004) *Appl. Phys. Lett.* **84** (12) 2106-2108.

L

Lalic, N. and Linnros, J. (1996). *J. Appl. Phys.* **80** (10) 5971-5977.
Lang, D. V. (1974) *J. Appl. Phys.* **45** (7) 3023-3032.
Leong, D., Harry, M., Reeson, K. J. and Homewood, K. P. (1997) *Nature* **387** 686-688.
Lemke, H. (1981) *Phys. Stat. Sol. A* **63** 389.
Liang, T. K. and Tsang, H. K. (2004) *Appl. Phys. Lett.* **84** 2745-2747.
Lin, C.-F., Chung, P.-F., Chen, M.-J. and Su, W-F. (2002) *Opt. Lett.* **27** 713.
Lockwood, D. J. (1994) *Solid State Commun.* **92** 101.
Lockwood, D. J. (1998) *Semiconductors and Semimetals* **49** 2-4.
Lourenço, M. A., Butler, T. M., Kewell, A.K., Gwilliam, R. M., Kirkby, K. J. and Homewood, K. P. (2001) *Jpn. J. Appl. Phys. Part 1* **40** (6A) 4041-4044.
Lourenço, M. A., Gwilliam, R. M., Shao, G. and Homewood, K. P. (2002) *Mat. Res. Soc. Symp. Proc.* **719** F5.1.1-F5.1.4.
Lourenço, M. A., Siddiqui, M. S. A., Gwilliam, R. M., Shao, G. and Homewood, K. P. (2003) *Physica E* **16** 376-381.
Lu, Z. H., Lockwood, D. J. and Baribeau, J. M. (1996) *Nature* **378** 258-260.

M

MacDonald, D. H., Maekel, H., Doshi, S., Brendle, W., Cuevas, A., Williams, J. S. and Conway, M. J. (2003) *Appl. Phys. Lett.* **82** (18) 2987-2989.
Magnea, N., Lazrak, A. and Pautrat, J. L. (1984) *Appl. Phys. Lett.* **45** 60.
Mallik, K., Falster, R. J. and Wilshaw, P. R. (2004) *Solid-State Electronics* **48** 231-238.
Marsh, C. D. (2001) *Private communication.*
Martin, I., Vetter, M., Orpella, A., Voz, C., Puigdollers, J., Alcubilla, R., Kharchenko, A. V., Roca, I. and Cabarrocas, P. (2004) *Appl. Phys. Letts.* **84** (9) 1474-1476.
Masini, G., Colace, L. and Assanto, G. (2002) *Mater. Sci. Eng.* B **89** 2-9.
de Mauduit, B., Laanab, L., Bergaud, C., Faye, M. M., Martinez, A. and Claverie, A. (1994) *Nucl. Instrum. Methods Phys. Res. B* **84** 190.
Meyer, M. (2000) *Compound Semicond*. **6** (2) 26-30.
Michaelis, W. and Pilkuhn, M. H. (1969) *Phys. Status Solidi* **36** 311.
Miller, G. L., Lang, D. V. and Kimerling, L. C. (1977) *Ann. Rev. Mater. Sci.* **7** 377.
Miller, D. A. (2000) *Proc. IEEE* **88** 728.
Milosavljević, M., Lourenço, M. A., Siddiqui, M. S. A., Shao, G., Gwilliam, R, M. and Homewood, K. P. (2003) *Inst. Phys. Conf. Ser.* **179** 99-102.
Milosavljević, M., Shao, G., Lourenço, M. A., Gwilliam, R, M. and Homewood, K. P. (2005) *J. Appl. Phys.* **97** (7) 073512.
Myers, S. M. and Follsteadt, D. M. (1995) *J. Appl. Phys.* **79** (3) 1337 – 1350.

N

Nayfeh, M. H., Barry, N., Therrien, J., Akcakir, O., Gratton, E. and Belomoin, G. (2001) *Appl. Phys. Lett.* **78** (8) 1131-1133.
Nayfeh, M. H., Rao, S. and Barry, N. (2002) *Appl. Phys. Lett.* **80** 121.
Nes, E. (1978) *Acta Metall.* **22** 81.
Ng. W. L. (2000). *PhD thesis, University of Surrey*.
Ng, W. L., Lourenço, M. A., Gwilliam, R. M., Ledain, S., Shao, G., and Homewood K. P. (2001) *Nature* **410** 192 – 194.
Nishino, T., Takeda, M. and Hamakawa, Y. (1973) *Solid State Commun.* **12** 1137.
Noda, T, (2006) *J. Appl. Phys.* 91 (2) 639 – 645.

O

Ong, T.-C., Terrill, K. W., Tam, S. and Hu, C. (1983) *IEEE Electron Dev. Lett.* **4** 460-462.
Oriel Instruments (2005) http://www.newport.com/servicesupport/Tutorials/default.
Ossicini, S., Pavesi, L. and Priolo, F. (2003) *Light Emitting Silicon for Microphotonics (Springer Tracts in Modern Physics)* (Berlin: Springer) visited July 2006.

P

Palais, O., Gervais, J., Yakimov, E. and Martinuzzi S. (2000) *Eur. Phys. J AP* **10** 157-162.

Pan, G. Z. and Tu, K. N. (1997) *J. Appl. Phys.* **82** 601.
Pan, G. Z., Tu, K. N. and Prussin, A. (1996) *Appl. Phys. Lett.* **68** 1654.
Pan, G. Z., Tu, K. N. and Prussin, A. (1997) *J. Appl. Phys.* **81** 78.
Pavesi, L. (2003) *J. Phys.: Condens. Matter* **15** R1169-R1196.
Pearsall, T. P., Bevk, J., Feldmann, L. C., Bonar, J. M., Mannaerts, J. P., and Ourmazd, A. (1987) *Phys. Rev. Lett.* **58** 729-732.
Petroff, P. M. and de Kock, A. J. R. (1976) *J. Cryst. Growth* **36** 4.
Polk, D. E. (1971) *J. Non-Cryst. Solids* **5** 365.
Prussin, S. and Jones, K. S. (1986) *Proc. At. Sci. Res. Soc.* **71**.

R

Raman, R., Law, M. E., Krishnamoorthy, V. and Jones, K. S. (1999) *Appl. Phys. Lett.* **74** 700.
Rebohle, L., von Borany, J., Borchert, D., Frob, H., Gebel, T., Helm, M., Moller, W. and Skorupa, W. (2001) *Electrochem. and solid state lett.* **4** (7) G57-G60.
Reed, G. T. and Knights, A. P. (2004) *Silicon Photonics: An Introduction* (John Wiley, Chichester, UK,).
Reiss, J. H., King, R. R. and Mitchell, K. W. (1996) *Appl. Phys. Lett.* **68** 3302.
Risch, L. (2002) *Mater. Sci. Eng. C* **19** 363.
Rodrigues, P. A. M., Araujo-Silva, M. A., Narvaez, G. A., Cerdeira, F., Bean, J. C., (1999) *Brazilian J. Phys.* **29** (3) 547-550.
Rong, H., Jones, R., Liu, A., Cohen, O., Hak, D., Fang, A. and Paniccia, M. (2005) *Nature* **433** 725-728.
Ruff, M., Fick, M., Linder, R., Rssler, U. and Helbig, R. (1993) *J. Appl. Phys.* **93** 1598.

S

Sacshe, J.-U., Weber, J. and Lemke, H. (2000) *Phys. Rev. B* **61** (3) 1924.
Sauer, R., Weber, J., Stolz, J., Weber, E. R., Kysters, K.-H. and Alexander, H. (1985) *Appl. Phys. A* **36** 1.
Sauer, R., Kisielowski-Kemmerich, C. and Alexander, H. (1986) *Phys. Rev. Lett.* **57** 1472.
Schmidt, J., Kerr, M. and Cuevas, A. (2001) *Semicon. Sci. Technol.* **16** (3) 164-170.
Schröter, W., Kronewitz, J., Gnauret, U., Ridel, F. and Seibt, M. (1995) *Phys. Rev. B* **52** (19) 13726.
Schröter, W. and Seibt, M. (1999). *Properties of crystalline silicon.* ed Hull, R. (London: IEE) p561.
Schröter, W. and Cerva, H. (2002) *Solid State Phenom.* **85-86** 67.
Seifert, W. and Kittler M. (2001) *Solid State Phenomena* **78-79** 253.
Shen, B., Sekiguchi, T. and Sumino, K. (1996) *Jpn. J. Appl. Phys.* **35** 3301.
Schlangenotto, H., Maeder, H. and Gerlach, W. (1974) *Phys. Status Solidi (A)* **21** 357-367.
Schuppler, S., Friedman, S. L., Marcus, M. A., Adler, D. L., Xie, Y. -H., Ross, F. M., Harris, T. D., Brown, W. L., Chabal, Y. J., Brus, L. E. and Citrin, P. H. (1994) *Phys. Rev. Lett.* **72** 2648.
Seibt, M. (1996) *Mater. Res. Soc. Symp. Proc.* **429** 109.
Seibt, M., Imscheliweiller, J. and Hefner, H. A. (1994) *Mater. Res. Soc. Symp. Proc.* **316** 167.
Seibt, M., Hedemann, H., Istratov, A. A., Riedel, F., Sattler, A. and Schröter, W. (1999) *Phys. Stat. Sol. (a)* **171** 301.
Seibt, M. and Schröter, W. (1989) *Phil. Mag. A* **59** 337.
Silcock, J. M. and Tunstall, W. J. (1964) *Phil. Mag.* **10** 361.
Sobolev, N. A., Emel'yanov, A. M., Shek, E. I. And Vdovin, V. I. (2003) *Physica B* **340-342** 1031-1035.
Sobolev, N. A., Emal'yanov, A. M., Shek, E. I. and Vdovin, V. I. (2004) *Physics of the Solid State* **46** (1) 35-39.
Soref, R. A. (1993) *Proc. IEEE* **81** 1687.
Steinman, E. A. (1994) *Mater. Sci. Forum* **143-147** 537.
Stickler, R. and Booker, G. R. (1963) *Phil. Mag.* **8** 859.
Stowe, D. J., Fraser, K. J., Galloway, S. A., Senkader, S., Falster, R. J. and Wilshaw, P. R. (2005) *Springer Proc. in Phys.* **107** (eds. Cullis, A. G. and Hutchinson J. L.) 355.
Suezawa, M., Sumino, K. and Nishina, Y. (1982) *J. J. Appl. Phys.* **21** L518.
Sun, J. M., Dekorsky, T., Skorupa. W., Schmidt, B. and Helm, M. (2003) *Appl. Phys. Letts.* **83** (19) 3885-3887.
Sun, J. M., Dekorsky, T., Skorupa, W., Schmidt, B., Müklich, A. and Helm, M. (2004) *Phys. Rev. B* **70** 155316.
Sveinbjörnsson, E. O. and Weber, J. (1996) *Appl. Phys. Lett.* **69** (18) 2686-2688.

Sze, S. M. (1981) *Physics of semiconductor devices 2nd edition* Wiley, New York.

T

Tan, T. Y., Foll, H. and Hu, S. M. (1981) *Phil. Mag A.* **44** 127.
Tan, S.-E., Schroder, D. K., Kohno, M. and Miyazaki, M. (2000) *IEEE Trans. Elec. Dev.* **47** (12) 2392.
Theis, T. N. (2000) *IBM J. Res. Dev.* **44** 379.
Tice, W. K. and Tan, T. Y. (1976) *Appl. Phys. Letts.* **28** (9) 564.
TRIM-95, after Ziegler, J. F., Biersack J. P. and Littmark, D. in *The Stopping and Ranges of Ions in Solids*, ed. Ziegler, J. F. (1985) Pergamon, NewYork, Vol. 1.
Troxell, J. R., Chattergee A. P., Watkins, G. D. and Kimerling, L. C. (1979) *Phys. Rev. B* **19** (10) 5336.
Trupke, T., Zhao, J. H., Wang, A. H., Corkish, R. and Green, M. A. (2003a) *Appl. Phys. Lett.* **82** (18) 2996.
Trupke, T., Green, M. A., Wűrfel, P., Altermatt, P. P., Wang, A., Zhao, J. and Corkish, R. (2003b) *Appl. Phys. Lett.* **94** (8) 4930-4937.
Trupke, T. (2006) *J. Appl. Phys.* **100** 063531.
Tsu, R. (1993). *Nature* **364**, 19.
Tsybeskov, L., Duttagupta, S. P., Hirschman, K. D., and Fauchet, P. M. (1996). *Appl. Phys. Letts.* **68** (15) 2058-2060.

UV

Uhlir, Jr., A. (1956) *Bell Syst. Tech. J.* **35** 333-347.
Van Hoy, G. (2004) http://www.gartner.com visited March 2005.
Vandervorst, W., Houghton, D. C., Shepherd, F. R., Swanson, M. L., Plattner, H. H. and Carpenter, G. J. C. (1985) *Can. J. Phys.* **63** 863.
Varshni, Y. P. (1969) *Phys. Status Solidi* **19** 459.
Veprek, S., Iqbal, Z. and Sarrott, F. A. (1982) *Phil. Mag. B* **45** 137.
Vouk, M. A. and Lightowlers, E. C. (1977) *J. Phys. C* **10** 3689; *J. Lumin.* **15** 17.

W

Wagner, J., Gelpey, J. C. and Hodgson, R. T. (1984) *Appl. Phys. Lett.* **45** 47.
Weber, E. and Alexander, H. (1979) *J. Physique Coll.* **40** C6 101.
Weman, H., Monemar, B. and Holtz, P. O. (1985) *Appl. Phys. Lett.* **47** 1110.
Weman, H., Monemar, B., Oehrlein, G. S. and Jeng, S. J. (1990) *Phys. Rev. B* **42** (5) 3109-3112.
Williams, J. S. (1998) *Mat. Sci. and Eng. A* **253** 8-15.
Williams, D. B. and Carter, C. B. (1996) *Transmission Electron Microscopy*, Plenum Press, New York.
Wilshaw P. R. (1984) *DPhil thesis*, Dept. of Materials, Univ. of Oxford.
Wilshaw, P. R., Fell, T. S. and Booker, G. R. (1989) in *Point and Extended Defects in Semiconductors*, (eds. Benedek, G. Cavallini, A. and Schröter W). (Plenum, New York, p. 243.)
Wilshaw, P. R., Fell, T. S., Amaku, C. A. and de Coteau, M. D. (1994) *Mater. Sci and Eng. B.* **24** 8-14.
www.intel.com:http://www.intel.com/pressroom/kits/events/moores_law_40th visited April 2006.

XYZ

Xuan, L., Zhang, S. B. and Wei, S. -H. (2002) *Phys. Rev. Lett.* **89** (7) 076802.
Yao, J. –H., Elder, K. R., Guo, H. and Grant, M. (1992) *Phys. Rev. B* **45** (14) 8173 -8176.
Yoffe, A. D. (1993) *Advan. Phys.* **42** 173-262.
Zachai, R., Eberl, K., Abstreter, G., Kasper, H. and Kibbel, H. (1990) *Phys. Rev. Lett.* **64** 1055-1058.
Zdetis, A. D. (1979) *Chem. Phys.* **40** 345.
Zheng, B., Michel, J., Ren, F. Y. G., Kimerling, L. C., Jacobson, D. C. and Poate, J. M. (1994) *Appl. Phys. Lett.* **64** (21) 2842-2844.